

FINAL

IN-45-CR

7895

11CIT. p. 139

Final Report on

**Continued Development and Validation of the AER Two-Dimensional  
Interactive Model**

(Contract NASW-4775)

by

M. K. W. Ko, N.-D. Sze, R.-L. Shia, R. M. MacKay, D. K. Weisenstein, and  
S. T. Zhou

Atmospheric and Environmental Research, Inc.  
840 Memorial Drive, Cambridge, MA 02139

Prepared for

National Aeronautics Space Administration  
Headquarters, Washington, DC 20546

December 1995

(NASA-CR-200141) CONTINUED  
DEVELOPMENT AND VALIDATION OF THE  
AER TWO-DIMENSIONAL INTERACTIVE  
MODEL Final Report, Jan. 1993 -  
Dec. 1995 (Atmospheric and  
Environmental Research) ~~132~~ p

241

N96-18522

Unclass

G3/45 0099867

## Table of Contents

Executive Summary .....	1
1. Refinements of the 2-D Chemistry Transport Model .....	2
2. Sulfur Model .....	7
3. Three-wave Model .....	8
4. 3-D Isentropic Transport Model .....	10
5. The AER Interactive Climate Chemistry Model (ICCM).....	11
6. Related Activities .....	18
7. Publications List.....	19
Appendix A Kotamarthi, V.R., M.K.W. Ko, D.K. Weisenstein, J.M. Rodriguez, and N.D. Sze (1994) The effect of lightning on the concentration of odd nitrogen species in the lower stratosphere: An update. <i>J. Geophys. Res.</i> , 99, 8167-8174.	
Appendix B Gunson, M.R. et al. (1994) Increase in levels of stratospheric chlorine and fluorine loading between 1985 and 1992. <i>Geophys. Res. Lett.</i> , 21, 2,223-2,226.	
Appendix C Zander, R., E., et al. (1994) Secular evolution of the vertical column abundances of CHClF <sub>2</sub> (HCFC-22) in the earth's atmosphere inferred from ground-based IR solar observations at the Jungfraujoch and at Kitt Peak, and comparison with model calculations. <i>J. Atmos. Chem.</i> , 18, 129-148	
Appendix D Weisenstein, Debra K., Glenn K. Yue, Malcolm K.W. Ko, Nien-Dak Sze, Jose M. Rodriguez, and Courtney J. Scott (1995) A Two Dimensional Model of Sulfur Species and Aerosols. Submitted to the <i>J. Geophys. Res.</i>	
Appendix E M.K.W. Ko, H.R. Schneider, R.L. Shia, D.K. Weisenstein, and N.D. Sze (1993) A two-dimensional model with coupled dynamics, radiation and photochemistry. 1. Simulation of the middle atmosphere. <i>J. Geophys. Res.</i> , 98, 20,429-20,440.	
Schneider, H.R., M.K.W. Ko, R.-L. Shia, and N.-D. Sze (1993) A two-dimensional model with coupled dynamics, radiative transfer and photochemistry. 2. Assessment of the response of stratospheric ozone to	

increased levels of CO<sub>2</sub>, N<sub>2</sub>O, CH<sub>4</sub> and CFCs. *J. Geophys. Res.*, **98**, 20,440-20,450.

- Appendix F Shia, R.-L., S. Zhou, M.K.W. Ko, N.-D. Sze, D. Salstein, and K. Cadypereira (1995) A three-wave atmospheric model with coupled dynamics, radiation and photochemistry. In preparation.
- Appendix G Shia, R.-L. and M.K.W. Ko (1995) Three-dimensional transport model and cross isentropic surface transport.
- Appendix H Molnar, G.I., M.K.W. Ko, S. Zhou, and N.D. Sze (1994) Climatic consequences of observed ozone loss in the 1980s: Relevance to the greenhouse problem. *J. Geophys. Res.*, **99**, 25,755-25,760
- Appendix I MacKay, R.M., M.K.W. Ko, S. Zhou, G. Molnar, R.-L. Shia, and Y. Yang (1995) An estimation of the climatic effects of ozone during the 1980s: The role of the ozone hole. Submitted to the *J. of Climate*.
- Appendix J Ko, M.K.W., R.M. MacKay, G. Molnar, Y. Yang, and S. Zhou (1995) The Global Change of Temperature and Ozone Simulated by a Coupled Climate-Chemistry Model. In preparation.
- Appendix K Proceedings of the PRC/USA Third Workshop on Atmospheric Chemistry Studies, Beijing, PRC, August 1-4, 1994.

## Executive Summary

Results from two-dimensional chemistry-transport models have been used to predict the future behavior of ozone in the stratosphere. Since the transport circulation, temperature, and aerosol surface area are fixed in these models, they cannot account for the effects of changes in these quantities, which could be modified because of ozone redistribution and/or other changes in the troposphere associated with climate changes. Interactive two-dimensional models, which calculate the transport circulation and temperature along with concentrations of the chemical species, could provide answers to complement the results from three-dimension model calculations. In this project, we performed the following tasks to in pursuant of the respective goals:

- (1) We continued to refine the 2-D chemistry-transport model so that appropriate parameterizations can be validated and incorporated into the 2-D interactive model.
- (2) We developed a microphysics model to calculate the aerosol loading and its size distribution. These properties are determined in the model by the abundances of the gas-phase precursors, the concentrations of key trace species such as ozone and OH, and the ambient temperature and water vapor concentrations.
- (3) The treatment of physics in the AER 2-D interactive model were refined in the following areas: the heating rate in the troposphere and wave-forcing from propagation of planetary waves. The former is achieved by coupling the AER 2-D interactive model to the AER 2-D climate model so that the heating rates in the troposphere are computed taking into account heating by latent heat exchange, ocean transport, and convection. The latter is acheived by developing the three-wave interactive two-dimensional model which calculates the amplitudes of the planetary waves explicitly.

We present the results from our three-year study in this report. We will concentrate on the model development aspects of the work. Applications of the models are reported in the parallel project, NASW-4774.

We summarize in section 6 the activities we participated in using support from this project. A list of publication is given in section 7.



## 1. Refinements of the 2-D Chemistry Transport Model

### Model Improvements

The AER 2-D chemistry-transport model has been upgraded during the period of this contract. The vertical resolution has been increased by a factor of three, from 3.5 km to 1.2 km. This provides the vertical resolution necessary to address certain problems, such as transport and heterogeneous chemistry in the lower stratosphere. Tropopause heights now are calculated monthly based on temperature gradients (Kotamarthi et al., 1994 see Appendix A). The temperature field adopted is the NMC 8-year average for the period 1979-1986.

A major improvement to the AER model was adoption of the photolysis code of Professor Michael Prather (University of California, Irvine), which has been used as the benchmark for the photolysis intercomparison exercise. The previous AER photolysis code was found to perform well with overhead sun, but not for low sun angle and when scattering is important. Reaction rates and photolysis cross-sections have been updated according to JPL-94 (DeMore et al., 1994). The heterogeneous reaction  $\text{BrNO}_3 + \text{H}_2\text{O} = \text{HOBr} + \text{HNO}_3$  (Hansen and Ravishankara, 1995) has been added to the model and found to have a significant impact on ozone depletion calculations.

The 2-D chemistry-transport model can now employ two different types of atmospheric circulations. The "Global Diffuser" model represents the normal circulation of the AER model, with significant lower stratospheric horizontal diffusion from the tropics to mid-latitudes. The "Tropical Barrier" model (Plumb 1995) substantially lowers the horizontal diffusion in the equatorial lower stratosphere, creating a "barrier" to cross-tropical transport from the tropopause up to 34 km by setting  $K_{yy}$  values to  $3.0 \times 10^8 \text{ cm}^2 \text{ sec}^{-1}$  between  $\pm 18.9$  degrees latitude. A number of calculations have been performed with both types of circulations for comparison. These will be discussed later.

### UNEP Simulations

AER participated in the preparation of the 1994 UNEP report "Scientific Assessment of Ozone Depletion: 1994". Malcolm Ko was the lead author for Chapter 6 "Model Simulations of Stratospheric Ozone" and Debra Weisenstein contributed model results. A total of 9 models participated in the intercomparison exercised presented in Chapter 6. Model-calculated total ozone for 1980 was compared with TOMS

observations, showing that most models are within 20% of observations outside the polar regions. Calculated ozone at 44 km is smaller than SBUV observations by 20-40%, an issue which has remained unresolved since the 1993 Models and Measurements Inter-comparison Workshop. Trends in ozone between 1980 and 1990 were also calculated and compared to various measurements. High latitude ozone trends were not reproduced by model calculations.

The effects of the Mt. Pinatubo volcanic eruption were simulated in model calculations by increasing aerosol surface area by a factor of 30 over background and then allowing it to decay with a time constant of one year. Models predict the greatest impact on ozone due to increased aerosol loading in 1992, with column depletions at 50°N ranging from 2% from the AER model to 8% for the Italy and NCAR models.

Model calculations were performed for two different projected future atmospheres. Scenario I assumes that the Copenhagen Amendments to the Montreal Protocol are followed and CH<sub>3</sub>Br is maintained at 1991 levels. This scenario was calculated out to 2050. Scenario II assumes only partial compliance with the protocol for CFCs, CH<sub>3</sub>CCl<sub>3</sub>, and CCl<sub>4</sub>. CH<sub>3</sub>Br emissions are also assumed larger. This scenario was calculated only to 2010. Maximum ozone decreases occurs in about 1998 and range from 4 to 9% below that of 1980 at 60°N.

Additional details of this work will be reported in NASW-4774.

### Sensitivity Studies

In the process of updating and testing the AER model, we have explored model sensitivity to a number of parameters. The impact on the model results of adopting the Prather (UCI) photolysis code is illustrated in Table 1 by the atmospheric lifetimes of N<sub>2</sub>O, CFCs, and other compounds using the old AER code (column 2) and the uci code (column 3). The difference in these results is due to spherical geometry, scattering, and the use of temperature-dependent cross-sections of O<sub>2</sub> and O<sub>3</sub> in overhead columns. Cross-sections, wavelength intervals, and solar fluxes are identical for both results shown. Though the lifetimes differ by only a few percent for the annual average global mean, photolysis rates at high zenith angle and high optical depth can be very different.

The use of the tropical barrier, or pipe, circulation also affects calculated species lifetimes. Columns 3 and 4 of Table 1 illustrate this. With the pipe circulation, all of the lifetimes become shorter, by as much as 25% for some species. This is because the pipe

circulation confines species in the tropical stratosphere for a longer period of time, where sunlight can dissociate the molecule, thus reducing its lifetime.

Another example of model sensitivity is illustrated in Figure 1, which shows calculated column ozone change at 57°N as a function of time following the Pinatubo eruption, using the aerosol parameterization discussed in section 1(b). In the figure, the curve labeled Model A represents the calculation published in WMO (1995) and discussed above. The curve labeled Model B represents the same calculation, but with the  $\text{BrNO}_3 + \text{H}_2\text{O}$  heterogeneous reaction added. Ozone column depletion due to the volcanic aerosol increases from 2.1% to over 3.2% due to this reaction alone. The curve labeled Model C represents a model with the tropical barrier circulation, but otherwise identical to Model B. The effect of the tropical barrier circulation was to increase ozone depletion again, up to 4%.

Table 1: Model-calculated lifetimes (years) using the AER model with and without the UCI method for photolysis rate calculation, and with and without the tropical barrier.

Species	Old AER Code Global Diffuser	UCI Code, Global Diffuser	UCI Code Tropical Barrier
$\text{N}_2\text{O}$	128.0	131.8	102.7
CFC-11	52.9	56.7	45.3
CFC-12	108.2	112.4	85.9
CFC-113	90.2	94.2	71.8
$\text{CCl}_4$	44.7	47.9	39.3

#### ODP and Lifetime Update

During the last year of this contract period, we have calculated ozone depletion potentials for 22 species using the most up-to-date AER model with the uci photolysis code and JPL-94 reaction rates. The tropical barrier circulation and the  $\text{BrNO}_3 + \text{H}_2\text{O}$  reaction were not used. For the most part, ODP values and atmospheric lifetimes have not changed substantially from previous calculations. The exceptions are CFC-113, CFC-114, HCFC-22, and HCFC-142b.

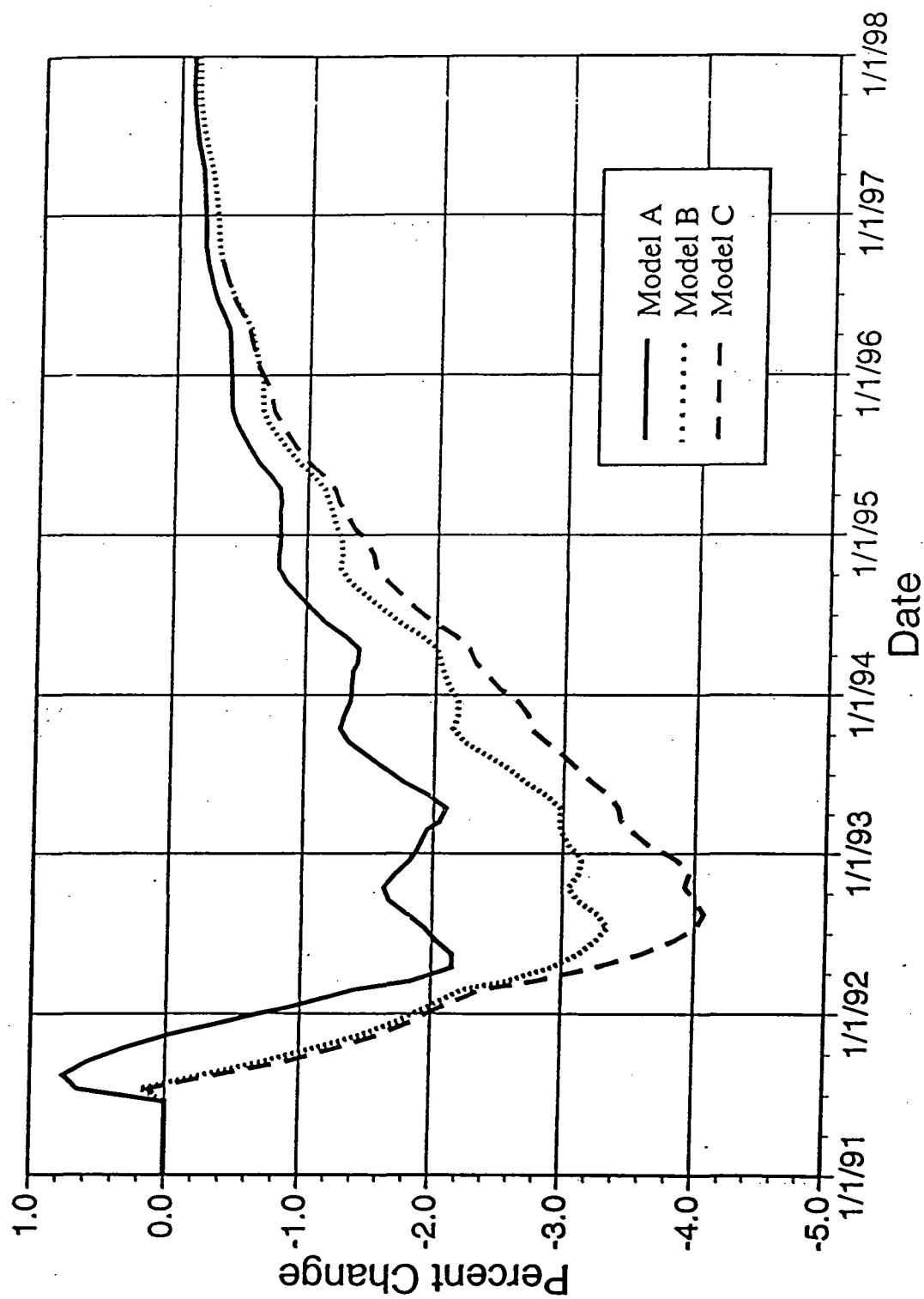


Figure 1.1: Calculated percent change in ozone column at 57°N due to heterogeneous chemistry on sulfate aerosols following the Mt. Pinatubo eruption. Model A is the calculation published in WMO (1995). Model B also includes the  $\text{BrNO}_3 + \text{H}_2\text{O}$  heterogeneous reaction. Model C includes this reaction and in addition uses the tropical barrier circulation.

Table 2a: Revised values of CLP and ODP based upon new lifetime

	Reference Lifetime (y)	CLP	ODP/CLP	ODP
CFC-11	50	1.00	1.00	1.00
CFC-12	111	1.50	0.65	0.97
CFC-113	93.6	1.22	0.65	0.79
CFC-114	216	2.06	0.31	0.65
CFC-115	714	3.76	0.11	0.40
CCl <sub>4</sub>	47.7	1.01	1.05	1.06
CH <sub>3</sub> CCl <sub>3</sub>	4.9	0.11	1.02	0.11
HCFC-22	12.2	0.14	0.19	0.03
HCFC-123	1.4	0.02	0.94	0.02
HCFC-124	6.2	0.04	0.36	0.02
HCFC-141b	9.5	0.16	0.76	0.12
HCFC-142b	19.1	0.19	0.19	0.04
HCFC-225ca	2.0	0.02	0.85	0.02
HCFC-225cb	6.2	0.06	0.43	0.03

Table 2b: Revised values of GWP based upon new lifetime

Compound	Reference Lifetime (y)	Forcing per unit mass*	GWP 20	GWP 100	GWP 500	HGWP
CFC-11	50	1.00	4950	3970	1440	1.00
CFC-12	111	1.45	7930	8740	4550	3.22
CFC-113	93.6	0.93	5035	5258	2491	1.74
CFC-114	216	1.18	6780	8690	6610	5.10
CFC-115	714	1.04	6162	8924	10744	14.85
CCl <sub>4</sub>	47.7	0.41	2015	1580	563	0.39
CH <sub>3</sub> CCl <sub>3</sub>	4.9	0.23	328	102	32	0.02
HCFC-22	12.2	1.37	4030	1530	479	0.33
HCFC-123	1.4	0.72	304	93	29	0.02
HCFC-124	6.2	0.88	1570	499	156	0.11
HCFC-141b	9.5	0.73	1407	490	153	0.14
HCFC-142b	19.1	1.12	4170	1960	615	0.43
HCFC-225ca	2.0	0.72	439	134	42	0.03
HCFC-225cb	6.2	0.87	1570	500	156	0.11
HFC-125	31.2	1.03	4570	2830	923	0.64
HFC-134a	14.0	1.04	3310	1330	417	0.29
HFC-143a	46.6	1.03	5030	3900	1380	0.96
HFC-152a	1.5	1.02	465	142	44	0.03

\* radiative forcing relative to CFC-11 per unit mass change in the atmosphere (WMO, 1995). GWP calculations use the Bern model CO<sub>2</sub> lifetime.

## Chlorine Budget

Under this contract, the AER 2D model was applied to analyze trends in HCFC-22, HF, and HCl for comparison with spectroscopic measurements. Ground-based IR observations of HCFC-22 at Kitt Peak and the Jungfraujoch are described in Zander et al. (1994). The AER model was used to simulate HCFC-22 at the same times (1986-1992) and locations as the observations and was found to agree well, giving confidence to reported emission data. Concentrations of HF and HCl above 50 km were measured by the ATMOS instrument aboard the space shuttle in 1985 and 1992 (Gunson et al., 1994). The observed trend in HCl was 0.13 ppbv per year and in HF was 0.07 ppbv per year, which agrees well with model predicted increases in ClY and HF. Such applications of the AER 2D model are extension of previous work in which reported releases of CFCs and HCFCs were used to calculate trends in ClY and to apportion the ClY among various source gases (Weissenstein et al., 1992). Zander et al. (1994) and Gunson et al. (1994) are included as Appendix B and Appendix C in their report.

## **2. Sulfur Model**

We have combined the AER chemical transport model for gas phase sulfur species with the aerosol microphysics code of Dr. Glenn Yue at NASA/Langley to produce a sulfate aerosol model. The gas phase sulfur species are DMS, MSA, H<sub>2</sub>S, CS<sub>2</sub>, OCS, SO<sub>2</sub>, SO<sub>3</sub>, and H<sub>2</sub>SO<sub>4</sub>. OCS is the major stratospheric source of SO<sub>2</sub>, producing 46 kilotons of sulfur per year. SO<sub>2</sub> oxidation leads to SO<sub>3</sub>, which has a lifetime of only minutes in the lower stratosphere due to reaction with H<sub>2</sub>O to produce H<sub>2</sub>SO<sub>4</sub>. Aerosols are represented in the model by 40 size bins, ranging from 0.39 nm to 3.2 μm. Model processes which convert gas phase H<sub>2</sub>SO<sub>4</sub> to aerosol particles are homogeneous nucleation, which produces new particles, and heteromolecular condensation, which increases the size of existing aerosol particles. Coagulation can also affect the distribution of aerosol particle sizes. Sedimentation rates are a function of aerosol size and air density, and partially control the stratospheric lifetime of aerosols. Aerosols evaporate in the upper stratosphere, yielding H<sub>2</sub>SO<sub>4</sub> gas which can photodissociate into SO<sub>3</sub> and eventually SO<sub>2</sub>.

The AER/Langley sulfate aerosol model is fairly successful at reproducing the background aerosol layer for non-volcanic conditions. Calculated background aerosol surface areas range from 0.4 in the tropics to 1.4 μm<sup>2</sup>/cm<sup>3</sup> at high latitudes. The calculated stratospheric aerosol burden is 283 kilotons. The estimated aerosol burden for

1979 was 540 kilotons (Kent and McCormick, 1984). Calculated optical depths at 1.02  $\mu\text{m}$  are about 30-50% lower than observations in the lower stratosphere, indicating that the model produced too many small particles.

Our sulfate model has been used to simulate the Mt. Pinatubo eruption of June 1991. With an injection of 17 megatons of  $\text{SO}_2$ , the model yields 28.6 megatons of aerosols five months after the eruption. The aerosol mass subsequently decays with a time constant of 13 months. These results are in very good agreement with both the magnitude and temporal evolution of the Mt. Pinatubo aerosols.

A paper including the aerosol model description, results for the background atmosphere, and the Mt. Pinatubo simulation has been submitted to *JGR* and is included here as Appendix D.

### 3. Three-wave Model

Two-dimensional (zonal mean) chemistry transport models (2-D CTM) have played an important role in understanding various physical and chemical processes which control the distributions of chemical constituents in the atmosphere. They have been extensively used to assess the atmospheric effects of anthropogenic pollutants and other events because comprehensive three-dimensional models with full chemistry are too computationally intensive to run for long term simulation of the atmosphere.

Most 2-D models belong to the 'off-line' category. This means that the transport and temperature fields used in the model are prescribed and the same data set is used for all model runs. In contrast, the interactive models calculate these fields along with the distributions of atmospheric constituents. Thus the interactive model includes feedback effects in the model simulations. When the perturbations are large, the feedback effects can be important. The AER 2-D interactive model (Ko et al., 1993, Appendix E) was used to study the response of stratospheric ozone to the increases of  $\text{CO}_2$ ,  $\text{N}_2\text{O}$ ,  $\text{CH}_4$ , and CFC's (Schneider et al., 1993, Appendix E) and to HSCT engine emissions (Shia et al., 1993, the interim report for NAS1-19422). Moderate effects due to radiative feedbacks through the change of circulation are found in these studies.

Two essential steps in any interactive 2-D model are the calculation of the E-P flux divergence and the parameterization of the eddy flux for trace species. Because the E-P flux divergence is related to the eddy flux of potential vorticity (PV) in quasi-geostrophic theory, both eddy fluxes can be viewed as contributions of eddy transport to

the evolution of zonal mean variables (PV and mixing ratio of tracers, respectively). They are closely related and should be calculated consistently (Tung, 1987). While it is commonly accepted that eddy transport in the middle atmosphere is mainly due to organized planetary waves (as opposed to chaotic or turbulence mixing), there are still controversies about how to parameterize the eddy fluxes.

A popular scheme is to assume that the eddy flux is a diffusive flux and the same diffusion coefficients are used in parameterization of the eddy flux for trace species and PV. Since winds derived from observations allow us to calculate the PV eddy flux  $(\overline{v' \cdot q'})$  and PV gradient  $\left(\frac{\partial \bar{q}}{\partial y}\right)$ , they can be used to determine the eddy diffusion

coefficients by

$$K \frac{q}{yy} = \frac{v' q'}{\frac{\partial q}{\partial y}}.$$

The eddy diffusion coefficients used in the AER 2-D interactive model (Ko et al., 1993) are calculated from the above relation using observed data. However, this scheme could overestimate the eddy diffusion coefficient because the PV eddy flux could include the contribution due to PV dissipation in addition to the eddy contribution which is the object of the eddy parameterization.

The AER 3-wave model couples a semi-spectral dynamical model with a zonal mean chemistry transport model and a radiative transfer code. The model calculates the E-P flux divergence and the eddy diffusion coefficients for chemical tracers in terms of the amplitudes, their time dependence and phases of dynamical waves simulated in the model. In addition, the eddy diffusion coefficient for a chemical tracer also contains a term related to the local chemical loss rate of the tracer. Compared with commonly used parameterized values, the model calculated eddy diffusion coefficients for chemical species are smaller, especially in subtropics. Therefore, some of the model results show the effects of the so called tropical barrier. The 3-wave model has been used to simulate the present day atmosphere. In spite of the high truncation in the dynamical module (only three longest waves are resolved), the model has simulated many observed characteristics of stratospheric dynamics and distributions of chemical species including ozone. Compared with commonly used parameterized values, the model calculated eddy diffusion coefficients for chemical species are smaller, especially in subtropics. Therefore, some of the model results show the effects of the so-called tropical barrier (Plumb 1995). The model results also show that the contribution to the eddy flux from



chemical reactions is not essential in determining the tracer distribution in the stratosphere. More details can be found in the Appendix F.

The 3-wave model was used to investigate the feedback effects of the ozone change in a HSCT scenario with Mach number = 2.4 and  $\text{NO}_x$  emission index (EI) = 15. The calculated changes in column ozone due to HSCT emissions shows considerable difference when the feedback is included, especially in the southern hemisphere. The change in circulation and the change in eddy diffusion coefficient are each responsible for about the same effects. But the feedback through the change of temperature is negligible just as in AER 2-D interactive model results as indicated in Schneider et al. (1993).

#### 4. 3-D Isentropic Transport Model

Vertical transport in isentropic coordinates is generated only by diabatic processes. Motions caused by adiabatic processes are absorbed into the motions of isentropic surfaces, which are the coordinate planes themselves. This provides much numerical simplification for both modeling and data analysis and is particularly useful in the stratosphere where the diabatic heating is relatively small and dominated by the radiative heating. For example, the trajectory calculations used in many studies to analyze the data from UARS (e.g. Manney et al. 1995; Rodriguez et al. 1995) are done either on the isentropic surface (neglecting the vertical transport) or using radiative heating rates to derive the vertical transport across the isentropic surface. Some 2-D modelers have made use of this early on (Ko, et al. 1985; Yang, et al. 1991; Kinnersley and Harwood, 1993) and their results are at least comparable with those from models formulated in pressure coordinates.

We think isentropic coordinate is also useful in 3-D modeling. Results of 3-D CTM in the pressure coordinates have shown some problems related to the treatment of vertical transport. The ozone simulations using winds from data assimilation system have shown large biases when compared with TOMS and LIMS measurements (Rood et al. 1991; Allen et al. 1991). It is argued that the periodic insertion of observational data during the assimilation process violates the thermodynamic balance and generates vertical velocities that disagree with vertical velocities of the residual circulation calculated using diabatic heating rates (Weaver et al. 1993). Using isentropical coordinates in 3-D model may be a way to solve this problem.

We have developed a three-dimensional transport model in isentropic coordinates. The daily NMC temperature and geopotential data are used to define the location of

isentropic surfaces and the Montgomery streamfunction. The horizontal velocities in the isentropic surface are calculated from the Montgomery streamfunction as the geostrophic winds or the "linear balance" winds. Three different sets of velocities across isentropic surfaces can be derived using three different methods. First, the velocity can be derived from the net radiative heating rates assuming that it is the dominant diabatic process. A fast radiation code is used to calculate the net heating rate from NMC temperature and SBUV ozone distribution. Two different sets of vertical transport velocities can be derived directly from the NMC temperature data. One uses the mass conservation equation and the other uses the Ertel's potential vorticity equation. The derived vertical velocities should include contributions from all diabatic processes, including radiative heating, friction and dissipation.

Our preliminary results show that the vertical velocities from the latter two approaches are much larger than the vertical velocity derived from the net radiative heating. It could mean that other diabatic processes are more important than the radiative heating. However, the vertical velocities derived from the mass conservation equation or from the potential vorticity equation are quite sensitive to the choice of horizontal velocity fields (calculated using geostrophic winds or balanced winds). We think it is premature to draw any conclusion from these experiments and further investigation is required.

The detailed description of the 3-D isentropic model and the preliminary model results can be found in Appendix G.

## **5. The AER Interactive Climate Chemistry Model (ICCM)**

Changes in temperature structure resulting from increased anthropogenic emissions of greenhouse gases can significantly alter both dynamical transport and the oxidizing capacity of the atmosphere, and hence its final chemical composition [see for example Hauglustaine et al., 1994, Schneider et al. 1993; Thompson 1992; and Crutzen and Zimmerman, 1991]. Several recent studies have been directed at estimating the climate-chemistry interactions for realistic atmospheric compositions of the past and present; see for example Hauglustaine et al., 1994, Crutzen and Brühl (1993), and Schneider et al. (1993), and Crutzen and Brühl (1993), using a 1.5-dimensional model with limited simulation of atmospheric dynamical transport, found that their model simulations of total ozone column abundance and atmospheric OH concentrations were relatively insensitive to the changes in atmospheric temperature and chemical

composition between glacial and preindustrial Holocene conditions. Schneider et al. (1993) examined how changes in stratospheric temperatures predicted from increased concentrations of greenhouse gases will alter chemical reaction rates to change the composition of the atmosphere. The simulations performed by Schneider et al. used prescribed changes in tropospheric temperatures for their perturbation studies which limited the ability of their model to simulate feedback processes relating climate change to changes in atmospheric transport. Furthermore, the dynamic formulation in their model (see Ko et al., 1993) is such that the feedback changes in atmospheric circulation is expected to be small.

Rind et al. (1990) have suggested that changes in circulation and eddy transport may be an important feedback connecting changes in climate to changes in atmospheric composition. It is important to use higher dimensional, at least 2-D, fully interactive climate-chemistry models to conduct "closed-loop" experiments to address such questions as how greenhouse forcing, the corresponding O<sub>3</sub> redistribution, and changes in dynamical heating and chemical transport in the stratosphere affect the tropospheric climate, and vice versa.

We have made substantial progress toward the development of such an interactive climate-chemistry (ICC) model. Our strategy has been to use the model of Ko et al. (1993) as a base model and enhance different aspects of it. To improve the ability of the Ko et al. model to simulate climate chemistry interactions two major enhancements were needed: I) couple the Ko et al (1993) model to a climate model so that changes in climatic state variables (temperature, moisture, wind fields, and surface features and processes) are calculated interactively with calculations of atmospheric chemistry; and II) improve the ability of the model to simulate dynamical wave-mean and wave-wave processes to enhance the coupling between tropospheric temperature and stratospheric circulation. This section describes progress made on enhancement I. Progress made on improving the simulation of atmospheric dynamics (enhancement II) is discussed in section 3 in connection with the 3-wave model.

A detailed description of the ICC model is given in Appendix H. Some results of recent experiments performed with the ICC model or its climate module are outlined below.

## Ozone and Climate Change

Since ozone is a good absorber of both solar and terrestrial radiation, and contributes to many of the reactions controlling the chemical composition of the atmosphere, an understanding of its role in global change is of central importance. There has been considerable previous research on the climatic effects of ozone (see for example: Ramanathan and Dickinson, 1979 ; Lacis et al., 1990; Ramaswamy et al., 1992). Many past studies have used the radiative forcing at the tropopause as a proxy of climate change. However, because of meridional heat transport, radiative forcing is actually a poor proxy for climate change ( Molnar et al., 1994). Molnar et al. (1994) [included as Appendix J] used the three zone version of the ASRD climate model (ASRD-3) to estimate the steady state influence of 1979 to 1990 changes in lower stratospheric ozone on the 1979 to 1990 steady state greenhouse warming due to increases in all other greenhouse gases ( $H_2O$ ,  $CO_2$ ,  $CH_4$ ,  $N_2O$ , CFC-11, and CFC-12) over the same time period. They found that when assumed lower stratospheric ozone losses were included in the 1979 to 1990 simulation, the steady state increase in surface air temperature was 28 % lower than when ozone levels were held fixed at their 1979 levels. This 28 % compensation in surface warming is significantly higher than the 17 % decrease in the adjusted radiative forcing calculated by them.

MacKay et al. (1995) [included as Appendix I], using the nineteen zone version of the ASRD climate model (ASRD-19), repeated the study of Molnar et al. (1994) to assess the importance of model resolution on the simulated climatic effects of ozone. They showed that for an assumed ozone loss confined to high latitude regions, based on the 1979 to 1990 TOMS observations, the global climate sensitivity (ratio of the change in steady state global mean annual average surface air temperature to global mean annual average adjusted forcing) was much larger (by a factor of three) than that obtained for a uniform change in greenhouse gases such as for a double  $CO_2$  experiment. For their 1979 to 1990 simulations of changes in steady state surface air temperature, the steady state increase in surface air temperature was 42 % lower when ozone reductions similar to the 1979 to 1990 decreases in lower stratospheric ozone were included in the simulation compared to when ozone levels were held fixed. Both results are consistent with the findings of Molnar et al. (1994), although the ASRD-19 results suggested that climatic effect of changes in high latitude lower stratospheric ozone may have been underestimated by Molnar et al. MacKay et al. identified increases in upper tropospheric meridional heat transport at high latitudes, combined with a decrease in the infrared

opacity of the high latitude lower stratosphere (both a consequence of high latitude lower stratospheric ozone loss) as physical processes responsible for this latitudinal dependent behavior. The sensitivity of the three zone model of M94 was smaller than the ASRD-19 because the three zone model resolution was not high enough to resolve the extreme temperature drops of the lower stratosphere at high latitudes associated with the large local reductions in ozone there. Averaging over the larger model grids associated with the low resolution model, weakened the influence of changes in the dynamical connection between low and high latitudes.

### Climate Chemistry Interaction Studies

To simulate the changes in atmospheric composition, dynamics and temperature structure associated with an increase in atmospheric carbon dioxide, we have run the ICC model to a steady state for  $1\times\text{CO}_2$  (334 ppmv) and  $2\times\text{CO}_2$  (668 ppmv). Since this experiment has been performed many times by others [including Schneider et al. (1993)] we use it as a bench mark of the sensitivity of the ICC model. There are several potential feedbacks included in this experiment. These include changes in atmospheric chemistry, water vapor, meridional heat transport in both the atmosphere and ocean, atmospheric lapse rate, sea-ice cover (ocean sector albedo), and land surface albedo. The change in global mean annual averaged surface air temperature,  $\Delta T_s$ , simulated by the ICC for a doubling of  $\text{CO}_2$  is 2.5 K. This compares well with the range of 1.5 K to 4.5 K given by the IPCC 1990 with a "best guess" of 2.5 K. Figure 5.1 shows the  $2\times\text{CO}_2$ - $1\times\text{CO}_2$  change in annual temperature simulated by the ICC model. Similar to most climate model double  $\text{CO}_2$  simulations the ICC model has greater warming at high latitudes than in the tropics and a substantial reduction in stratospheric temperatures.

The reduced stratospheric temperatures for the double  $\text{CO}_2$  simulation reduces the reaction rates for ozone destruction and hence results in an increase in column ozone. Fig. 5.2 shows the  $2\times\text{CO}_2$ - $1\times\text{CO}_2$  change in column ozone as a function of time of year. The global average annual mean increase in column ozone is 3.7 %. This in agreement with the 3.1 % increase simulated by Schneider et al. (1993), although about 20 % higher. This greater increase in column ozone predicted by the ICC model relative to the model of Schneider et al. is attributable to the difference in simulated temperature change for the lower stratosphere simulated by the two models. For the simulations of Schneider et al. (1993),  $2\times\text{CO}_2$ - $1\times\text{CO}_2$  temperature changes were negative for regions of the atmosphere above about 20 km, and for the ICC model simulations  $2\times\text{CO}_2$ - $1\times\text{CO}_2$  temperature

changes are negative for regions above 13 to 17 km depending on the latitude (see Fig. 5.1). This additional cooling in the lower stratosphere, where ozone concentrations are relatively high, simulated by the ICC model results in its slightly larger  $2\times\text{CO}_2$ - $1\times\text{CO}_2$  increase in column ozone relative to that predicted by Schneider et al.

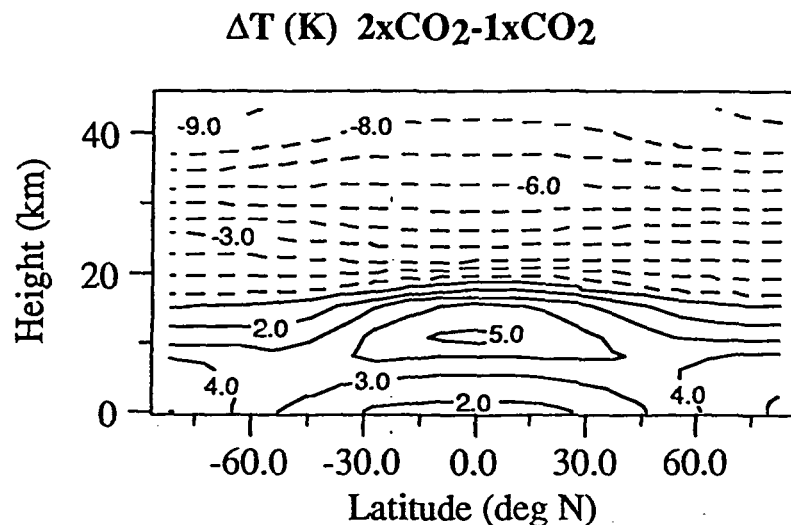


Fig. 5.1.  $2\times\text{CO}_2$ - $1\times\text{CO}_2$  change in annual temperature simulated by the ICC model

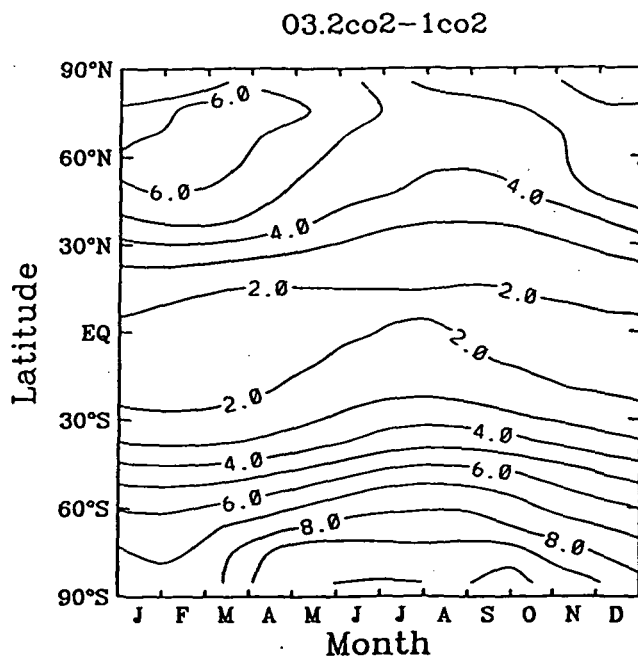


Fig. 5.2  $2\times\text{CO}_2$ - $1\times\text{CO}_2$  change in column ozone simulated by the ICC model

To estimate the changes in surface air temperature brought about by the  $2\times\text{CO}_2$ - $1\times\text{CO}_2$  changes in ozone we have performed a steady state simulation of  $1\times\text{CO}_2$  conditions with sustained  $2\times\text{CO}_2$  ozone concentration profiles and have compared it to the  $1\times\text{CO}_2$  control simulation. Although there are changes in the temperature structure in the stratosphere and upper troposphere resulting from changes in ozone profile, the surface air temperature is essentially unaffected by the  $2\times\text{CO}_2$ - $1\times\text{CO}_2$  changes in ozone. The reason for this is that the percent ozone change is distributed throughout the stratosphere with the largest percent change in mixing ratio located around 40 km. As noted by Lacis et al. (1990) ozone increases above 25 to 30 km result in decreases in surface air temperature and ozone increases below 25 to 30 km result in increases in surface air temperature. Thus for our simulation, the net change in surface air temperature is negligible. As the ozone concentrations increase in the stratosphere the temperature tends to increase there. This acts as a negative feedback which limits both the magnitude of the stratospheric temperature decreases associated with increased greenhouse gases and the magnitude of the ozone increase associated with reductions in stratospheric temperature. As in the simulations of Schneider et al. (1993) the ozone concentrations in the lower tropical stratosphere decrease with doubled  $\text{CO}_2$  despite the decrease in temperatures there. This reverse self healing effect simulated by the ICC model, due to the decrease in photochemical production of ozone associated with the photon shielding from the increased ozone concentrations above, is comparable in magnitude to that simulated by Schneider et al. (1993).

The  $2\times\text{CO}_2$ - $1\times\text{CO}_2$  changes in the concentrations methane, nitrous oxide are shown and discussed in Appendix H. For the troposphere and lower stratosphere the concentrations of these greenhouse gases are affected very little by doubling carbon dioxide. However, there are substantial increases of methane and nitrous oxide in the middle to upper stratosphere. The increased concentrations of methane and nitrous oxide in the middle to upper stratosphere amplify the temperature reductions there beyond what would be expected from doubling of  $\text{CO}_2$  alone.

The  $2\times\text{CO}_2$  change in zonal mean zonal velocity for January is shown in Fig. 5.3. We have not included a physically based parameterization of the eddy momentum fluxes in these calculations to simulate wave-mean and wave-wave interactions. There are substantial increases in the easterlies at middle latitudes of both winter hemispheres in the upper stratosphere near 50 km. However, the changes in atmospheric dynamics in the lower stratosphere and troposphere are much smaller. We will incorporate the latest

version of the three wave interactive chemistry/dynamics model in the near future to improve our simulation of the interaction between atmospheric chemistry and climate.

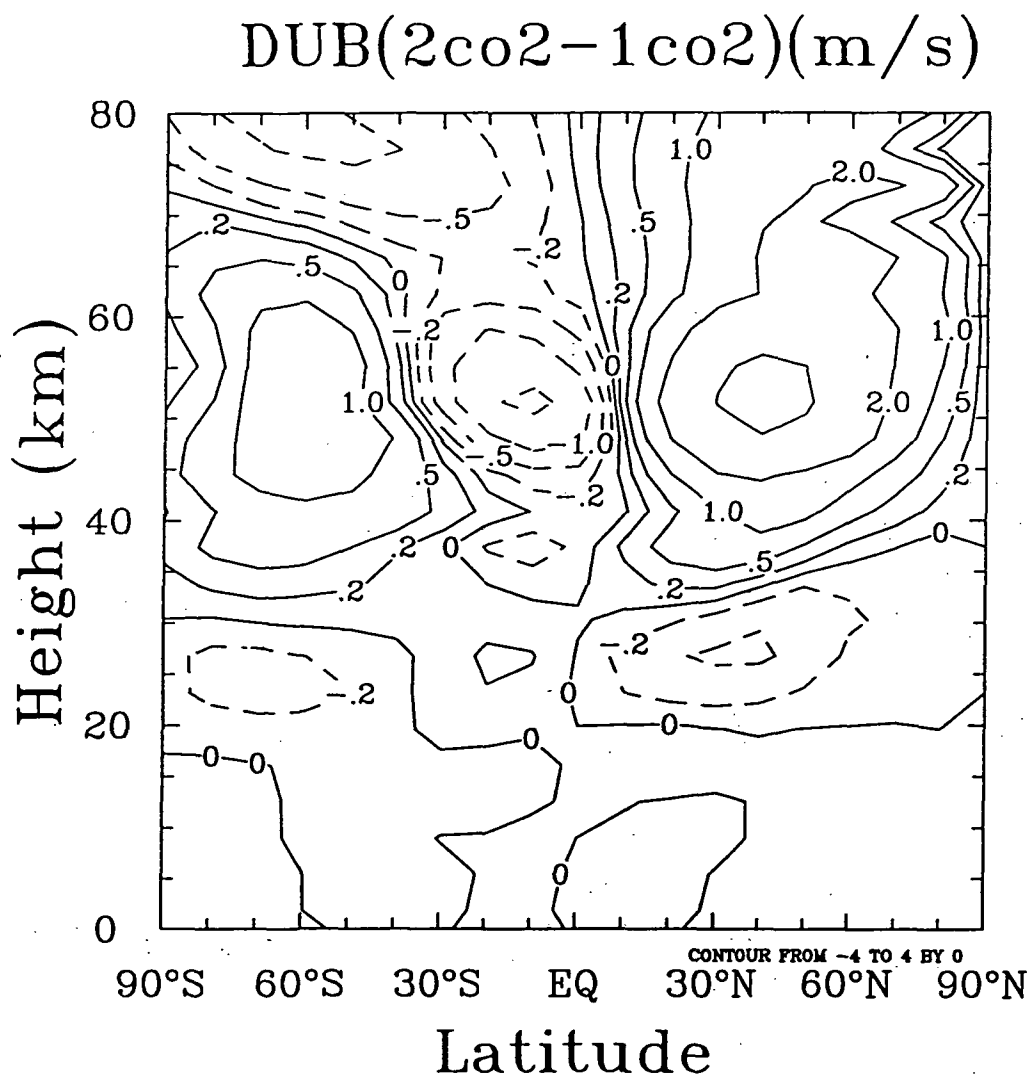


**Fig. 5.3.**  $2xCO_2-1xCO_2$  steady state changes in zonal mean zonal velocity (m/s) simulated by the ICC model for January. Contours are: -2, -1, -0.5, -0.2, 0, 0.2, 0.5, 1.0, 2.0, 4.0.



## 6. Related Activities

We participated in a number of activities that were funded by this contract:

- The CFC Lifetime Report

Malcolm Ko, Debra Weisenstein, Nien-Dak Sze and Jose Rodriguez participated and contributed to the "Report on Concentrations, Lifetimes, and Trends of CFCs, Halons, and Related Species" (Kaye et al., 1994). Malcolm Ko is lead author for Chapter 5: "Model Calculations of Atmospheric Lifetime".

- The 1995 WMO/UNEP Ozone Assessment Report

Staff from AER participated in the preparation of the 1995 WMO/UNEP Ozone Assessment Report. Malcolm Ko is lead author for chapter 6: "Model Simulations of Stratospheric Ozone". Jose Rodriguez is co-author for chapter 10: "Methyl Bromide"; and contributors for chapter 12: "Atmospheric Degradation of Halocarbon Substitutes". Nien-Dak Sze is co-author for chapter 13: "Ozone Depletion Potentials, Global Warming Potentials, and Future Chlorine/Bromine Loading". Debra Weisenstein is a contributor for chapters 6 and 13. Malcolm Ko also attended the peer-review meetings.

- Tropospheric Chemistry Assessment Workshop, April 27-29 1993, Washington, DC.

Malcolm Ko attended the workshop.

- Heterogeneous Chemistry Workshop, November 8-12, 1993, Boulder Colorado.

Malcolm Ko attended the meeting and made presentation.

- The Workshop on Parameterization of Sub-grid Scale Tracer Transport, Nov. 30 - Dec. 31, 1993, Virginia Beach, VA.

Run-Li Shia attended the work shop.

- The 1994 IPCC Report Workshop, Irvine, Ca, January 11-13, 1994.

Malcolm Ko attended the workshop.

- The PRC/USA Third Workshop on Atmospheric Chemistry, August 1-4, 1994, Beijing, China

Nien-Dak Sze helped co-ordinate the meeting. Malcolm Ko and Nien-Dak Sze attended the workshop and made presentation. Nien-Dak Sze worked with the Chinese counterpart to prepare the workshop proceeding. A copy of the proceeding is included as appendix K in this report.

- Launch Vehicles Working Group Technical Interchange Meeting sponsored by NASA-AF/SMC, September 15-16, 1994, Washington, DC.

Malcolm Ko attended the workshop and made presentations.

- The Workshop on Data Needs for Modeling Aqueous Chemical Kinetics for the Global Atmosphere, November 1-2, 1994, Gaithersburg, MD.

Malcolm Ko attended the workshop.

- Science Team meeting of the Stratospheric Tracers of Atmospheric Transport, January 11-12, 1995, Washington DC.; October 23-25 1995, NASA Ames.

Malcolm Ko and Jose Rodriguez attended the workshop.

- Atmospheric Science Measurements from the Space Shuttle, March 21-23, 1995, Washington, DC

Malcolm Ko attended the meeting and made presentations.

## 7. Publications List

- 1 M.K.W. Ko, H.R. Schneider, R.L. Shia, D.K. Weisenstein, and N.D. Sze (1993) A two-dimensional model with coupled dynamics, radiation and photochemistry. 1. Simulation of the middle atmosphere. *J. Geophys. Res.*, 98, 20,429-20,440.
- 2 Schneider, H.R., M.K.W. Ko, R.-L. Shia, and N.-D. Sze (1993) A two-dimensional model with coupled dynamics, radiative transfer and photochemistry. 2. Assessment of the response of stratospheric ozone to increased levels of CO<sub>2</sub>, N<sub>2</sub>O, CH<sub>4</sub> and CFCs. *J. Geophys. Res.*, 98, 20,440-20,450.
- 3 Ko, M. K. W., et al. (1993) Atmospheric sulfur hexafluoride: Sources, sinks and greenhouse warming. *J. Geophys. Res.*, 98, 10,499-10,507.
- 4 Ko, M. K. W. and C.H. Jackman. Model Calculations of Atmospheric Lifetime (1994) Chapter 5 In: *Report on Concentrations, Lifetimes, and Trends of CFCs, Halons, and Related Species*, Edited by J.A. Kay and S.A. Penkett, NASA Reference Publication 1339, Washington, DC.
- 5 Molnar, G.I., M.K.W. Ko, S. Zhou, and N.D. Sze (1994) Climatic consequences of observed ozone loss in the 1980s: Relevance to the greenhouse problem. *J. Geophys. Res.*, 99, 25,755-25,760
- 6 Kotamarthi, V.R., M.K.W. Ko, D.K. Weisenstein, J.M. Rodriguez, and N.D. Sze (1994) The effect of lightning on the concentration of odd nitrogen species in the lower stratosphere: An update. *J. Geophys. Res.*, 99, 8167-8174.
- 7 Gunson, M.R. et al. (1994) Increase in levels of stratospheric chlorine and fluorine loading between 1985 and 1992. *Geophys. Res. Lett.*, 21, 2,223-2,226.
- 8 Zander, R., E., et al. (1994) Secular evolution of the vertical column abundances of CHClF<sub>2</sub> (HCFC-22) in the earth's atmosphere inferred from ground-based IR solar observations at the Jungfraujoch and at Kitt Peak, and comparison with model calculations. *J. Atmos. Chem.*, 18, 129-148.

- 9 Ko, M. K. W. (1995) Model simulations of stratospheric ozone. Chapter 6 In *Scientific Assessment of Ozone Depletion: 1994*. World Meteorological Organization, Global Ozone Research and Monitoring Project, Report No. 37, United Nations Environment Programme/WMO, Geneva, 1995.
- 10 Penkett, S. A., et al. (1995) Methyl Bromide. Chapter 10 In *Scientific Assessment of Ozone Depletion: 1994*. World Meteorological Organization, Global Ozone Research and Monitoring Project, Report No. 37, United Nations Environment Programme/WMO, Geneva, 1995.
- 11 Solomon, S., et al. (1995) Ozone depletion potentials, global warming potentials, and future chlorine/bromine loading. Chapter 13 In *Scientific Assessment of Ozone Depletion: 1994*. World Meteorological Organization, Global Ozone Research and Monitoring Project, Report No. 37, United Nations Environment Programme/WMO, Geneva, 1995.
- 12 Weisenstein, Debra K., Glenn K. Yue, Malcolm K.W. Ko, Nien-Dak Sze, Jose M. Rodriguez, and Courtney J. Scott (1995) A Two Dimensional Model of Sulfur Species and Aerosols. Submitted to the *J. Geophys. Res.*
- 13 Shia, R.-L., S. Zhou, M.K.W. Ko, N.-D. Sze, D. Salstein, and K. Cady-Pereira (1995) A three-wave atmospheric model with coupled dynamics, radiation and photochemistry. In preparation.
- 14 MacKay, R.M., M.K.W. Ko, S. Zhou, G. Molnar, R.-L. Shia, and Y. Yang (1995) An estimation of the climatic effects of ozone during the 1980s: The role of the ozone hole. Submitted to the *J. of Climate*.
- 15 Ko, M.K.W., R.M. MacKay, G. Molnar, Y. Yang, and S. Zhou (1995) The Global Change of Temperature and Ozone Simulated by a Coupled Climate-Chemistry Model. In Preparation.

## 8. References Cited

- Allen, D. J., A. R. Douglass, and R. B. Rood (1991) Application of a monotonic upstream transport scheme to three-dimensional constituent transport calculations. *Mon. Wea. Rev.*, **119**, 2456-2464.
- Crutzen, P.J. and C. Brühl (1993) A model study of atmospheric temperatures and the concentrations of ozone, hydroxyl, and some other photochemically active gases during the glacial, the preindustrial Holocene, and the present, *Geophys. Res. Lett.*, **20**, (11), 1047-1050.
- Crutzen, P.J. and P.H. Zimmerman (1991) The changing chemistry of the troposphere, *Tellus*, **43A**, 136-151.
- DeMore, W.B., et al., Editors (1994) Chemical Kinetics and Photochemical Data for Use in Stratospheric Modeling, Evaluation Number 11, JPL Publication 94-26, NASA/Jet Propulsion Laboratory, Pasadena, California.

- Gunson, M.R. et al. (1994) Increase in levels of stratospheric chlorine and fluorine loading between 1985 and 1992. *Geophys. Res. Lett.*, **21**, 2,223-2,226.
- Hauglustaine, D.A., C. Granier, G.P. Brasseur, G. Megie (1994) The importance of atmospheric chemistry in the calculation of radiative forcing on the climate system, *J. Geophys. Res.*, **99**, 1173-1186.
- Intergovernmental Panel on Climate Change (Houghton et al. eds.), 1990. *Climate Change: The IPCC Scientific Assessment*. WMO, UNEP, Cambridge University Press, Cambridge, New York pp i-364.
- Kaye, J. A., Penkett, S. A. and Ormond, F. M. (1994) *Report on concentrations lifetimes, and trends of CFCs, Halons, and Related Species*, NASA reference publication 1339, Washington, DC.
- Kent, G. S. and M. P. McCormick (1984) SAGE and SAM II measurements of global stratospheric aerosol optical depth and mass loading. *J. Geophys. Res.*, **89**, 5303 - 5314.
- Kinnersley, J. S. and R. S. Harwood, 1993. An isentropic 2-dimensional model with an interactive parameterization of dynamical and chemical planetary-wave fluxes. *Q. J. Roy. Met. Soc.*, **119**, 1167-1193.
- Ko, M. K. W., K. K. Tung, D. Weisenstein, and N. D. Sze (1985) A zonal mean model of stratospheric tracer transport in isentropic coordinates: Numerical simulations for nitrous oxide and nitric acid. *J. Geophys. Res.*, **90**, 2313-2329.
- Ko, M. K. W., D. Weisenstein, N. D. Sze, and K. K. Tung (1985) Simulation of O<sub>3</sub> distribution using a two-dimensional zonal-mean model in isentropic coordinate. In *Atmospheric Ozone*, C. S. Zerefos and A. Ghazi (eds.), Proceedings of the Quadrennial Ozone Symposium held in Halkidiki, Greece, 3-7 September 1984. D. Reidel Publishing Company.
- Ko, M. K. W., H. R. Schneider, R.-L. Shia, D. K. Weisenstein, and N. D. Sze (1993) A two-dimensional model with coupled dynamics, radiation, and photochemistry: 1. Simulation of the middle atmosphere. *J. Geophys. Res.*, **98**, 20429-20440.
- Kotamarthi, V.R., M.K.W. Ko, D.K. Weisenstein, J.M. Rodriguez, and N.D. Sze (1994) The effect of lightning on the concentration of odd nitrogen species in the lower stratosphere: An update. *J. Geophys. Res.*, **99**, 8167-8174.
- Lacis, A., D. Wuebbles, and J. Logan (1990) Radiative forcing of climate by changes in the vertical distribution of ozone. *J. Geophys. Res.*, **95**, 9971-9981.
- MacKay, R.M., M.K.W. Ko, S. Zhou, G. Molnar, R-L Shia, Y. Yang, An estimate of the climatic effect of ozone during the 1980s, EOS, American Geophysical Union, Vol. 76, No. 17. paper A51B-11. (Summary of the 1995 Spring Meeting of the American Geophysical Union held in Baltimore, MD.) Full paper submitted to *J. Geophys. Res.* - *Atmospheres*, 1995.
- Manney, G. L., R. W. Zurek, W. L. Lahoz, R. S. Harwood, J. C. Gille, J. B. Kumer, J. L. Mergenthaler, A. E. Roche, A. O'neil, R. Swinbank, and J. W. Waters (1995)

- Lagrangian transport calculations using UARS data. Part I: Passive tracers. *J. Atmos. Sci.*, **52**, pp. 3049-3068.
- Molnar, G. I., M. K. W. Ko, S. Zhou, and N.-D. Sze (1994) Climatic consequences of the observed ozone loss in the 1980s: Relevance to the greenhouse problem. *J. Geophys. Res.*, **99**, 25755-25760.
- Plumb, R. A., M.K.W. Ko, and R.L. Shia (1995) Representation of localized aircraft NO<sub>y</sub> emissions in a two-dimensional model of stratospheric ozone. *J. Geophys. Res.*, **100**, 20,901-20,911.
- Ramanathan, V. and R.E. Dickinson (1979) The Role of Stratospheric Ozone in the Zonal and Seasonal Radiative Energy Balance of the Earth-Troposphere System. *J. Atmos. Sci.*, **36**, 1084-1104.
- Ramaswamy, V., M. D. Schwarzkopf, and K. P. Shine (1992) Radiative forcing of climate from halocarbon-induced global stratospheric ozone loss. *Nature*, **355**, 810-812.
- Rind, D., R. Suozzo, N. K. Balachandran, and M. J. Prather, 1990: Climate Change and the Middle Atmosphere. Part I: The Doubled CO<sub>2</sub> Climate. *J. Atmos. Sci.*, **47**, 475-494.
- Rodriguez, J. M., W. Hu, M. Y. Danilin, M. K. W. Ko, and N. D. Sze (1995) Impact of the Mt. Pinatubo eruption on stratospheric chemistry: Analysis using UARS data, AGU Fall Meeting, San Francisco.
- Rood, R. B., A. R. Douglass, J. A. Kaye, M. A. Geller, C. Yuechen, D. J. Allen, E. M. Larson, E. R. Nash, and J. E. Nielsen (1991) Three-dimensional simulations of wintertime ozone variability in the lower stratosphere. *J. Geophys. Res.*, **96**, 5055-5071.
- Schneider, H. R., M. K. W. Ko, R.-L. Shia and N.-D. Sze (1993) A two-dimensional model with coupled dynamics, radiative transfer, and photochemistry: 2. Assessment of the response of stratospheric ozone to increased levels of CO<sub>2</sub>, N<sub>2</sub>O, CH<sub>4</sub> and CFC. *J. Geophys. Res.*, **98**, 20441-20449.
- Thompson, A.M. (1992) The Oxidizing capacity of the Earth's atmosphere: Probable past and future changes, *Science* **256**, 1157-1165.
- Tung, K. K., A coupled model of zonally averaged dynamics, radiation and chemistry. in Transport processes in the middle atmosphere. G. Visconti and R. R. Garcia, Eds., 183-198, 1987.
- Weaver, C. J., A. R. Douglass and R. B. Rood (1993) Thermodynamic Balance of three-dimensional stratospheric winds derived from a data assimilation procedure. *J. Atmos. Sci.*, **50**, 2987-2993.
- Weisenstein, D., M.K.W. Ko and N.D. Sze (1992) The chlorine budget of the present day atmosphere: A modeling study. *J. Geophys. Res.*, **97**, 2547-2559.

World Meteorological Organization (1995) Scientific Assessment of Ozone Depletion: 1994, World Meteorological Organization/United Nations Environmental Program, Global Ozone Research and Monitoring Project, Report No. 37, Geneva, pp. iii-C.3.

Yang, H., E. Olaguer, and K. K. Tung (1991) Simulation of the present-day atmospheric ozone, odd nitrogen, chlorine and other species using a coupled 2-D model in isentropic coordinates. *J. Atmos. Sci.*, **48**, 442 - 471.

Zander, R., E., et al. (1994) Secular evolution of the vertical column abundances of CHClF<sub>2</sub> (HCFC-22) in the earth's atmosphere inferred from ground-based IR solar observations at the Jungfraujoch and at Kitt Peak, and comparison with model calculations. *J. Atmos. Chem.*, **18**, 129-148.

## Appendix A

Kotamarthi, V.R., M.K.W. Ko, D.K. Weisenstein, J.M. Rodriguez, and N.D. Sze (1994) The effect of lightning on the concentration of odd nitrogen species in the lower stratosphere: An update. *J. Geophys. Res.*, **99**, 8167-8174.

## Effect of lightning on the concentration of odd nitrogen species in the lower stratosphere: An update

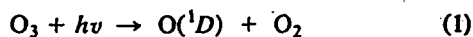
V. R. Kotamarthi, M. K. W. Ko, D. K. Weisenstein,  
Jose M. Rodriguez, and N. D. Sze

Atmospheric and Environmental Research, Incorporated, Cambridge, Massachusetts

**Abstract.** Revised model estimates of the effect of lightning on the lower stratospheric  $\text{NO}_y$  are presented. Several changes in the Atmospheric and Environmental Research Incorporated model were made since the last evaluation of the impact of lightning. Improvements were made in the model circulation and location of tropopause in the tropics, which is now calculated from the National Meteorological Center temperature data. Changes in model circulation reduced the mass flux from the troposphere to the tropical stratosphere. The calculated mass fluxes are found to agree better with some recent estimates. The circulation changes also reduced the advective mass flux from the tropical lower stratosphere to the midlatitudes. The change in circulation and the change in the tropopause height lead to increases in the calculated concentration of  $\text{N}_2\text{O}$ ,  $\text{O}_3$  and  $\text{NO}_y$  in the tropical lower stratosphere. The effect of lightning is to increase the calculated concentration of  $\text{NO}_y$  around 64 mbar by a factor of 2, compared to a factor of 10 enhancement in the previous calculations. Comparison with the Stratosphere Troposphere Exchange Project 1987 data indicates that the inclusion of a lightning source brings the model results in closer agreement with the observations.

### 1. Introduction

The concentration of  $\text{NO}_y$  ( $\text{N}$ ,  $\text{NO}$ ,  $\text{NO}_2$ ,  $\text{NO}_3$ ,  $\text{N}_2\text{O}_5$ ,  $\text{HNO}_2$ ,  $\text{HO}_2\text{NO}_2$ ,  $\text{HNO}_3$ , and  $\text{ClONO}_2$ ) in the lower stratosphere plays a significant role in determining the local photochemical removal rate of ozone and the response of ozone to increases in chlorine [Prather *et al.*, 1984; Weisenstein *et al.*, 1992]. The local production of  $\text{NO}_y$  in the lower stratosphere is controlled by the available amount of  $\text{N}_2\text{O}$  and  $\text{O}_3$  which generate  $\text{NO}$  through the reaction steps



This reaction scheme is believed to produce more than 90% of the  $\text{NO}_y$  in the stratosphere in the altitude range of 20–50 km. Smaller amounts of  $\text{NO}$  are produced from the dissociation of molecular nitrogen during solar proton events and by cosmic rays [Jackman *et al.*, 1980, 1990; Callis *et al.*, 1991]. The  $\text{NO}_y$  budget in the lower stratosphere can also be influenced by sources such as lightning in the tropics [Ko *et al.*, 1986] (hereafter labeled K86). Because of uncertainties in the location and magnitude of the lightning source, it is difficult to quantify its effect on the stratospheric  $\text{NO}_y$  budget.

The location and extent of the lightning sources has been the subject of several studies. Early estimates of source strengths of lightning ranged from 3  $\text{MT}(\text{N}) \text{ yr}^{-1}$  [Borucki and Chameides, 1984] to 8  $\text{MT}(\text{N}) \text{ yr}^{-1}$  [Logan, 1983]. Later, Chameides *et al.* [1987] used the  $\text{NO}_x$  data collected during the GTE/CITE 1 aircraft campaign to compute a

source of 7  $\text{MT}(\text{N}) \text{ yr}^{-1}$ . On the basis of results from field experiments, Franzblau and Popp [1989] have concluded that these estimates are a factor of 10 too small. Liaw *et al.* [1990] come to the same conclusion after recalculating previously reported data in the literature using a common number of lightning strokes per second and energy per flash.

Here we will discuss the application of a two-dimensional transport-chemistry model to study the effect of the  $\text{NO}_y$  lightning source on the lower stratosphere. Even though a two-dimensional model is probably not the best tool available to explore the impacts of  $\text{NO}_y$  produced by lightning, it still can provide valuable information, if we can clearly state the limitations of the approach and not overinterpret the results. An issue of central interest in studying the effect of lightning sources on the lower stratospheric  $\text{NO}_y$  is the representation of cross-tropopause exchange. The vertical flux of any chemical species can be represented as the sum of the mean and eddy components as follows:

$$F_t = \langle w \rangle \langle f_t \rangle + \langle w' f_t' \rangle, \quad (3)$$

where the angle brackets denote the spatial and temporal averaging as dictated by the spatial resolution and time step used in the model. In the two-dimensional model the fluxes are due to mean advection and large-scale eddies. This cannot account for the fast turnover times represented by deep convective events frequent in the tropics, where lightning is most prevalent. Thus the two-dimensional modeling results may be thought of as an effective bulk transport rather than a quantity calculated from a detailed overall description of lightning sources.

Analysis of the  $\text{NO}_y$  and ozone data from the Stratosphere-Troposphere Exchange Project 1987 (STEP'87) mission conducted in the tropical regions based at Darwin (12.23°S and 130.44°E), Australia, were reported by Murphy



Table 1. Strength and Location of the Lightning Source

Model Run Name	Integrated Source, kt of N yr <sup>-1</sup>	Altitude Distribution of Source, km	Flux Across the 100-mbar Surface From 30°N–30°S, kt N yr <sup>-1</sup>
L2	2	4–11	31
L4	4	4–11	52
H2	2	4–15	53
H4	4	4–15	98

The flux across the 100-mbar surface as calculated by the current version of the model. The lightning source is uniformly distributed for all the seasons and between 30°N and 30°S latitudes.

*et al.*, [1993]. On the basis of these data, they concluded that air with a NO<sub>y</sub> mixing ratio of about 150–600 pptv enters the lower stratosphere from the tropics. Using *Holton's* [1990] estimate of vertical air mass flux across the 100-mbar surface from the tropics for the winter months, *Murphy et al.* [1993] estimate a NO<sub>y</sub> flux in the range of 22–85 kt (N) yr<sup>-1</sup> entering the lower stratosphere.

An investigation of the effect of lightning as a source for lower stratospheric NO<sub>y</sub> was reported previously using the 1986 version of the Atmospheric and Environmental Research (AER) Incorporated two-dimensional chemistry-transport model (K86). The K86 study examined four distinct cases, L2, L4, H2, and H4 differentiated by the magnitude of the lightning source and its location. The location of the lightning sources introduced and its spatial extent is shown in Table 1. The flux of NO<sub>y</sub> across the 18-km surface and between 30°N and 30°S was used to estimate the flux of NO<sub>y</sub> into the stratosphere. The NO<sub>y</sub> reported in K86 fluxes are much larger than the estimates of *Murphy et al.* [1993]. Our review of K86 model indicates that because of the vertical resolution (3 km) and the assignment of the K<sub>zz</sub> values (vertical eddy mixing coefficients), material between 18 and 21 km and 30°N and 30°S is rapidly mixed with material from below 18 km. This effectively puts the grid box in the troposphere. Consequently, the fluxes reported in K86 should not be interpreted as the cross-tropopause fluxes.

Several improvements have since been made to the AER two-dimensional model. Changes were implemented in spatial resolution of the model, model circulation, tropopause height, and eddy mixing coefficients in an effort to better represent the observed ozone data. Changes in circulation were made to reduce the mass flux across the 18-km surface in the tropics. At the same time the horizontal flux from the tropics to the midlatitude lower stratosphere is also smaller. A consequence of these changes is that the updated version of the model has significantly more ozone and N<sub>2</sub>O [*Ko et al.*, 1991] between 18 and 21 km in the tropics. The changes in O<sub>3</sub> and N<sub>2</sub>O mixing ratios have a direct effect on the in situ formation rate of NO through reaction (1) and (2). In this paper we examine the lower stratospheric NO<sub>y</sub> budget with the updated version of the two-dimensional model in a box extending from the model tropopause (16.5 km) to an altitude of 21 km and spanning the latitude region from 30°N to 30°S to evaluate the effects of these changes on the tropical lower stratospheric NO<sub>y</sub> budget. The calculated NO<sub>y</sub> will also be

compared with the recent data from STEP'87. In section 2 the current version of the AER two-dimensional model is discussed. The effects of these changes on NO<sub>y</sub> and O<sub>3</sub> and the model-calculated impact of lightning are presented in section 3.

## 2. Current Version of the AER Two-Dimensional Model

The vertical resolution of the model was increased by a factor of 3 in the current version, to approximately 1.2 km from approximately 3.5 km in K86. The changes in the model residual circulation have been carried out in an effort to improve the agreement between the calculated and measured ozone columns. These changes have reduced the mass flux across the tropical tropopause. The current model uses log-pressure coordinates but maintains diffusion along isentropic surfaces by projecting the horizontal diffusion, which is assumed to be acting along isentropic surfaces, to the model's log-pressure grid to obtain additional K<sub>yy</sub> and K<sub>zz</sub> components of diffusion. The constant value of K<sub>yy</sub> of  $3.0 \times 10^9 \text{ cm}^2 \text{ s}^{-1}$ , used throughout the stratosphere in K86 is now replaced by higher values in the midlatitude lower stratosphere. In summer the K<sub>yy</sub> value in the middle and high latitude lower stratosphere is  $1.0 \times 10^{10}$ , and in winter it is  $6.0 \times 10^9 \text{ cm}^2 \text{ s}^{-1}$ . The value of  $3.0 \times 10^9 \text{ cm}^2 \text{ s}^{-1}$  is still used for the tropical lower stratosphere and for the entire stratosphere above 25 km. These coefficients give a good fit to the observed ozone in the lower stratosphere and are comparable to the values reported by *Newman et al.* [1986]. This version of the model was used in the models and measurement study [*Prather and Remsberg*, 1993] and as a part of the NASA program to study the effect of stratospheric aircraft's on the background stratosphere [*Stolarski and Wesely*, 1993].

The tropopause height is now calculated using the World Meteorological Organization (WMO) definition of the tropopause applied to model temperatures. The WMO defines the tropopause as the first occurrence of a lapse rate of less than  $2 \text{ K km}^{-1}$  above 500 mbar for more than 2 km. We have conducted a study of the seasonal variability of tropopause height using a zonally averaged twice daily temperature data set from the National Meteorological Center. The data extend from the beginning of October 1989 to the end of July 1992 and includes the mandatory pressure levels extending from 1000 to 50 mbar at latitude intervals of 5°. The data were further filtered to obtain weekly averages, which were used to study the seasonal variability of the tropopause height. Linear interpolation was used in the vertical to locate the first occurrence of the lapse rate of less than  $2 \text{ K km}^{-1}$  to obtain the tropopause as defined above. An annual mean tropopause height and its variability were calculated with 5° latitude resolution.

Figures 1a and 1b show the tropopause heights during the summer (northern hemisphere) and winter (northern hemisphere) months, respectively. The summer mean is an average over the months June, July, and August, whereas the winter is defined as an average over December, January, and February. The seasonal variations along the equatorial region are generally negligible, with the tropopause height nearly constant at about 110 mbar from the equator to 30° latitude on both sides of the equator. Thereafter the calculated tropopause heights decrease uniformly with increasing

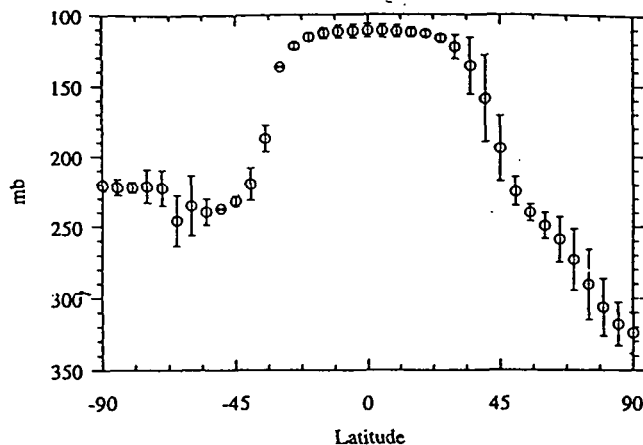


Figure 1a. Mean tropopause height for northern hemisphere summer (bars denote standard deviation from seasonal mean based on three years of data).

latitude in the summer hemisphere. In the winter hemisphere, tropopause heights decrease up to 50°–60° latitude, increasing thereafter toward the poles. These figures also show that in general the variations in the middle and upper latitude tropopause heights are more pronounced in the summer hemisphere than in the winter hemisphere. The annual variability of the tropopause height (Figure 2) shows more variations in the southern hemisphere than in the northern hemisphere. This could be due to the poorer quality of the raw data in the southern hemisphere.

### 3. Effects of the Model Changes

#### 3.1. Budget of an Inert Tracer in the Tropical Lower Stratosphere

The budget of an inert tracer in a box located in the tropical lower stratosphere is shown in Figure 3. The box has a uniform mixing ratio of 1 ppbv throughout the model domain. The flux across the 18-km surface in the current model is  $61 \times 10^8 \text{ kg s}^{-1}$  as compared to  $108 \times 10^8 \text{ kg s}^{-1}$  in the K86 version of the model. The mass flux across the lower boundary of the box in Figure 3, situated at 100 mbar, is  $71 \times 10^8 \text{ kg s}^{-1}$ . Holton [1990] has computed an annual average vertical mass flux of  $64.8 \times 10^8 \text{ kg s}^{-1}$  from the tropical regions, across the 100-mbar surface, into the stratosphere. The present AER model results are in good agreement with this number and provide further justification to the changes made in the circulation. The advective circulation transports material from the sides of the box into middle latitudes and from the top of the box to higher altitude as expected.

#### 3.2. Changes in Ozone

In the case of nonuniformly distributed species, additional effects due to changes in the eddy diffusion coefficients and the changes in the tropopause heights can be expected to come into play. The current version of the model has 100 to 200% more ozone in this model grid box. The changes in the model calculated ozone profiles at the equator is shown in Figure 4. Data obtained from the NIMBUS 7 solar backscattered ultraviolet (SBUV) instrument [McPeters et al., 1984] and STEP'87 are also plotted on the graph. It is readily

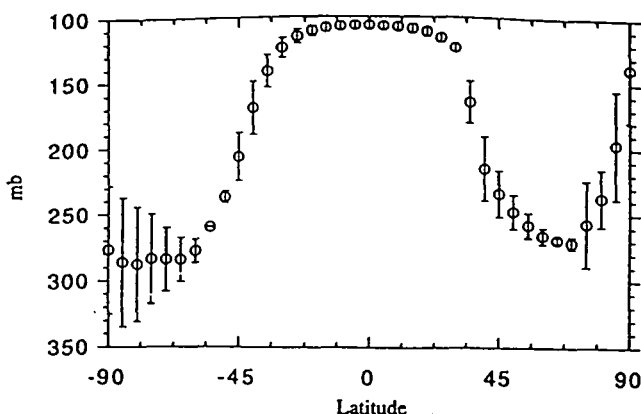


Figure 1b. Mean tropopause height for northern hemisphere winter (bars denote standard deviation from seasonal mean based on three years of data).

apparent that the current version of the model does a better job of reproducing the ozone profile above the tropopause.

The smaller-ozone concentration below 105 mbar in the current model can be explained in terms of the differences in the position of the tropopause in the two versions of the model. The tropopause in the current model is set at about 16.5 km (105 mbar) in the tropics compared to 50 mbar in K86. Any ozone produced below 50-mbar level is available for rapid mixing throughout the troposphere in the K86 model. Since the production rate of ozone at 64 mbar is about 3 times larger than the ozone produced at 105 mbar, the concentrations in the K86 version of the model are considerably larger.

#### 3.3. Effects on NO<sub>y</sub>

As reported by Ko et al. [1991], the change in circulation and tropopause height also results in an increase in the calculated concentration of N<sub>2</sub>O in the lower tropical stratosphere. The increases in O<sub>3</sub> and N<sub>2</sub>O results in a 200% increase in the local production of NO<sub>y</sub>. Figure 5 shows the NO<sub>y</sub> budget for the no lightning case as calculated by the current version of the model in the same box shown in Figure 3.

The NO<sub>y</sub> mass flux entering from the higher latitudes is

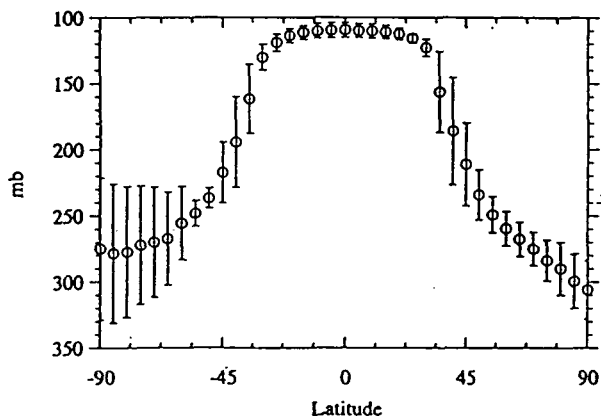


Figure 2. Annual mean tropopause height based on three years of temperature data (bars denote deviations from the annual mean).

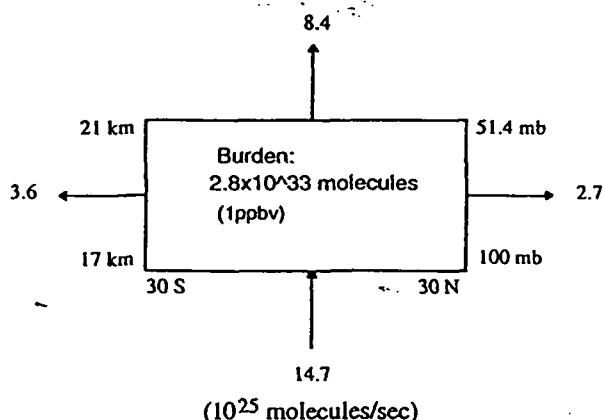


Figure 3. Diagram showing the annual averaged fluxes of an uniformly distributed inert tracer across the boundaries of the box of dimensions shown. The fluxes are in units of  $10^{25}$  molecules/s. Results are from the current version of the model.

the single largest contributor to the net flux inputs into the box (76%) followed by local production (21%), and flux from below the box (3%). Figure 3 shows that the advective flux is directed away from the tropics to midlatitudes. The eddy flux is zero for that case, as the uniformly distributed inert tracer has no gradients. With the large gradients of the calculated NO<sub>y</sub> in the model, the eddy flux is larger than the advective flux resulting in a net inward flux.

The four cases L2, L4, H2, and H4 (Table 1) were used again to study the impact of tropospheric lightning sources on the lower stratospheric NO<sub>y</sub> and to investigate the changes in the impacts as a result of changes in the model. Figure 6 shows the NO<sub>y</sub> fluxes into and out of the tropical box for the four cases of lightning sources considered with the new model. The results of *Murphy et al.* [1993] imply an annual input of 22–85 kt (N) yr<sup>-1</sup> from the troposphere to the

stratosphere. The calculated flux inputs from the bottom of the boxes (across the 100-mbar surface) are 5 kt (N) yr<sup>-1</sup> for the no lightning case, 31 kt (N) yr<sup>-1</sup> for L2, 52 kt (N) yr<sup>-1</sup> for L4, 53 kt (N) yr<sup>-1</sup> for H2 and 98 kt (N) yr<sup>-1</sup> for H4. All the calculated fluxes, except for H4, are within the range estimated by *Murphy et al.* [1993].

Figure 7 shows the vertical profiles of NO<sub>y</sub> from the two-dimensional model for lightning sources corresponding to the cases L2, L4, H2, and H4 at the equator for January. The impact of a lightning source on the lower stratosphere is largest for H4 followed by H2, L4, and L2. The effect of lightning is significant at all levels below the tropopause (which is at 16.5 km for all the runs) for all the cases. In the grid point immediately above the tropopause located at 17.1 km, the NO<sub>y</sub> mixing ratios for H4 and for the case without lightning differ by a factor of 5.0. At an altitude of 22 km the difference between no lightning and for case H4 is reduced to a factor of 1.2.

Figure 7 also shows the NO<sub>y</sub> data obtained during the STEP'87 mission. The NO<sub>y</sub> data shown are a composite of all the flights conducted during the period January–February 1987, in the latitude range of 0°–30°S and an altitude range of 0–22 km. The mean values are obtained by binning the data into a series of 2-km altitude bins starting at 5 km and extending to an height of 21 km. Further details of the STEP'87 can be obtained from *Russel et al.* [1993]. The addition of a lightning source leads to significant improvements in the agreement between the model results and measurement for the troposphere. The lower stratospheric model results are also in the general range of the data. The considerable variations in the NO<sub>y</sub> data with altitude in the region of 17–21 km precludes us from making any firm conclusions as to the extent of the lightning-derived NO<sub>y</sub> entering the stratosphere. However, in general, only the run H4 is outside the range of the STEP'87 data.

Figure 8 shows a scatterplot of the calculated NO<sub>y</sub> and O<sub>3</sub>

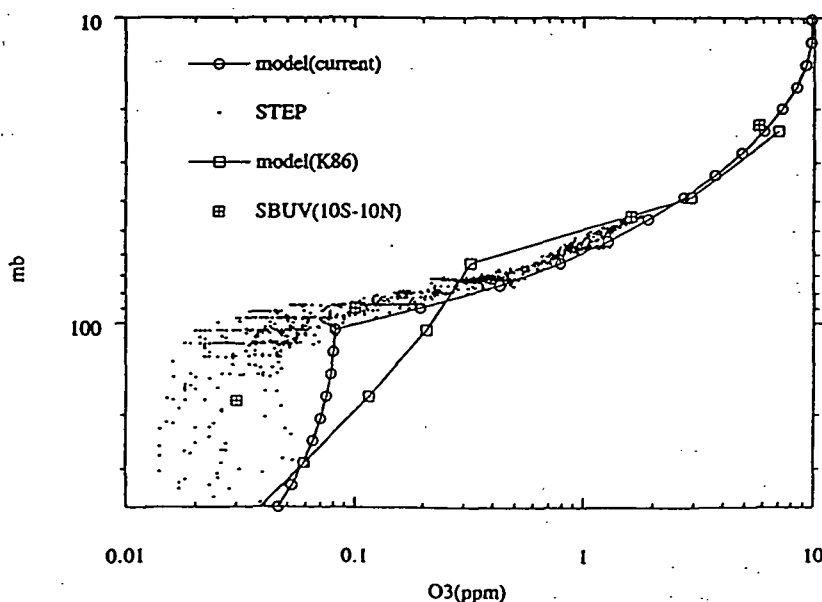


Figure 4. Ozone profiles calculated with the current and K86 versions of the two-dimensional model for January 1 at the equator and measured data from STEP'87 [*Murphy et al.*, 1993] and SBUV [*McPeters et al.*, 1984].

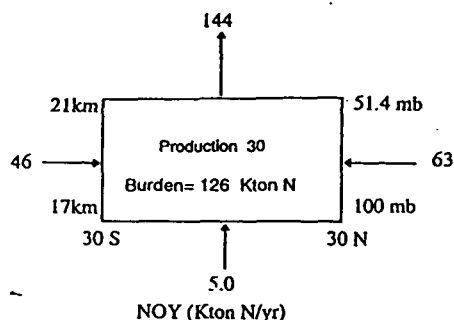


Figure 5. Diagram showing the annual average fluxes of NO<sub>y</sub> with no lightning sources. The production rate and fluxes are in units of kt (N) yr<sup>-1</sup>.

together with data from STEP'87. The data plotted in this figure is obtained from a total of 11 flights conducted in the region 0° to 30°S and extending from 6 to 22 km. The model values above 100 ppb of O<sub>3</sub> are in the stratosphere for the two-dimensional model, and the same is true for the STEP'87 data [Murphy *et al.*, 1993]. The observed correlation is best reproduced by cases H2 and L4, both in the

troposphere and stratosphere. Even with the present improvements in the model, lightning sources of NO<sub>y</sub> are necessary in the 17–25 km range to obtain agreement with the data.

Considering the uncertainties such as tropopause location, and the model circulation in the lower stratosphere still present in the model, it would be impossible to totally rule out lightning as a source of NO<sub>y</sub> in the tropical lower stratosphere or conclusively state the extent of the source required. As seen in the Figures 7 and 8, the addition of lightning provides small but significant amounts of NO<sub>y</sub> at the grid points immediately above the tropopause to bring the model results in line with the observations. It should also be noted that the limb-infrared monitor of the stratosphere data used to constrain the model calculations in K86 fall within the range of the STEP data shown here for the altitudes under consideration.

#### 4. Conclusions

Several improvements were made to the AER two-dimensional model since the investigation of the effects of lightning on the lower stratospheric NO<sub>y</sub> reported in K86.

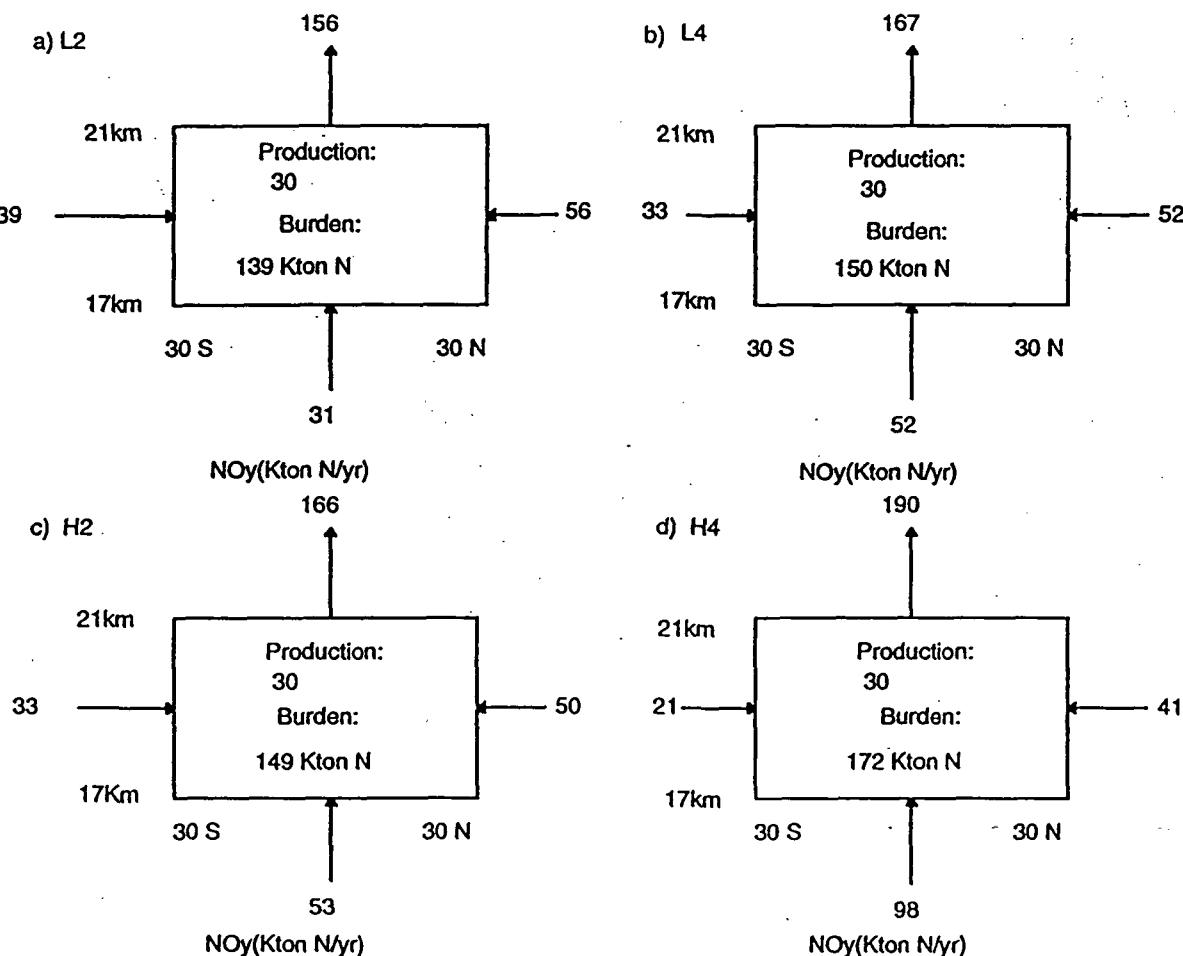


Figure 6. Diagram showing the annual averaged fluxes of NO<sub>y</sub> with lightning source from the two-dimensional model. (a) Case L2 with 2 Mt of (N) yr<sup>-1</sup>, distributed from 4–11 km altitude region and from 30°S to 30°N latitude band. (b) Case L4 with source of 4 Mt of (N) yr<sup>-1</sup> with source located as above. (c) Case H2 with source of 2 Mt(N) yr<sup>-1</sup> uniformly distributed from 4–14 km altitude region and with same latitudinal distribution as above. (d) Case H4 with a source of 4 Mt(N) yr<sup>-1</sup> distributed as in H2.

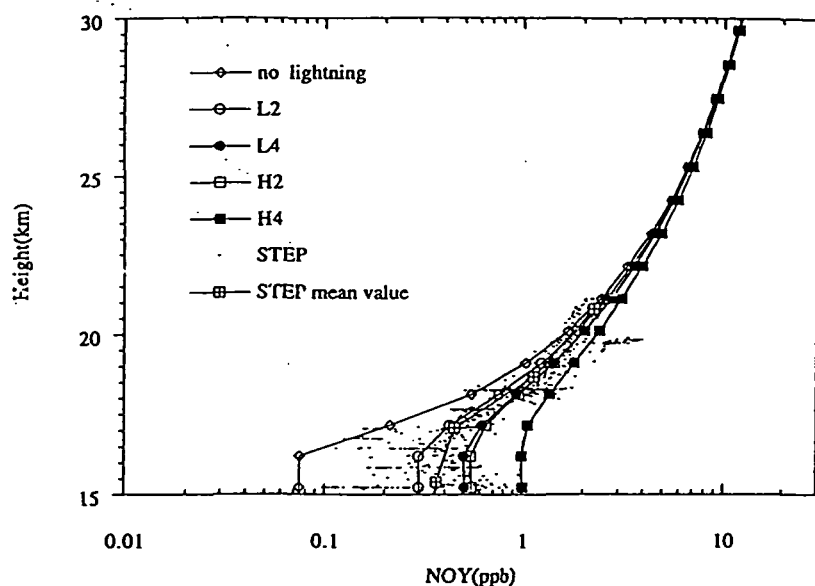


Figure 7. Comparison of the calculated NO<sub>y</sub> for all the cases for January and the measured data from STEP'87 [Murphy *et al.*, 1993].

These improvements resulted in lowering the mass exchange across the tropopause, increasing ozone and N<sub>2</sub>O in the altitude range of 17–22 km in the tropical lower stratosphere. These changes increased the local production of NO<sub>y</sub> in this altitude range by a factor of 4 compared to K86. The changes in the circulation resulted in a smaller calculated NO<sub>y</sub> flux into the tropical stratosphere from the tropical troposphere with a lightning source and at the same time gave a net lateral

flux of NO<sub>y</sub> into the lower stratospheric tropical regions from the higher latitudes. As a result, the impact of lightning on the lower stratospheric NO<sub>y</sub> is smaller than previously reported. A net flux input of 50 kt (N) yr<sup>-1</sup> from the troposphere into the lower stratosphere is sufficient to produce agreement of the model results with the available data. The fluxes required are in the range estimated by Murphy *et al.* [1993] based on the STEP'87 data.

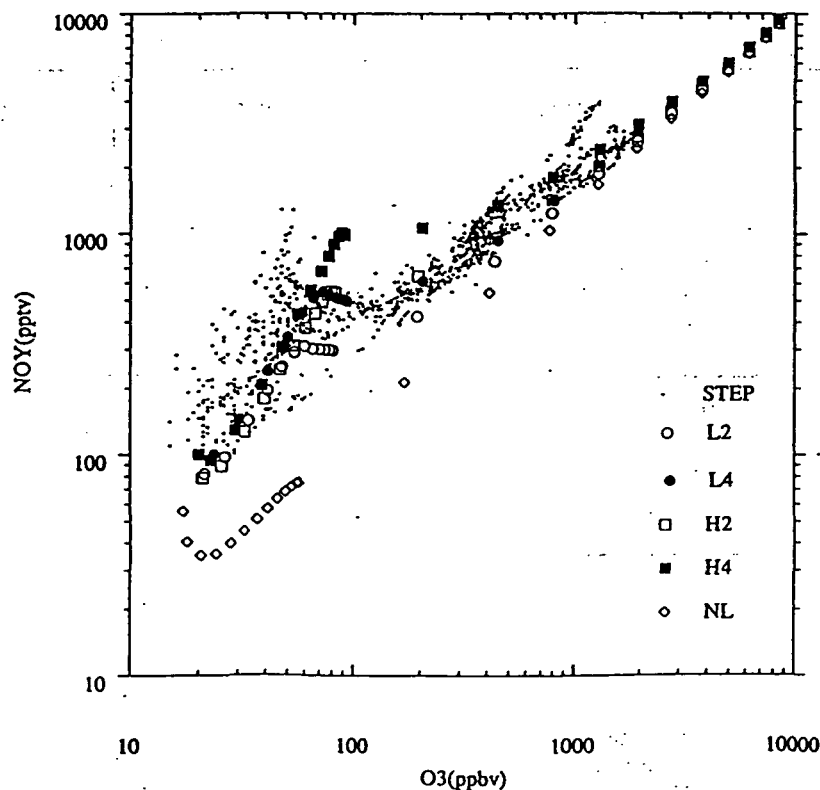


Figure 8. Calculated NO<sub>y</sub> and O<sub>3</sub> for cases L2, L4, H2, H4, and NL (no lightning) for the month of January. STEP'87 data [Murphy *et al.*, 1993] are also shown.

The issue of the lightning source strength is complex due to the inhomogeneity of the source distribution. The estimate source strength depends on the estimated lightning frequency, the energy per flash and the number of NO molecules produced per unit energy [Goldenbaum and Dickerson, 1993] in each flash. If in-cloud discharges occur 4 times more frequently than cloud to ground and that the in-cloud lightning has 1/3 the power of the cloud-to-ground stroke [Franzblau and Popp, 1989], then about 60% of the lightning produced NO<sub>x</sub> is by in-cloud lightning (~10 km) and 40% is from cloud-to-ground strikes (below 4 km). This would give a 60 Mt(N) yr<sup>-1</sup> source in the 4–11 km range if a global source of 100 Mt(N) per year is assumed. Other estimates based on higher energy estimates for cloud-to-ground strikes compared to in-cloud lightning, decrease the lightning source in the upper troposphere by a factor of 2 to about 30 Mt N yr<sup>-1</sup>. A source of 20 Mt(N) yr<sup>-1</sup> distributed as in H<sub>2</sub> gave calculated NO<sub>x</sub> fluxes into the lower tropical stratosphere about a factor of 10 higher than H<sub>2</sub> and concentrations outside the range of the STEP'87 data. However, as noted in K86, because of the uncertainties in modeling the tropospheric process in the framework of a two-dimensional model, it would be difficult to directly relate the extent of the lightning source to the fluxes across the tropopause with certainty. Future measurement and improved three dimensional modeling studies with a focus on the altitude distribution of the lightning source and better representation of the deep convective mixing and process important in the troposphere would help to resolve this issue.

**Acknowledgments.** We thank the National Aeronautics Space Administration, Ames for providing us with the STEP data. This work was supported by NASA grants NASW-4433 and NAS1-19192.

## References

- Borucki, W. J., and W. L. Chameides, Lightning, estimates of the rates of energy dissipation of nitrogen fixation, *Rev. Geophys.*, **22**, 363–372, 1984.
- Callis, L. B., M. Natarajan, and J. M. Russel III, Estimates of the stratospheric distributions of odd nitrogen from the LIMS data, *Geophys. Res. Lett.*, **12**, 259–262, 1985.
- Callis, L. B., D. N. Baker, J. B. Blake, J. D. Lambert, R. E. Boughner, M. Natarajan, R. W. Klebesadel, and D. J. Gorney, Precipitating relativistic electrons: Their long-term effect on the stratospheric odd nitrogen levels, *J. Geophys. Res.*, **96**, 2939–2976, 1991.
- Chameides, W. L., D. D. Davis, J. Bradshaw, M. Rodgers, S. Sandholm, and D. B. Bai, An estimate of the NO<sub>x</sub> production rate in the electrified clouds based on NO observations from the GTE/CITE 1 fall 1983 field operation, *J. Geophys. Res.*, **92**, 2153–2156, 1987.
- Franzblau, E., and C. J. Popp, Nitrogen oxides produced from lightning, *J. Geophys. Res.*, **94**, 11,089–11,104, 1989.
- Goldenbaum, G. C., and R. R. Dickerson, Nitric oxide production by lightning discharges, *J. Geophys. Res.*, **98**, 18,333–18,338, 1993.
- Holton, J. R., On the global exchange of mass between the stratosphere and troposphere, *J. Atmos. Sci.*, **47**, 392–395, 1990.
- Jackman, C. H., J. E. Frederick, and R. S. Stolarski, Production of odd nitrogen in the stratosphere and mesosphere: An intercomparison of source strengths, *J. Geophys. Res.*, **85**, 7495–7505, 1980.
- Jackman, C. H., A. R. Douglas, R. B. Rood, and R. D. McPeters, Effect of solar proton events on the middle atmosphere during the past two solar cycles as computed using a two-dimensional model, *J. Geophys. Res.*, **95**, 7417–7428, 1990.
- Ko, M. K. W., M. B. McElroy, D. K. Weisenstein, and N. D. Sze, Lightning: A possible source of stratospheric odd nitrogen, *J. Geophys. Res.*, **91**, 5395–5404, 1986.
- Ko, M. K. W., N. D. Sze, and D. K. Weisenstein, Use of satellite data to constrain the model-calculated atmospheric lifetimes of N<sub>2</sub>O: Implications for other trace gases, *J. Geophys. Res.*, **96**, 7547–7552, 1991.
- Liaw, Y. P., D. L. Sisterson, and N. L. Miller, Comparison of field, laboratory, and theoretical estimates of global nitrogen fixation by lightning, *J. Geophys. Res.*, **95**, 22,489–22,494, 1990.
- Logan, J. A., Nitrogen oxides in the troposphere: Global and regional budgets, *J. Geophys. Res.*, **88**, 10,785–10,807, 1983.
- McPeters, R. D., D. F. Heath, and P. K. Bhartia, Average ozone profiles for 1979 from the NIMBUS 7 SBUV instrument, *J. Geophys. Res.*, **89**, 5199–5214, 1984.
- Murphy, D. M., D. W. Fahey, M. H. Proffitt, S. C. Liu, K. R. Chan, C. S. Eubank, S. R. Kawa, and K. K. Kelly, Reactive nitrogen and its correlation with ozone in the lower stratosphere and upper troposphere, *J. Geophys. Res.*, **98**, 8751–8773, 1993.
- Newman, P. A., M. R. Schoeberl, and R. A. Plumb, Horizontal mixing coefficients for two-dimensional chemical models calculated from National Meteorological Center data, *J. Geophys. Res.*, **91**, 7919–7924, 1986.
- Prather, M. J., M. B. McElroy, and S. C. Wofsy, Reductions in ozone at high concentrations of stratospheric halogens, *Nature*, **312**, 227–231, 1984.
- Prather, M. J., and E. E. Remsberg (eds.), The atmospheric effects of stratospheric aircraft: Report of the 1992 Models and Measurements Workshop, *NASA Ref. Publ.*, **1292**, II, A1–G67, 1993.
- Russell, P. B., L. Pfister, and H. B. Selkirk, The Tropical Experiment of the Stratosphere-Troposphere Exchange Project (STEP): Science objectives, operations, and summary findings, *J. Geophys. Res.*, **98**, 8563–8589, 1993.
- Stolarski, R. S., and H. L. Wesoky (eds.), The Atmospheric Effects of Stratospheric Aircraft: A Second Report, *NASA Ref. Publ.*, **1293**, 85–113, 1993.
- Weisenstein, D. K., M. K. W. Ko, and N. D. Sze, The chlorine budget of the present-day atmosphere: A modeling study, *J. Geophys. Res.*, **97**, 2547–2559, 1992.
- M. K. W. Ko, V. R. Kotamarthi, D. K. Weisenstein, J. M. Rodriguez, and N. D. Sze, Atmospheric and Environmental Research, Incorporated, 840 Memorial Drive, Cambridge, MA 02139.

(Received April 28, 1993; revised November 9, 1993; accepted December 7, 1993.)

## Appendix B

Gunson, M.R. et al. (1994) Increase in levels of stratospheric chlorine and fluorine loading between 1985 and 1992. *Geophys. Res. Lett.*, **21**, 2,223-2,226.

## Increase in levels of stratospheric chlorine and fluorine loading between 1985 and 1992

M. R. Gunson, M. C. Abrams, and L. L. Lowes

Jet Propulsion Laboratory, California Institute of Technology, Pasadena, California

E. Mahieu and R. Zander

Institut d'Astrophysique, Université de Liège, Liège, Belgium

C. P. Rinsland

Atmospheric Sciences Division, NASA Langley Research Center, Hampton, Virginia

M. K. W. Ko, N. D. Sze, and D. K. Weisenstein

Atmospheric and Environmental Research, Inc., Cambridge, Massachusetts

**Abstract.** Mixing ratios of 3.44 ppbv (parts per billion by volume) and 1.23 ppbv for HCl and HF above 50 km, surrogates for total chlorine and fluorine, have been measured by the Atmospheric Trace Molecule Spectroscopy (ATMOS) experiment on a March 1992 flight of the Space Shuttle. Compared to the measured values obtained on a 1985 flight, these correspond to a 37% and 62% increase for HCl and HF, respectively. The derived trend in HCl ( $\sim 0.13$  ppbv per year) is in good agreement with the model-predicted increase in chlorine loading of 0.13 ppbv per year [Prather and Watson, 1990], and with the measured trends in HCl total column abundance from reported ground-based observations. The main source of this change can be attributed to the release of man-made chlorofluorocarbons (CFCs) and hydrochlorofluorocarbons (HCFCs). This new value for HCl represents an upper limit to the inorganic chlorine concentration in the stratosphere available for participation in photochemical processes which destroy ozone.

rine-containing gases as a function of altitude from about 10 to 60 km [Zander *et al.*, 1992]. This study demonstrated that the mixing ratios of HCl and HF above 50 km are approximately equal to the mixing ratios of total chlorine and fluorine respectively. The HCl volume mixing ratio at this height represents an upper limit on the mixing ratio of the inorganic chlorine available to participate in ozone removal chemistry in the lower stratosphere. It is thus a measure of the effective atmospheric chlorine loading, which is a good proxy for the ozone depletion potential [Prather and Watson, 1990].

During the 1985 SL-3 mission, ATMOS observations were limited to two latitudes centered at 30°N and 48°S. The mixing ratios of HCl and HF between 50 and 60 km were measured to be  $2.55 \pm 0.28$  and  $0.77 \pm 0.10$  ppbv, respectively [Zander *et al.*, 1990], from an analysis of the average spectra created from the available sunset observations (4 for HCl and only 2 for HF). The absolute concentrations of the gases above 60 km were too small to be detected at the signal-to-noise of these ATMOS spectral data.

### Introduction

The ATMOS instrument is a Fourier transform spectrometer designed to operate on board the Space Shuttle where it obtains high resolution infrared solar observations during orbital sunrises and sunset [Farmer, 1987]. These data are used to infer the vertical concentration profiles of a large number of atmospheric constituents, including HCl, HF, and other major chlorine and fluorine bearing gases [Zander *et al.*, 1987a; Zander *et al.*, 1990] including both organic source molecules and their degradation products. The ATMOS measurements of these gases obtained during the Spacelab 3 (SL-3) shuttle mission of March 29 - April 6, 1985, together with measurements from other instruments for those gases which were below the detection limits of the ATMOS instrument, have been used to study the partitioning of chlorine- and fluo-

### ATMOS ATLAS-1 Measurements

Between March 24 and April 2, 1992, ATMOS was flown for a second time as part of the Atmospheric Laboratory for Applications and Science (ATLAS-1) shuttle mission. The more numerous observations made during this recent flight covered a broader range of latitudes, i.e. between 28°N and 54°S. HCl and HF profiles have been inferred from these data using analysis procedures and methods previously developed for the SL-3 data set [Zander *et al.*, 1990; Norton and Rinsland, 1991]. From these new observations, no statistically significant latitudinal gradients were found in the distribution of HCl above 45 km, or above 50 km in HF; therefore, both halogen sink species appear well-mixed over these latitude and altitude ranges.

To provide a more precise estimate of the HCl and HF concentrations in the upper stratosphere, we have analyzed the spectra formed by averaging in 5 km altitude bins. Typically, 27 spectra were available for the HCl spectral averages, and 14 for the HF spectral averages, using both sunset and sunrise data. It is clear from these average spectra that the concentrations of HCl and HF have increased sufficiently so as

Copyright 1994 by the American Geophysical Union.

Paper number 94GL02077

0094-8534/94/94GL-02077\$03.00



to make their spectral signatures evident at much higher altitudes (Figure 1 and 2). As they appear to retain a constant mixing ratio up to 65–70 km, this further suggests that there is no significant loss mechanism or sink for either of these gases in this upper height range. The mean concentrations derived from the ATLAS-1 observations are  $3.44 \pm 0.30$  ppbv for HCl and  $1.23 \pm 0.12$  ppbv for HF. The uncertainties quoted represent an estimated accuracy following the assessment provided originally in Zander *et al.* [1990] and then in Gunson *et al.* [1990]. The error estimates include the error of the mean in the observations, 5% for HCl and 6% for HF, combined with an estimated root-sum-square of systematic error sources of 7%. No other reservoir species of chlorine or fluorine (for example  $\text{ClONO}_2$  and  $\text{COF}_2$ ) were found to be measurable at these higher altitudes although their stratospheric abundance and distribution is discussed in other papers [Rinsland *et al.*, 1994; Zander *et al.*, 1994]. From the earlier study by Zander *et al.* [1992], other species are estimated to contribute much less than 0.1 ppbv to the total chlorine at these heights. This would correspond to less than a 3% systematic error in using this measurement of HCl as a surrogate for the atmospheric chlorine burden.

## Discussion

The increase in the values for the upper stratospheric mixing ratios of HCl and HF determined from these two ATMOS missions can be compared with the rate of increase in the total column amounts of these gases measured from ground-based infrared spectrometers [e.g., Zander *et al.*, 1987bc; Wallace and Livingston, 1991; Rinsland *et al.*, 1991]. The ATMOS measurements represent an increase of  $0.13 \text{ ppbv yr}^{-1}$  and  $0.07 \text{ ppbv yr}^{-1}$  in HCl and HF respectively, or annual percentage increases of  $5 \% \text{ yr}^{-1}$  and  $9 \% \text{ yr}^{-1}$  for these gases referenced to their 1985 values. These are in almost direct agreement, for example, with the linear rates of increase measured by Wallace and Livingston [1991] of  $6 \% \text{ yr}^{-1}$  and  $9 \% \text{ yr}^{-1}$  in HCl and HF total columns referenced to 1984

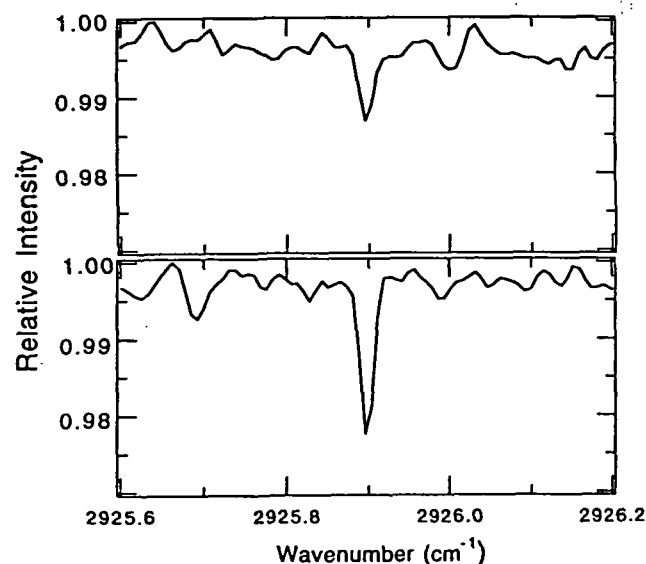


Figure 1. These panels show a small region around the absorption of the HCl R1 line in spectra created by averaging all those available from the 1992 ATMOS flight in 5 km bins around 70 km (upper) and 65 km (lower) tangent altitudes.

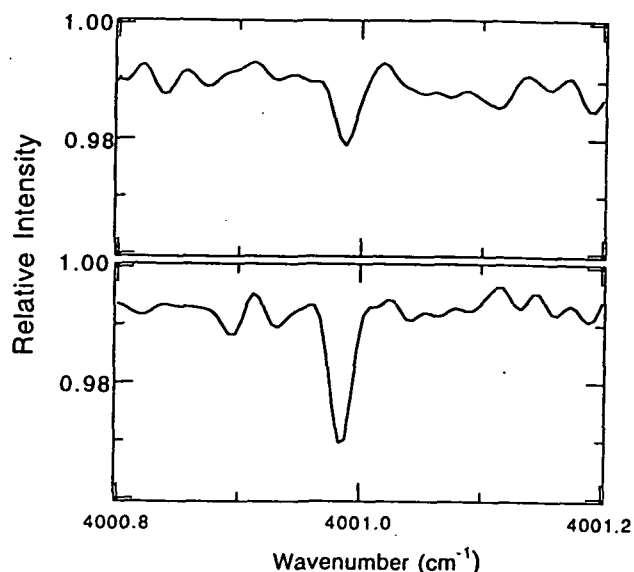


Figure 2. As in Figure 2 except this spectral region encompasses the HF R0 line at 70 km (upper) and 65 km (lower) tangent heights.

values. In general, good agreement is found with other reported values (see Table 1, Rinsland *et al.*, [1991] for summary of reported trends). Exact comparisons are difficult as the total column abundance trends reflect changes at all heights, although weighted to the lower stratosphere and the peak concentration of these two trace gases. For confirmation of the upper stratospheric mixing ratio of HCl, a direct comparison can be made with the profile of HCl reported from measurements by the Grille spectrometer during the same ATLAS-1 mission [De Maziere *et al.*, 1993]. At an altitude of 55 km these authors report a value of  $3.4 \pm 1.3$  ppbv, with an estimated trend of 25% at 40 km in comparison to the ATMOS/SL-3 values, for the period 1985 to 1992. At this lower altitude the partitioning between the inorganic chlorine reservoir species must be considered to understand fully the inferred trend. The changes and vertical distribution of HCl and HF over the whole stratosphere as measured in the ATMOS ATLAS-1 observations will be reported in other papers with consideration of the measurements of  $\text{ClONO}_2$  and  $\text{COF}_2$ .

Until recently, there has been some question as to whether significant amounts of HCl are injected into the stratosphere following volcanic eruptions which would contribute to some of the observed changes. While the ATLAS-1 mission followed 9 months after one of the largest volcanic eruptions of this century, that of Mount Pinatubo in June 1991, measurements of the total column burden of HCl before and immediately after this eruption indicate that little HCl reached the stratosphere [Mankin *et al.*, 1992; Wallace and Livingston, 1992]. This observation is further supported by a recent model study which suggests that HCl is successfully scavenged from volcanic plumes and removed in solution by condensing supercooled water [Tabazadeh and Turco, 1993]. Thus, the increase in stratospheric chlorine is almost wholly related to the continued build up of industrial halocarbons rather than to any natural events. Much stronger evidence of this is found in the increase in HF for which there are no known significant natural sources.

Historical and future stratospheric chlorine and fluorine levels can be modeled based on release and use of CFCs and their replacements as set out in the Montreal Protocol and its subsequent amendments (Figure 3). The ATMOS measurements of HCl and HF match the modeled growth in Cly and Fy data as surrogates for this change in total stratospheric chlorine and fluorine. The upper stratospheric HCl and HF values lie below the model curves in Figure 3, reflecting the time for vertical transport and mixing from the surface up to heights of 50 km and higher. Similar measurements in the future will reflect the phase out and replacement policy adopted after 1996 for the CFCs, and the exact mix of HCFCs (hydrochlorofluorocarbons) with HFCs (hydrofluorocarbons) used as substitutes. However, the modeled chlorine loading suggests some leveling off and reduction in stratospheric levels by the end of the century.

The future for stratospheric fluorine levels is more uncertain, as this will depend more critically on the exact mix of HCFCs and HFCs. Current understanding indicates that inorganic fluorine does not play a significant role in the catalytic destruction of ozone; its primary interest is as a measure of the destruction of the precursors. To date, the rapid growth in HF remains the strongest indicator that the source of active chlorine in the stratosphere is the photolysis of CFCs. As reductions in future chlorine loading is achieved, the primary environmental concern will shift from issues related to stratospheric ozone loss, to the global warming potential

of halocarbons [Ko *et al.*, 1993]. The changes observed in HF in the next decades will be an indicator of the mix of HCFCs and then HFCs which will be present in the atmosphere. Continued measurements of the stratospheric concentrations of HCl and HF through a series of planned flights of the ATMOS instrument on board the Space Shuttle will provide a better prognosis of future stratospheric trends. Model calculations based on these measured levels predict the growth and subsequent decline of atmospheric chlorine to span several decades before returning to the critical value of below 2 ppbv, at which the Antarctic ozone "hole" is believed to have been initiated. Future measurements of HCl and HF can be used as an accurate measure of chlorine loading, and will help monitor what kind of chemicals are being used to replace the CFCs.

**Acknowledgments.** This work was carried out at the Jet Propulsion Laboratory, California Institute of Technology, under contract to the National Aeronautics and Space Administration, and supported at the Atmospheric and Environmental Research, Inc., by a NASA grant.

## References

- Farmer, C. B., High resolution infrared spectroscopy of the Sun and Earth's atmosphere from space, *Mikrochim. Acta [Wien]*, **III**, 189-214, 1987.
- De Maziere, M., C. Muller, C. Lippens, J. Vercheval, D. Fonteyn, R. Armante, C. Camy-Peyret, V. Achard, J. Besson, J. Marcault, D. Henry, N. Papineau, J. P. Meyer, and D. Frimout, Second flight of the Spacelab Grille spectrometer during the ATLAS-1 mission, *Geophys. Res. Lett.*, **20**, 503-506, 1993.
- Gunson, M. R., C. B. Farmer, R. H. Norton, R. Zander, C. P. Rinsland, J. H. Shaw, and B.-C. Gao, Measurements of CH<sub>4</sub>, N<sub>2</sub>O, CO, H<sub>2</sub>O, and O<sub>3</sub> in the middle atmosphere by the Atmospheric Trace Molecule Spectroscopy experiment on Spacelab 3, *J. Geophys. Res.*, **95**, 13867-13882, 1990.
- Ko, M. K. W., N. D. Sze, G. Molnar and M. J. Prather, Global warming potentials from chlorofluorocarbons and their alternatives - time scales of chemistry and climate, *Atmospheric Environment*, **27A**, 581-587, 1993.
- Mankin, W. G., M. T. Coffey, and A. Goldman, Airborne observations of SO<sub>2</sub>, HCl, and O<sub>3</sub> in the stratospheric plume of the Pinatubo volcano in July 1991, *Geophys. Res. Lett.*, **19**, 179-182, 1992.
- Norton, R. H., and C. P. Rinsland, ATMOS data processing and analysis, *Appl. Opt.*, **30**, 389-400, 1991.
- Prather, M. J., and R. T. Watson, Stratospheric ozone depletion and future levels of atmospheric chlorine and bromine, *Nature*, **344**, 729-733, 1990.
- Rinsland, C. P., J. S. Levine, A. Goldman, N. D. Sze, M. K. W. Ko, and D. W. Johnson, Infrared measurements of HF and HCl total column abundance's above Kitt Peak, 1977-1990: Seasonal cycles, long-term increases, and comparisons with model calculations, *J. Geophys. Res.*, **96**, 15523-15540, 1991.
- Rinsland, C. P., M. R. Gunson, M. C. Abrams, R. Zander, E. Mahieu, A. Goldman, M. K. W. Ko, J. M. Rodriguez, and N. D. Sze, Profiles of stratospheric chlorine nitrate (ClONO<sub>2</sub>) from ATMOS/ATLAS 1 infrared solar occultation spectra, *J. Geophys. Res.*, in press, 1994.
- Tabazadeh, A., and R. P. Turco, Stratospheric chlorine injection by volcanic eruptions - HCl scavenging and implications for ozone, *Science*, **260**, 1082-1086, 1993.
- Wallace, L., and W. Livingston, The effect of the Pinatubo cloud on hydrogen chloride and hydrogen fluoride, *Geophys. Res. Lett.*, **19**, 1209, 1992.
- Wallace, L., and W. Livingston, Spectroscopic observations of atmospheric trace gases over Kitt Peak 3. Long-term trends of hydrogen chloride and hydrogen fluoride from 1978 to 1990, *J. Geophys. Res.*, **96**, 15513-15521, 1991.

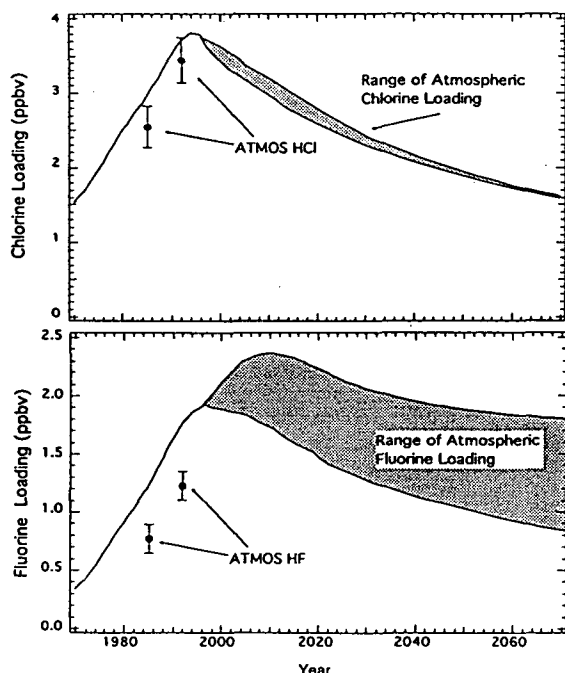


**Figure 3.** Upper and lower panels represent modeled changes in total chlorine (Cly) and fluorine (Fy), respectively, from the present through the next century. Added to these are values reported in this paper of the ATMOS measurements of the upper stratospheric HCl and HF mixing ratios from 1985 and 1992. The modeled curves are calculated from the assumed emissions and lifetimes using the methods described in Prather and Watson [1990]. The shaded regions in both panels represents the range in future levels depending on the exact mix of substitutes (HCFCs and HFCs) used following the phase-out of CFCs in 1996.

- Zander, R., C. P. Rinsland, C. B. Farmer, and R. H. Norton, Infrared spectroscopic measurements of halogenated source gases in the stratosphere with the ATMOS instrument, *J. Geophys. Res.*, **92**, 9836-9850, 1987a.
- Zander, R., G. Roland, L. Delbouille, A. Sauval, C. B. Farmer, and R. H. Norton, Monitoring the integrated column of hydrogen fluoride above the Jungfraujoch station since 1977 - The HF/HCl column ratio, *J. Atmos. Chem.*, **5**, 385-394, 1987b.
- Zander, R., G. Roland, L. Delbouille, A. Sauval, C. B. Farmer, and R. H. Norton, Column abundance and long-term trend of hydrogen chloride (HCl) above the Jungfraujoch station, *J. Atmos. Chem.*, **5**, 395-404, 1987c.
- Zander, R., M. R. Gunson, J. C. Foster, C. P. Rinsland, and J. Namkung, Stratospheric ClONO<sub>2</sub>, HCl, and HF concentration profiles derived from Atmospheric Trace Molecule Spectroscopy experiment Spacelab 3 observations: An update, *J. Geophys. Res.*, **95**, 20519-20525, 1990.
- Zander, R., M. R. Gunson, C. B. Farmer, C. P. Rinsland, F. W. Irion, E. Mahieu, The 1985 chlorine and fluorine inventories in the stratosphere based on ATMOS observations at 30° North latitude, *J. Atmos. Chem.*, **15**, 171-186, 1992.
- Zander, R., C. P. Rinsland, E. Mahieu, M. R. Gunson, C. B. Farmer, M. C. Abrams, and M. K. W. Ko, Increase in carbonyl fluoride (COF<sub>2</sub>) in the stratosphere and its contribution to the 1992 budget of inorganic fluorine in the upper stratosphere, *J. Geophys. Res.*, in press, 1994.
- M. R. Gunson, M. C. Abrams, and L. L. Lowes, Jet Propulsion Laboratory, California Institute of Technology, 4800 Oak Grove Drive, Pasadena, California 91109 (e-mail: mrg@atmosmips.jpl.nasa.gov)
- E. Mahieu and R. Zander, Institut d'Astrophysique, Université de Liège, Liège-Conite, Belgium
- C. P. Rinsland, Atmospheric Sciences Division, NASA Langley Research Center, Hampton, Virginia 23681-0001
- M. K. W. Ko, N. D. Sze, and D. K. Weisenstein, Atmospheric and Environmental Research, Inc., 840 Memorial Drive, Cambridge, Massachusetts 02139

(Received June 7, 1994; accepted July 20, 1994)

## Appendix C

Zander, R., E., et al. (1994) Secular evolution of the vertical column abundances of  $\text{CHClF}_2$  (HCFC-22) in the earth's atmosphere inferred from ground-based IR solar observations at the Jingfaujoch and at Kitt Peak, and comparison with model calculations. *J. Atmos. Chem.*, **18**, 129-148

## Secular Evolution of the Vertical Column Abundances of $\text{CHClF}_2$ (HCFC-22) in the Earth's Atmosphere Inferred from Ground-Based IR Solar Observations at the Jungfraujoch and at Kitt Peak, and Comparison with Model Calculations

R. ZANDER, E. MAHIEU and PH. DEMOULIN

*Institute of Astrophysics, University of Liège, 4000 Liège, Belgium*

C. P. RINSLAND

*Atmospheric Sciences Division, NASA Langley Research Center, Hampton, VA 23681, U.S.A.*

D. K. WEISENSTEIN, M. K. W. KO and N. D. SZE

*Atmospheric and Environmental Research, Inc., Cambridge, MA 02139, U.S.A.*

and

M. R. GUNSON

*Jet Propulsion Laboratory, California Institute of Technology, Pasadena, CA 91109, U.S.A.*

(Received: 21 January 1993; in final form: 13 April 1993)

**Abstract.** Series of high-resolution infrared solar spectra recorded at the International Scientific Station of the Jungfraujoch, Switzerland, between 06/1986 and 11/1992, and at Kitt Peak National Observatory, Tucson, Arizona (U.S.A.), from 12/1980 to 04/1992, have been analyzed to provide a comprehensive ensemble of vertical column abundances of  $\text{CHClF}_2$  (HCFC-22; Freon-22) above the European and the North American continents. The columns were derived from nonlinear least-squares curve fittings between synthetic spectra and the observations containing the unresolved  $2\nu_6$  Q-branch absorption of  $\text{CHClF}_2$  at  $829.05\text{ cm}^{-1}$ . The changes versus time observed in these columns were modeled assuming both an exponential and a linear increase with time. The exponential rates of increase at one-sigma uncertainties were found equal to  $(7.0 \pm 0.35)\%/yr$  for the Jungfraujoch data and  $(7.0 \pm 0.23)\%/yr$  for the Kitt Peak data. The exponential trend of  $7.0\%/yr$  found at both stations widely separated in location can be considered as representative of the global increase of the  $\text{CHClF}_2$  burden in the Earth's atmosphere during the period 1980 to 1992. When assuming two realistic vertical volume mixing ratio profiles for  $\text{CHClF}_2$  in the troposphere, one quasi constant and the other decreasing by about 13% from the ground to the tropopause, the concentrations for mid-1990 were found to lie between 97 and 111 pptv (parts per trillion by volume) at the 3.58 km altitude of the Jungfraujoch and between 97 and 103 pptv at Kitt Peak, 2.09 km above sea level. Corresponding values derived from calculations using a high vertical resolution-2D model and recently compiled HCFC-22 releases to the atmosphere, were equal to 107 and 105 pptv, respectively, in excellent agreement with the measurements. The model calculated lifetime of  $\text{CHClF}_2$  was found equal to 15.6 years. The present results are compared critically with similar data found in the literature. On average, the concentrations found here are lower by 15–20% than those derived from in situ investigations; this difference cannot be explained by the absolute uncertainty of  $\pm 11\%$  assigned presently to the

infrared remote measurements.

**Key words:** CHClF<sub>2</sub>, atmospheric composition, infrared solar observations.

## 1. Introduction

In 1990, CFCl<sub>3</sub> (CFC-11), CF<sub>2</sub>Cl<sub>2</sub> (CFC-12) and CHClF<sub>2</sub> (HCFC-22) remained by far the three 'Freons' most produced in the world, with reported 1990 productions, expressed in metric tons (mt), equal to 232,916 mt, 230,950 mt, and 213,714 mt, respectively [see AFEAS, 1991a, b, for all numerical quantities and uncertainties (including nonreporting countries) dealing with production and releases to the atmosphere of CFC-11, CFC-12, and HCFC-22 referred to in this work]. However, CFC-11 and CFC-12, still intensively used in the refrigeration industry, as aerosol propellants and as foam blowing agents, have undergone a stagnating production during 1975–1987, followed by a marked decrease of almost 50% from 1987 to 1990 as a consequence of the regulations by the 'Montreal Protocol on substances that deplete the ozone layer' and by the London Amendment [e.g., Johnston, 1987; WMO-Report No. 25, 1992]. That regulated decrease is supposed to further apply throughout the 90s, until full elimination by the year 2000. Best estimates of total cumulative production and releases to the atmosphere up to 1990 amounted to  $7.98 \times 10^6$  mt and  $6.98 \times 10^6$  mt for CFC-11, and  $10.4 \times 10^6$  mt and  $9.84 \times 10^6$  mt for CFC-12. HCFC-22, on the other hand, has seen its production steadily on the rise since its first reported production of 56,071 mt in 1970, doubling between 1978 and 1990; its reported total cumulative production and release to the atmosphere until 1990 were equal to  $2.96 \times 10^6$  mt and  $2.46 \times 10^6$  mt, respectively [AFEAS-1991b]. The main uses of CHClF<sub>2</sub> are also aerosol propulsion, refrigeration and as a foam blowing agent. Nonregulation of HCFC-22 by the Montreal Protocol resulted from the fact that the existence of one (or more) hydrogen atom in the HCFCs' (hydrochloro-fluoro-carbons, mainly CHClF<sub>2</sub>) structures implies that these compounds are partly removed in the lower atmosphere by reactions with the hydroxyl radical OH, and consequently have shorter lifetimes than fully halogenated gases such as CFC-11 and CFC-12. HCFCs are, therefore, expected to have less effect on ozone depletion in the stratosphere and on global warming in the troposphere [see Ch. 6 and 7 in WMO-Report No. 25, 1992]. The lifetimes of CFC-11 and CFC-12 are not yet known with great accuracy [see Ch. 8 in WMO-Report No. 25, 1992]. For HCFC-22, reported lifetimes have ranged from ~20 years (Prinn, 1988) to 15.5 years (Golombek and Prinn, 1989), with the most likely value now appearing to be 15.8 years, based on 2- and 3-D model calculations incorporating production- and release data [see Ch. 8 in WMO-Report No. 25, 1992]. It is because of the unregulated production increase of HCFC-22 and the tendency for industry to substitute it for the regulated CFC-11 and CFC-12 applications that careful monitoring of the atmospheric burden of the former one has become critical.

CHClF<sub>2</sub> was measured for the first time in ground-level air by Rasmussen *et al.* (1980). The Oregon Graduate Institute/Department of Environmental Science group pioneered in the late 70s then remained active in gathering in situ measurements of CHClF<sub>2</sub> in the boundary layer at various locations extending from the Arctic to the South Pole. Extensive data sets and derived trends for CHClF<sub>2</sub> were reported for the Pacific Northwest coast between 1976 and 1981 (11.7%/yr; Khalil and Rasmussen, 1981), for Cape Grim, Tasmania, from 1984 to 1987 (8.4%/yr; Khalil and Rasmussen, 1987), and over Hawaii from 1980 to 1987 (7.9%/yr at Cape Kumukahi, and 8.2%/yr at Mauna Loa; Khalil and Rasmussen, 1991). When analyzed by Fraser *et al.* (1989), the Cape Grim data set of 1984–87 returned a rate of increase equal to  $(7.1 \pm 0.3)\%/yr$  for 1987; these measurements indicated an average 1985 concentration of 77 pptv (parts per trillion,  $10^{-12}$ , by volume). Assuming an interhemispheric concentration ratio of 1.16 (WMO-Report No. 16, 1986), a global 1986 tropospheric concentration of 92 pptv, increasing at a rate of 7.1%/yr for that same year was calculated for the WMO-Report No. 18, 1989. An analysis combining Pacific Northwest and South Pole measurements made over the period 1979–1987 has recently been reported by Khalil and Rasmussen [1990], with a derived global rate of increase of 6.1%/yr for January 1987. It should be noted here that the in-situ concentrations mentioned above apply to the boundary layer where the HCFC-22 release takes place.

The first remote measurement of atmospheric HCFC-22 was made from infrared (IR) solar observations by balloon in which Goldman *et al.* (1981) identified the  $2\nu_6$  Q-branch of CHClF<sub>2</sub>. That same absorption feature was quantified in ground-based IR solar observations by Zander *et al.* (1983) and in IR solar occultation observations obtained from space with the ATMOS instrument in 1985 (Zander *et al.*, 1987, 1992). More recently, Rinsland *et al.* (1989) analyzed the  $2\nu_6$  Q-branch in a set of IR solar spectra recorded at Kitt Peak National Observatory on nine different days between 1980 and 1988, and derived an increase rate of  $(7.8 \pm 1)\%/yr$  in the vertical column abundance of HCFC-22 above that station; all of this last data set, supplemented by observations extending to mid-1992, also recorded at Kitt Peak, have been reanalyzed as input to this paper, using the same updated set of line parameters. Complete stratospheric profiles of CHClF<sub>2</sub> up to 33 km altitude were first obtained by Fabian *et al.* (1985) using airborne cryogenic samplers during balloon flights made in 1982 and 1983 near 44° N latitude. These data, supplemented by similar measurements repeated in 1987, led Fabian *et al.* (1989) to derive an average growth rate of 10% at tropopause heights. Two IR balloon observations made in 1981 and in 1988 by the University of Denver group were further analyzed by Rinsland *et al.* (1990) to derive the first CHClF<sub>2</sub> trend near 15 km altitude, i.e.,  $(9.4 \pm 1.3)\%/yr$ .

In this paper, we report measurements of vertical column abundances of CHClF<sub>2</sub> above the Jungfraujoch station, Switzerland, between 06/1986 and 11/1992, and compare them to those derived from an updated investigation of the Kitt Peak data base which now extends from 12/1980 to 04/1992. From these column investiga-

tions, the secular trends as well as local concentrations will be derived for both sites. These results will be compared with other measurements and with calculations using a high vertical resolution version of the AER 2-D model based on the  $\text{CHClF}_2$  releases compiled as part of the Alternative Fluorocarbon Environmental Acceptability Study (AFEAS, 1991b).

## 2. Observations and Analysis

The present study is based on IR remote solar observations from the ground carried out (by PhD.) at the International Scientific Station of the Jungfraujoch (ISSJ), Switzerland (altitude 3580 m; latitude  $46.5^\circ$  N; longitude  $8.0^\circ$  E) from 06/86 to 06/92, and at the National Solar Observatory McMath solar telescope facility on Kitt Peak (KPNSO), Tucson, Arizona (altitude 2090 m; latitude  $31.9^\circ$  N; longitude  $111.6^\circ$  W) between 12/1980 and 04/1992; these were recorded by one of us (C.P.R.) after 10/1987, the earlier ones being part of the KPNSO archive. All observations were made regularly with Fourier transform spectrometers operated at each site at an unapodized resolution of about  $0.005\text{ cm}^{-1}$  in the spectral region encompassing the  $2\nu_6$  Q-branch of  $\text{CHClF}_2$  located at  $829.05\text{ cm}^{-1}$  (for further instrumental details, see Rinsland *et al.*, 1991a). The ISSJ results reported in this work include 38 monthly mean vertical column abundances of  $\text{CHClF}_2$  derived from sets of monthly mean spectra with solar zenith angles of about  $76^\circ$ ,  $80^\circ$ , and  $84^\circ$ , encompassing over 480 individual observations; the reasons to proceed in this way have been discussed in an earlier paper dealing with  $\text{HNO}_3$  investigations in the  $860\text{--}880\text{ cm}^{-1}$  region (Rinsland *et al.*, 1991a). The KPNSO results are daily average columns of  $\text{CHClF}_2$  obtained from some 160 individual spectra recorded on 31 different days during the 11.5 years time base.

$\text{CHClF}_2$  possesses significant and wide absorptions in the  $780\text{--}840\text{ cm}^{-1}$  and  $1080\text{--}1150\text{ cm}^{-1}$  regions (Murcray *et al.*, 1984), but the  $2\nu_6$  Q-branch at  $829.05\text{ cm}^{-1}$  has been the only feature used so far in quantitative IR remote sensing studies (Goldman *et al.*, 1981; Zander *et al.*, 1983, 1987, 1992; Rinsland *et al.*, 1989, 1990), being strong, well isolated, and the only narrow feature of that molecule. As is the case for most 'Freon'-produced absorptions (e.g., Zander *et al.*, 1987; Brown *et al.*, 1987), the rotational study of the unresolved  $2\nu_6$  Q-branch of  $\text{CHClF}_2$  has not yet been performed and classical spectroscopic parameters (ensemble of discrete transitions with their positions, strengths, half-widths, lower state energies) are not available. Therefore, an empirical set of line parameters was concocted (Zander *et al.*, 1992) in order to model the observed  $\text{CHClF}_2$   $2\nu_6$  Q-branch synthetically, using the conventional least-squares curve fitting algorithms that are routinely adopted to compute the atmospheric transmission with line parameters available from regularly updated compilations (Rothman *et al.*, 1992). That set contains 70 transitions whose sum of the strengths was assigned a value equal to  $2.79 \times 10^{-19}\text{ cm}^{-1}/\text{molec.cm}^{-2}$ , i.e., some 23% smaller than in an earlier set (Zander *et al.*, 1987), in order to account for improved absorption cross-sections derived from



laboratory measurements by McDaniel *et al.* (1991). A line half-width equal to  $0.030 \text{ cm}^{-1}/\text{atm}$ , at 296 K and a  $T^{-0.5}$  temperature dependence were adopted for all components, as these values provide good match between the calculated Q branch and observations under various slant path geometries from both the ground and from space. A lower state energy of  $230 \text{ cm}^{-1}$  was further assigned to all transitions, meaning that little temperature dependence of the Q branch is assumed over the atmospheric temperature range encountered in remote sensing studies; this is a reasonable assumption when considering the changes in cross-sections reported by McDaniel *et al.* (1991) between 203 and 293 K, also noting that the bulk of CHClF<sub>2</sub> for ground-based measurements is located in the first kilometers above the observational site, with temperature changes not exceeding 40 K. The vibrational partition function was computed with the harmonic oscillator approximation and the assignments and fundamental frequencies of Brown *et al.* (1988). Recent validation exercises undertaken at the Jet Propulsion Laboratory by F. W. Irion (private communication, 1992) have further confirmed that the strength of the  $2\nu_6$  Q-branch of CHClF<sub>2</sub> adopted here is also consistent with new absorption cross-sections derived by Varanasi (1992) from high-resolution ( $0.0001 \text{ cm}^{-1}$ ) laboratory spectra recorded at temperatures ranging from 216 to 294 K. As the  $2\nu_6$  Q-branch strength used in this work is confirmed by the two most recent laboratory investigations (McDaniel *et al.*, 1991; Varanasi, 1992) we believe that its absolute uncertainty is less than  $\pm 7\%$ .

The algorithm employed to fit the observations made at both ISSJ and at KPNSO was developed at the Langley Research Center by one of us (C.P.R.) in the mid-80s, with steady improvements since then (e.g., Rinsland *et al.*, 1982, 1984, 1991b; Norton and Rinsland, 1991). It is based on a 29 layers curved atmosphere with each layer being considered homogeneous in terms of temperature, pressure and constituents' volume mixing ratios (VMRs). The atmospheric layering as well as the 'reference' VMR profiles adopted as initial values to fit the absorption of the CHClF<sub>2</sub> target molecule are given in Table I. The initial VMR profiles for other gases whose absorptions interfere with the  $2\nu_6$  Q-branch of CHClF<sub>2</sub> (mainly O<sub>3</sub>, CO<sub>2</sub>, and C<sub>2</sub>H<sub>6</sub>) were taken from a set of realistic profiles assembled by Smith (1982), with updated adjustments whenever appropriate. The spectral fittings are achieved by multiplicative scaling of the entire initial VMR profile of each of up to five molecules – target and main interfering combined – with the absorption contributions of up to 15 other gases also included. In addition to the CHClF<sub>2</sub> spectroscopic parameters discussed before, the AFGL-1992 line parameters compilation (Rothman *et al.*, 1992) was used to compute interfering absorptions caused by other telluric gases. The physical models adopted for ISSJ were based on typical seasonal temperature profiles validated with respect to radiosonde measurements made at Payerne, Switzerland, while the KPNSO related analysis relied primarily on temperature sounding data calculated by the National Meteorological Center for the dates and time of the spectral measurements (K. W. Johnson and M. Gelman, private communications, 1985– 1992), with additional profiles derived from

Table I. Layering of the atmosphere for the algorithms used in this research, and initial relative 'reference' profiles adopted for CHClF<sub>2</sub> column and VMR retrievals

Layer No.	Layer limits (in km)		Initial concentration profiles in pptv ( $10^{-12}$ by volume)	
	ISSJ	KPNSO	'Reference 1'	'Reference 2'
29	above 80	above 80	—	—
28	70–80	70–80	—	—
27	60–70	60–70	—	—
26	50–60	50–60	—	—
25	45–50	45–50	3.0	9.1
24	40–45	40–45	9.0	10.8
23	35–40	35–40	15.5	14.4
22	32–35	32–35	21.7	18.5
21	30–32	30–32	24.7	20.9
20	28–30	28–30	26.9	22.6
19	26–28	26–28	29.4	24.3
18	24–26	24–26	33.2	25.9
17	22–24	22–24	37.8	27.8
16	20–22	20–22	45.3	30.3
15	18–20	18–20	52.1	32.8
14	16–18	16–18	53.3	36.6
13	15–16	14–16	54.3	43.8
12	14–15	13–14	54.5	46.0
11	13–14	12–13	54.6	48.7
10	12–13	11–12	54.7	49.9
9	11–12	10–11	54.7	50.2
8	10–11	9–10	54.8	50.6
7	9–10	8–9	54.8	51.1
6	8–9	7–8	54.9	51.7
5	7–8	6–7	54.9	52.4
4	6–7	5–6	54.9	52.9
3	5–6	4–5	55.0	53.4
2	4–5	3–4	55.0	53.9
1	3.58–4	2.09–3	55.0	55.0

measurements by radiosondes released from the Tucson airport, about 60 km north-east of Kitt Peak. Errors from not incorporating the real atmospheric conditions have been evaluated in terms of retrieved column abundances uncertainties (see Table II), with the adopted temperature sensitivity of the  $2\nu_6$  Q-branch of CHClF<sub>2</sub> equal to 0.1%/K.

It is because of the limited observational information on the concentration of CHClF<sub>2</sub> throughout the troposphere that the interpretation of the ISSJ and KPNSO measurements was undertaken, using two VMR 'reference' profiles given

Table II. Random and systematic error sources and resulting one sigma uncertainties for a typical individual monthly mean ISSJ spectrum or a typical individual KPNSO spectrum

Error sources	1-sigma uncertainty in % of column	
	ISSJ	KPNSO
<i>Random</i>		
Finite signal-to-noise	2	2
Zero transmission level offset	1	1
Error in 100% transmission level	1	2
Interfering absorptions	2	2
P-T profiles uncertainty	3	1
Variability in assumed VMR profile	<2	<2
Observational geometry and averaging	<u>1</u>	<u>3</u>
Root-sum-square total random:	4.9	5.2
<i>Systematic</i>		
Total spectroscopic parameters uncertainty	10	10
Bias due to assumed VMR profile	2	2
Algorithm uncertainty	<u>3</u>	<u>3</u>
Root-sum square total systematic:	10.6	10.6

in Table I. The 'reference 1' profile was assembled by adopting the mean relative variation versus altitude derived above 12 km from the 1985-ATMOS remote shuttle observations (Zander *et al.*, 1987), then extending it further down by assuming an almost constant VMR value; this tropospheric part of the profile is consistent with in situ measurements made by Leifer *et al.* (1981) near 20° N on 05/13/1980 from aboard a U-2 airplane flying between 4.6 and 19.2 km altitude, and showing no significant gradient in the VMRs below 14 km. The 'reference 2' profile is typical of the results calculated specifically with the AER model to support this research, and which are discussed later in the text. It is characterized by a decrease in the VMR of CHClF<sub>2</sub> of about 13% between the sites' altitude and their mean tropopause height (~10.5 km for ISSJ and ~13.5 km for KPNSO); such a decrease is consistent with few experimental measurements reported in WMO-Report No. 16 (1986) and based on in situ measurements by Fabian *et al.* (1985) and by Rasmussen and Khalil (1983). As no recent investigations have dealt specifically with measurements of VMRs of CHClF<sub>2</sub> in the troposphere, we can only assume that the two 'reference' profiles described before are equally realistic and likely to bracket the real CHClF<sub>2</sub> concentration profiles in the troposphere (both 'reference' profiles are reproduced in the right-hand part of Figure 4 for comparison with model calculations (left-hand part) discussed later in the text).

The main frames of Figures 1 and 2 reproduce two typical nonlinear least-squares curve fitting examples of observations encompassing the 2ν<sub>6</sub> Q-branch of

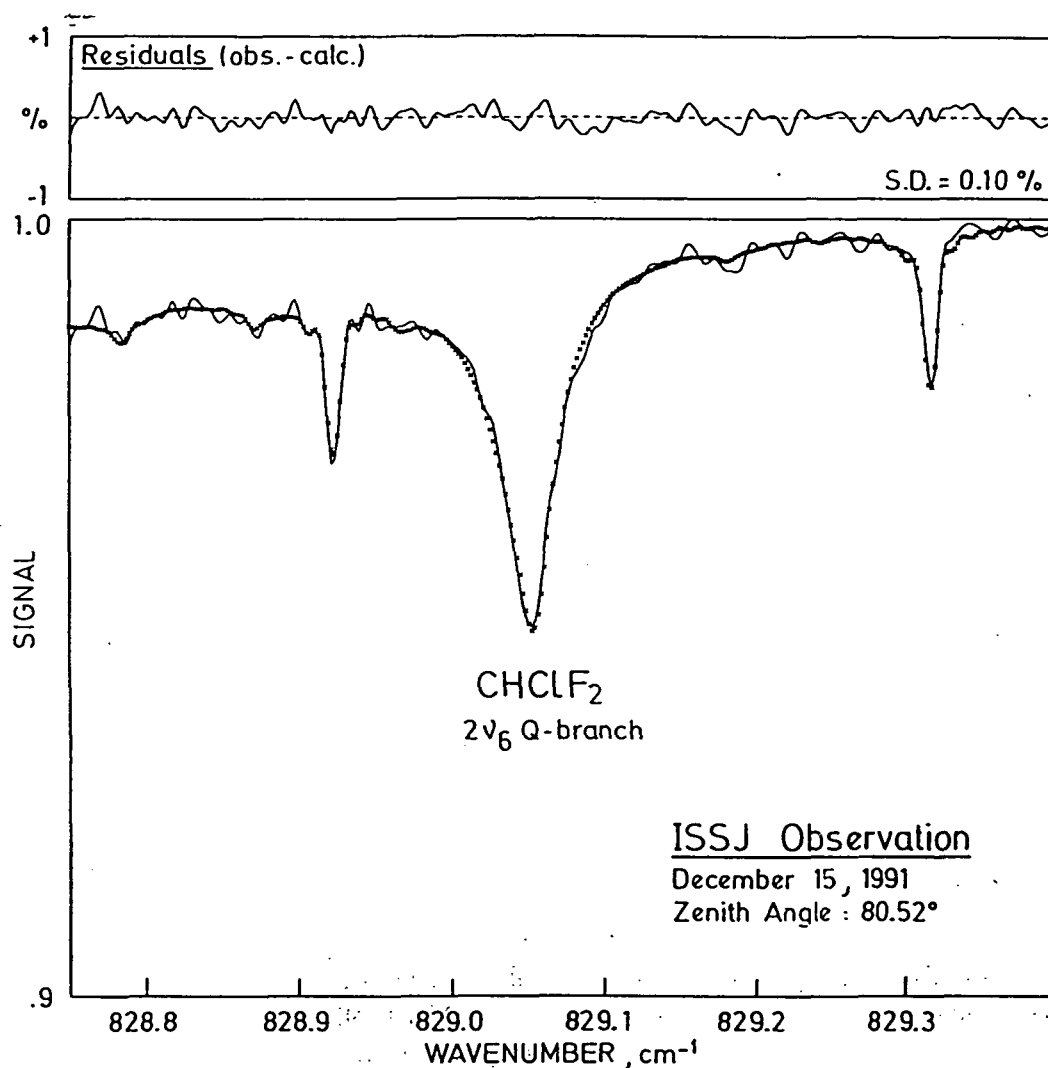


Fig. 1. Example of a nonlinear least-squares curve fitting (crosses) to a sample spectrum recorded at the Jungfraujoch on 12/15/1991, encompassing the  $2\nu_6$  Q-branch of  $\text{CHClF}_2$  centered at  $829.05 \text{ cm}^{-1}$ . The two well defined narrow lines are due to ozone, while a few additional weaker features are caused by  $\text{CO}_2$  and by  $\text{C}_2\text{H}_6$  interferences. The upper frame shows the residuals of the fit, i.e., the observed minus the calculated signals; the standard deviation of 0.1% corresponds to the root-square of the sum of the squares of the residuals over the entire spectral interval reproduced in the figure.

$\text{CHClF}_2$ , respectively made at ISSJ in December 1991 at a mean solar zenith angle of  $80.52^\circ$ , and at KPNSO on 21 April 1992 at a solar zenith angle of  $72.83^\circ$ , using the 'reference 1' profile of Table I. The upper frames of Figures 1 and 2 show the residuals of the fits, i.e., the observed minus calculated signals; they visualize the overall quality of the observations and the goodness of the fits. Similar good fits were obtained when using the 'reference 2' profile of Table I.

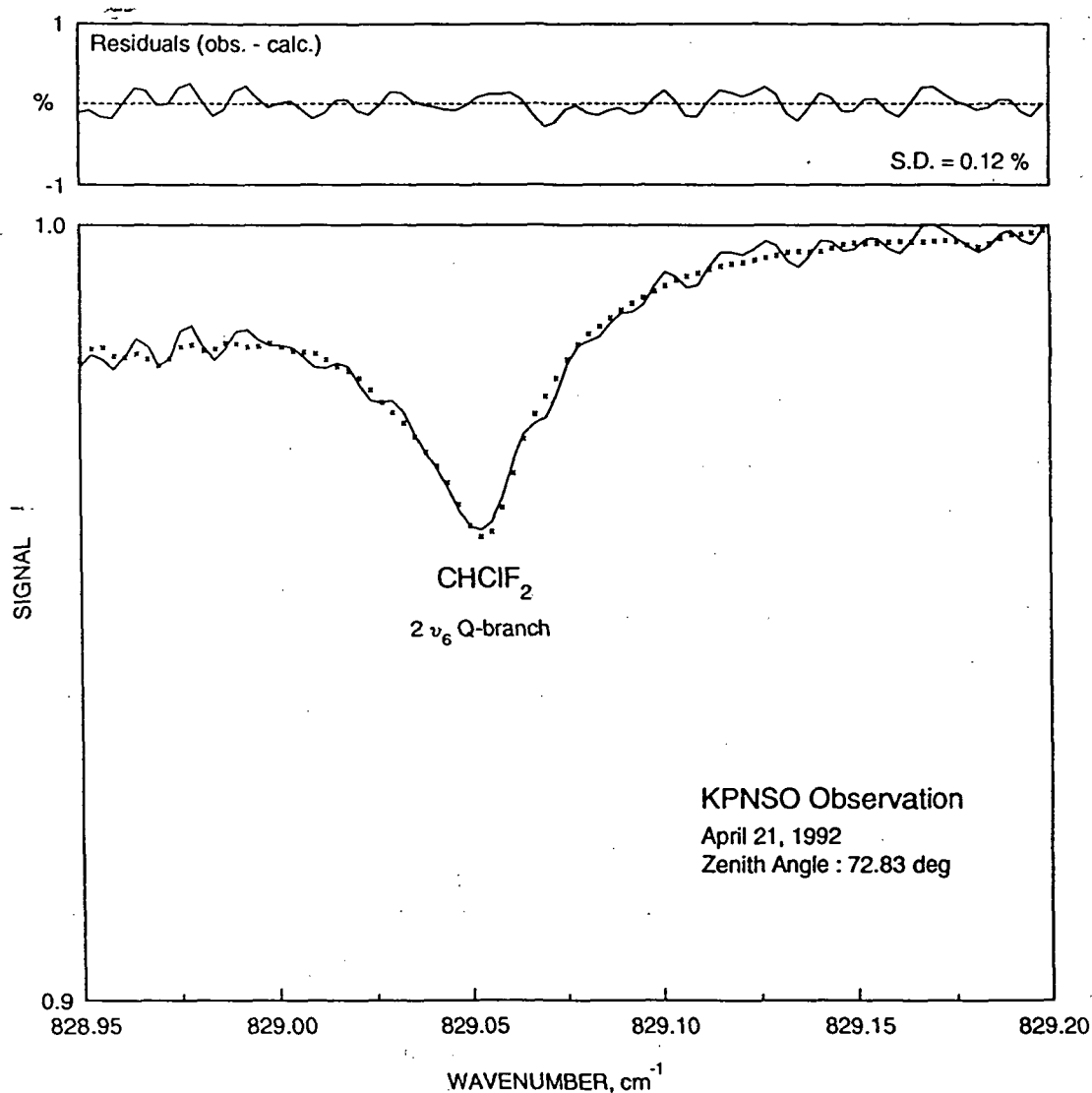


Fig. 2. Example of a nonlinear least-squares curve fitting (crosses) to a sample spectrum recorded at Kitt Peak on 04/21/1992, encompassing the  $2\nu_6$  Q-branch of  $\text{CHClF}_2$  at  $829.05 \text{ cm}^{-1}$ . As in Figure 1, the upper frame shows the residuals of the fit, whose standard deviation over the  $828.9$  to  $829.2 \text{ cm}^{-1}$  is equal to  $0.12\%$  (the interval fitted here is only about half that adopted in Figure 1).

### 3. Observational Results

Figure 3 reproduces the two ensembles of vertical column abundances of  $\text{CHClF}_2$  derived from the ISSJ and KPNSO infrared solar observations, respectively marked by full dots and full triangles. As mentioned earlier, the ISSJ columns are monthly means (total of 38 months involving 480 individual observations) while the KPNSO values are daily means (total of 31 days and 160 individual spectra). To within uncertainties detailed in Table II, fittings applied to individual spectra taken during

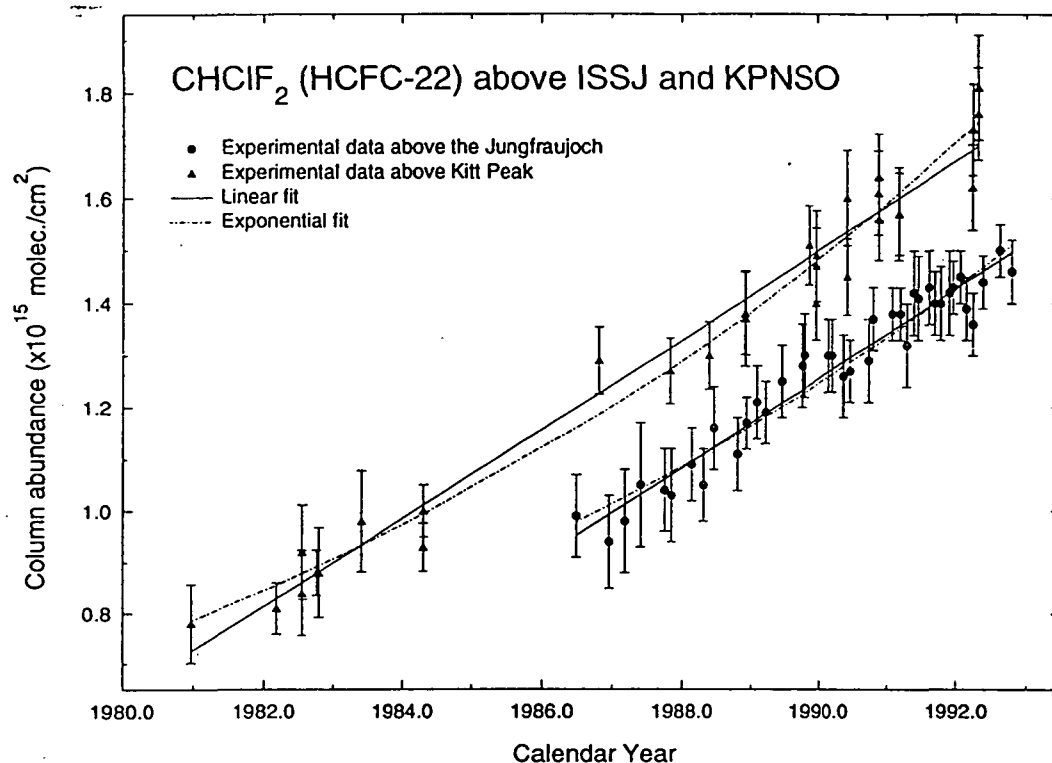


Fig. 3. Timely representation of the vertical column abundances measured in this work. Each full triangle represents a daily data point obtained from spectra recorded at KPNSO, while the full circles correspond to monthly values obtained for ISSJ. All vertical error bars are two-sigma uncertainties evaluated on the basis of the error sources quantified in Table II. The full and dot-dashed curves correspond, respectively, to linear and exponential fittings to the data points obtained at both sites.

the same day at either station do not show evidence for statistically meaningful short term variability in the CHClF<sub>2</sub> columns.

Table II presents the important error sources that need to be considered in evaluating the random and systematic uncertainties of the results. The procedure adopted for determining the reported error magnitudes per individual monthly mean spectrum for ISSJ and per individual daily spectrum for KPNSO, was essentially based on sensitivity tests such as described earlier (e.g., Rinsland *et al.*, 1982, 1984; Zander *et al.*, 1989a, 1989b); the uncertainties are given at the one-sigma level and expressed in percentage of the total vertical column abundances above either ISSJ or KPNSO. Assuming that the individual error sources are unrelated, the total random and systematic uncertainties have been calculated by taking the square root of the sum of the squares of the individual components. When more than one spectrum was included in an averaging, some of the random errors could still be reduced by the square root of the number of the spectra involved. With only a few exceptions, the results derived in this work are precise to  $\pm 5\%$ ; this is the uncertainty affecting the trends determination. Despite the improvement reported

earlier regarding the absolute uncertainty affecting the strength of the  $2\nu_6$  Q-branch of CHClF<sub>2</sub>, Table II clearly indicates that it is still the ensemble of the spectroscopic parameters needed in the inversion process of the measured absorption (strength, half-widths, temperature dependence) that contributes predominantly to the total systematic root-sum-square error of about  $\pm 11\%$ ; this is the uncertainty that needs to be taken into consideration when comparing the CHClF<sub>2</sub> columns reported here with those obtained by other techniques (i.e., in situ) or determined from model calculations. The error bars associated with the ISSJ vertical columns displayed in Figure 3 incorporate the total two-sigma random error as per Table II, to which was added the standard deviation among the columns derived from independent spectra making up one data point in the figure. The error bars assigned to the KPNSO data points in Figure 3 are two sigma estimates of the random error only, ranging between  $\pm 5\%$  for multiple observations in good agreement, to  $\pm 10\%$  for a single retrieved data point.

In order to characterize the timely evolution of the measured vertical column abundances, various modeling options were used to fit the observational data points of Figure 3, i.e., (i) an exponential growth with time, (ii) a linear increase with time, (iii) either of these increasing functions superimposed on a sinusoidal seasonal cycle. The formulation of these options has been described by Rinsland *et al.* (1991b). The exponential rate of increase at one-sigma uncertainty returned from the fit to the ISSJ data points (dotted curve in Figure 3) was equal to  $(6.99 \pm 0.35)\%/yr$ , with a standard deviation of 0.041 expressed in units of  $10^{15}$  molec./cm<sup>2</sup>. A fit to the ISSJ columns assuming a linear increase (straight full line) returned a corresponding result equal to  $(7.45 \pm 0.34)\%/yr$  for 1989, with a standard deviation of  $0.038 \times 10^{15}$  molec./cm<sup>2</sup>. The small difference in the standard deviations for both fitting cases precludes a clear choice between either functional trend representation applied here, a presumed consequence of temporary 'anomalies' in the ISSJ column evolution (e.g., a high column in 06/86; some stagnating columns during 1990, and low values in early 1992), likely to reflect peculiar meteorological conditions such as those encountered during the winter of 1991–92 at mid- and high northern latitudes. The mid-1990 vertical column abundances read off the exponential- and linear- curves fitted to the ISSJ data points of Figure 3 are equal to 1.29 and  $1.31 \times 10^{15}$  molec./cm<sup>2</sup>, respectively.

The KPNSO daily mean columns are reproduced in Figure 3 by the full triangles. Although less dense in measurement points than the ISSJ set, they encompass a longer time interval, about 11.5 years spanning from December 1980 to April 1992. Fitting the KPNSO data set with an exponential and a linear function (see the dotted curve and the straight full line through the KPNSO data points in Figure 3, respectively) resulted in increase rates and one-sigma uncertainties equal to  $(7.0 \pm 0.23)\%/yr$  and  $(6.16 \pm 0.20)\%/yr$  for 1989, respectively. The corresponding standard deviations were equal to 0.050 and 0.053, in units of  $10^{15}$  molec./cm<sup>2</sup>. Even over this longer time base as compared to the ISSJ one, it remains unclear which fitting function best represents the secular evolution of CHClF<sub>2</sub> above

Table III. Vertical column abundances of  $\text{CHClF}_2$  above ISSJ derived from Figure 3 at each mid-year, local VMRs obtained with the 'reference' profiles of Table I, and results from AER-model calculations

Mid-year	Columns above ISSJ ( $\times 10^{15}$ molec./cm <sup>2</sup> )		Local VMRs at ISSJ (in pptv) using profiles		
	Measured <sup>a</sup>	Model calc.	'Reference 1'	'Reference 2'	Model calc.
86.5	0.96	0.94	72.2	82.1	79.2
87.5	1.04	1.01	78.2	88.9	85.1
88.5	1.12	1.09	84.4	96.0	91.9
89.5	1.21	1.18	90.8	103.2	99.7
90.5	1.30	1.28	97.4	110.7	107.4
91.5	1.39	1.36	104.3	118.6	114.4
92.5	1.48	1.45	111.5	126.8	120.7

<sup>a</sup> Obtained by averaging values from exponential and linear fits to the retrieved columns.

KPNSO. When read off the logarithmic and the linear fitted curves, the vertical column abundances of  $\text{CHClF}_2$  above KPNSO for mid-1990 are equal to 1.57 and  $1.59 \times 10^{15}$  molec./cm<sup>2</sup>, respectively.

Because of a similar conclusion arrived at for both ISSJ and KPNSO data sets, i.e., equally good fittings of the columns with either an exponential or a linear function, we shall deal in the rest of this paper with vertical column abundances of  $\text{CHClF}_2$  corresponding to the mean of the values read off the two fitting curves. These average columns interpolated among the measurements are given in Table III (col. 2) for ISSJ and in Table IV (col. 2) for KPNSO, for each mid-year of the time bases encompassed at each station.

#### 4. Comparison with Model Calculations

How do the measurements reported here compare with results from model computations?

The AER-2D model was specifically run to produce vertical column abundances and local VMRs of  $\text{CHClF}_2$  for the particular locations of ISSJ and KPNSO, and over the time periods covered by the observations. The calculations were based on the release data reported in AFEAS-1991b. To extend the calculations to the end of 1992, the lacking emission data for 1991 and 1992 were simply assumed to be equivalent to the 1990 values. A high-resolution version of the AER 2-D model was used for these calculations, with a vertical resolution of approximately 1.2 km. The latitudinal resolution was 9.5 degrees. Model temperatures were an 8-years average of NMC temperatures, and tropopause heights were calculated monthly, based on temperature slope inversions. The model tropopause heights for ISSJ varied from 10.2 to 12.3 km and for KPNSO from 13.6 to 14.7 km, with higher values found in the summer; these values agree reasonably well with those derived



Table IV. Vertical column abundances of CHClF<sub>2</sub> above KPNSO derived from Figure 3 at each mid-year, local VMRs obtained with the 'reference' profiles of Table I, and results from AER-model calculations

Mid-year	Columns above KPNSO ( $\times 10^{15}$ molec/cm <sup>2</sup> )		Local VMRs at KPNSO (in pptv) using profiles		
	Measured <sup>a</sup>	Model calc.	'Reference 1'	'Reference 2'	Model calc.
81.5	0.81	0.76	49.9	53.1	51.6
82.5	0.88	0.84	54.5	58.0	56.1
83.5	0.97	0.91	59.2	63.0	61.0
84.5	1.05	0.99	64.1	68.2	66.3
85.5	1.13	1.07	69.1	73.5	71.7
86.5	1.21	1.16	74.3	79.1	77.2
87.5	1.30	1.24	79.8	84.4	82.9
88.5	1.39	1.34	85.4	90.8	89.5
89.5	1.48	1.45	91.2	97.0	97.1
90.5	1.58	1.57	97.2	103.4	104.7
91.5	1.69	1.68	103.5	110.0	111.5
92.5	1.79	1.78	110.0	117.0	117.8

<sup>a</sup> Obtained by averaging values from exponential and linear fits to the retrieved columns.

from temperature soundings at the meteorological stations of Payerne, Switzerland, and at Tucson, Arizona, U.S.A. OH concentrations and overhead ozone columns were taken from a simulation using the AER fine resolution model with reaction rates from DeMore *et al.* (1992). The simulation included complete chemistry for 1990. Thus the loss rate of CHClF<sub>2</sub> had no temporal trend over the 1980 to 1992 period. The model calculated lifetime of CHClF<sub>2</sub> was found equal to 15.6 years, in excellent agreement with a lifetime of 15.5 years derived by Golombek and Prinn (1989) from a 3-D model investigation.

The model-calculated vertical column abundances above ISSJ and KPNSO are given in columns 3 of Tables III and IV, respectively; they are in excellent agreement and consistent with the experimental results (column 2 of Table IV for ISSJ and of Table IV for KPNSO), differing on average by only a few percent (the maximum is 6% for KPNSO during the early 1980s). The VMRs calculated at the altitudes of the stations by the AER model are also to within a few percent of those derived from the observations with the 'reference 2' VMR profile (compare columns 5 and 6 of Tables III and IV); they differ by up to 10% when treating the observations with the 'reference 1' profile (compare columns 4 and 6 of Tables III and IV). This larger discrepancy is not unexpected when recalling that the 'reference 1' profile is characterized by a quasi constant VMR value throughout the entire troposphere (with less relative contribution by the lowermost layers), while the 'reference 2' profile is in much better agreement with the model-calculated profiles showing decreasing VMRs with increasing altitude throughout the troposphere. Typical VMR profiles returned by the model calculations for mid-1981 at three northern

- Rinsland, C. P., Goldman, A., Murcray, F. J., Blatherwick, R. D., and Murcray, D. G., 1988, Infrared measurements of atmospheric gases above Mauna Loa, Hawai, in February 1987, *J. Geophys. Res.* **93**, 12,607–12,626.
- Rinsland, C. P., Johnson, D. W., Goldman, A., and Levine, J. S., 1989, Evidence for a decline in the atmospheric accumulation rate of  $\text{CHClF}_2$  (CFC-22), *Nature* **337**, 535–537.
- Rinsland, C. P., Goldman, A., Murcray, F. J., Blatherwick, R. D., Kusters, J. J., Murcray, D. G., Sze, N. D., and Massie, S. T., 1990, Long-term trends in the concentrations of  $\text{SF}_6$ ,  $\text{CHClF}_2$ , and  $\text{COF}_2$  in the lower stratosphere from analysis of high-resolution infrared solar occultation spectra, *J. Geophys. Res.* **95**, 16,477–16,490.
- Rinsland, C. P., Zander, R., and Demoulin, Ph., 1991a, Ground-based infrared measurements of  $\text{HNO}_3$  total column abundances: long-term trend and variability, *J. Geophys. Res.* **96**, 9379–9389.
- Rinsland, C. P., Levine, J. S., Goldman, A., Sze, N. D., Ko, M. K. W., and Johnson, D. W., 1991b, Infrared measurements of HF and HCl total column abundances above Kitt Peak, 1977–1990: seasonal cycles, long-term increases, and comparisons with model calculations, *J. Geophys. Res.* **96**, 15,523–15,540.
- Rothman, L. S., Gamache, R. R., Tipping, R. H., Rinsland, C. P., Smith, M. A. H., Benner, D. C., Malathy Devi, V., Flaud, J.-M., Camy-Peyret, C., Perrin, A., Goldman, A., Massie, S. T., Brown, L. R., and Toth, R. A., 1992, The HITRAN molecular database: Editions of 1991 and 1992, *J. Quant. Spectrosc. Radiat. Transfer* **48**, 469–508.
- Smith, M. A. H., 1982, Compilation of atmospheric gas concentration profiles from 0 to 50 km, NASA Technical Memo., TM 83289.
- Varanasi, P., 1992, Absorption spectra of HCFC-22 around  $829\text{ cm}^{-1}$  at atmospheric conditions, *J. Quant. Spectrosc. Radiat. Transfer* **47**, 251–255.
- WMO Report No. 16, 1986, Atmospheric ozone 1985-Assessment of our understanding of the processes controlling its present distribution and change, World Meteorological Organization, CH 1211 Geneva 20, Switzerland.
- WMO Report No. 18, 1989, Report of the international ozone trends panel 1988, World Meteorological Organization, CH 1211 Geneva 20.
- WMO Report No. 25, 1992, Scientific assessment of ozone depletion: 1991, World Meteorological Organization, CH 1211 Geneva 20.
- Zander, R., Stokes, G. M., and Brault, J. W., 1983, Simultaneous detection of FC-11, FC-12 and FC-22, through 8 to 13 micrometers IR solar observations from the ground, *Geophys. Res. Lett.* **10**, 521–524.
- Zander, R., Rinsland, C. P., Farmer, C. B., and Norton, R. H., 1987, Infrared spectroscopic measurements of halogenated source gases in the stratosphere with the ATMOS instrument, *J. Geophys. Res.* **92**, 9836–9850.
- Zander, R., Demoulin, Ph., Ehhalt, D. H., Schmidt, U., and Rinsland, C. P., 1989a, Secular increase of the total vertical column abundance of carbon monoxide above central Europe since 1950, *J. Geophys. Res.* **94**, 11,021–11,028.
- Zander, R., Demoulin, Ph., Ehhalt, D. H., and Schmidt, U., 1989b, Secular increase of the vertical column abundance of methane derived from IR solar spectra recorded at the Jungfraujoch station, *J. Geophys. Res.* **94**, 11,029–11,039.
- Zander, R., Gunson, M. R., Farmer, C. B., Rinsland, C. P., Irion, F. W., and Mahieu, E., 1992, The 1985 chlorine and fluorine inventories in the stratosphere based on ATMOS observations at  $30^\circ$  north latitudes, *J. Atmos. Chem.* **15**, 171–186.

## **Appendix D**

Weisenstein, Debra K., Glenn K. Yue, Malcolm K.W. Ko, Nien-Dak Sze, Jose M. Rodriguez, and Courtney J. Scott (1995) A Two Dimensional Model of Sulfur Species and Aerosols. Submitted to the *J. Geophys. Res.*

A Two Dimensional Model of Sulfur Species  
and Aerosols

Debra K. Weisenstein  
Atmospheric and Environmental Research, Inc.  
840 Memorial Dr., Cambridge, MA 02139

Glenn K. Yue  
NASA Langley Research Center  
Hampton, VA 23681

Malcolm K.W. Ko, Nien-Dak Sze, Jose M. Rodriguez, and Courtney J. Scott  
Atmospheric and Environmental Research, Inc.  
840 Memorial Dr., Cambridge, MA 02139

Submitted to  
Journal of Geophysical Research

December 5, 1995

## Abstract

A two-dimensional model of sulfate aerosols has been developed. The model includes the sulfate precursor species  $\text{H}_2\text{S}$ ,  $\text{CS}_2$ ,  $\text{DMS}$ ,  $\text{OCS}$  and  $\text{SO}_2$ . Oxidation of  $\text{SO}_2$  yields  $\text{H}_2\text{SO}_4$  in the lower and middle stratosphere, which can form aerosols by homogeneous nucleation or by condensation onto existing aerosol particles. Aerosols grow when the ambient partial pressure of  $\text{H}_2\text{SO}_4$  is greater than the vapor pressure of  $\text{H}_2\text{SO}_4$  above the surface of the aerosol droplet, and they evaporate when the ambient partial vapor pressure is less than the vapor pressure above the droplet surface. Aerosols also grow by the process of coagulation, in which the small particles combine into larger particles. Removal of sulfate from the stratosphere is achieved by bulk transport to the troposphere and by sedimentation. Tropospheric aerosols are removed by washout processes and by surface deposition. Our model is successful at both reproducing the stratospheric aerosol surface area under background conditions and at reproducing the magnitude and temporal behavior of stratospheric aerosol loading following the Mt. Pinatubo eruption. The importance of homogeneous nucleation to the accurate modeling of stratospheric aerosols is demonstrated.

## 1. Introduction

There is a background layer of sulfuric acid aerosol particles in the lower stratosphere. The sulfate concentration in the layer is maintained by natural and anthropogenic emissions of sulfur-containing compounds at the earth's surface and by intermittent volcanic eruptions which may inject large quantities of sulfur directly into the stratosphere. This layer plays a significant role in the earth's radiative balance (Michaelangeli et al., 1989) and provides a surface for heterogeneous chemistry, which has an important influence on ozone (Rodriguez et al., 1991; Hofmann and Solomon, 1989). Aircraft which fly in the upper troposphere and lower stratosphere may be contributing to the sulfate loading of the stratosphere (Hofmann, 1990).

We have developed a two-dimensional model including aerosol processes which successfully reproduces the stratospheric aerosol surface area under background conditions and the magnitude and temporal behavior of stratospheric aerosol loading following the Mt. Pinatubo eruption. In section 2, we will describe the aerosol model, including both gas phase reactions and aerosol microphysics. In section 3, we will show results for both the stratospheric and tropospheric sulfate loading for a background atmosphere in the absence of volcanic influence. Section 4 will present results for a simulation of the Mt. Pinatubo volcanic eruption. Section 5 will present discussion, conclusions, and future work.

## 2. The Aerosol Model

The chemistry of sulfur has been incorporated into the framework of the AER two-dimensional model (Kotamarthi et al., 1994; Weisenstein, et al., 1993). The model uses a diabatic circulation in log-pressure coordinates, along with eddy diffusion adjusted to act along isentropes, to transport trace species. It has a vertical resolution of approximately 1.2 km and extends from the ground to 60 km. The horizontal resolution is 9.5

degrees. Model temperatures are taken as the monthly averages of NMC temperatures over the 1979-1986 period. Tropopause heights are based on gradients of these temperatures and range from 10.2 to 12.3 km at 45°N (Shia et al., 1993). The model time step for advection is 2 hours. A major change in model dynamics over our previous work is the inclusion of the "tropical pipe" theory proposed by Plumb (1995). This theory states that there is a barrier to tracer transport between the mid latitude lower stratosphere and the tropical lower stratosphere, i.e., tracers from the upper troposphere enter the stratosphere in the tropics but do not diffuse to higher latitude within the lower stratosphere (20°S-20°N). We have simulated this type of atmospheric circulation by reducing the horizontal diffusion coefficient,  $K_{yy}$ , to values of  $3 \times 10^8$  cm<sup>2</sup>/sec within the tropical lower stratosphere. Outside this region,  $K_{yy}$  values are  $3-10 \times 10^9$  cm<sup>2</sup>/sec in the lower stratosphere and  $3 \times 10^9$  cm<sup>2</sup>/sec in the upper stratosphere. This has a very significant effect on our model simulations of aerosols due to the tropical nature of the aerosol source and of the Mt. Pinatubo volcanic eruption.

The quasi-biennial oscillation (QBO) is known to affect aerosol transport (Trepte and Hitchman, 1992; Trepte et al., 1993). Advective winds in our model are climatological and do not vary from year to year. Thus our model cannot simulate the dynamics of the atmosphere for particular times and may be missing some important contributions to the general circulation as well. The absence of a QBO and other interannual variability in our model makes it difficult to compare aerosol measurements for specific years with model results. Because aerosol amounts are often in flux due to the intermittent nature of volcanic eruptions, the only year for which global data exists that could represent near-background aerosol conditions is 1979. Thus comparisons of model and observations appropriate to background aerosol levels will be made against 1979 data rather than an average over several years of data, which would be preferable.

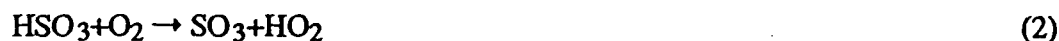
In this model, we choose to deal with homogeneous nucleation as the only mechanism to form new sulfate particles in the stratosphere. Omission of heterogeneous

nucleation probably results in lower calculated values of stratospheric aerosol mass than observed during background conditions. However, our calculation of increases in aerosol mass due to perturbations in SO<sub>2</sub> should be fairly accurate, as homogeneous nucleation is the only mechanism which can produce new particles from gas phase sulfate without a simultaneous increase in condensation nuclei. In very cold regions of the atmosphere (T<195K) aerosols take up HNO<sub>3</sub> (Tabazedeh et al., 1994). We have chosen to deal with only binary solutions (H<sub>2</sub>SO<sub>4</sub> and H<sub>2</sub>O) in this model and do not include processes specific to the polar regions.

#### a) Chemistry

The chemical scheme for the sulfur species generally follows Sze and Ko (1980). The sulfur species included in the model are carbon disulfide (CS<sub>2</sub>), dimethyl sulfide (DMS), hydrogen sulfide (H<sub>2</sub>S), methyl sulfonic acid (MSA), carbonyl sulfide (OCS), sulfur dioxide (SO<sub>2</sub>), sulfur trioxide (SO<sub>3</sub>) and sulfuric acid (H<sub>2</sub>SO<sub>4</sub>). Concentrations of OH, O, NO<sub>3</sub>, H<sub>2</sub>O and O<sub>3</sub> are taken from a previous calculation with the AER 2D model (Kotamarthi, et al 1994; Weisenstein, et al., 1993). Reaction rates (see table 1) are taken from JPL-94 (DeMore et al., 1994) where available. The rate for the abstraction pathway of the reaction of DMS with OH is taken from Chatfield and Crutzen (1990).

There have been some important developments recently in our understanding of the cycling between gas phase SO<sub>2</sub> and H<sub>2</sub>SO<sub>4</sub>. Conversion is initiated by reaction of SO<sub>2</sub> with OH, producing HSO<sub>3</sub>. HSO<sub>3</sub> reacts very rapidly with O<sub>2</sub> to produce SO<sub>3</sub>. The rate of conversion of SO<sub>3</sub> to gas phase H<sub>2</sub>SO<sub>4</sub> in the presence of water vapor is measured to be quadratic in H<sub>2</sub>O (Kolb et al., 1994; Jayne et al., 1995). Thus the oxidation of SO<sub>2</sub> to H<sub>2</sub>SO<sub>4</sub> can be represented by the following reaction sequence:



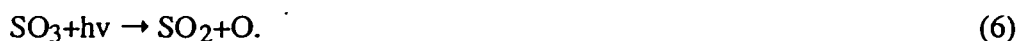


The time constant for reaction (3) is about 1 second at 20 km, 1 minute at 30 km, and 8 hours at 40 km, though there is uncertainty in the rate at low temperatures and pressures. Thus, conversion of SO<sub>2</sub> to H<sub>2</sub>SO<sub>4</sub> is limited only by the oxidation rate of SO<sub>2</sub> below 40 km.

Photolysis of H<sub>2</sub>SO<sub>4</sub> leads to SO<sub>3</sub> formation via the following mechanism:



SO<sub>3</sub> can either photolyze to form SO<sub>2</sub>



or react with H<sub>2</sub>O via reaction (3) to form H<sub>2</sub>SO<sub>4</sub>. In the upper stratosphere, photolysis dominates and thus SO<sub>2</sub> is the end product of H<sub>2</sub>SO<sub>4</sub> photolysis. This appears likely based on recent analysis of the ATMOS data by Rinsland et al. (1995) which indicates that SO<sub>2</sub> concentrations increase with altitude in the middle stratosphere. The photolysis cross-section of H<sub>2</sub>SO<sub>4</sub> is assumed similar to that of HCl. The cross-section of SO<sub>3</sub> is taken from Fajans and Goodeve (1936).

Heterogeneous removal of MSA, SO<sub>2</sub>, and H<sub>2</sub>SO<sub>4</sub> is included in the troposphere. Wet removal of SO<sub>2</sub> is used as a surrogate for all tropospheric loss processes which are not explicitly modeled here, such as heterogeneous reaction with H<sub>2</sub>O<sub>2</sub> and O<sub>3</sub>. Based on results of a three-dimensional model by Benkovitz et al. (1994), we adopt a total tropospheric wet removal rate for SO<sub>2</sub> of 2.5 days mean lifetime, with vertical variations from 1.5 days at ground level to 10 days at 10 km. Wet removal rates of H<sub>2</sub>SO<sub>4</sub> and MSA are 5 days mean lifetime in the troposphere, again following Benkovitz et al. (1994). The chemical scheme and rates used are summarized in Table 1, where the reaction products listed are the end oxidation products; short-lived intermediate radicals such as S, SO, and HSO<sub>3</sub> are omitted.

Estimated surface fluxes of 1 teragram of sulfur per year for CS<sub>2</sub> and 40 teragrams of sulfur per year for DMS are used as boundary conditions between 52°S and

52°N. These emissions are mainly biogenic in origin (Bates, 1992). Anthropogenic emissions of 77.5 teragrams of sulfur per year are input mainly between 24°N and 62°N as SO<sub>2</sub> (Spiro et al., 1992), representing industrial activities, fuel combustion, and biomass burning. H<sub>2</sub>S is set to 30 pptv at the surface, and OCS to 500 pptv (Carroll, 1985; Inn et al., 1979). A deposition velocity of 1 cm/sec is applied at the surface for MSA, SO<sub>2</sub> and H<sub>2</sub>SO<sub>4</sub>. Model boundary conditions are listed in Table 2.

#### b) Aerosol microphysics

Natural aerosol particles usually have radii spanning several orders of magnitude. Thus, we decided to utilize a set of geometrically increasing particle size categories in our model. Our 40 particle sizes bins correspond to particle radii from 0.00039 μm to 3.2 μm with the radius of bin k equal to 2<sup>1/3</sup> times the radius of bin k-1. This is equivalent to having the volume of each bin equal to twice the volume of the preceding bin. The smallest bin size corresponds roughly to the size of particles formed by homogeneous nucleation. The size distribution of aerosols is characterized by the set of number densities  $n_k(I, J)$  for each size bin k at grid-point identified by latitude index I and altitude index J.

Aerosol composition (i.e., weight percent of sulfuric acid,  $W(I, J)$ ) is calculated interactively in the model based on ambient water vapor and temperature according to the formula of Hanson et al. (1994):

$$W(I, J) = \frac{T * (0.6246 * Z - 14.458) + 3565}{-0.19988 * T + 1.3204 * Z + 44.777}$$

where Z is the logarithm of the partial pressure of water vapor in millibars. The mass of H<sub>2</sub>SO<sub>4</sub> bound in particles in bin k at grid point (I, J) is:

$$M_k(I, J) = \frac{4}{3} \pi r_k^3 D(I, J) * W(I, J) * n_k(I, J)$$

where  $D(I,J)$  represents the bulk density of aerosol particles in  $\text{grams cm}^{-3}$ . Our tabulated values of bulk density depend on temperature and aerosol composition and are taken from standard references (Washburn, 1928; Perry and Chilton, 1973).

The microphysical processes simulated in our model are homogeneous nucleation, condensation, evaporation, and coagulation. The first two processes result in conversion of gas phase  $\text{H}_2\text{SO}_4$  to aerosol particles. Evaporation converts aerosol particles back to gas phase  $\text{H}_2\text{SO}_4$ . Coagulation changes the size distribution of particles when the particles collide and fuse. Dynamical transport and sedimentation also influence the distribution and mean lifetime of aerosol particles.

#### (i) Homogeneous nucleation

The process of direct gas to particle conversion (homogeneous nucleation) occurs only in areas of low temperature and high ambient sulfuric acid or water vapor concentration (Yue, 1981; Yue and Deepak, 1982). The homogeneous nucleation rate  $J$  (embryos formed per  $\text{cm}^3$  per sec) in the binary  $\text{H}_2\text{SO}_4\text{-H}_2\text{O}$  system, where the number concentration of water ( $N_w$ ) is much greater than the number concentration of sulfuric acid ( $N_s$ ), is given by:

$$J = 4 \pi r^{*2} \beta_s N_w \exp[(-\Delta G^*)/(kT)]$$

where  $r^*$  is the radius of the embryo,  $\beta_s$  is the impinging rate of gaseous sulfuric acid molecules,  $k$  is the Boltzman constant, and  $T$  is the temperature. The Gibbs free energy change due to particle formation will be a function of temperature and aerosol composition and will have a saddle point or minimum value,  $\Delta G^*$ , which is related to the radius of the embryo  $r^*$  by the formula

$$\Delta G^* = 4/3 \pi \sigma r^{*2},$$

where  $\sigma$  is the microscopic surface tension. The impinging rate of gaseous sulfuric acid molecules,  $\beta_s$  is given by:

$$\beta_s = N_s [kT/(2\pi M_s)]^{1/2}$$

where  $M_s$  is the mass of one molecule of  $H_2SO_4$ .

Under background conditions, new particles form primarily near the tropopause, in the tropics and at high latitudes in winter. The time constant for this process may be less than a day in localized areas.  $H_2SO_4$  removed from the gas phase is put into the smallest aerosol size bin. An appropriate amount of water vapor is also condensed to maintain the proper composition. After new particles are formed, they may grow into larger particles by coagulation and heteromolecular growth processes.

#### (ii) Condensation and Evaporation

The heteromolecular condensation process is simulated in our model and the growth rate of particles by this process is described by Hamill and Yue [1979]. The change of particle radius due to heteromolecular condensation or evaporation is given by the equation:

$$\frac{dr}{dt} = \frac{\bar{v}D(P_s - P_s^0)/(kT)}{r\chi(1 + \lambda K_n)}$$

where  $\bar{v}$  is the average volume per molecule in the droplet,  $D$  is the diffusion coefficient,  $\chi$  is the concentration of  $H_2SO_4$  in the droplet,  $\lambda$  is the correction factor,  $K_n$  is the Knudsen number,  $P_s$  is the vapor pressure of ambient sulfuric acid,  $P_s^0$  is the partial vapor pressure of sulfuric acid over the droplet surface. If  $(P_s - P_s^0) > 0$ , growth by condensation occurs. If  $(P_s - P_s^0) < 0$ , evaporation occurs.

Condensation of  $H_2SO_4$  will increase the percentage of sulfuric acid in the particle, and hence reduce the partial vapor pressure of water. Since sulfate particles are continuously being bombarded by gas phase water and sulfuric acid molecules and the concentration of water molecules is so much greater than the concentration of sulfuric acid in the environment, the sulfate particles will quickly come into equilibrium with the water vapor. We assume that the condensation of  $H_2O$  occurs instantaneously.

Above 30-35 km, the ambient vapor pressure of  $\text{H}_2\text{SO}_4$  is usually lower than the partial vapor pressure of  $\text{H}_2\text{SO}_4$  over the surface of the sulfate particles, and  $\text{H}_2\text{SO}_4$  evaporates from the surface. Water vapor also evaporates to maintain the equilibrium composition. Thus aerosol mass decreases rapidly above 35 km because most sulfur is found in the vapor phase, either as  $\text{H}_2\text{SO}_4$ ,  $\text{SO}_3$ , or  $\text{SO}_2$ .

Under normal stratospheric conditions, most of the gas-to-particle conversion occurs by condensation of water vapor and sulfuric acid on the surface of pre-existing aerosol particles. This occurs throughout the stratosphere with a time constant ranging from hours to weeks. The distribution of aerosol particle sizes at a given location, however, depends strongly on proximity to an area in which new particles are forming. The stratospheric lifetime of aerosol particles is long (greater than one year) when small particles predominate and short (less than one year) when large particles predominate.

### (iii) Coagulation

The change of aerosol particles due to coagulation can be described by the following equation:

$$\begin{aligned} \frac{\partial n_k}{\partial t} = & -n_k \sum_{m \neq k} K_{km} n_m - \frac{1}{2} K_{kk} n_k^2 + \frac{1}{2} K_{k-1, k-1} n_{k-1}^2 \\ & + n_k \sum_{m < k} \left(1 - \frac{V_m}{V_k}\right) K_{km} n_m + \sum_{m < k-1} \frac{V_m}{V_{k-1}} K_{k-1, m} n_{k-1} n_m \end{aligned}$$

where  $K_{km}$  is the coagulation kernel between particles with size indices  $k$  and  $m$ . The first two terms on the right say that the number of particles in bin  $k$  is decreased by collisions between particles in bin  $k$  and particles in bin  $m$ , and the last three terms gives the increment added to bin  $k$  due to collisions between bins  $k-1$  and  $k-1$ , bin  $k$  and bins less than  $k$ , and bins  $k-1$  and bins less than  $k-1$ . Because bin  $k$  has twice the volume of bin  $k-1$ , collisions between bin  $k$  and bin  $m$ , where  $m$  is less than  $k$ , result in particles of volume intermediate between bins  $k$  and  $k+1$ . The volume ratio  $V_m/V_k$  is the fraction added to

the larger bin by this collision. The calculation of  $K_{km}$  is described in Yue and Deepak (1979).

### (c) Transport

Gas phase species and aerosol particles are transported with the same mean circulation. Each aerosol size bin is transported separately. In addition, aerosol particles experience sedimentation. The falling speed of sulfate particles due to gravity is a function of particle density, radius, and altitude (Kasten, 1968). When ambient concentrations of water vapor or temperature change or when the particles are transported to a new environment, the particles will grow or evaporate until their partial water vapor pressure is in equilibrium with the ambient water vapor pressure. A detailed discussion of this microphysical process is given by Yue and Deepak (1981). Adjustment of  $H_2O$  concentration in aerosol particles is assumed to happen instantaneously and not to affect ambient  $H_2O$  vapor concentrations since they are so much greater than the liquid water content of aerosols.

Aerosols are transported out of the stratosphere by large-scale atmospheric motions and by sedimentation. In the troposphere, the processes of washout and deposition, combined with large diffusion, act to remove aerosols from the atmosphere. Aerosols tend to grow in the lowest 10 km of the troposphere because of the high concentrations of  $SO_2$  and  $H_2O$  in this region. Our model treats aerosol microphysics in the troposphere identically to the stratosphere except that nucleation is not allowed in the troposphere. Tropospheric aerosol processes are actually more complex than stratospheric processes because of additional dissolved chemicals, cloud processes, and local sources and sinks. Note that calculated tropospheric aerosols contain greater than 50% water by weight and thus are not properly sulfate aerosols.

## 3. The sulfate budget

Calculated profiles of species mixing ratio at the equator and 45°N are shown in figure 1 for CS<sub>2</sub>, DMS, H<sub>2</sub>S, OCS, MSA, SO<sub>2</sub>, SO<sub>3</sub> and H<sub>2</sub>SO<sub>4</sub> for annual average conditions without volcanic influence. CS<sub>2</sub>, DMS, and H<sub>2</sub>S react rapidly with OH in the troposphere and contribute little directly to the stratospheric sulfate burden. MSA is one of the products of DMS oxidation. Its only atmospheric loss is by heterogeneous removal in the troposphere, and thus its mixing ratio is relatively constant with altitude in the stratosphere. OCS has both surface fluxes and in situ production from CS<sub>2</sub>. It is the main source gas for sulfur in the stratosphere. It is lost both through photodissociation and reaction with O and OH, leading to SO<sub>2</sub> formation. The calculated profile of OCS compares favorably with atmospheric measurements of this gas.

Significant anthropogenic emissions of SO<sub>2</sub> produce the large surface concentration of this gas in the troposphere, especially in the northern hemisphere. There is a maximum in SO<sub>2</sub> mixing ratio at 28 km at 45°N and at 32 km at the equator due to OCS dissociation. Above this altitude, SO<sub>2</sub> decreases, but then rises again due to SO<sub>2</sub> production from H<sub>2</sub>SO<sub>4</sub> photolysis. Measurements from the ATMOS instrument flown on the ATLAS-1 space shuttle mission (Rinsland et al., 1995) indicate a similar increase in SO<sub>2</sub> mixing ratio with altitude above 35 km, but show no systematic variations with latitude. H<sub>2</sub>SO<sub>4</sub> mixing ratio profiles are shown for both the gaseous form and the aerosol form. Most sulfate is in the aerosol form below 36 km and in the gas form above.

The dashed lines in figure 1 indicate calculated concentrations of SO<sub>2</sub> and aerosol sulfate in a modeled atmosphere with OCS as the only sulfate source gas; i.e., surface fluxes of CS<sub>2</sub>, H<sub>2</sub>S, DMS, and SO<sub>2</sub> have been set to zero. SO<sub>2</sub> concentrations above 16 km are the same with or without the surface fluxes, though aerosol concentrations differ at altitudes up to 18 km at 45°N and up to 26 km at the equator. Clearly the large calculated aerosol concentrations below 15 km are due to surface emissions of sulfate-bearing gases other than OCS. These results can be viewed as a lower limit for calculated aerosols

in the troposphere and lower stratosphere due to model uncertainties in oxidation rates, OH concentration, tropospheric dynamics, and tropospheric aerosol formation. A schematic diagram of the model-calculated atmospheric sulfur budget is shown in figure 2. The boxes show the tropospheric and stratospheric burden of each gas in kilotons of sulfur and the arrows indicate either fluxes from the surface, fluxes across the tropopause, or chemical transformation rates in kilotons of sulfur per year. Boxes are omitted where the burden is less than 0.1 kiloton of sulfur. Surface emissions of sulfur occur in the forms of  $\text{SO}_2$ , DMS,  $\text{H}_2\text{S}$ , and  $\text{CS}_2$ . Each of these species has a lifetime of less than one week in the troposphere. DMS and  $\text{CS}_2$  do not significantly impact the sulfur burden of the stratosphere. Of the  $\text{SO}_2$  emitted into the troposphere and produced locally, 94% is removed by washout. The tropospheric reservoir of OCS is large because the surface concentration is held at 500 pptv. However, the flux required to maintain it is modest because of the 5 year lifetime of this gas, as compared to the 7 day lifetime of its precursor  $\text{CS}_2$ . Budget analysis of the model results shows that conversion of  $\text{CS}_2$  to OCS more than supports the observed 500 pptv surface mixing ratio, and requires a downward surface flux of OCS.

Almost all stratospheric  $\text{SO}_2$  comes from OCS, though photolysis of  $\text{H}_2\text{S}$  also accounts for 1 kiloton per year of  $\text{SO}_2$  production in the stratosphere.  $\text{SO}_2$  produces  $\text{SO}_3$  through reactions (1) and (2). The lifetime of  $\text{HSO}_3$  is so short that its atmospheric burden is negligible. The stratospheric production rate of  $\text{H}_2\text{SO}_4$  from reaction (3) is 63 kilotons per year, though 15 kilotons per year are removed by photodissociation in the upper stratosphere (reaction 4), yielding a net  $\text{H}_2\text{SO}_4$  production rate of 48 kilotons per year. Of the 53 kilotons per year of  $\text{H}_2\text{SO}_4$  converted from gas phase to aerosol in the stratosphere, condensation onto the surface of existing particles accounts for 99% and homogeneous nucleation accounts for 1%. Evaporation of aerosols in the upper stratosphere converts 5 kilotons/year of aerosol back to gas phase  $\text{H}_2\text{SO}_4$ . The calculated stratospheric burden of  $\text{H}_2\text{SO}_4$  in both the gas and aerosol phases is 86 kilotons of sulfur.



Our model-calculated burden of  $\text{H}_2\text{SO}_4$ , combined with the production rate of 63 kilotons (S)/yr, yields a lifetime for stratospheric  $\text{H}_2\text{SO}_4$  of 1.4 years. The stratospheric lifetime of total sulfur ( $\text{SO}_2$ ,  $\text{SO}_3$ , and  $\text{H}_2\text{SO}_4$ ) is 2.0 years, the same as the estimated 2 year turnover time for stratospheric air (Rosenlof and Holton, 1993). With surface emissions of  $\text{CS}_2$ , DMS,  $\text{H}_2\text{S}$ , and  $\text{SO}_2$  omitted from the model, the calculated  $\text{H}_2\text{SO}_4$  stratospheric burden is 73 kilotons of sulfur.

The stratospheric aerosol mass (both water and sulfate) calculated from 2 km above the tropopause is 283 kilotons in our model. The global aerosol mass in the stratosphere from 2 km above the tropopause was estimated to be 570 kilotons (+/- 25%) in 1979, a year considered to represent background aerosol values (Kent and McCormick, 1984). Our calculated aerosol mass is 50% lower than observations. One possible reason for this discrepancy could be the lack of heterogeneous nucleation in our model. Heterogeneous nucleation on Aitken particles is thought to be significant for background aerosol conditions (Hamill et al., 1977). Though this process would not increase the sulfate content of the stratosphere, it would result in inclusions inside the sulfate particles which would increase their diameter. Because aerosol mass is estimated from the optical properties of the particles, it could be larger than the actual mass of sulfate and water. The sulfate content in our model could be increased by including additional sulfur species which penetrate the stratosphere. Model transport parameters could also influence our calculation of stratospheric aerosol mass. We estimate this effect to be no more than 20%.

Figure 3(a) shows the calculated aerosol surface area for background conditions and figure 3(b) shows the aerosol surface area recommended by WMO (1993) for evaluating the impact of heterogeneous chemistry on ozone under non-volcanic conditions. The calculated surface area is comparable to the WMO (1993) surface area, though smaller by 30% in the tropical lower stratosphere and the southern polar region and larger by 30-40% in the northern polar region. The calculated annual average surface area is

greatest at northern high latitudes, while the WMO surface area is larger in the southern high latitudes. This is true even for the calculation without surface fluxes of  $\text{SO}_2$ . Our calculated background surface area is also comparable to, but somewhat lower than, the April 1991 surface areas deduced from SAGE II by Yue et al. (1994). Figure 3(c) shows a climatology of aerosol surface area averaged for the ~9 years of SAGE and SAM II data (Hitchman et al., 1994). The 9 year climatology is expected to be much greater than background conditions since several volcanic eruptions influenced the stratosphere during the time period.

A more accurately measured quantity than total aerosol surface area is the distribution of aerosol particles with radii greater than 0.15 micron. This quantity is shown in figure 4(a) for a model simulation of June conditions and in figure 4(b) for June 1973 observations from Rosen et al. (1975). The maximum number of particles per milligram of air is 11 for both the model and observations, however, the model maximum occurs at 30 km and the observational maximum at 25 km in the tropics. The model results show the same general pattern in the stratosphere as the measurements but vertical gradients are not nearly as sharp as observations. Values of 2 particles per milligram of air are found near the tropopause, and the model reproduced this.

Aerosol optical depths have been calculated using the scattering code of Hansen and Travis (1974; code updated through April 1995). Figure 5(a) shows the calculated aerosol extinction at  $1.02 \mu\text{m}$  for April, while figure 5(b) show SAGE observations of the same quantity for April 1979 (McCormick, 1981). Model values of optical depth are lower than observations by factors of 3-4 in the lower stratosphere. This indicates fewer particles of a size that scatters  $1.02 \mu\text{m}$  light, namely, particles of about  $1 \mu\text{m}$  radius. Since the calculated surface area is much closer to observations, we conclude that our model has more small particles which compensate for the lack of large particles in the surface area. Heterogeneous nucleation, if included in our model, would have the effect of increasing the mean particle radius. The model-calculated aerosol optical depth at  $1.02$

microns from 2 km above the tropopause is  $2.7 \times 10^{-4}$ , as compared with observations for 1979 background aerosol loading of  $1.25 \times 10^{-3}$  (Kent and McCormick, 1984).

The number density of aerosol particles as a function of particle radius is shown in Figure 6 for the equator and for 57°N for several altitudes. The lower altitude at both the equator and 57°N is dominated by small particles of radius 0.01 micron, though even smaller particles are found at the equator in December, when significant nucleation occurs in the tropics. At lower altitudes, closer to the tropopause, ever smaller particles predominate. The size distribution peaks with larger particles at higher altitudes (0.03-0.04 microns at 25-30 km), up to the altitude at which aerosols begin to evaporate (35-40 km), and then the mean particle size decreases. Because nucleation occurs only within a few kilometers of the tropopause, there is an abundance of new and very small particles near the tropopause. In the process of being transported from the lower to the middle stratosphere, aerosol particles grow by condensation of  $\text{H}_2\text{SO}_4$  and  $\text{H}_2\text{O}$  vapor and by coagulation of small particles into larger particles. The stratospheric aerosol mass per cubic centimeter at the equator is greatest at 29 km and at 57°N the aerosol mass per cubic centimeter is greatest at 15 km.

#### 4. Pinatubo Simulation

We have performed a numerical experiment to simulate the effect of the eruption of Mt. Pinatubo in June of 1991. We initialized our model for June 15, 1991 with a volcanic injection of 17 Megatons of  $\text{SO}_2$  spread between 5°S and 14°N and between 16 and 26 km altitude (Bluth et al., 1992; Read et al., 1993). The model-calculated e-folding rate for  $\text{SO}_2$  removal from the stratosphere is 35 days when calculated over the first 2 months following the eruption. The MLS-measured e-folding rate for the 21-31 km layer is 33 days (Read et al., 1993) and from TOMS data is 35 days (Bluth et al., 1992). Bekki and Pyle (1994) calculated 40 days from their aerosol model. Note that the OH concentration is fixed in our model and does not decrease due to reaction with  $\text{SO}_2$ , even under

volcanic conditions. Bekki (1995) found minimal changes in  $\text{SO}_2$  lifetime due to changes in OH following the Pinatubo volcano, but found a substantial effect for a volcanic sulfur loading of 200 Megatons.

The calculated aerosol mass in the stratosphere from 2 km above the tropopause peaks at 28.6 Megatons five months after the eruption. The estimated maximum of stratospheric aerosol loading following Pinatubo was about 30 Megatons (McCormick et al., 1995) and the peak was observed about 6 months after the eruption. Figure 7 shows calculated stratospheric aerosol mass as a function of time for the two years following the Mt. Pinatubo volcanic eruption. SAGE II data for the same period are also shown. The method of converting SAGE II measured multiwavelength aerosol extinction to aerosol mass concentration is described in a paper by Yue et al. (1986). The calculation and the SAGE data both show a peak aerosol loading of about 30 Megatons in early December of 1991 and subsequent falloff at about the same rate. The calculated e-folding time for aerosol decay in the whole stratosphere was 13 months in our model, in general agreement with data from several volcanic events (McCormick et al., 1978; Yue et al., 1991). However, growth of aerosol loading in the early months following the eruption is much sharper in the calculation than in the SAGE data. This is due to inability of the SAGE instrument to penetrate thick clouds of high optical depth, resulting in truncation of the retrieved profile at the "aerosol cloud top". The aerosol cloud top was at 22 km in the tropics during June, July, and August 1991 (McCormick and Veiga, 1992), so quantitative measurements could not be made below this altitude due to instrument saturation. HIRS measurements of global aerosol mass loadings (Baran and Foot, 1994) show rapid growth with time following the eruption, similar to the model calculation.

When we omit homogeneous nucleation from the calculation, we find that the peak stratospheric aerosol mass loading is only 26 megatons and occurs three months after the eruption. The e-folding time for stratospheric aerosol decay was 10 months in this case. This result (also shown in figure 7) is very similar to the results of Bekki and

Pyle (1994), whose model contained no homogeneous nucleation. Without nucleation, the model response to addition of sulfate is a growth in the size of existing particles, leading to faster sedimentation and significant aerosol removal within the first few months following the eruption. Homogeneous nucleation is the dominant gas-to-particle conversion mechanism in our model for the first month following the Pinatubo eruption. In subsequent months, growth of existing particles is the dominant gas-to-particle conversion mechanism. Four months after the eruption, the rate of aerosol loss from the stratosphere due to sedimentation becomes equal to the rate of aerosol growth, and the stratospheric mass loading begins to fall. Thus the effect of homogeneous nucleation in a model simulation of  $\text{SO}_2$  perturbation is to increase the residence time and the peak burden of stratospheric aerosols, yielding a larger perturbation.

## 5. Summary and Conclusion

We have constructed a 2-D model of sulfate chemistry and aerosol microphysics and have presented results for the calculated background atmosphere and for the immediate aftermath of the Mt. Pinatubo eruption. The model presents a reasonable simulation of the aerosol surface area for background conditions. However, the calculated stratospheric aerosol burden is 50% lower than estimates for background conditions. The reasons for this are not clear but may be related to the lack of heterogeneous nucleation in our model. Inclusion of heterogeneous nucleation should also increase the mean particle size in the model and result in closer agreement with optical depth measurements. We intend to pursue this in a future paper.

Our simulation of  $\text{SO}_2$  and aerosol mass following the Pinatubo eruption gives good agreement with observations of stratospheric decay times. Both the magnitude and temporal behavior of the stratospheric aerosol loading agree quite well with SAGE data. In contrast, a model without homogeneous nucleation generates an aerosol loading which

peaks too early and begins to decay after only three months. The inclusion of homogeneous nucleation in a model is important to the temporal behavior of the aerosol size distribution following perturbations in  $\text{SO}_2$  loading and, because of the strong size dependence of sedimentation, the global aerosol burden. Tie et al. (1994a and 1994b) studied aerosol evolution following the El Chichon and Mt. Pinatubo volcanoes using a two-dimensional coupled dynamical/chemical/microphysical model without homogeneous nucleation and concluded that injection of  $\text{SO}_2$  alone could not explain the observed aerosol loading. When they assumed that 10-20% of the injected sulfur was emitted by the volcano as aerosol particles, they obtained results consistent with observations. This again indicates the importance of new particle formation following volcanic eruptions.

There are many uncertainties in the present model, including uncertainties in the application of the microphysical theories employed here to stratospheric conditions, uncertainties in the gas phase chemistry and surface emission rates, and uncertainties in model dynamics. Continued observation of aerosols in the stratosphere during both volcanic and background conditions, along with further laboratory work, may help resolve some of the issues discussed here.

#### Acknowledgment

We thank Chuck Kolb, Doug Worsnop, and John Jayne for helpful discussions on the chemistry of  $\text{SO}_3$  and for supplying us with relevant rate data. Work at AER was supported by NASA Atmospheric Effects of Aviation Program (AEAP) NAS1-19422 and NASA Atmospheric Chemistry Modeling and Analysis Program (ACMAP) NASW-4775.

## References:

- Baran, A.J. and J.S. Foot, New application of the operational sounder HIRS in determining a climatology of sulphuric acid aerosol from the Pinatubo eruption, *J. Geophys. Res.*, **99**, 25673-25679, 1994.
- Bates, T.S., B.K. Lamb, A. Guenther, J. Dignon, and R.E. Stoiber, Sulfur emissions to the atmosphere from natural sources, *J. Atmos. Chem.*, **14**, 315-337, 1992.
- Bekki, S. and J.A. Pyle, A two-dimensional modeling study of the volcanic eruption of Mount Pinatubo, *J. Geophys. Res.*, **99**, 18861-18869, 1994.
- Bekki, S., Oxidation of volcanic SO<sub>2</sub>: a sink for stratospheric OH and H<sub>2</sub>O, *Geophys. Res. Lett.*, **22**, 913-916, 1995.
- Benkovitz, C.M., C.M. Berkowitz, R.C. Easter, S. Nemesure, R. Wagener, and S.E. Schwartz, Sulfate over the North Atlantic and adjacent continental regions: Evaluation for October and November 1986 using a three-dimensional model driven by observation-derived meteorology, *J. Geophys. Res.*, **99**, 20725-20756, 1994.
- Bluth, G.J.S., S.D. Doiron, C.C. Schnetzler, A.J. Krueger, and L.S. Walter, Global tracking of the SO<sub>2</sub> clouds from the June, 1991 Mount Pinatubo eruptions, *Geophys. Res. Lett.*, **19**, 151-154, 1992.
- Carroll, M.A., Measurements of OCS and CS<sub>2</sub> in the free troposphere, *J. Geophys. Res.*, **90**, 10483-10486, 1985.
- Chatfield, R.B. and P.J. Crutzen, Are there interactions of iodine and sulfur species in marine air photochemistry?, *J. Geophys. Res.*, **95**, 22,319-22,341, 1990.
- DeMore, W.B., S.P. Sander, D.M. Golden, R.F. Hampson, M.J. Kurylo, C.J. Howard, A.R. Ravishankara, C.E. Kolb, and M.J. Molina, *Chemical Kinetics and Photochemical Data for Use in Stratospheric Modeling*, Evaluation Number 11, JPL Publication 94-26, Jet Propulsion Laboratory, Pasadena, CA, 1994.
- Fajans, E. and C.F. Goodeve, The absorption spectrum of sulphur trioxide, *Trans. Faraday Soc.*, **32**, 511-514, 1936.
- Hamill, P., O.B. Toon, and C.S. Kiang, Microphysical processes affecting stratospheric aerosol particles, *J. Atmos. Sci.*, **34**, 1104-1119, 1977.
- Hamill, P. and G. K. Yue, A simplified model for the production of sulfate aerosols, in *Environmental and Climatic Impact of Coal Utilization*, pp. 255-274, J. J. Singh and A. Deepak, Eds., Academic Press, New York, 1979.
- Hansen, J.E. and L.D. Travis, Light scattering in planetary atmospheres, *Space Science Reviews*, **16**, 527-610, 1974.
- Hitchman, M.H., M. McKay, and C.R. Trepte, A climatology of stratospheric aerosol, *J. Geophys. Res.*, **99**, 20,689-20,700, 1994.

Hofmann, D.J., Increase in the stratospheric background sulfuric acid aerosol mass in the past 10 years, *Science*, **248**, 996-1000, 1990.

Hofmann, D.J. and S. Solomon, Ozone destruction through heterogeneous chemistry following the eruption of El Chichon, *J. Geophys. Res.*, **94**, 5029-5041, 1989.

Inn, E.C.Y., J.F. Vedder, B.J. Tyson, and D. O'Hara, COS in the stratosphere, *Geophys. Res. Lett.*, **6**, 191-193, 1979.

Jayne, J.T., D.R. Worsnop, C.E. Kolb, R.F. Meads, M.J. Molina, A.A. Viggiano, Stratospheric sulfur oxidation kinetics, presented at NASA AEAP Meeting, Virginia Beach, VA, 1995.

Kasten, F., Falling speed of aerosol particles, *J. App. Meteorology*, **7**, 944-947, 1968.

Kent, G.S. and M.P. McCormick, SAGE and SAM II measurements of global stratospheric aerosol optical depth and mass loading, *J. Geophys. Res.*, **89**, 5303-5314, 1984.

Kolb, C.E., J.T. Jayne, and D.R. Worsnop, Gas phase reaction of sulfur trioxide with water vapor, *J. of the Am. Chem. Soc.*, **116**, 10314-10315, 1994.

Kotamarthi, V.R., M.K.W. Ko, D.K. Weisenstein, J.M. Rodriguez, and N.D. Sze, Effect of lightning on the concentration of odd nitrogen species in the lower stratosphere: An update, *J. Geophys. Res.*, **99**, 8167-8173, 1994.

McCormick, M.P., Stratospheric aerosols, NASA Tech Memo., TM-83217, 1981.

McCormick, M.P., T.J. Swissler, W.P. Chu, and W.H. Fuller, Jr., Post-volcanic stratospheric aerosol decay as measured by lidar, *J. Atmos. Sci.*, **35**, 1296-1303, 1978.

McCormick, M.P. and R.E. Veiga, SAGE II measurements of early Pinatubo aerosols, *Geophys. Res. Lett.*, **19**, 155-158, 1992.

McCormick, M.P., L.W. Thomason, and C.R. Trepte, Atmospheric effects of the Mt. Pinatubo eruption, *Nature*, **373**, 399-404, 1995.

Michaelangeli, D., M. Allen, and Y.L. Yung, El Chichon volcanic aerosols: Impact of radiative, thermal and chemical perturbations, *J. Geophys. Res.*, **94**, 18,429-18,443, 1989.

Perry, R.H. and C.H. Chilton (Eds.), *Chemical Engineers' Handbook*, McGraw-Hill, New York, 1973.

Plumb, R.A., A "tropical pipe" model of stratospheric transport, *J. Geophys. Res.*, in press, 1995.

Read, W.G., L. Froidevaux, and J.W. Waters, Microwave limb sounder measurements of stratospheric SO<sub>2</sub> from the Mt. Pinatubo volcano, *Geophys. Res. Lett.*, **20**, 1993.

Rinsland, C.P., M.R. Gunson, M.K. Ko, D.W. Weisenstein, R. Zander, M.C. Abrams, A. Goldman, N.D. Sze, and G.K. Yue, H<sub>2</sub>SO<sub>4</sub> photolysis: A source of sulfur dioxide in the upper stratosphere, *Geophys. Res. Letters*, **22**, 1109-1112, 1995.

Rosen, J.M., D.J. Hofmann, and J. Laby, Stratospheric aerosol measurements, II, the world-wide distribution, *J. Atmos. Sci.*, **32**, 1457-1462, 1975.



- Rosenlof, K.H. and J.R. Holton, Estimates of the stratospheric residual circulation using the downward control principle, *J. Geophys. Res.*, **98**, 10,465-10,479, 1993.
- Rodriguez, J.M., M.K.W. Ko, and N.D. Sze, Role of heterogeneous conversion of  $\text{N}_2\text{O}_5$  on sulphate aerosols in global ozone losses, *Nature*, **352**, 134-137, 1991.
- Shia, R.-L., M.K.W. Ko, M. Zou, and V.R. Kotamarthi, Cross-tropopause transport of excess  $^{14}\text{C}$  in a two-dimensional model, *J. Geophys. Res.*, **98**, 18,599-18,606, 1993.
- Spiro, P.A., D.J. Jacob, and J.A. Logan, Global inventory of sulfur emissions with  $1^\circ \times 1^\circ$  resolution, *J. Geophys. Res.*, **97**, 6023-6036, 1992.
- Sze, N.D. and M.K.W. Ko, Photochemistry of COS,  $\text{CH}_3\text{SCH}_3$  and  $\text{H}_2\text{S}$ : Implications for the atmospheric sulfur cycle, *Atmospheric Environment*, **14**, 1223-1239, 1980.
- Tabazedeh, A., R.P. Turco, and M.Z. Jacobson, A model for studying the composition and chemical effects of stratospheric aerosols, *J. Geophys. Res.*, **99**, 12897-12914, 1994.
- Tie, X.X., X. Lin, and G. Brasseur, Two-dimensional coupled dynamical/chemical/microphysical simulation of global distribution of El Chichon volcanic aerosols, *J. Geophys. Res.*, **99**, 16779-16792, 1994a.
- Tie, X.X., G. Brasseur, B. Briegleb, and C. Granier, Two-dimensional simulation of Pinatubo aerosol and its effect on stratospheric ozone, *J. Geophys. Res.*, **99**, 20545-20562, 1994b.
- Trepte, C.R. and M.H. Hitchman, Tropical stratospheric circulation deduced from satellite aerosol data, *Nature*, **355**, 626-628, 1992.
- Trepte, C.R., R.E. Veiga, and M.P. McCormick, The poleward dispersal of Mount Pinatubo volcanic aerosol, *J. Geophys. Res.*, **98**, 18,563-18,573, 1993.
- Washburn, E.W. (Ed.), *International Critical Tables*, vol. 3, p. 56, McGraw-Hill, New York, 1928.
- Weisenstein, D.K., M.K.W. Ko, J.M. Rodriguez, and N.D. Sze, Effects on stratospheric ozone from high-speed civil transport: Sensitivity to stratospheric aerosol loading, *J. Geophys. Res.*, **98**, 23133-23140, 1993.
- WMO, *Scientific Assessment of Ozone Depletion: 1991*, World Meteorological Organization, Global ozone research and monitoring project-Report No. 25, 1993.
- Yue, G. K. The formation and growth of sulfate aerosols in the stratosphere, *Atmospheric Environment*, **15**, 549-556, 1981.
- Yue, G. K. and A. Deepak, Modeling of Coagulation-Sedimentation Effects on Transmission of Visible IR Laser Beams in Aerosol Media, *Appl. Opt.*, **18**, pp. 3918-3925, 1979.
- Yue, G. K. and A. Deepak, Modeling of growth and evaporation effects on the extinction of 1.0 mm solar radiation traversing stratospheric sulfuric acid aerosols, *Applied Optics*, **20**, 3669-3675, 1981.

Yue, G. K. and A. Deepak, Temperature dependence of the formation of sulfate aerosols in the stratosphere, *J. Geophys. Res.*, **87**, 3128-3134, 1982.

Yue, G. K., M. P. McCormick, and W. P. Chu, Retrieval of composition and size distribution of stratospheric aerosols with the SAGE II satellite experiment, *J. Atmos. Oceanic Technol.*, **3**, 372-380, 1986.

Yue, G.K., M.P. McCormick, and E.W. Chiou, Stratospheric aerosol optical depth observed by the stratospheric aerosol and gas experiment II: Decay of the El Chichon and Ruiz volcanic perturbations, *J. Geophys. Res.*, **96**, 5209-5219, 1991.

Yue, G. K., L. R. Poole, P. -H. Wang, and E. W. Chiou, Stratospheric aerosol acidity, density, and refractive index deduced from SAGE II and NMC temperature data, *J. Geophys. Res.*, **99**, 3727-3738, 1994.

Table 1: Chemical reactions of sulfur species included in the model. The reaction products listed are the end oxidation products; short-lived intermediate radicals are omitted.

$\text{CS}_2 + h\nu \rightarrow \text{OCS} + \text{SO}_2$	
$\text{OCS} + h\nu \rightarrow \text{CO} + \text{SO}_2$	
$\text{H}_2\text{SO}_4 + h\nu \rightarrow \text{SO}_3 + \text{OH}$	
$\text{SO}_3 + h\nu \rightarrow \text{SO}_2 + \text{O}$	
$\text{CS}_2 + \text{O} \rightarrow 0.09\text{CO} + 0.91\text{OCS} + 1.09\text{SO}_2$	$3.2 \times 10^{-11} \exp\left(\frac{-650}{T}\right)$
$\text{CS}_2 + \text{OH} \rightarrow \text{OCS} + \text{SO}_2$	$1.25 \times 10^{-16} \alpha^{-1} \exp\left(\frac{4550}{T}\right)$ $\alpha = T + 1.81 \times 10^{-3} \exp\left(\frac{3400}{T}\right)$
$\text{DMS} + \text{O} \rightarrow \text{SO}_2 + \text{Products}$	$1.3 \times 10^{-11} \exp\left(\frac{410}{T}\right)$
$\text{DMS} + \text{OH} \rightarrow \text{SO}_2 + \text{Products}$	$1.2 \times 10^{-11} \exp\left(\frac{-260}{T}\right)$
$\text{DMS} + \text{OH} \rightarrow 0.25\text{MSA} + 0.75\text{SO}_2$	$3.04 \times 10^{-12} \exp\left(\frac{350}{T}\right) \frac{\beta}{1+\beta}$ $\beta = 5.531 \times 10^{-31} \exp\left(\frac{7460}{T}\right) [\text{O}_2]$
$\text{DMS} + \text{NO}_3 \rightarrow \text{SO}_2 + \text{Products}$	$1.9 \times 10^{-13} \exp\left(\frac{500}{T}\right)$
$\text{H}_2\text{S} + \text{O} \rightarrow \text{OH} + \text{SO}_2$	$9.2 \times 10^{-12} \exp\left(\frac{-1800}{T}\right)$
$\text{H}_2\text{S} + \text{OH} \rightarrow \text{H}_2\text{O} + \text{SO}_2$	$6.0 \times 10^{-12} \exp\left(\frac{-75}{T}\right)$
$\text{OCS} + \text{O} \rightarrow \text{CO} + \text{SO}_2$	$2.1 \times 10^{-11} \exp\left(\frac{-2200}{T}\right)$
$\text{OCS} + \text{OH} \rightarrow \text{CO}_2 + \text{SO}_2$	$1.1 \times 10^{-13} \exp\left(\frac{-1200}{T}\right)$
$\text{SO}_2 + \text{OH} \rightarrow \text{SO}_3$	$\frac{A}{1+B} * 0.6 \left[1 + (\log B)^2\right]$ $A = 3.0 \times 10^{-31} \left(\frac{300}{T}\right)^{3.3} M$ $B = A / 1.5 \times 10^{-12}$
$\text{SO}_2 + \text{O}_3 \rightarrow \text{SO}_3$	$3.0 \times 10^{-12} \exp\left(\frac{-7000}{T}\right)$
$\text{SO}_3 + \text{H}_2\text{O} + \text{H}_2\text{O} \rightarrow \text{H}_2\text{SO}_4$	$1.0 \times 10^{-42} \exp\left(\frac{8100}{T}\right)$

MSA heterogeneous removal (rainout and washout)  
 $\text{SO}_2$  heterogeneous removal (rainout and washout)  
 $\text{H}_2\text{SO}_4$  heterogeneous removal (rainout and washout)

Table 2: Model boundary conditions

Specie	Boundary Value	Boundary Condition
CS <sub>2</sub>	1.0 TgS/yr	Surface Emissions 52°S-52°N
DMS	40. TgS/yr	Surface Emissions 52°S-52°N
H <sub>2</sub> S	30. pptv	Surface Mixing Ratio
MSA	1.0 cm/sec	Deposition Velocity
OCS	500. pptv	Surface Mixing Ratio
SO <sub>2</sub>	77.5 TgS/yr	Surface Emissions
SO <sub>2</sub>	1.0 cm/sec	Deposition Velocity
H <sub>2</sub> SO <sub>4</sub>	1.0 cm/sec	Deposition Velocity

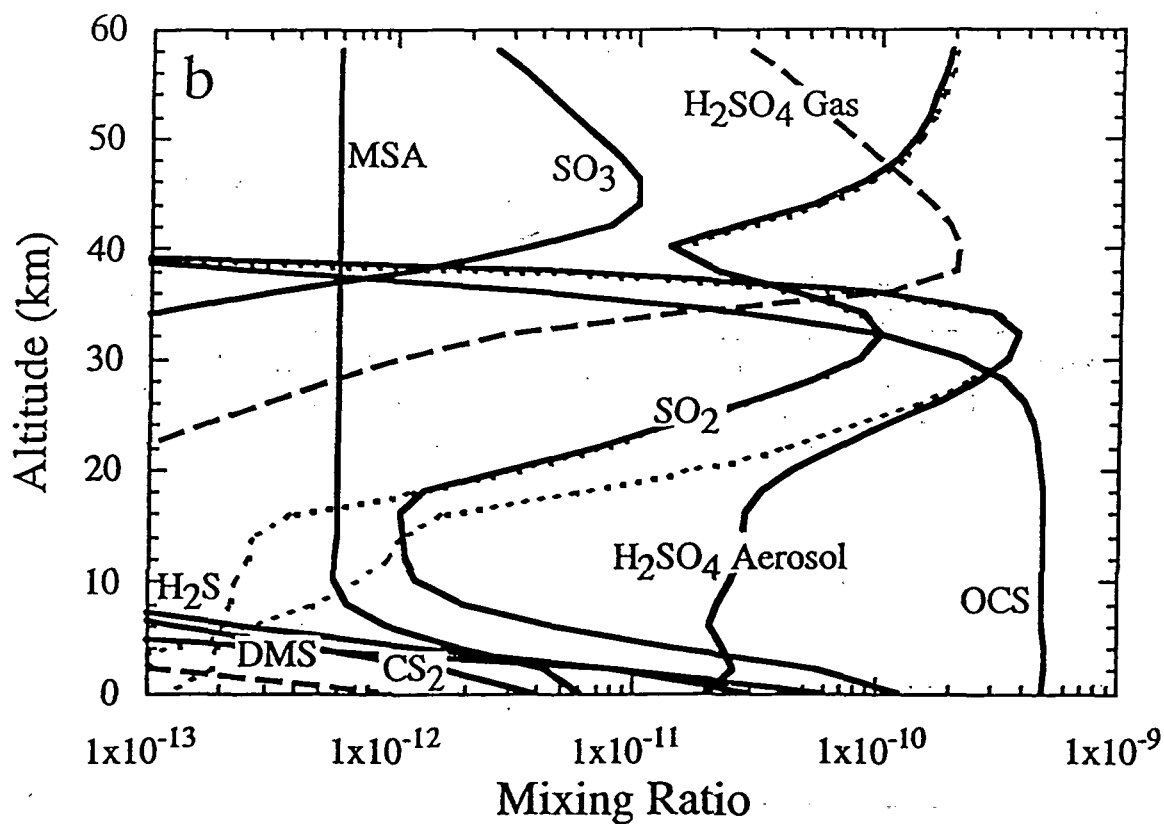
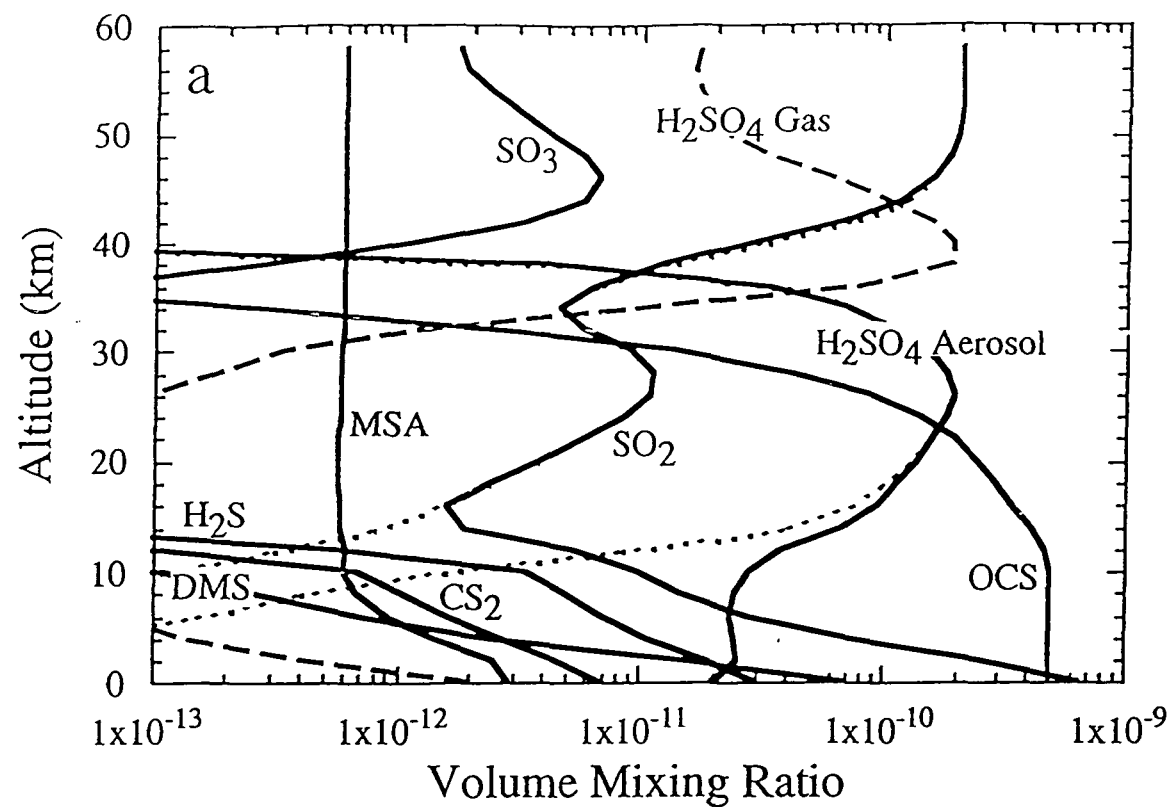


Figure 1: Vertical profiles of model-calculated sulfur species mixing ratios at (a) 45°N and (b) the equator for annual-average conditions. Dashed lines represent a model calculation with surface fluxes of  $\text{CS}_2$ , DMS,  $\text{H}_2\text{S}$ , and  $\text{SO}_2$  set to zero, i.e. OCS is the only source gas for sulfate species.

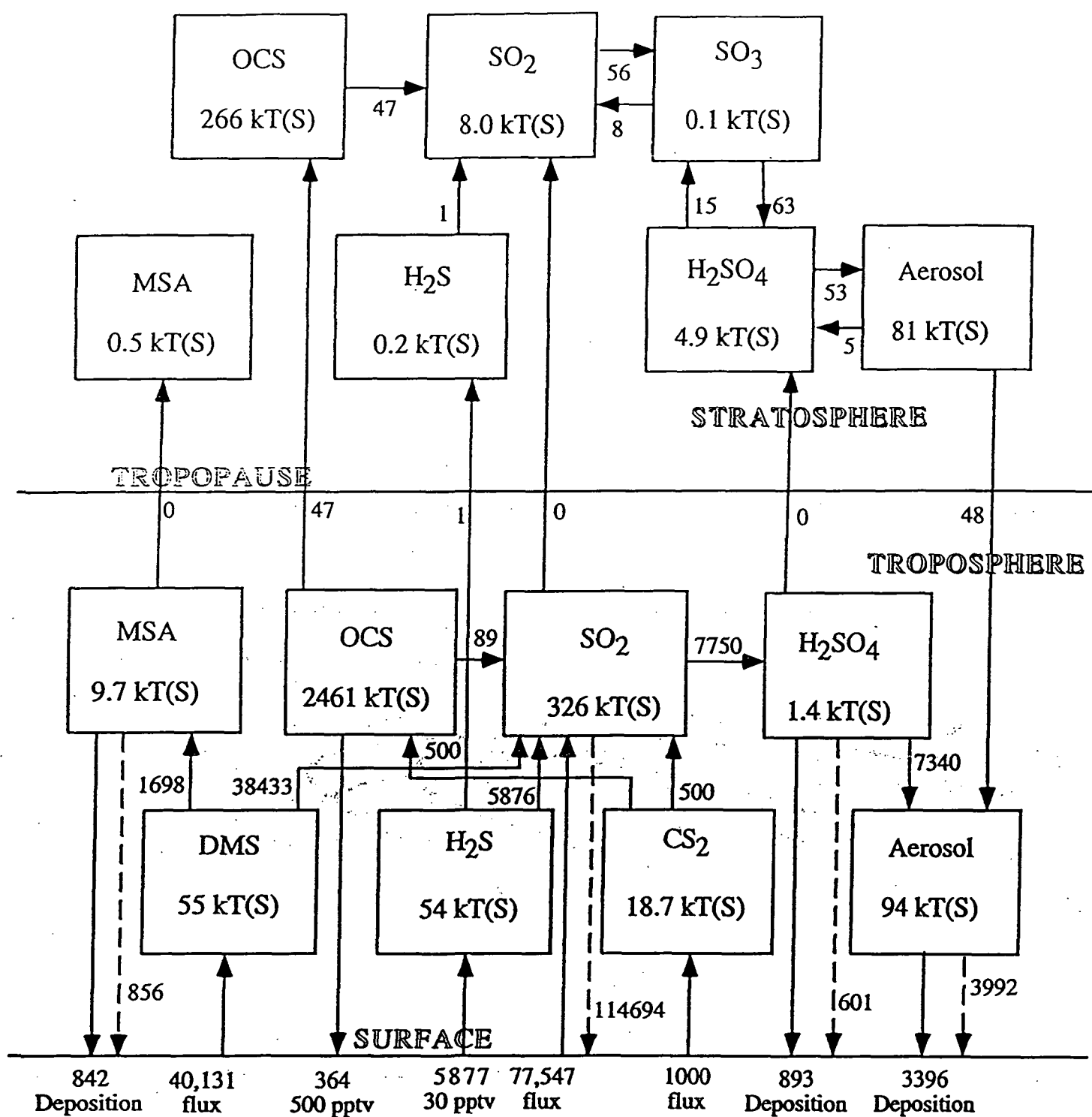


Figure 2: Schematic diagram of the model-calculated sulfate budget. Boxes show the quantity of sulfur, expressed as kilotons, in each reservoir in the troposphere and stratosphere. Arrows show net fluxes from the surface, across the tropopause, or chemical exchange rates expressed as kilotons of sulfur per year. Dashed lines with arrows represent washout.

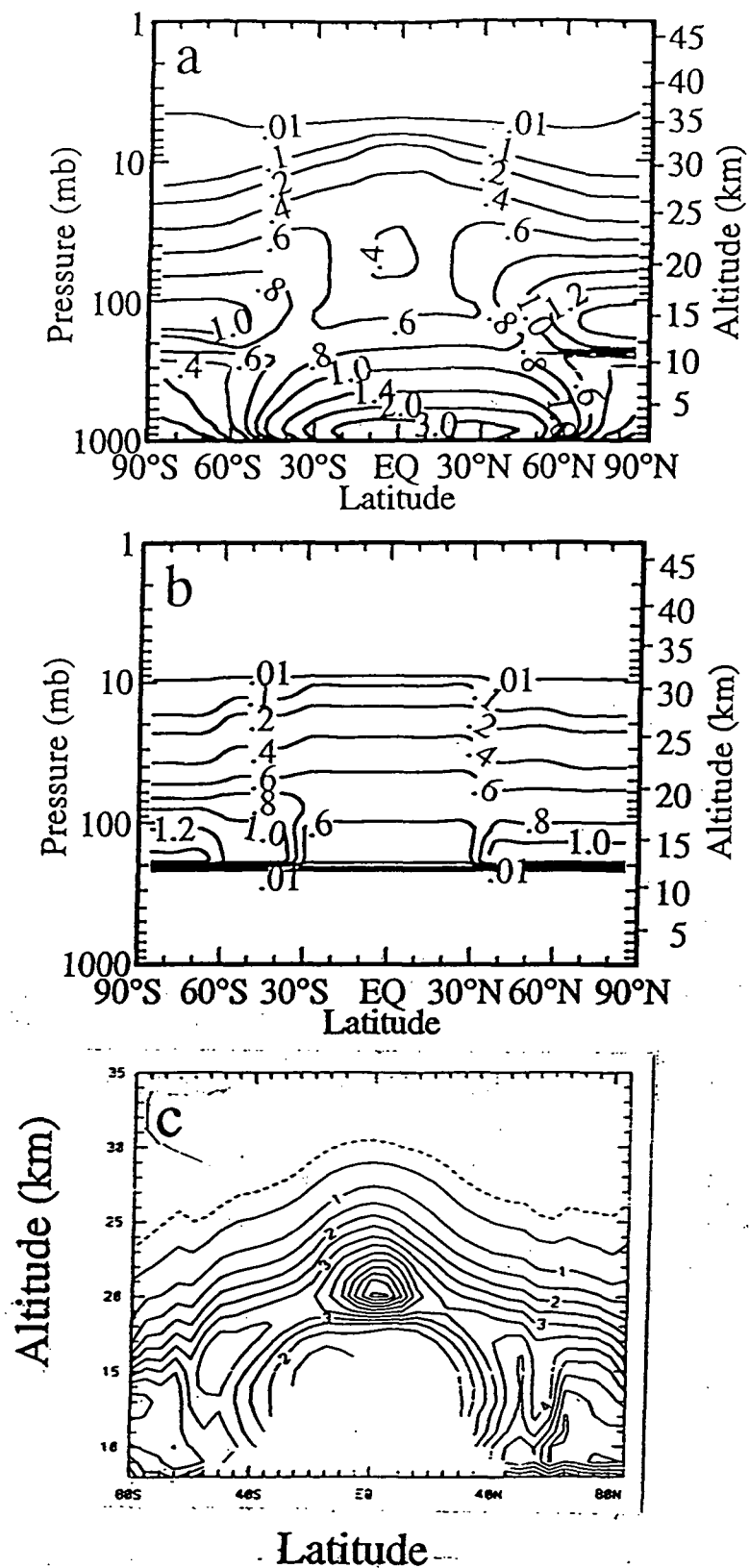


Figure 3: Latitude-altitude cross-section of aerosol surface area for annual average conditions in units of  $10^{-8} \text{ cm}^{-1}$ . The model calculation for background conditions is shown in (a) and that recommended by WMO (1993) for evaluating the impact of heterogeneous chemistry on ozone is shown in (b). Figure (c) represents climatological average conditions from 1979-1981 and 1984-1990 (Hitchman et al., 1994). Note different altitude range in (c).



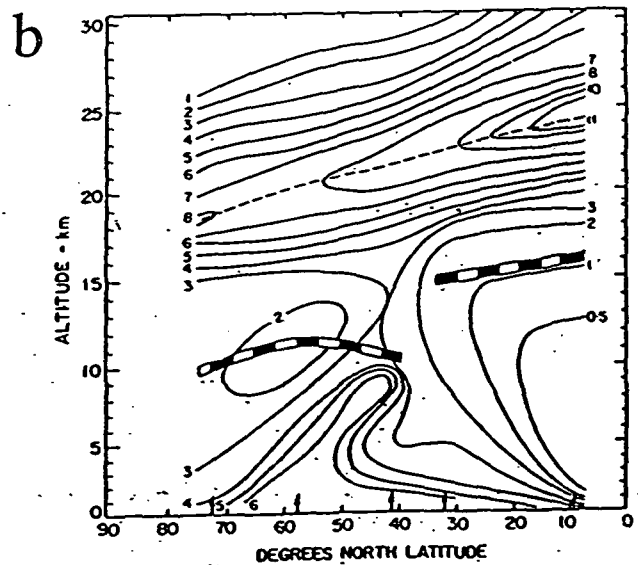
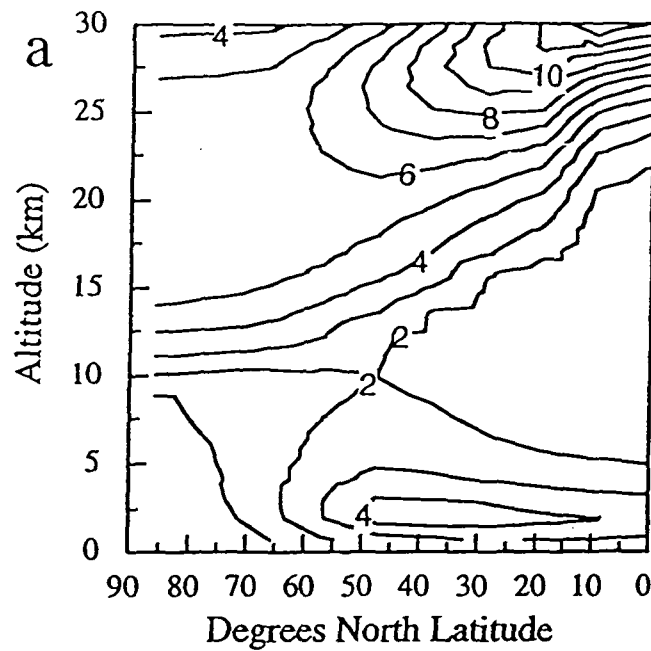


Figure 4: Distribution of aerosol particles with radii greater than 0.15 microns as a function of latitude and altitude in units of particles per milligram of air. Model results for June are shown in (a). Observations from 1973 (Rosen et al., 1975) are shown in (b).

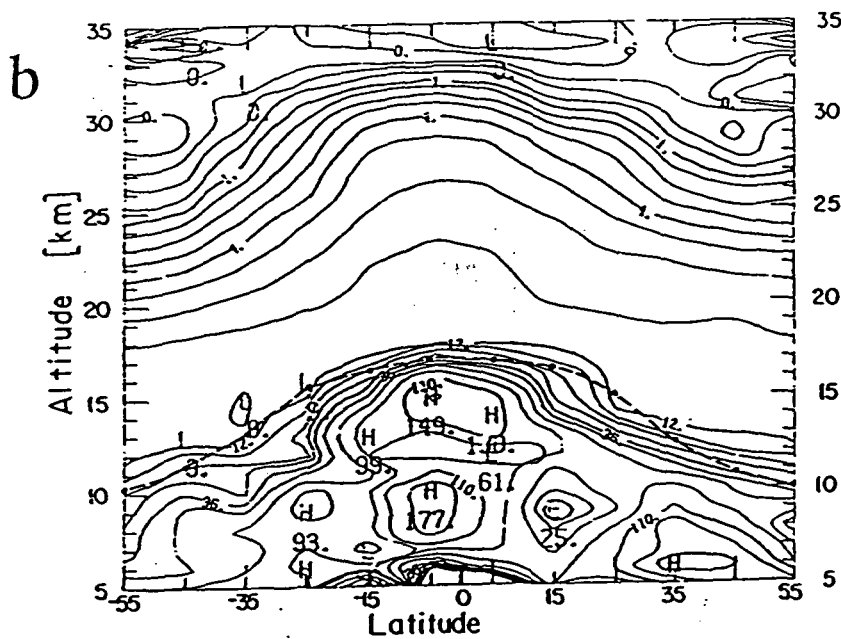
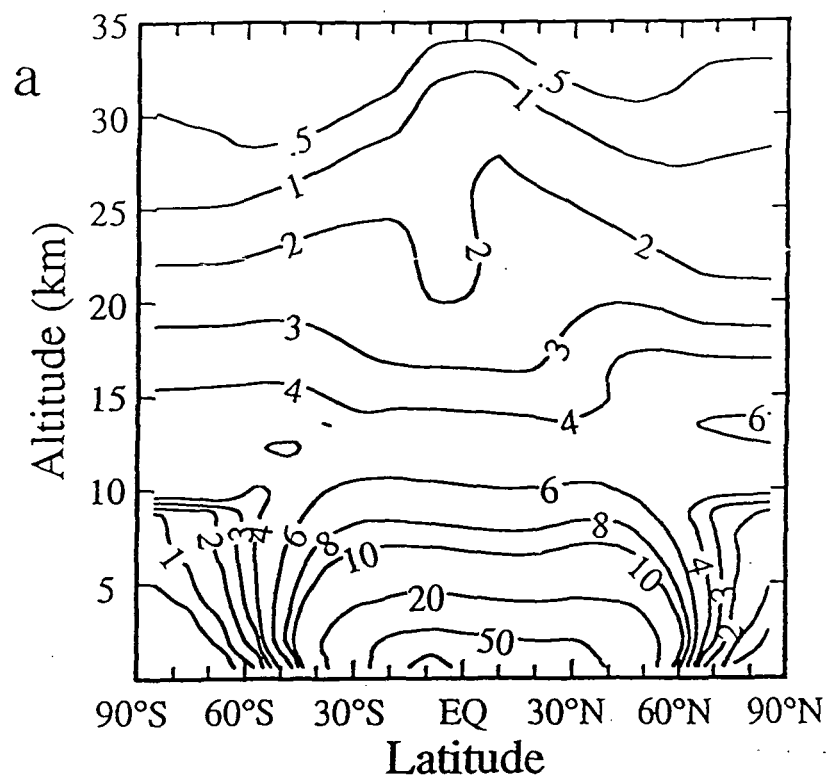


Figure 5: Aerosol extinction at  $1.02 \mu\text{m}$  in units of  $10^{-5} \text{ km}^{-1}$  for (a) model-calculated background atmosphere in April and (b) SAGE observations from April 1979 (from McCormick, 1981).

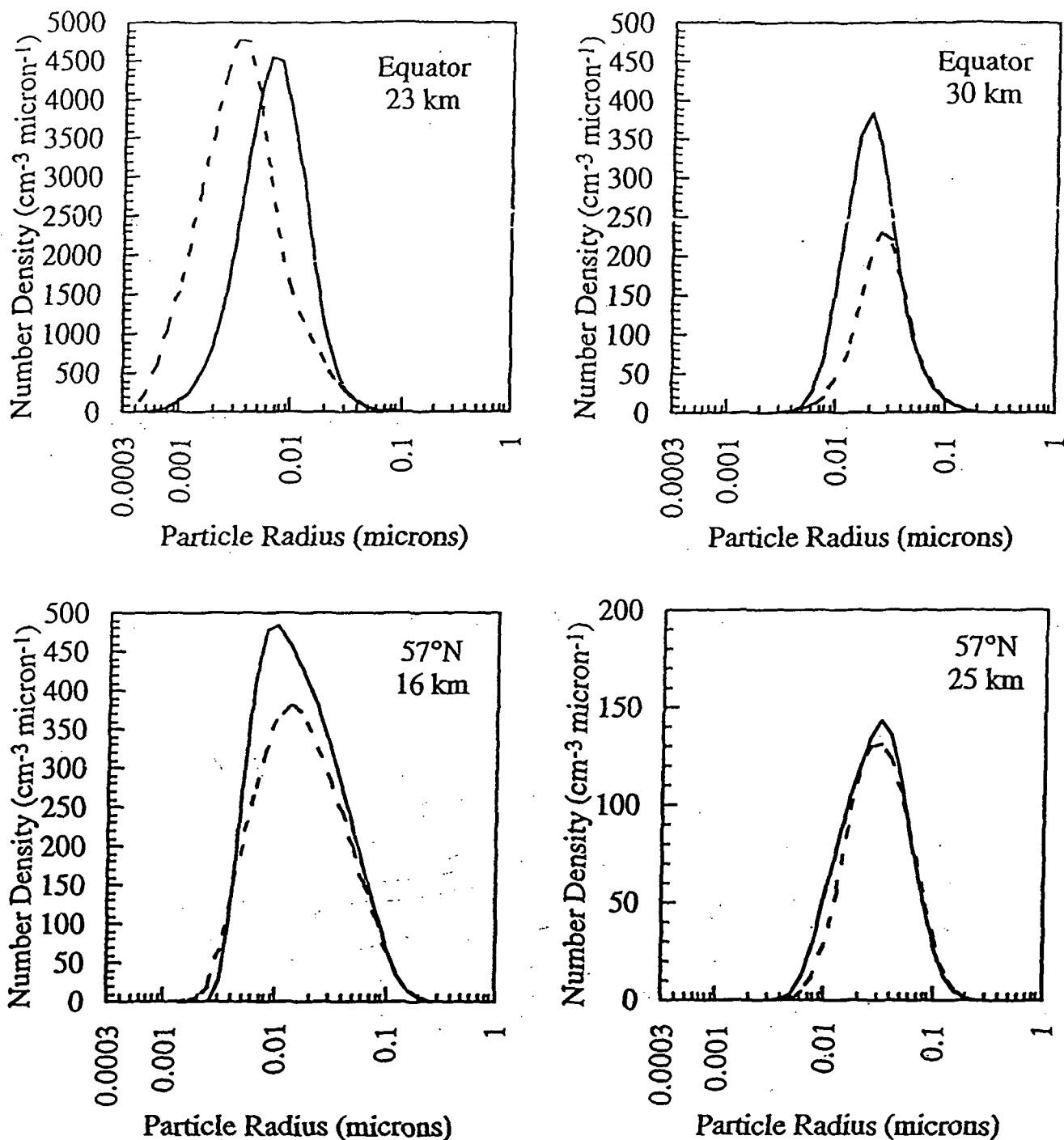


Figure 6: Distributions of aerosol number density as a function of aerosol radius in units of particles/cm<sup>3</sup>/micron at (a) Equator and 23 km, (b) Equator and 30 km, (c) 57°N at 16 km, and (d) 57°N and 25 km in June (solid line) and December (dashed line) for background aerosol conditions.

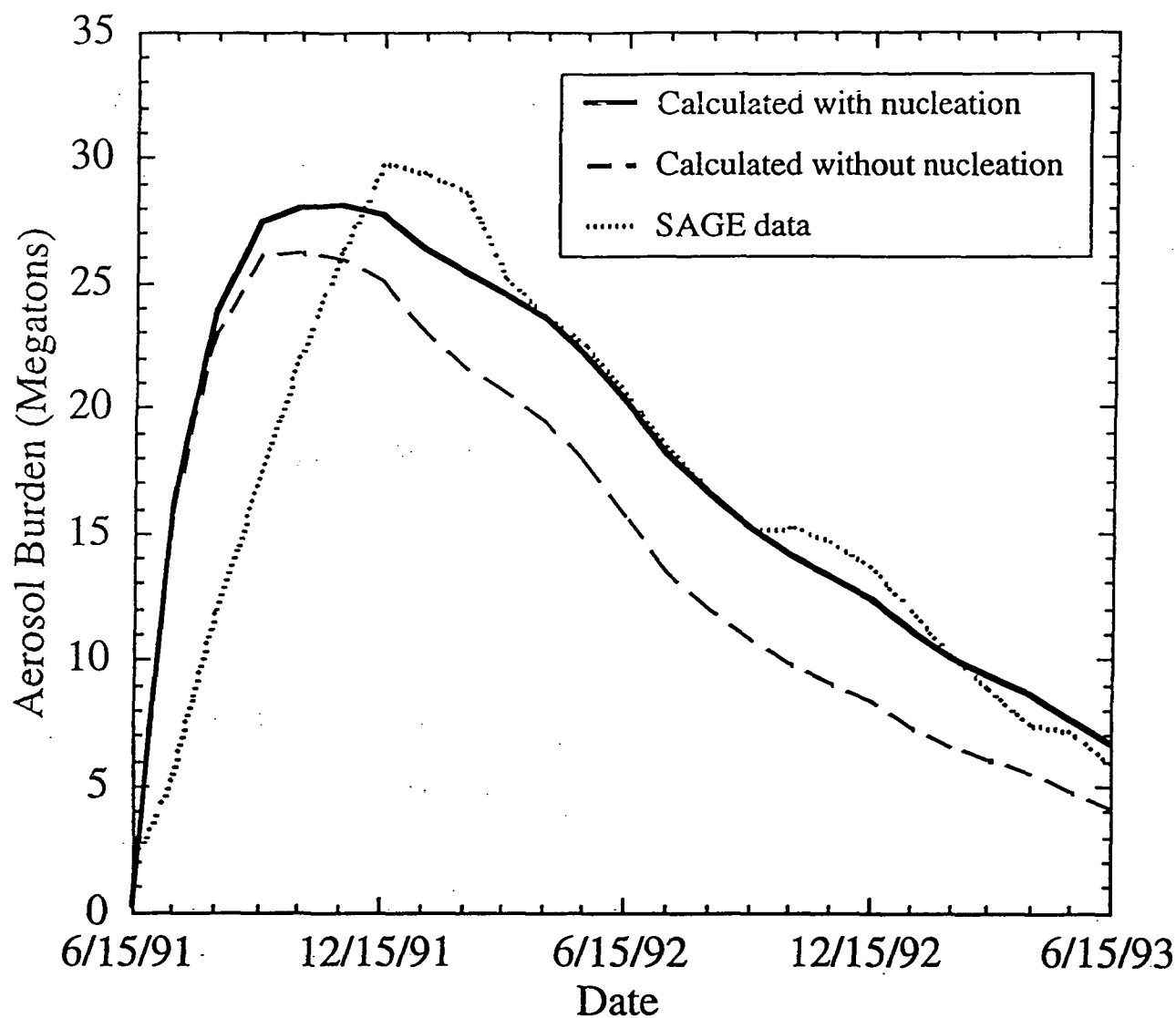


Figure 7: Stratospheric aerosol burden from 2 km above the tropopause to 30 km in megatons as a function of time following the eruption of Mt. Pinatubo on June 15, 1991. Observations from SAGE II instrument are shown, along with two model calculations, one including homogeneous nucleation and one excluding homogeneous nucleation. The volcanic eruption is model by a one-time input of 17 megatons of  $\text{SO}_2$  between 16 and 26 km and  $5^\circ\text{S}$  and  $14^\circ\text{N}$ .

## Appendix E

M.K.W. Ko, H.R. Schneider, R.L. Shia, D.K. Weisenstein, and N.D. Sze (1993) A two-dimensional model with coupled dynamics, radiation and photochemistry. 1. Simulation of the middle atmosphere. *J. Geophys. Res.*, 98, 20,429-20,440.

Schneider, H.R., M.K.W. Ko, R.-L. Shia, and N.-D. Sze (1993) A two-dimensional model with coupled dynamics, radiative transfer and photochemistry. 2. Assessment of the response of stratospheric ozone to increased levels of CO<sub>2</sub>, N<sub>2</sub>O, CH<sub>4</sub> and CFCs. *J. Geophys. Res.*, 98, 20,440-20,450.

# A Two-Dimensional Model With Coupled Dynamics, Radiation, and Photochemistry

## 1. Simulation of the Middle Atmosphere

MALCOLM K. W. KO, HANS R. SCHNEIDER,<sup>1</sup> RUN-LIE SHIA, DEBRA K. WEISENSTEIN, AND NIEN-DAK SZE

*Atmospheric and Environmental Research, Incorporated, Cambridge, Massachusetts*

Spatial and seasonal distribution of ozone and other trace gases are simulated using the interactive two-dimensional model of the stratosphere (Schneider et al., 1989) updated to include full gas phase chemistry. The model consists of a primitive equation dynamics module, a full radiative transfer scheme, and a comprehensive gas phase chemistry module. The circulation is derived from heating rates in the stratosphere that are calculated using model-generated ozone. In the troposphere, parameterized heating rates are adopted. The eddy momentum flux divergence in the zonal mean momentum equation is given by the eddy fluxes of potential vorticity. Eddy fluxes of potential vorticity and tracers are parameterized using a set of predetermined diffusion coefficients. The adopted values for  $K_{yy}$ , which are based on values derived by Newman et al. (1988), show a hemispherical asymmetry in that the values in the lower stratosphere are consistently smaller in the southern hemisphere. The asymmetry in  $K_{yy}$  and in the parameterization of the tropospheric heating rate results in an asymmetry in the circulation giving rise to unique signatures in the trace gas distributions. The model successfully simulates the observed asymmetry in the column abundance of the springtime ozone maxima between northern and southern hemisphere. Results for other trace gases are in agreement with the gross observed features although specific differences exist.

### 1. INTRODUCTION

During the past two decades, zonally averaged (two dimensional) chemistry transport models have been extensively used to simulate the distribution of tracers in the atmosphere. The model results, combined with data from in situ measurement, laboratory experiments, and satellite observations have greatly enhanced our knowledge of the photochemistry and dynamic transport processes in the atmosphere. Two-dimensional models are indispensable, especially for the study of ozone response to natural or anthropogenic disturbances. In most of the previous studies using chemistry-transport (CT) models, the atmosphere is described as a fixed background with a prescribed seasonal transport field and temperature in which the tracers move around and interact with each other. However, changes in certain trace gases, such as ozone, can change the flow and the temperature in the atmosphere. The prescribed velocity field, eddy diffusion coefficients, and temperature used in the CT model do not allow for this feedback. That is why the interactive models, which include interactions between different processes in the atmosphere, are needed for studying effects of large disturbances on the atmosphere.

This paper is the first of two papers which report the results of the investigation using a two-dimensional model with coupled dynamics, radiative transfer, and photochemistry developed at Atmospheric Environmental Research (AER). A brief review of the work in this area is presented in section 2. The AER model is described in section 3. Simulations of dynamic variables, ozone, and other trace gases in the present-day atmosphere are discussed in section 4.

Conclusions are presented in section 5. The second paper addresses the issue of ozone response to perturbations of the present-day atmosphere.

### 2. APPROACHES IN INTERACTIVE MODELS

To put the AER model in perspective, we will briefly review the features of interactive two-dimensional models by other researchers. One common feature among the interactive models is that the heating rate is calculated using the model-generated ozone distribution. They all differ in the radiative transfer treatment, the parameterization of the eddy momentum flux and eddy transport in the tracer equation, the photochemical content, and the numerical scheme. The first two-dimensional interactive model described by Harwood and Pyle [1975] is based on an Eulerian mean formulation and uses vertical and horizontal diffusion coefficients derived by Luther [1973]. The eddy momentum flux divergence for the zonal mean momentum equation is externally specified based on values derived from observations. The model of Vupputuri [1979] uses exactly the same formalism. As discussed by Schneider and Ko [1990], this may bias the model toward a radiative response to perturbations in heating rates. A version of this model, formulated in the residual circulation framework, was described by Pyle and Rogers [1980a]. However, results for the simulated trace gas distributions were not presented.

The Garcia and Solomon [1983] model is one of the earliest interactive models formulated using the residual mean circulation. Their model starts from 100 mbar, which is about 16 km above the surface. Lower boundary conditions, including vertical velocity at 100 mbar, are specified to account for all the influence the troposphere exerts on the middle atmosphere. There is no planetary wave forcing term in the momentum equation. Forcing is provided by a Raleigh frictional term and gravity wave breaking. Eddy transport of chemical tracers due to steady state planetary waves is

<sup>1</sup>Now at Division of Applied Sciences, Harvard University, Cambridge, Massachusetts.

parameterized in the transport equation by assigned values of  $K_{yy}$  and  $K_{zz}$ .

In the new version of their model, *Garcia et al.* [1992] extended the model domain to 2 km above the surface to include the troposphere and a potential vorticity equation for a single planetary scale Rossby wave (wave number 1) is solved along with the zonal mean momentum equation. The eddy diffusion coefficient  $K_{yy}$  due to wave breaking is then obtained from the planetary wave dissipation rate. With more interactions included in the model, the results of the simulated methane and nitrous oxide reproduce several observed features.

In the model developed by *Brasseur et al.* [1990], the Eliassen-Palm (E-P) flux divergence in the stratosphere is calculated in the model by solving an equation for planetary wave activity using a specified tropospheric wave activity to maintain the planetary wave action in the middle atmosphere. This wave activity equation is derived from the Rossby wave closure scheme described by *Hitchman and Brasseur* [1988]. However, tropospheric dynamics and the vertical velocities at the tropopause, which by and large determine the strength of the circulation in the lower stratosphere, are prescribed. Once the E-P flux divergence is known, the circulation is calculated from the heating rate. The eddy diffusion coefficient  $K_{yy}$  can be derived as a function of the zonal mean state from an expression which relates the E-P flux divergence and horizontal flux of potential vorticity [*Edmon et al.*, 1980]. An explicit gravity wave breaking scheme [*Holton and Schoeberl*, 1988] is also used to parameterize the vertical eddy diffusion coefficient  $K_{zz}$ . The eddy diffusion coefficients are then used in the tracer transport equation.

In the model of *Yang et al.* [1991] the processed National Meteorological Center (NMC) temperature data are used as input to the model. The heating rates, zonal mean velocity, eddy diffusion coefficients  $K_{yy}$ , and the diabatic circulation in isentropic coordinates are computed consistently along with chemical tracers. Because the temperature is specified, this model is not a predictive model in the usual sense. The simulation of tracers in this model compares very well with observations, including some features of interannual variations.

### 3. MODEL DESCRIPTION

The model used in this study consists of three modules, which calculate the zonal mean dynamical fields, the radiative transfer, and the photochemical reactions, respectively. The model configuration is the same as in the interactive model with simplified chemistry, described by *Schneider et al.* [1989]. Details of the dynamics module and the radiative transfer scheme can be found in the appendix of that paper. Only a brief summary is given here.

The model extends from the ground (1000 mbar) to approximately 82 km with levels equally spaced in  $\log(p)$ , where  $p$  is the pressure. The vertical resolution is half of the atmospheric scale height (about 3.5 km). The horizontal resolution is  $9.47^\circ$  (19 boxes from pole to pole). The radiative heating is calculated between 12 km and 55 km, using a narrow-band radiative transfer model. The effect of  $\text{CO}_2$ ,  $\text{O}_3$ ,  $\text{N}_2\text{O}$ ,  $\text{NO}_2$ , CFC 11, CFC 12,  $\text{CH}_4$ , and  $\text{H}_2\text{O}$  is included in the radiative transfer calculation in the infrared wavelengths. Above 55 km a relaxation to standard atmosphere

temperatures is used. Parameterized heating rates [*Cunnold et al.*, 1975] are used for the troposphere. The calculated heating rates are matched to the tropospheric parameterization between 12 and 15 km.

The equations used in the dynamics module are the zonal mean of the primitive equations and the thermodynamic equation in  $\log(p)$  coordinates. Gravity wave drag is incorporated in the momentum equation as a simple Rayleigh friction. The frictional damping time is set to about 30 days in the troposphere, 300 days at stratospheric levels below 40 km, and decreases to about 1 day at 80 km. The wave forcing in the momentum equation is specified as  $K_{yy}\bar{q}^y$ , where  $\bar{q}^y$  is the horizontal gradient of the quasi-geostrophic zonal mean potential vorticity on pressure surfaces. The frictional dissipation in the stratosphere is chosen to be sufficiently small (timescale larger than a season) so that the model diabatic circulation is controlled by the eddy potential vorticity flux. This allows the model to simulate the observed hemispheric asymmetry in total ozone from assumed asymmetry in  $K_{yy}$ .

The coefficients  $K_{yy}$  are externally specified. For this study, an analytic fit to the seasonally and latitudinally varying eddy diffusion coefficients derived by *Newman et al.* [1988] was used. The values of the coefficients for different times of the year are plotted in Figure 1. Typical values of  $K_{yy}$  in the tropical lower stratosphere are less than  $10^5 \text{ m}^2/\text{s}$ . Values in the northern midlatitude lower stratosphere range from  $3 \times 10^5 \text{ m}^2/\text{s}$  to a maximum value of  $10^6 \text{ m}^2/\text{s}$  in June. In the southern hemisphere, below 30 km altitude, the values are smaller than  $10^5 \text{ m}^2/\text{s}$ . Since the wave forcing in the model is defined as  $K_{yy}\bar{q}^y$ , the forcing in the southern hemisphere is consistently smaller than that in the northern hemisphere. As will be discussed in section 4, the asymmetry in  $K_{yy}$  is responsible for a north-south asymmetry in the circulation. The asymmetry in the circulation, not the asymmetry in the eddy diffusion terms of the tracer transport equation, gives rise to hemispheric differences of calculated trace gas concentrations.

Tracer diffusion is assumed to be along isentropic surfaces. The dominant component of the diffusion tensor in the tracer transport equation,  $K_{yy}$ , has the same numerical values used to parameterize the potential vorticity flux in the zonal mean momentum equation, as described above. The remaining components of the tensor are calculated as a function of the slope of the isentropes with respect to the pressure surfaces. The value of  $K_{yy}$  is the same in pressure and isentropic coordinates to first order, as the angle of rotation is small. In addition, a strong vertical diffusion ( $K_{zz} = 10 \text{ m}^2/\text{s}$ ) is added in the transport equation to simulate the rapid mixing in the troposphere, and a much smaller diffusion coefficient ( $K_{zz} = 10^{-1} \text{ m}^2/\text{s}$ ) is assigned for the stratosphere. The boundary of these two regions with different values of  $K_{zz}$  defines the tropopause in the model. Its position is prescribed as a part of input parameters instead of being calculated in the model.

The chemical module is adapted from the AER two-dimensional photochemical transport model [*Ko et al.*, 1984, 1985, 1989]. This is a comprehensive gas phase photochemistry model using a family approach in order to avoid small time steps due to species with very short lifetimes. The  $\text{O}_x$ ,  $\text{HO}_x$ ,  $\text{Br}_y$ ,  $\text{Cl}_y$ ,  $\text{NO}_y$ , and methyl families are included in the model. Water vapor concentration in the stratosphere is fixed based on observed values from Limb Infrared Monitor

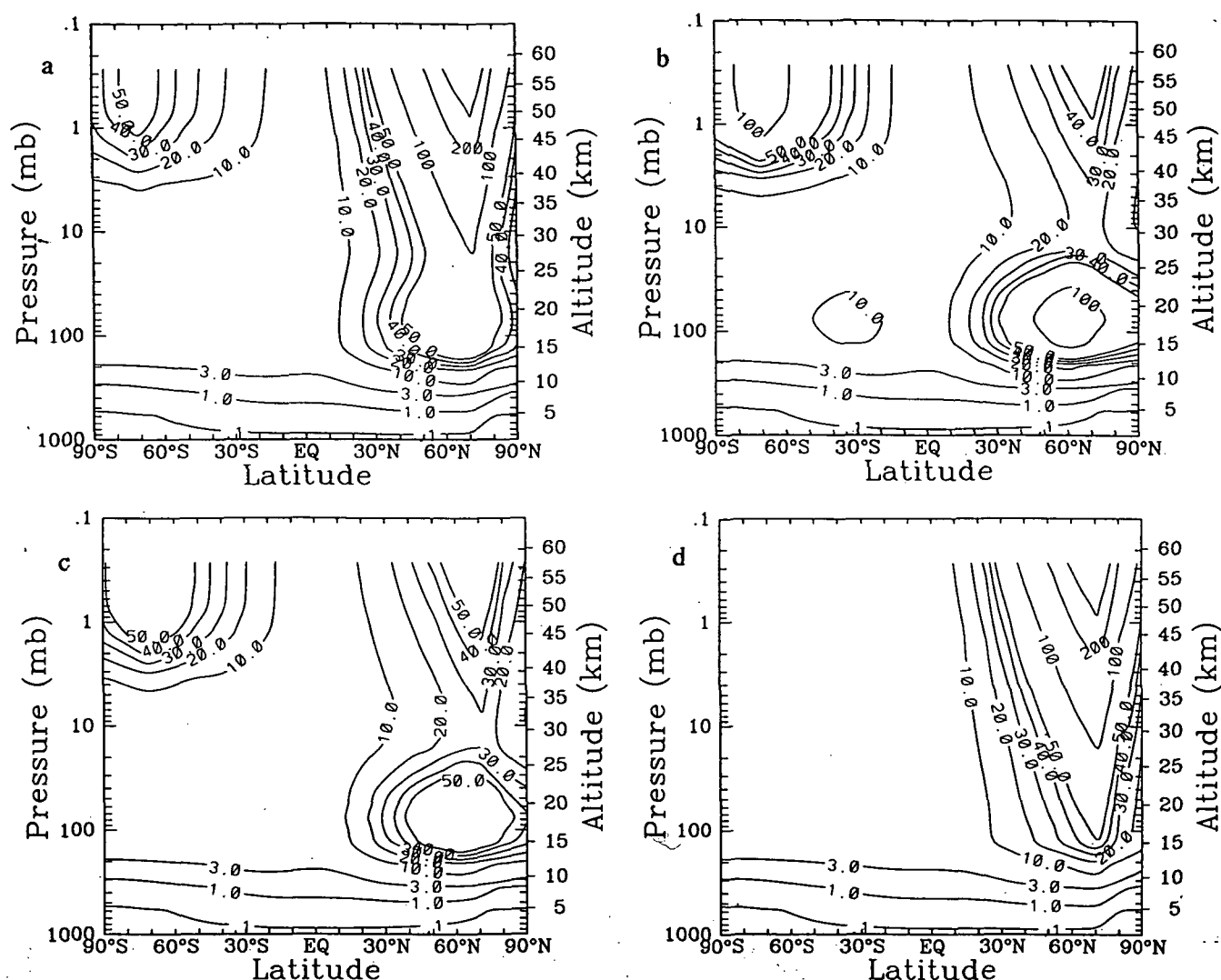


Fig. 1. The horizontal diffusion coefficient  $K_{yy}$  used in the model for four seasons: (a) March, (b) June, (c) September, and (d) December. The values are obtained through an analytic fit to the coefficients derived by Newman *et al.* [1988]. The contours represented are 0.1, 1, 3, 10, 20, 30, 40, 50, 100, 200, 300, 500. The unit used here is  $10^4 \text{ m}^2 \text{ s}^{-1}$ .

of the Stratosphere (LIMS) [Remsberg *et al.*, 1984]. Tropospheric water vapor concentration is calculated from the assumed climatological mean relative humidity. Effects of heterogeneous reactions on the surface of ice particles and sulfate aerosols are not included in the results discussed here. Since the heterogeneous reactions do not change the background ozone very much [Weissenstein *et al.*, 1991], we expect that most features of the model results presented in this paper will stay the same when heterogeneous chemistry is included.

The results presented in the following are from model runs with fixed boundary conditions for atmospheric source gases to simulate the atmosphere in 1985. The model was integrated until an annually periodic behavior was reached. For most cases this took about 10 years of integration when the model was started with initial tracer distributions from the AER chemistry-transport model.

#### 4. NUMERICAL RESULTS AND DISCUSSIONS

Previous studies showed that results from the AER CT model are in reasonable agreement with observation. The

first concern in comparison with available observations is whether the model can simulate the observed temperature and whether the calculated circulation can produce trace gas distribution that are in agreement with available observations.

##### 4.1. Temperature and Velocity Fields

Figure 2 shows the temperature and mean zonal wind for solstices produced by the model. The temperature distributions are reasonably close to observations throughout much of the model domain. The high-latitude regions at and above the tropopause are about  $10^\circ\text{K}$  too cold and the tropospheric jets consequently somewhat too strong. Also, the tropospheric westerlies in the summer hemisphere extend to higher altitudes than observed. This calculated behavior is a result of the small frictional dissipation assumed in the stratosphere. A larger damping would improve the agreement between the calculated and the observed zonal winds in the summer stratosphere but also overwhelm any response of the circulation to reasonable variations in  $K_{yy}$ .

The calculated meridional velocity fields are shown in



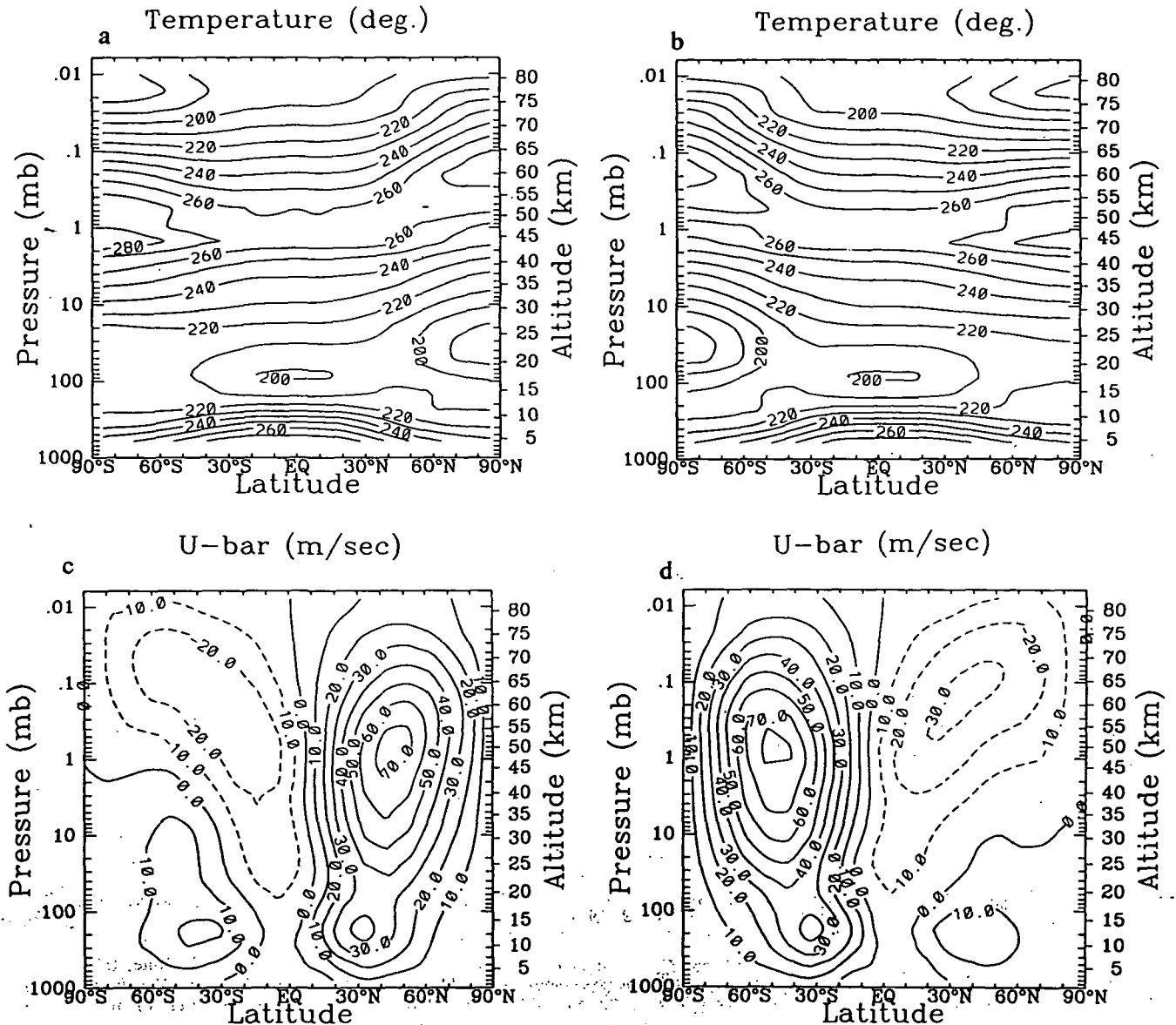


Fig. 2. (a) and (b) Calculated temperature and (c) and (d) mean zonal wind for January and July. The contours for temperature are from 180°K to 270°K with 10° increment and the contours for zonal wind are from  $-30 \text{ m s}^{-1}$  to  $80 \text{ m s}^{-1}$  with  $10 \text{ m s}^{-1}$  increment.

Figure 3. The downward velocities in the northern hemisphere winter are stronger than their southern winter counterparts at stratospheric levels. Also, in the southern winter the horizontal gradient in the vertical velocity field at high latitudes is smaller than its northern counterpart. This asymmetry in the circulation is seen better in the meridional stream function, shown in Figures 4a and 4b for the northern and southern winters, respectively. In the high-latitude southern hemisphere the streamlines are shifted to lower latitudes and are more vertical than their counterparts in the northern winter.

The asymmetry in the residual circulation is mostly a direct consequence of the different strengths of the wave forcing calculated in the hemispheres, with the parameterization of the tropospheric heating rates contributing a second-order effect. The effects of this asymmetry is evident in the asymmetries in tracer distributions between the hemispheres [Pyle and Rogers, 1980b; Hou et al., 1990]. In

particular, the asymmetry helps to maintain different ozone spring maxima in the two hemispheres. The latitudinal slopes of the lines of constant mixing ratios for a vertically stratified tracer are also steeper in the midlatitudes of the southern hemisphere as compared to the northern hemisphere. These characteristics can be seen in the calculated tracer distributions discussed in the following, although the asymmetries are reduced somewhat by the effect of eddy diffusion in the trace transport equation.

#### 4.2. Trace Gas Distributions

4.2.1. *Ozone.* Simulation of ozone is the main concern of most modeling efforts. Ozone is produced through the photodissociation of molecular oxygen in the stratosphere and destroyed through recombination either directly with atomic oxygen or through catalytic cycles involving  $\text{NO}_y$ ,  $\text{HO}_x$ , and  $\text{Cl}_y$ . The spatial and temporal distributions of

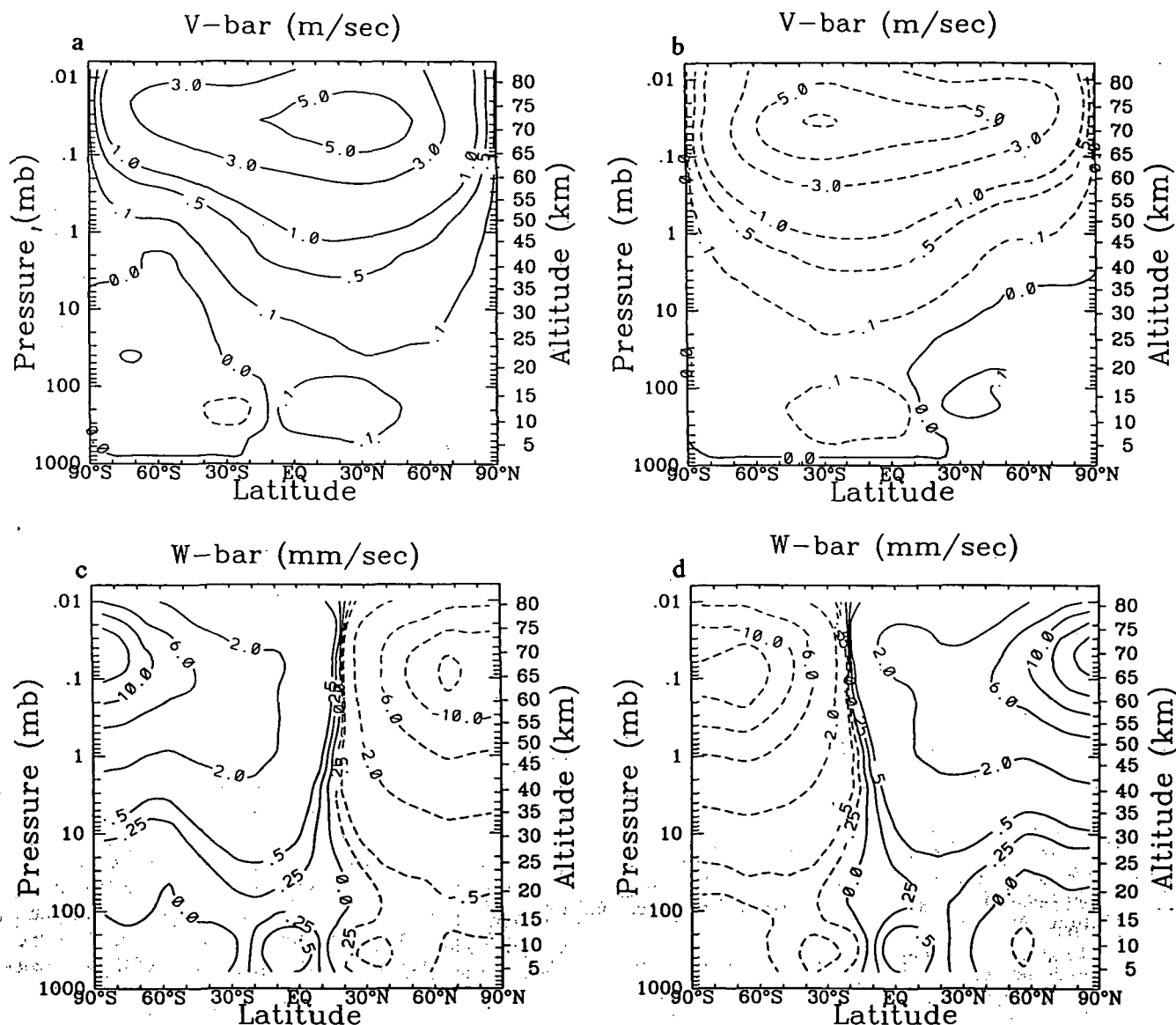


Fig. 3. Calculated wind components in the residual circulation: (a) horizontal component for January, (b) horizontal component for July, (c) vertical component for January, and (d) vertical component for July. The contours represented are (a) and (b)  $-7, -6, -5, -4, -3, -2, -1, -0.5, -0.25, -0.1, 0, 0.1, 0.25, 0.5, 1, 2, 3, 4, 5, 6, 7, \times$  ( $\text{m s}^{-1}$ ) for horizontal component and  $-15, -13, -10, -8, -6, -4, -3, -2, -1, -0.5, -0.25, 0, 0.25, 0.5, 1, 2, 4, 6, 8, 10, 12, 14, 16, 18 \times$  ( $\text{mm s}^{-1}$ ) for vertical component.

ozone reflect the results of competition between photochemistry and dynamic transport [see Ko *et al.*, 1989], especially in lower stratosphere, where most ozone resides. So the correct simulation of ozone distributions requires accurate computation of radiative, chemical, and dynamic processes.

Although the main features of time-latitude section of the simulated ozone in our interactive model (Figure 5a) are similar to the observations (Figure 5b), there are several important differences. The calculated column ozone in the equatorial region and midlatitudes is about 30 Dobson units (DU) higher than observations. More detailed diagnosis, which divides the whole column into three sections, 1000–100 mbar, 100–10 mbar, and 10–1 mbar (Figure 6), shows that the discrepancy is largest in the 100-mbar to 10-mbar section when compared to solar backscatter UV (SBUV) data (Figure 7). Additional calculations performed by one of us (H.R.S.) indicate that the overestimating at the tropics

may be due to the coarse vertical resolution of the model. With a 3.5-km resolution, the model underestimates the IR heating above the tropopause, and, consequently, upward transport is too slow in this region.

The spring maximum of the northern hemisphere appears to persist longer than observed and, as a result, the high-latitude ozone column in autumn is too high. This feature is also present in our chemistry-transport model [Ko *et al.*, 1991] despite efforts to adjust the zonal mean circulation. It would suggest that the discrepancy may be related to the photochemical treatment or the inability of the present formulation to correctly simulate the transport during the breakdown of the spring maximum in the northern hemisphere. The 60- to 80-DU surplus in northern high latitudes and 40- to 60-DU surplus in southern high latitudes of simulated ozone column abundance between the surface and the 100 mbar (Figures 6a and 7a) reflect poor simulation of

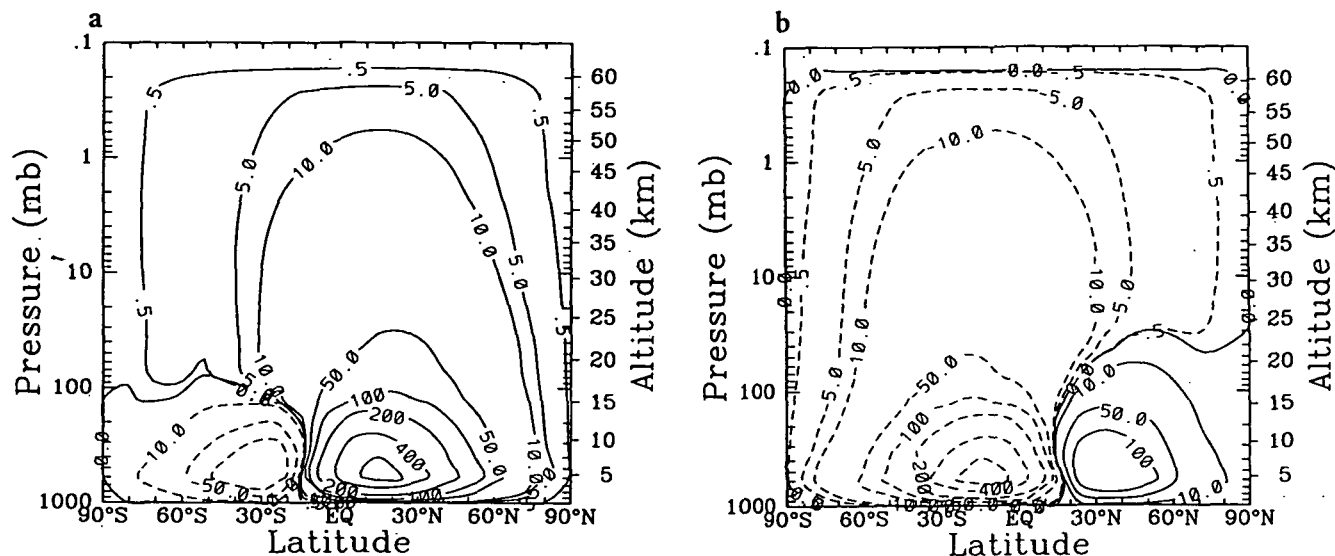


Fig. 4. Calculated mean meridional mass stream functions for (a) January and (b) July. The contours represented are  $-600, -500, -400, -200, -160, -120, -80, -40, -20, -16, -12, -8, -4, -2, -1.2, -0.8, -0.4, 0, 0.4, 0.8, 1.2, 2, 4, 8, 12, 16, 20, 40, 80, 120 \times (10^{-5} \text{ m}^2 \text{ s}^{-1})$ . Values correspond to the mass flux scaled by  $(2A\rho_s)$ , where  $A$  is the radius of the Earth and  $\rho_s$  is the surface air density.

both dynamics and photochemistry in the polar lower stratosphere.

The north-south asymmetry in the spring maxima is reproduced very well in the model. The behavior of the spring maxima for a model with simplified chemistry was discussed by Hou *et al.* [1990]. The same argument applies here: For the model to be able to reproduce the observed asymmetry in the column ozone distribution, frictional dissipation in the stratosphere has to be very small (timescales longer than a season) and the eddy diffusion coefficients in the southern hemisphere lower stratosphere have to be smaller than  $10^5 \text{ m}^2/\text{s}$ .

Latitude-altitude cross sections of calculated ozone mix-

ing ratio for different seasons are shown in Figure 8. The maxima of the calculated ozone mixing ratio are close to measured values. However, the ozone maximum is situated about 3 km lower than indicated in the SBUV data. Furthermore, the simulated ozone mixing ratios around 40 km are roughly 20% smaller than observations, a problem common to most photochemical models [World Meteorological Organization (WMO)/NASA, 1986].

**4.2.2. Upward diffusing species.** Nitrous oxide ( $\text{N}_2\text{O}$ ) and the chlorofluorocarbons (CFCs) are long-lived species which enter the stratosphere by upward transport and are removed mainly through photodissociation in the stratosphere. Because of the long lifetimes of these species in the

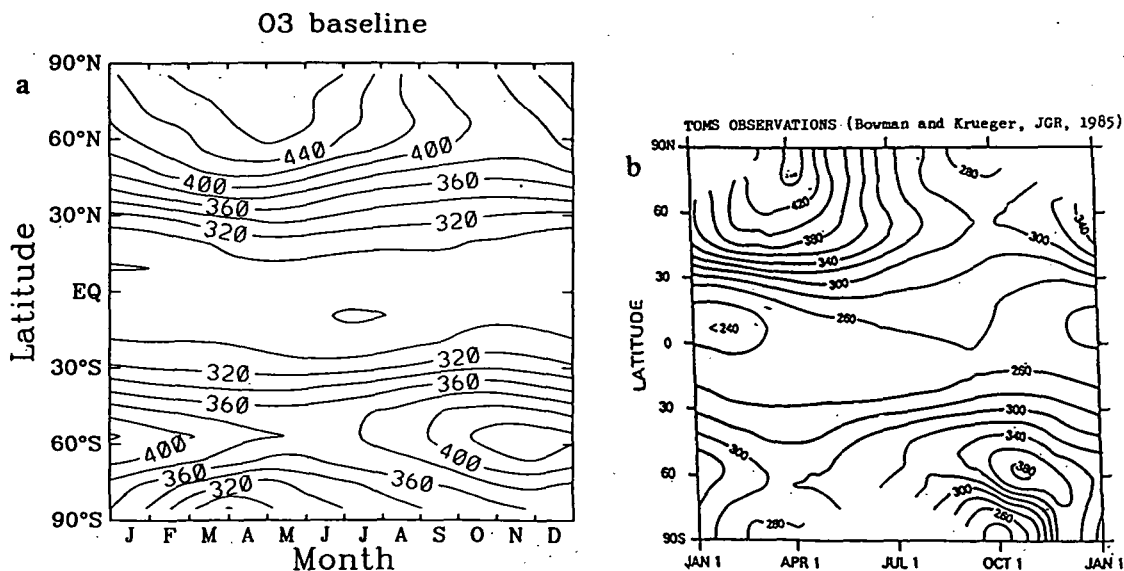


Fig. 5. (a) Calculated ozone column abundance in Dobson units (DU) as a function of latitude and time of the year. (b) Observed ozone column, total ozone mapping spectrometer (TOMS), taken from Bowman and Krueger [1985]. The contours represented are from 240 to 460 DU with a 20-DU increment.

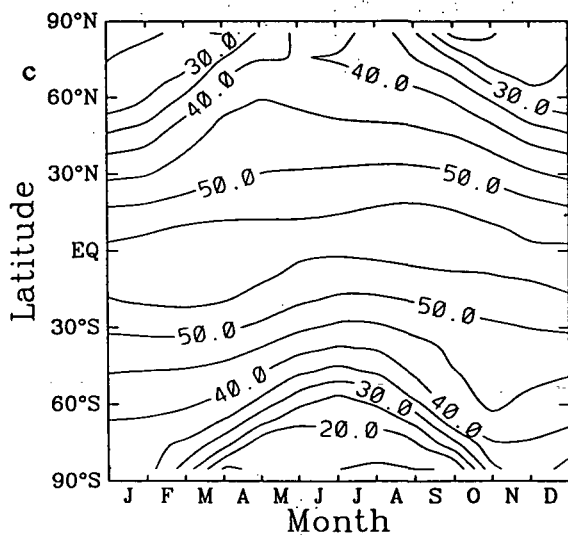
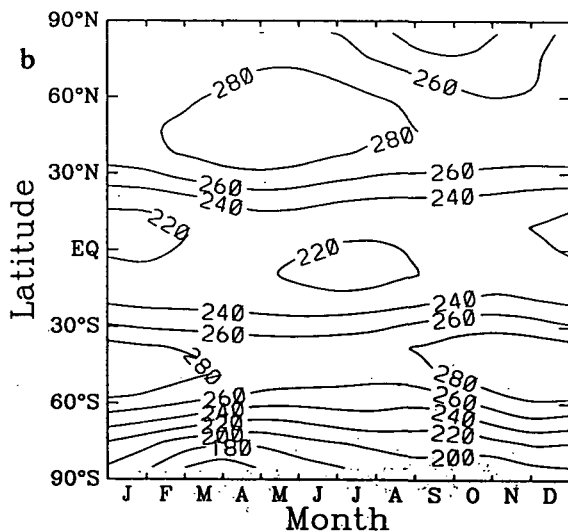
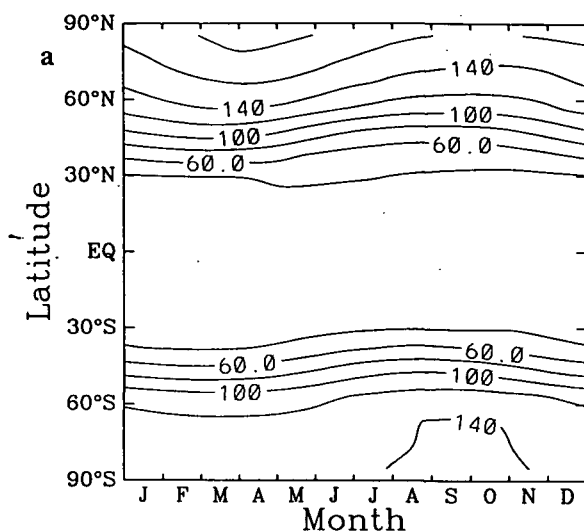


Fig. 6. Calculated total ozone in three layers: (a) 1000–100 mbar, (b) 100–10 mbar, (c) 10–1 mbar. The contours represented are from 20 to 180 DU with a 20-DU increment in (a), from 140 to 280 DU with a 20-DU increment in (b) and from 10 to 55 DU with a 5-DU increment in (c).

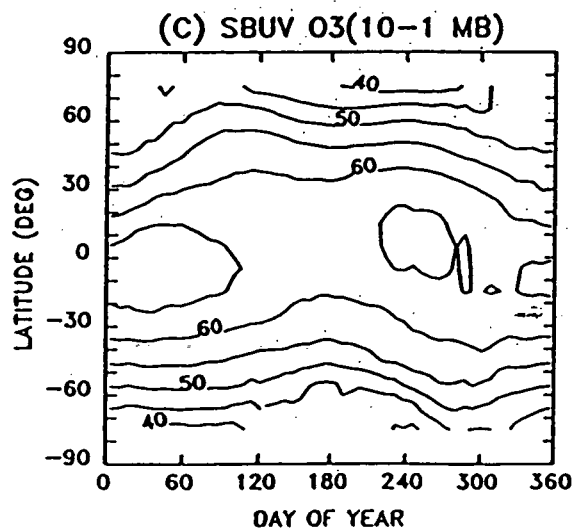
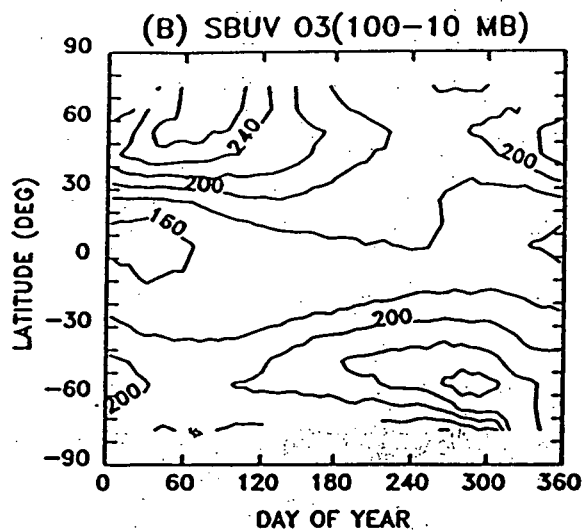
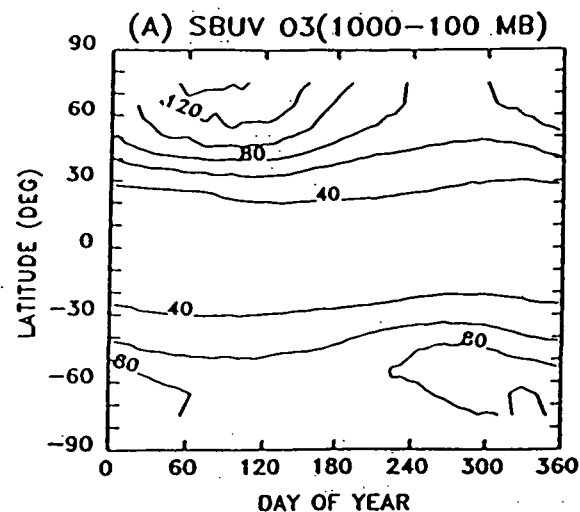


Fig. 7. Same as Figure 6 but from solar backscattered UV (SBUV) data as compiled by Jackman *et al.* [1989].

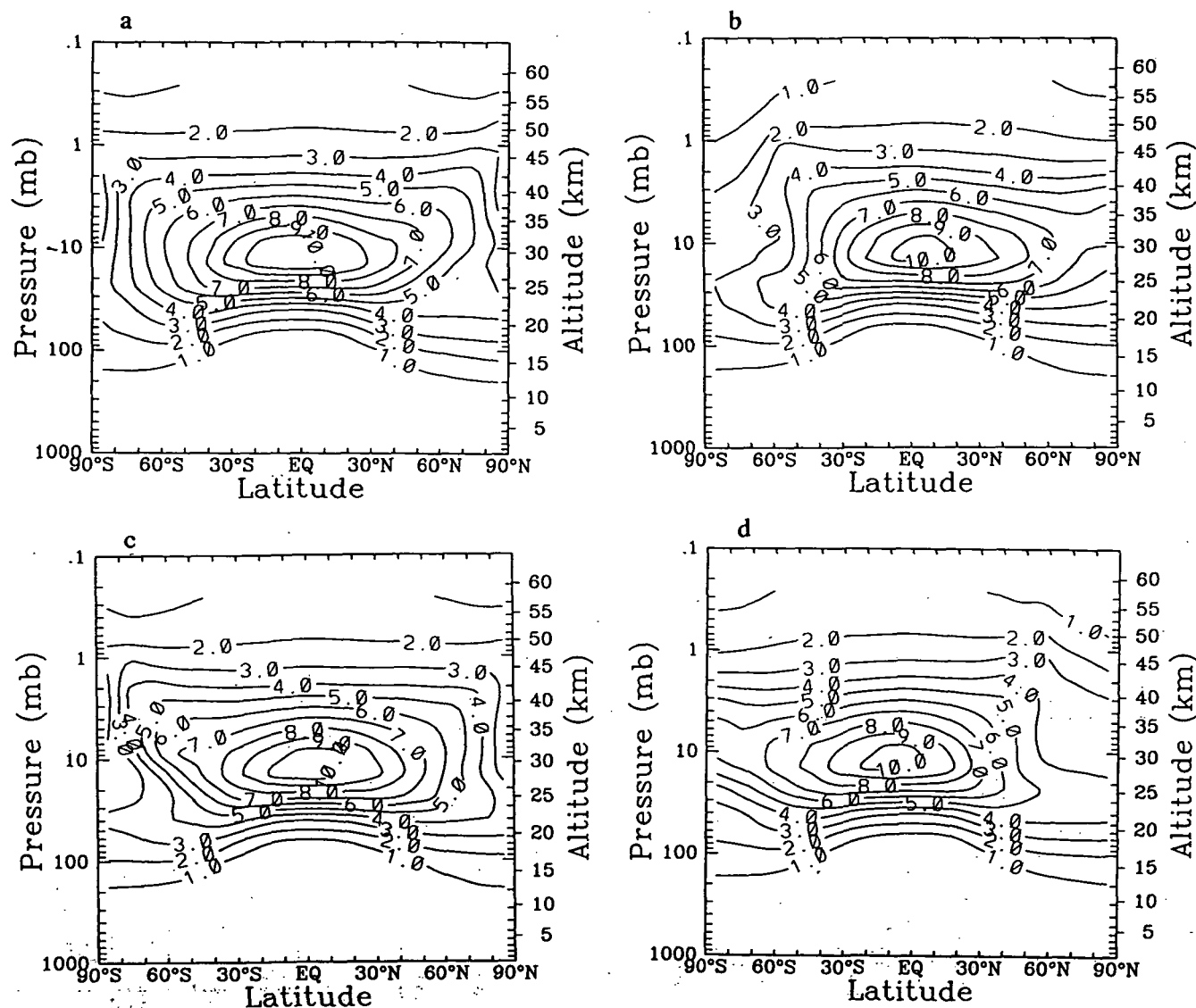


Fig. 8. Simulated distribution of  $O_3$  mixing ratios (parts per million by volume) for four seasons: (a) March, (b) June, (c) September, and (d) December. The contours represented are 1 to 10 with 1 increment.

lower stratosphere, their distribution reflects the meridional circulation pattern with upwelling over the equator and downward motion at high latitudes. The model-calculated lifetimes for CFC 11, CFC 12, and  $N_2O$  are 51 years; 90 years, and 106 years, respectively. These values, which are consistent with the values from the AER CT model [Ko *et al.*, 1991], are considerably shorter than values previously reported in the literature [United Nations Environment Program (UNEP), 1992].

The effect of the asymmetry on high-latitude profiles can be seen in Figure 9, where  $N_2O$  profiles for 66°N in March and 66°S in September are plotted. Above 20 km the model-calculated mixing ratios differ by almost a factor of 2. Measurements taken during the Airborne Antarctic Ozone Experiment (AAOE) campaign [Loewenstein *et al.*, 1989] are also plotted in this figure. The AAOE data are representative of September in the southern hemisphere. Most of the data fall between the model profiles for the two hemispheres.

The calculated distribution of  $CH_4$  has exhibited features similar to the  $N_2O$  mixing ratios. Both are quite close to the

results of the AER CT model. The seasonal shift of the peak mixing ratios at high altitudes (about 1 mbar), which has been seen in stratospheric and mesospheric sounder (SAMS) data [Jones and Pyle, 1984], is not represented well by the model.

CFCs are the major source of stratospheric chlorine. Correct simulation of CFCs is therefore critical for the assessment of future changes in the ozone layer due to the increasing chlorine content of the stratosphere. The simulated vertical distribution of CFC 11 and CFC 12 are plotted against AAOE data [Heidt *et al.*, 1989] in Figure 10a and 10b, respectively. The agreement between measurements and the model simulation is not very satisfactory especially for CFC 11.

The correlation diagram [Plumb and Ko, 1992] between  $N_2O$  and CFC 11 is illustrated in Figure 11 for both model results and AAOE data [Loewenstein *et al.*, 1989; Heidt *et al.*, 1989]. The simulated correlations for both hemispheres at 66° in spring are plotted on the figure to show the asymmetry between the two hemispheres. Note that relative

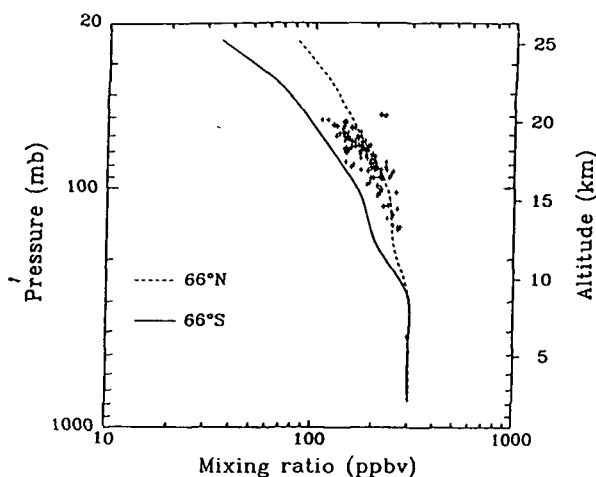


Fig. 9. Comparison of calculated  $\text{N}_2\text{O}$  profile for September at  $66^\circ\text{S}$  (solid line) to Airborne Antarctic Ozone Experiment (AAOE) data [Loewenstein et al., 1989]. The dashed line indicates the calculated profile for March at  $66^\circ\text{N}$ .

to  $\text{N}_2\text{O}$ , the calculated CFC 11 concentration is actually smaller in the northern hemisphere. The agreement between simulations and observations is not very satisfactory for the baseline simulation (Figure 11a), which represents the atmosphere in 1980 with less CFCs accumulated. If we increase the surface mixing ratios of CFCs to the level of 1990, better agreement is obtained for the troposphere. However, the model still overestimates the CFC 11 concentration by a significant amount.

**4.2.3. Downward diffusing species.** The latitudinal-altitude behavior of  $\text{NO}_y$ , the total odd nitrogen species, defined as the sum of  $\text{HNO}_3 + \text{NO} + \text{NO}_2 + 2 \times \text{N}_2\text{O}_5 + \text{NO}_3 + \text{ClONO}_2 + \text{HO}_2\text{NO}_2 + \text{N}$ , and  $\text{Cl}_y$ , the total chlorine species, defined as the sum of  $\text{Cl} + \text{ClO} + \text{HCl} + \text{OCIO} + 2\text{Cl}_2\text{O}_2 + \text{ClONO}_2 + \text{HOCl}$ , is typical of the downward diffusing species, which are formed by in situ production in the stratosphere and thermosphere and are transported into the lower stratosphere and the troposphere.  $\text{NO}_y$  and  $\text{Cl}_y$  are

treated as long-lived trace species in the model. Their distributions are important for correct simulation of other species, especially ozone.

Comparisons of the calculated  $\text{NO}_y$  profiles near the equator and at  $38^\circ\text{N}$  with the observed nighttime mixing ratios of  $\text{NO}_2 + \text{HNO}_3$  [Callis et al., 1985] from LIMS [Russel et al., 1984; Gille and Russell, 1984] are shown in Figures 12a and 12b. With the tropospheric lightning sources in the model [Ko et al., 1986] the model simulation of  $\text{NO}_y$  compares very favorably with the observations. Yang et al. [1990] suggested high concentrations of  $\text{NO}_y$  can be maintained in the lower stratosphere without a lightning source if the upwelling at the equator across the tropopause is sufficiently weak. Their model produced quite realistic  $\text{NO}_y$  simulations. Our results show that the  $\text{NO}_y$  concentration simulated by the interactive model is similar to that simulated by the AER CT model [Ko et al., 1986], even though the interactive model has 20% less upwelling in the lower tropical stratosphere. We tested the interactive model without the lightning source and the resulting concentration of  $\text{NO}_y$  in the lower tropical stratosphere is a factor of 10 smaller. So for the choice of the tropopause height and the transport parameters in our interactive model the lightning source is necessary to produce correct  $\text{NO}_y$  distribution in the tropics. Our recent work with the CT model [Shia et al., 1993; V. R. Kotamarthi et al., The effect of lightning on the concentration of odd nitrogen species in the lower stratosphere: An update, submitted to *Journal of Geophysical Research*, 1993] suggests that the tropopause may be set too high in the model. A lower tropopause will reduce the effect of the lightning source.

## 5. CONCLUDING REMARKS

The simulated distributions of ozone and other trace gases have been compared with available data. The model is capable of reproducing many of the observed characteristics of tracer concentrations. The hemispheric asymmetry, observed for column ozone amounts is simulated with a minimum number of assumptions. North-south asymmetries for other species are also predicted by the model.

Despite the overall agreement between the model simula-

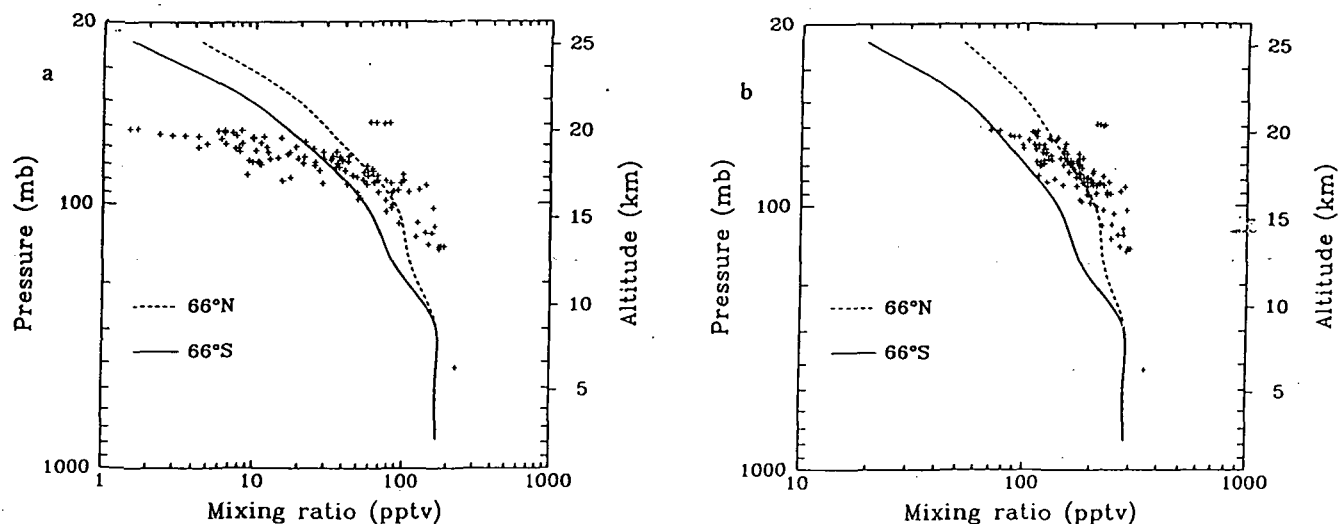


Fig. 10. Same as Figure 9 except for (a) CFC 11 and (b) CFC 12 and AAOE data from Heidt et al. [1989].

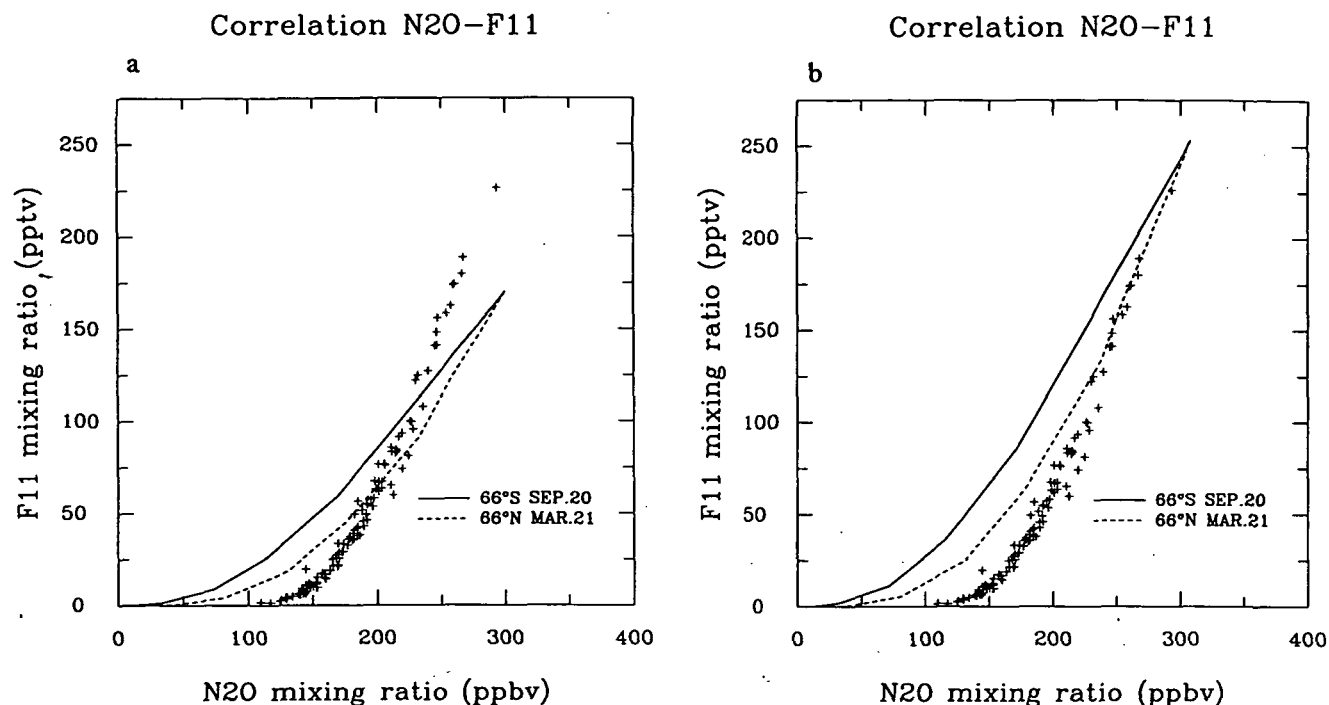


Fig. 11. Simulated and observed (AAOE [Heidt *et al.*, 1989 and Loewenstein *et al.*, 1989]) correlation between CFF 11 and N<sub>2</sub>O, with simulated results for (a) 1980 and (b) 1990.

tion and the observations, several aspects of the tracer distributions demand further investigation. In the case of ozone distribution the long-standing problem of underpredicting ozone mixing ratios at 40 km remains. The spring maxima in the ozone column distribution last too long and, as a result, the total column amount of ozone in fall at high latitudes is not well simulated. This may be an indication that the rapid transport occurring during the final warming is not included in the  $K_{yy}$  parameterization used in the current version of the model. For species like N<sub>2</sub>O and methane, the seasonal cycles at high altitudes are not reproduced satisfac-

torily. This may be interpreted as indication that details of the circulation at high altitude are still missing.

A crucial question in development of zonal mean models is whether the eddy formulation is capable of simulating the zonal-mean behavior of trace species. The issue concerning eddy fluxes in the transport equation has been the focus of chemistry-transport models. In the interactive model, the additional issue of how to specify the eddy momentum fluxes in terms of zonal mean quantities must also be addressed. Based on the results presented in this paper, the performance of the interactive model in simulating the trace gas

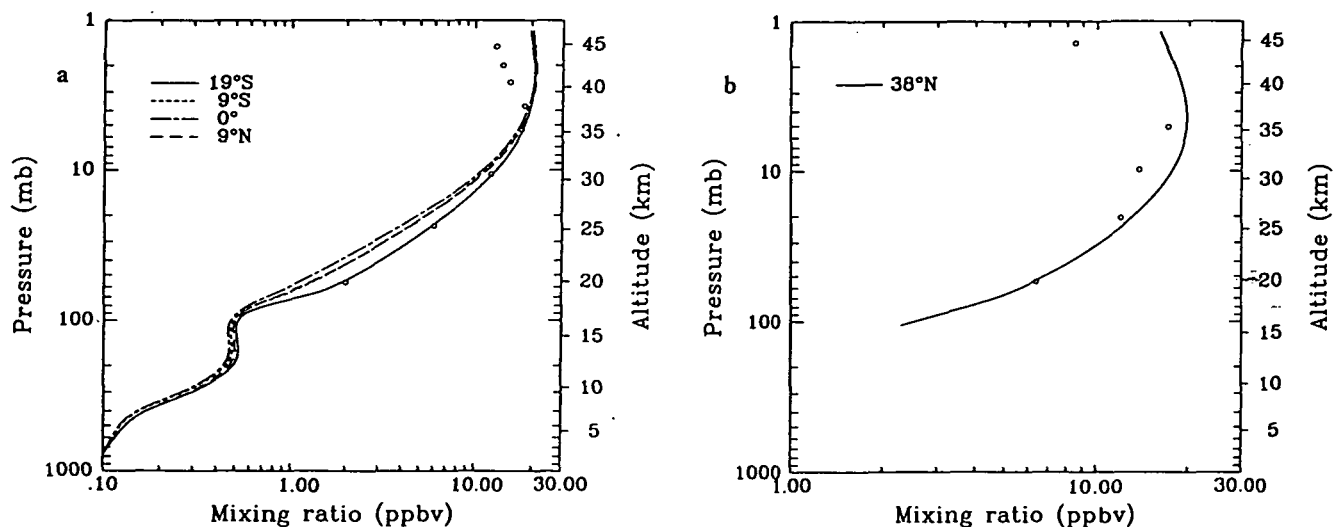


Fig. 12. Comparison of calculated NO<sub>y</sub> profiles to limb infrared monitor of the stratosphere (LIMS) data (circles), in (a) low latitudes (solid line is for 19°S, dotted line for 9°S, dashed-dotted line for equator, and dashed line for 9°N) and (b) at 38°N.

distributions in the present-day atmosphere is comparable to that of the chemistry-transport model. We have pointed out in our discussion several shortcomings common to both types of models. Additional criteria for judging the performance of the models can be obtained by comparing the results from three-dimensional models. Once their utilities and limitations are established, zonal mean models can then be used to provide results for specific studies.

In the present version of the model the interaction between the stratosphere and the troposphere is limited by the parameterization of the tropospheric heating rate. Eliminating this parameterization and adding hydrologic cycle into the model will allow more feedbacks inside the troposphere and between the troposphere and the stratosphere. Recent calculations [Ramaswamy *et al.*, 1992] indicate that the ozone decrease in the lower stratosphere/upper troposphere has a large impact on the radiative forcing for the troposphere. We intend to add more interactions among radiation, dynamics, and photochemical processes to account for different feedback channels.

**Acknowledgments.** This work was supported by the NASA Upper Atmosphere Theory and Data Analysis Program under contract NASW 4080 and NASW 4428, the Fluorocarbon Program Panel of the Chemical Manufacturers Association, and AFEAS. Thanks are due to Jose Rodriguez and Arthur Hou for many helpful discussions.

#### REFERENCES

- Bowman, K. P., and A. J. Krueger, A global climatology of total ozone from the Nimbus 7 total ozone mapping spectrometer (TOMS), *J. Geophys. Res.*, **90**, 7967–7976, 1985.
- Brasseur, G., M. H. Hitchman, S. Walters, M. Dymek, E. Falise, and M. Pirre, An interactive chemical-dynamical radiative two-dimensional model of the middle atmosphere, *J. Geophys. Res.*, **95**, 5639–5655, 1990.
- Callis, L. B., M. Natarajan, and J. M. Russell III, Estimates of the stratospheric distributions of odd nitrogen from LIMS data, *Geophys. Res. Lett.*, **12**, 259–262, 1985.
- Cunnold, D., F. Alyea, N. Phillips, and R. Prinn, A three-dimensional dynamical-chemical model of atmospheric ozone, *J. Atmos. Sci.*, **32**, 170–194, 1975.
- Edmon, H. J., Jr., B. J. Hoskins, and M. E. McIntyre, Eliassen-Palm cross sections for the troposphere, *J. Atmos. Sci.*, **37**, 2600–2616, 1980.
- Garcia, R. R., and S. Solomon, A numerical model of the zonally averaged dynamical and chemical structure of the middle atmosphere, *J. Geophys. Res.*, **88**, 1379–1400, 1983.
- Garcia, R. R., F. Stordal, S. Solomon, and J. F. Kiehl, A new numerical model of the middle atmosphere, 1, Dynamics and transport of tropospheric source gases, *J. Geophys. Res.*, **97**, 12,967–12,991, 1992.
- Gille, J. C., and J. M. Russell III, The limb infrared monitor of the stratosphere: Experiment description, performance, and results, *J. Geophys. Res.*, **89**, 5125–5140, 1984.
- Harwood, R. S., and J. A. Pyle, A two-dimensional mean circulation model for the atmosphere below 80 km, *Q. J. R. Meteorol. Soc.*, **101**, 723–748, 1975.
- Heidt, L. E., J. F. Vedder, W. H. Pollock, R. A. Lueb, and B. E. Henry, Trace gases in Antarctic atmosphere, *J. Geophys. Res.*, **94**, 11,599–11,611, 1989.
- Hitchman, M. H., and G. Brasseur, Rossby wave activity in a two-dimensional model: Closure for wave driving and meridional eddy diffusivity, *J. Geophys. Res.*, **93**, 9405–9417, 1988.
- Holton, J. R., and M. R. Schoeberl, The role of gravity wave generated advection and diffusion in transport of tracers in the mesosphere, *J. Geophys. Res.*, **93**, 11,075–11,082, 1988.
- Hou, A. Y., H. R. Schneider, and M. K. W. Ko, A dynamical explanation for the asymmetry in zonally averaged column abundance of ozone between northern and southern springs, *J. Atmos. Sci.*, **47**, 547–556, 1990.
- Jackman, C. H., A. R. Douglass, P. D. Guthrie, and R. S. Stolarski, The sensitivity of total ozone and ozone perturbation scenarios in a two-dimensional model due to dynamical inputs, *J. Geophys. Res.*, **94**, 9873–9887, 1989.
- Jones, R. L., and J. A. Pyle, Observations of CH<sub>4</sub> and N<sub>2</sub>O by the Nimbus 7 SAMS: A comparison with in situ data and two-dimensional numerical model calculations, *J. Geophys. Res.*, **89**, 5263–5279, 1984.
- Ko, M. K. W., N. D. Sze, M. Livshits, M. B. McElroy, and J. A. Pyle, The seasonal and latitudinal behavior of trace gases and O<sub>3</sub> as simulated by a two-dimensional model of the atmosphere, *J. Atmos. Sci.*, **41**, 2381–2408, 1984.
- Ko, M. K. W., K. K. Tung, D. K. Weisenstein, and N. D. Sze, A zonal mean model of stratospheric tracer transport in isentropic coordinates: Numerical simulation for nitrous oxide and nitric acid, *J. Geophys. Res.*, **90**, 2313–2329, 1985.
- Ko, M. K. W., M. B. McElroy, D. K. Weisenstein, and N. D. Sze, Lightning: A possible source of stratospheric odd nitrogen, *J. Geophys. Res.*, **91**, 5395–5404, 1986.
- Ko, M. K. W., N. D. Sze, and D. K. Weisenstein, The roles of dynamical and chemical processes in determining the stratospheric concentration of ozone in one-dimensional and two-dimensional models, *J. Geophys. Res.*, **94**, 9889–9896, 1989.
- Ko, M. K. W., N. D. Sze, and D. K. Weisenstein, Use of satellite data to constrain model-calculated atmospheric lifetimes for N<sub>2</sub>O: Implications for other trace gases, *J. Geophys. Res.*, **96**, 7547–7552, 1991.
- Loewenstein, M., J. R. Podolske, K. R. Chen, and S. E. Strahan, Nitrous oxide as a dynamical tracer in the 1987 Airborne Antarctic Ozone Experiment, *J. Geophys. Res.*, **94**, 11,589–11,598, 1989.
- Luther, F. M., Monthly mean values of eddy diffusion coefficients in the lower stratosphere, *AIAA Pap.*, **73-498**, Am. Inst. of Aeronaut. and Astronaut., New York, 1973.
- Newman, P. A., M. R. Schoeberl, R. A. Plumb, and J. E. Rosenfield, Mixing rates calculated from potential vorticity, *J. Geophys. Res.*, **93**, 5221–5240, 1988.
- Plumb, R. A., and M. K. W. Ko, Interrelationships between mixing ratios of long-lived stratospheric constituents, *J. Geophys. Res.*, **97**, 10,145–10,156, 1992.
- Pyle, J. A., and C. F. Rogers, Stratospheric transport by stationary planetary waves: The importance of chemical processes, *Q. J. R. Meteorol. Soc.*, **106**, 421–446, 1980a.
- Pyle, J. A., and C. F. Rogers, A modified diabatic circulation model for stratospheric tracer transport, *Nature*, **287**, 711–714, 1980b.
- Ramaswamy, V., M. D. Schwarzkopf, and K. P. Shine, Radiative forcing of climate from halocarbon-induced global stratospheric ozone loss, *Nature*, **355**, 810–812, 1992.
- Remsberg, E. E., J. M. Russell III, L. L. Gordley, J. C. Gille, and P. L. Bailey, Implications of the stratospheric water vapor distribution as determined from the Nimbus 7 LIMS experiment, *J. Atmos. Sci.*, **41**, 2934–2945, 1984.
- Russell, J. M., III, J. C. Gille, E. E. Remsburg, L. L. Gordley, S. R. Drayson, J. Fischer, A. Girard, J. E. Harries, and W. F. J. Evans, Validation of nitrogen dioxide results measured by the Limb Infrared Monitor of the Stratosphere experiment on Nimbus 7, *J. Geophys. Res.*, **89**, 5099–5107, 1984.
- Schneider, H. R., and M. K. W. Ko, Response of an interactive two-dimensional model to ozone changes: An estimate of the radiative dynamical feedback effect, *J. Geophys. Res.*, **95**, 5657–5668, 1990.
- Schneider, H. R., M. K. W. Ko, N. D. Sze, G.-Y. Shi, and W.-C. Wang, An evaluation of eddy diffusion in stratospheric interactive two-dimensional models, *J. Atmos. Sci.*, **46**, 2079–2093, 1989.
- Shia, R. L., M. K. W. Ko, M. Zou, and V. R. Kotamarthi, Cross-tropopause transport of excess <sup>14</sup>C in a two-dimensional model, *J. Geophys. Res.*, in press, 1993.
- United Nations Environment Program (UNEP), Scientific assessment of ozone depletion: 1991, *WMO Rep. 25*, World Meteorol. Organ., Global Ozone Res. and Monit. Proj., Geneva, 1992.
- Vupputuri, R. K., The structure of the natural stratosphere and the impact of chlorofluoromethanes on the ozone layer investigated in a 2-D time dependent model, *Pure Appl. Geophys.*, **117**, 448–485, 1979.
- Weisenstein, D. K., M. K. W. Ko, J. M. Rodriguez, and N.-D. Sze,



- Impact of heterogeneous chemistry on model calculated ozone change due to high speed civil transport aircraft, *Geophys. Res. Lett.*, **18**, 1991–1994, 1991.
- World Meteorological Organization (WMO)/NASA, Atmospheric ozone 1985, *WMO Rep. 16*, Global Ozone Res. and Monit. Proj., Geneva, 1986.
- Yang, H., E. Olaguer, and K. K. Tung, Simulation of the present-day atmospheric ozone, odd nitrogen, chlorine and other species using a coupled 2-D model in isentropic coordinates, *J. Atmos. Sci.*, **48**, 442–471, 1991.
- M. K. W. Ko, R.-L. Shia, N.-D. Sze, and D. K. Weisenstein, Atmospheric and Environmental Research, Inc., 840 Memorial Drive, Cambridge, MA 02139.
- H. R. Schneider, Division of Applied Sciences, Pierce Hall, Harvard University, Cambridge, MA 02138.

(Received January 22, 1993;  
revised July 9, 1993;  
accepted July 9, 1993.)

# A Two-Dimensional Model With Coupled Dynamics, Radiative Transfer, and Photochemistry

## 2. Assessment of the Response of Stratospheric Ozone to Increased Levels of CO<sub>2</sub>, N<sub>2</sub>O, CH<sub>4</sub>, and CFC

HANS R. SCHNEIDER,<sup>1</sup> MALCOLM K. W. KO, RUN-LIE SHIA, AND NIEN-DAK SZE

*Atmospheric and Environmental Research, Incorporated, Cambridge, Massachusetts*

The impact of increased levels of carbon dioxide (CO<sub>2</sub>), chlorofluorocarbons (CFCs), and other trace gases on stratospheric ozone is investigated with an interactive, two-dimensional model of gas phase chemistry, dynamics, and radiation. The scenarios considered are (1) a doubling of the CO<sub>2</sub> concentration, (2) increases of CFCs, (3) CFC increases combined with increases of nitrous oxide (N<sub>2</sub>O) and methane CH<sub>4</sub>, and (4) the simultaneous increase of CO<sub>2</sub>, CFCs, N<sub>2</sub>O, and CH<sub>4</sub>. The radiative feedback and the effect of temperature and circulation changes are studied for each scenario. For the double CO<sub>2</sub> calculations the tropospheric warming was specified. The CO<sub>2</sub> doubling leads to a 3.1% increase in the global ozone content. Doubling of the CO<sub>2</sub> concentrations would lead to a maximum cooling of about 12°C at 45 km if the ozone concentration were held fixed. The cooling of the stratosphere leads to an ozone increase with an associated increase in solar heating, reducing the maximum temperature drop by about 3°C. The CFC increase from continuous emissions at 1985 rate causes a 4.5% loss of ozone. For the combined perturbation a net loss of 1.3% is calculated. The structure of the perturbations shows a north-south asymmetry. Ozone losses (when expressed in terms of percent changes) are generally larger in the high latitudes of the southern hemisphere as a result of the eddy mixing being smaller than in the northern hemisphere. Increase of chlorine leads to ozone losses above 30 km altitude where the radiative feedback results in a cooler temperature and an ozone recovery of about one quarter of the losses predicted with a noninteractive model. In all the cases, changes in circulation are small. In the chlorine case, circulation changes reduce the calculated column depletion by about one tenth compared to offline calculations.

### 1. INTRODUCTION

The concentrations of various trace gases in the Earth's atmosphere are known to be increasing [see *United Nations Environment Program (UNEP)*, 1992]. The CO<sub>2</sub> content is expected to double by the middle of the next century. Methane (CH<sub>4</sub>) and nitrous oxide (N<sub>2</sub>O) have been observed to increase. The chlorine levels in the stratosphere will continue to increase with releases of chlorofluorocarbon compounds. All of these trace gases affect the chemistry of stratospheric ozone. The effect of increasing CO<sub>2</sub> is to lower temperatures in the middle atmosphere, slowing down ozone-removing reactions and resulting in an ozone increase. Increase in chlorine and N<sub>2</sub>O will enhance the chlorine and nitrogen-catalyzed ozone removal cycles.

Assessments of the global impact of these trace gas changes on the ozone layer require models capable of treating chemistry, dynamics, and radiation as well as the interactions between these components. Ultimately, three-dimensional models will have to provide reliable assessment results. At present, only few three-dimensional calculations have been done which include the stratosphere [Rind *et al.*, 1990; Pitari *et al.*, 1992], and even these are not fully consistent and subject to uncertainties due to limitations in our understanding of the effect of small-scale processes on the large-scale circulation and the variability of long waves

in the troposphere and their effect on the stratosphere. In addition, the computer time required by a general circulation model with a stratosphere and chemistry is very large. For these reasons, most assessment calculations are done with simplified, i.e., two-dimensional models (for references, see *World Meteorological Organization (WMO)/NASA* [1986]).

While two-dimensional models have many inherent inconsistencies and uncertainties, we have gained some understanding of their sensitivities [Schneider *et al.*, 1989; Jackman *et al.*, 1989; Schneider and Ko, 1990; Hou *et al.*, 1990]. Simulations of the present-day atmosphere depend strongly on heating rates calculated for the lower stratosphere and the treatment of eddy fluxes. Calculated trace gas perturbations show much smaller variations with model parameters than the basic state as long as ratios of perturbed to unperturbed quantities are considered. Although differences exist in the perturbation assessment results [WMO/NASA, 1986; UNEP, 1992], the broad pattern of the ozone change obtained with different models is fairly uniform.

In this paper we present an estimate of the impact of hypothetical changes in trace gas concentrations on ozone, using an interactive two-dimensional model. The effects of increasing trace gas levels individually as well as several gases simultaneously are discussed. The role of the radiative feedback is analyzed for each scenario. For all cases the relative perturbation of ozone is larger in the southern hemisphere than in the northern hemisphere. This asymmetry is diagnosed to be due to smaller advective and diffusive horizontal equator to pole transport in the southern stratosphere.

A description of the model is given by Ko *et al.* [this issue]. The chemical module is described by Ko *et al.* [1985]

<sup>1</sup>Now at Division of Applied Sciences, Harvard University, Cambridge, Massachusetts.

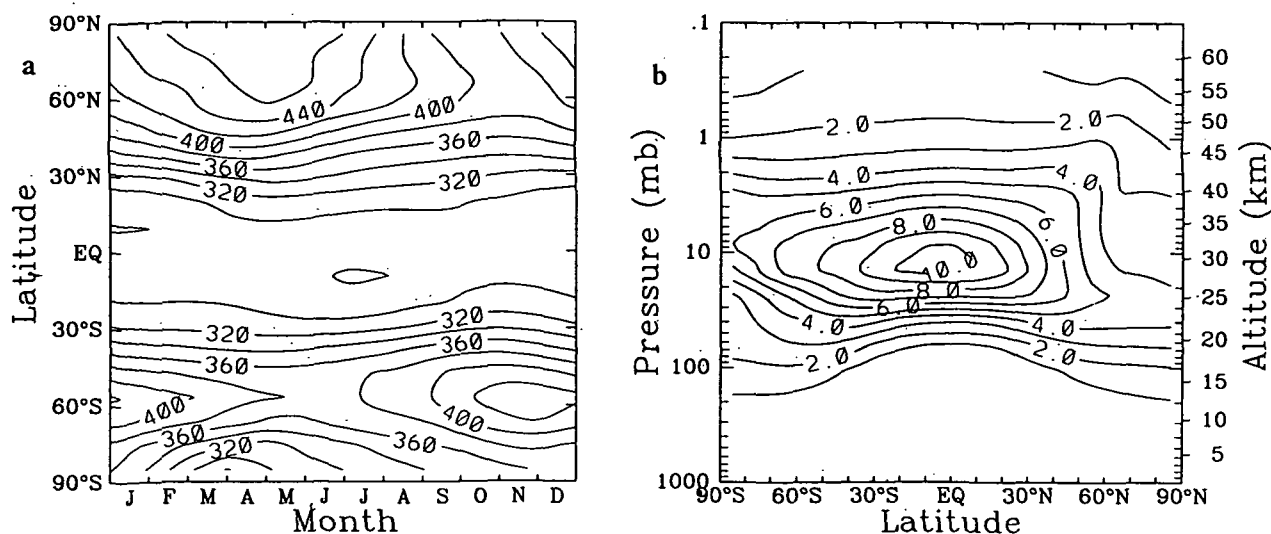


Fig. 1. Calculated baseline ozone distribution for the present-day atmosphere. (a) Column abundances as a function of latitude and time of the year (Dobson units). (b) Ozone mixing ratios for December (parts per million by volume).

and includes the reactions of the  $O_x$ ,  $HO_x$ ,  $Cl_x$ ,  $Br_x$ ,  $NO_x$ , and methyl families. Although heterogeneous reactions [see UNEP, 1992] and seasonal Antarctic ozone variations [Sze *et al.*, 1989; Prather *et al.*, 1990] have been identified as crucial elements in affecting the ozone distribution, they have not been included in the present model calculations. The radiative scheme is a narrow-band transfer model described by Wang and Ryan [1983]. Tropospheric heating rates are parameterized. The dynamical module is based on the primitive equations in two dimensions. Mesospheric drag is represented as a Rayleigh friction, and eddy mixing coefficients are specified externally. The values of the eddy coefficients are obtained through an analytic fit to the seasonally and latitudinally varying mixing coefficients derived by Newman *et al.* [1988]. Eddy mixing coefficients are used consistently in the zonal mean momentum equation and the tracer transport equation.

The model-simulated present-day atmosphere is discussed by Ko *et al.* [this issue]. Most of the perturbation results discussed in the following section will be expressed as percentage deviations from the baseline concentrations. The model generated time-latitude cross section of column ozone for present-day conditions is shown in Figure 1a. Figure 1b shows the ozone mixing ratios for December. The observed north-south asymmetry of column ozone is reproduced quite well by the model.

The perturbation simulations fall into two groups. In the first group, the study is designed to analyze how increase in chlorine affects the ozone chemistry directly and reduces ozone concentrations in the stratosphere and how the reduction in ozone feeds back to the dynamics via changed solar-heating rates. The second group of experiments examines how increases of  $CO_2$  lead to enhanced thermal cooling of the stratosphere and temperature decreases which then affect the ozone chemistry leading to an ozone increase. The model response to separate increases of CFCs and  $CO_2$  will be discussed in sections 2 and 3, respectively. Compensating effects for combined increases of CFCs,  $N_2O$ , and  $CH_4$  are described in section 4 as well as results of for the simultaneous increase of CFCs,  $N_2O$ ,  $CH_4$ , and  $CO_2$ . Conclusions are summarized in section 5.

## 2. RESPONSE TO CHLOROFLUOROCARBONS (CFC) INCREASES

In this section, the results of increasing CFCs only are discussed. The lower boundary mixing ratios specified for CFC 11 and CFC 12 for this model run are given in Table 1. These values are based on assuming continued emission at the present level until the middle of next century and correspond to a  $Cl_y$  increase in the upper stratosphere from 2.4 to 8.0 ppb. This scenario is not the most realistic one, considering current agreements; however, it serves as a benchmark for comparison with other predictions.

Using the boundary conditions given in Table 1, we calculate the stream function ( $\Psi_0$ ), temperature ( $T_0$ ), and ozone ( $O_3$  [2.4 ppb  $Cl$ ,  $\Psi_0$ ,  $T_0$ ]) for the present-day atmosphere. We then change the boundary conditions for CFC 11 and CFC 12 to simulate the perturbed atmosphere calculating a stream function ( $\Psi_1$ ), temperature ( $T_1$ ), and ozone ( $O_3$  [8.0 ppb  $Cl$ ,  $\Psi_1$ ,  $T_1$ ]). In simulating the perturbed atmosphere, we ignore the direct effect of the CFC increase on surface warming and cooling of the stratosphere. The model cannot calculate the surface warming since the tropospheric heating rate is parameterized. The direct effect of the CFC increase on stratospheric temperature has been shown to be small [Wang *et al.*, 1991].

The model-calculated ozone depletion for this scenario is shown in Figure 2. Figure 2a shows the calculated column differences with respect to the baseline; Figure 2b shows the differences in local concentration obtained for December.

TABLE 1. Boundary Conditions for Model Simulations

	I Present Day "1980"	II Perturbed
$N_2O$	300 ppb	360 ppb
$CH_4$	1.6 ppm	3.2 ppm
$CFCl_3$ (CFC 11)	170 ppt	800 ppt
$CF_2Cl_2$ (CFC 12)	285 ppt	2200 ppt
$CH_3Cl$	700 ppt	unchanged
$CH_3CCl_3$	100 ppt	unchanged
$CCl_4$	100 ppt	unchanged

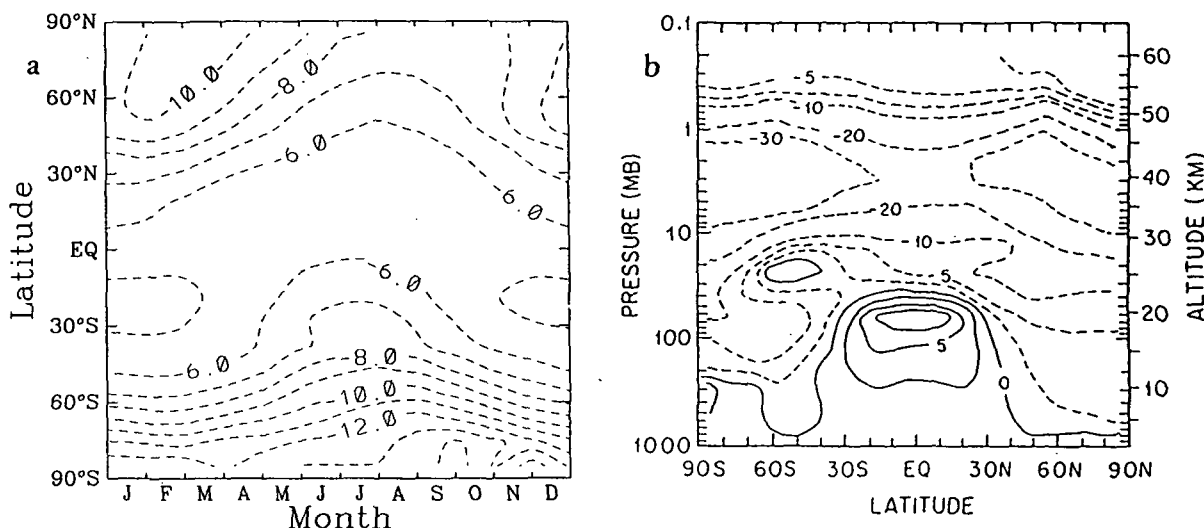


Fig. 2. Calculated ozone depletion for the chlorofluorocarbon (CFC) increase scenario. Values shown are percent differences with respect to the ozone distributions shown in Figure 1. (a) Column differences and (b) mixing ratio differences for December.

The largest ozone decreases are obtained at high altitudes. A self-healing due to increases of UV penetration of more than 10% can be observed in the tropical lower stratosphere. In middle and high latitudes, ozone losses below 30 km are generally smaller than 10%. The largest ozone loss occurs during the spring maxima in each hemisphere. The calculated reduction in annual mean global total ozone for this scenario is 4.5%.

The calculated relative decrease of ozone in the southern hemisphere is larger than in the northern hemisphere. Hemispheric asymmetries are introduced in the model by slightly different tropospheric heating rates in the two hemispheres (an adjusted *Cunnold* [1975] parameterization has been used) and through north-south asymmetries in the eddy diffusion coefficients. A similar asymmetry of the ozone perturbation was noted by *Schneider and Ko* [1990]. The circulation in a two-dimensional model is determined by upper level momentum dissipation, potential vorticity transport by large-scale eddies in the stratosphere, and by the lower boundary specification, i.e., the parameterization of the model troposphere [*Hou et al.*, 1990]. Small eddy mixing, i.e., small meridional coupling in the stratosphere means that the circulation is mainly forced above and below, extending through the stratosphere by continuity. Therefore the vertical mass flux,  $\bar{p}w$ , tends to be constant with height in this region and the horizontal velocity,  $v$ , nearly zero. Streamlines are aligned more or less vertically in the stratosphere. In addition, the strength of the circulation in high latitudes is diminished compared to the large eddy diffusion case. Consequently, there is very little horizontal advective transport from the self-healing region to high latitudes. Since the same eddy mixing coefficients appear in the tracer transport equation, diffusive quasi-horizontal transport is reduced also. Compared to the northern hemisphere winter with its large eddy mixing, the high-latitude lower stratosphere and ozone column amounts in the southern hemisphere are controlled to a greater extent by the perturbation at high altitudes where the photochemistry is more effective.

Figures 3a and 3b show the temperature and zonal mean wind changes induced by the ozone decreases in response to

CFC increase. The temperature decreases are largest in the 40- to 50-km altitude region. Smaller changes occur in the lower stratosphere. The zonal mean wind changes are quite small everywhere. This leads us to believe that with the present model configuration, allowing the eddy mixing coefficients to change with the mean winds would not alter the results appreciably. Other models may have different sensitivities in this respect [*Brasseur et al.*, 1990].

The role of the radiative feedback on ozone in these calculations is illustrated in Figures 4 and 5. The model run with increased CFC levels was repeated in off-line mode using the stream function ( $\Psi_0$ ) and temperature ( $T_0$ ) of the present-day atmosphere as input for the chemistry-transport (CT) model. The resulting ozone distribution ( $O_3$ [8 ppb Cl,  $\Psi_0$ ,  $T_0$ ]) is compared to the ozone calculated for the present-day atmosphere ( $O_3$ [2.4 ppb Cl,  $\Psi_0$ ,  $T_0$ ]). Figures 4a and 4b show the percent difference in column and local concentration, respectively. Comparison of Figures 2b and 4b indicate that ignoring the changes in circulation and temperature would overstate the calculated decrease in ozone at 40 km by a factor of 1.25. For the column the effect amounts to roughly a one-tenth correction.

To gain a qualitative understanding of the separate roles of temperature and circulation changes on the ozone perturbation, we performed additional off-line calculations to obtain ( $O_3$ [8 ppb Cl,  $\Psi_0$ ,  $T_1$ ]) and ( $O_3$ [8 ppb Cl,  $\Psi_1$ ,  $T_0$ ]). Figure 5 shows the temperature and circulation effects of the feedback separately. Most of the feedback at high altitudes consists of a local response to the cooler temperatures. At or below the 30-km altitude the ozone perturbation was small to begin with and therefore solar heating changes are very small in this altitude region. The contribution from the circulation change is shown in Figure 5c. Figures 5a and 5c show that the change in temperature and circulation contribute about equal amounts to the adjustment in the column abundance of ozone. The change in the circulation can be understood in terms of the increased heating in the self-healing region, intensifying the circulation in low and midlatitudes [*Schneider and Ko*, 1990].

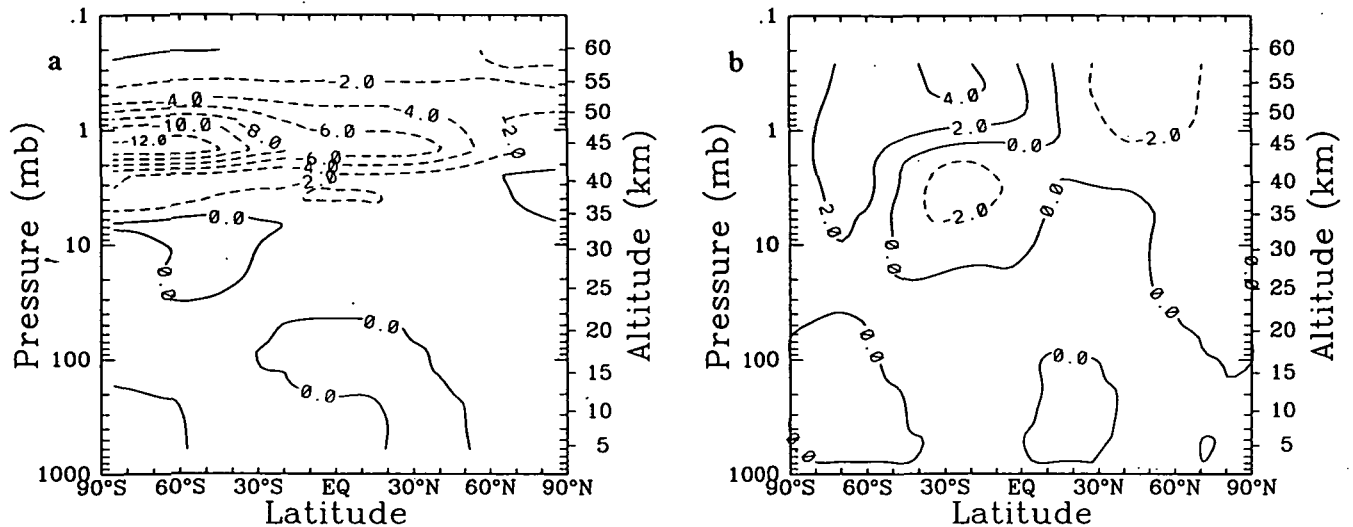


Fig. 3. (a) Temperature difference (degrees) and (b) mean zonal wind difference ( $\text{m s}^{-1}$ ), obtained as a result of increase in CFCs. Values shown are for December.

### 3. RESPONSE TO $\text{CO}_2$ DOUBLING

In the  $\text{CO}_2$  doubling experiment, the effect of increased  $\text{CO}_2$  concentration is explicitly taken into account in calculating the local heating rate above 12 km. Surface warming cannot be calculated consistently in our model because tropospheric heating rates are parameterized using *Cunnold et al.*'s [1975] method. Heating rates above 12 km are influenced by the model tropospheric temperatures as the radiative transfer equation is solved from the ground up. The amount of the tropospheric warming and the latitudinal structure of the warming have to be estimated from three-dimensional climate model runs. There is, at present, no firm agreement about the magnitude or the structure of the temperature increase (see the discussion by *Rind et al.* [1990]). For our double  $\text{CO}_2$  runs we have adjusted the tropospheric heating rates to give  $4^\circ$  to  $5^\circ$  higher temperatures near the surface. The assigned warming decreases with

altitude to zero near the tropopause. We made several runs, specifying tropospheric temperature increases with and without latitudinal gradients. The calculated changes in the stratosphere were not very sensitive to the temperature changes imposed on the model tropopause.

Temperature changes throughout the model domain resulting from doubling  $\text{CO}_2$  are shown in Figure 6. The stratospheric temperature reductions obtained within the two-dimensional model are more or less uniform with latitude. This result is different from the Goddard Institute for Space Studies (GISS) model [*Rind et al.*, 1990], where a temperature increase in the northern hemisphere winter stratosphere was calculated. The feature is attributed to changes in wave propagation. In our two-dimensional model, which includes only a radiative feedback and no information about changes in wave propagation, the differential heating in the stratosphere and, consequently, the

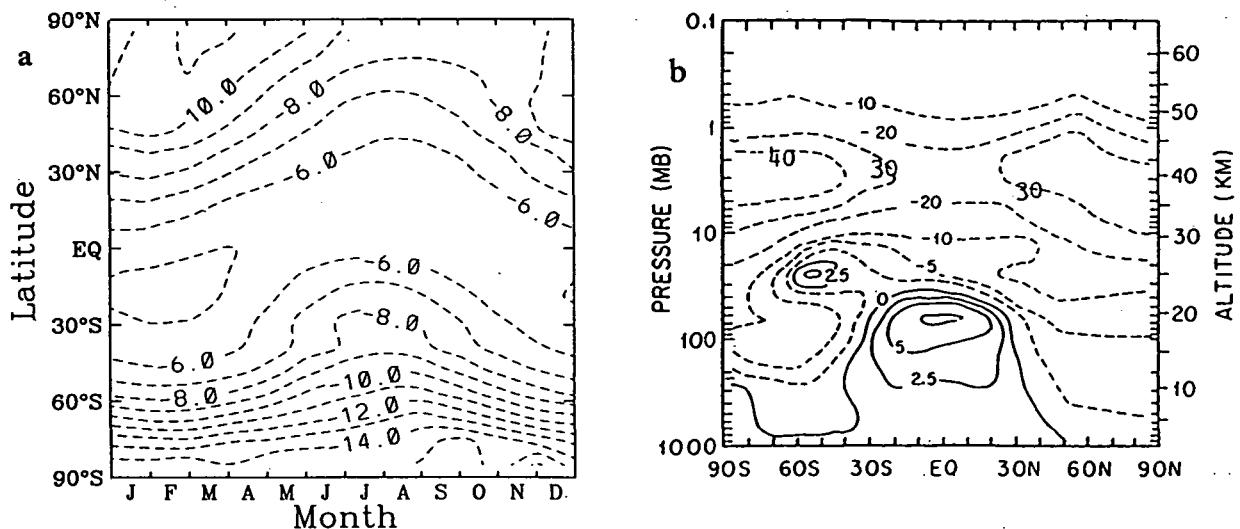


Fig. 4. Ozone reduction (percent with respect to baseline) due to CFC increase obtained in an off-line calculation using the baseline temperature and stream function ( $T_0$ ,  $\Psi_0$ ). (a) Percent change in column abundance. (b) Percent change in local concentration for December.

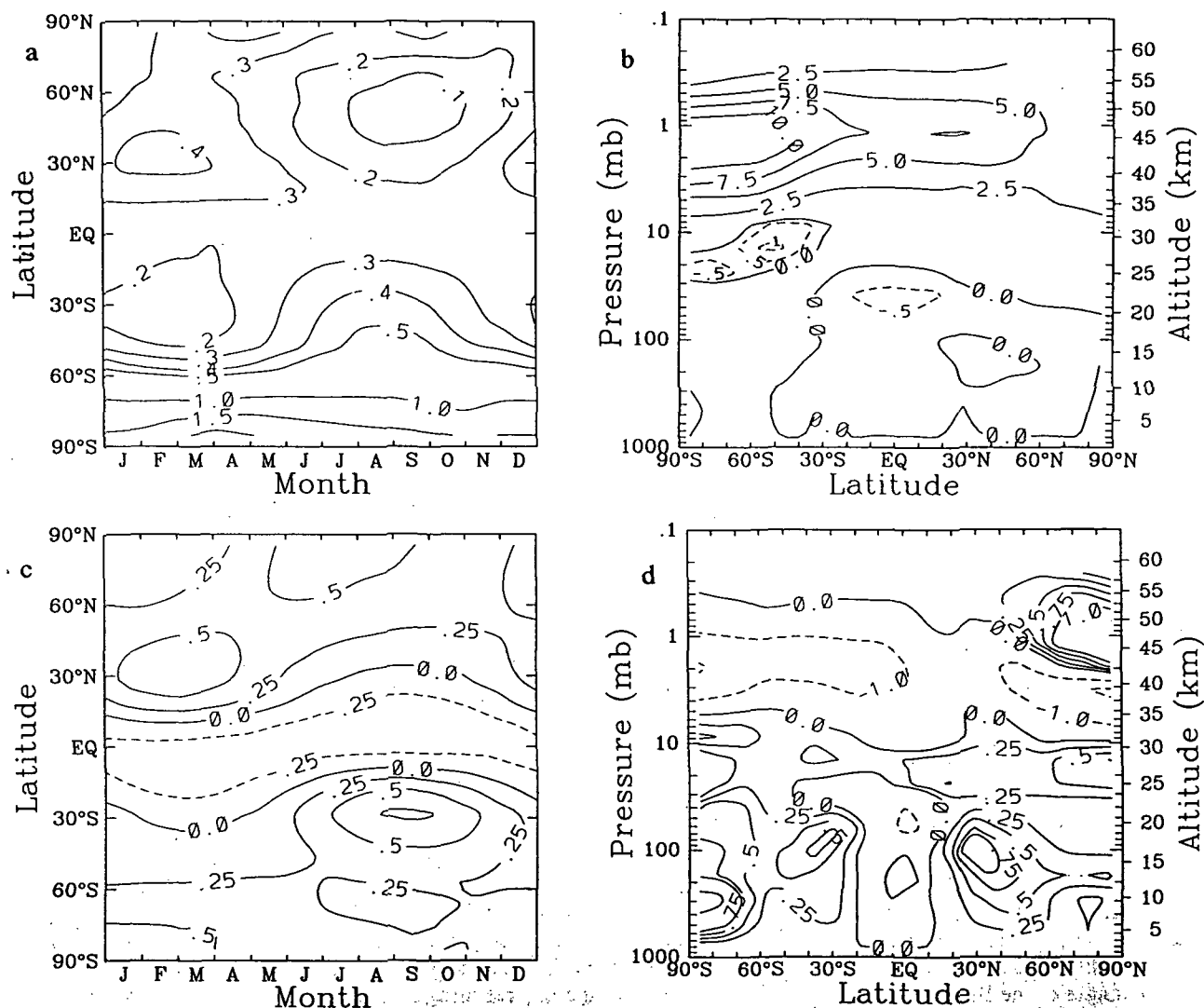


Fig. 5. Effect of temperature and circulation feedbacks on ozone. (a) and (b) Calculated percent changes in column abundance and local concentration of ozone for  $\{O_3[8.0 \text{ ppb Cl}, \Psi_0, T_1] - O_3[8.0 \text{ ppb Cl}, \Psi_0, T_0]\}$ . (c) and (d) Percent changes corresponding to  $\{O_3[8.0 \text{ ppb Cl}, \Psi_1, T_1] - O_3[8.0 \text{ ppb Cl}, \Psi_0, T_1]\}$ .

adiabatic circulation undergo only small changes, as discussed below.

Ozone chemistry responds to cooler temperatures by slowed down reaction rates for some of the removal cycles, thereby giving rise to higher ozone concentrations. The percentage change of the column amount relative to the baseline is shown in Figure 7a. The overall gain in global annual mean ozone is 3.1%. Figure 7b show the local ozone changes for December. A 10 to 15% increase can be seen in the upper stratosphere and a reverse self-healing effect of up to 3% in the tropical lower stratosphere. As in the CFC increase scenario, the ozone response in the southern hemisphere middle and high latitudes is larger than in the northern hemisphere due to less intense equator to pole transport at lower levels.

The calculated ozone increase in the stratosphere results in temperatures around 50 km that are about 3°C warmer than they would be if ozone were kept fixed. Figure 8 shows the calculated temperature difference for January with respect to the present-day atmosphere when ozone is held fixed at present-day levels.

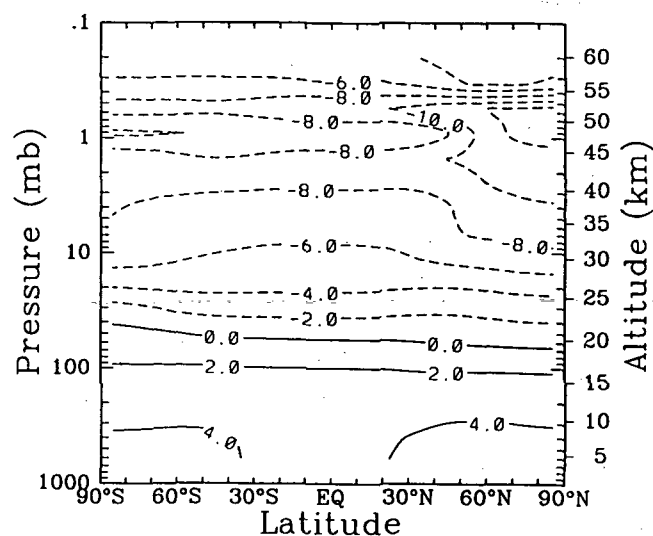


Fig. 6. Temperature difference calculated as a result of doubling CO<sub>2</sub> for December.

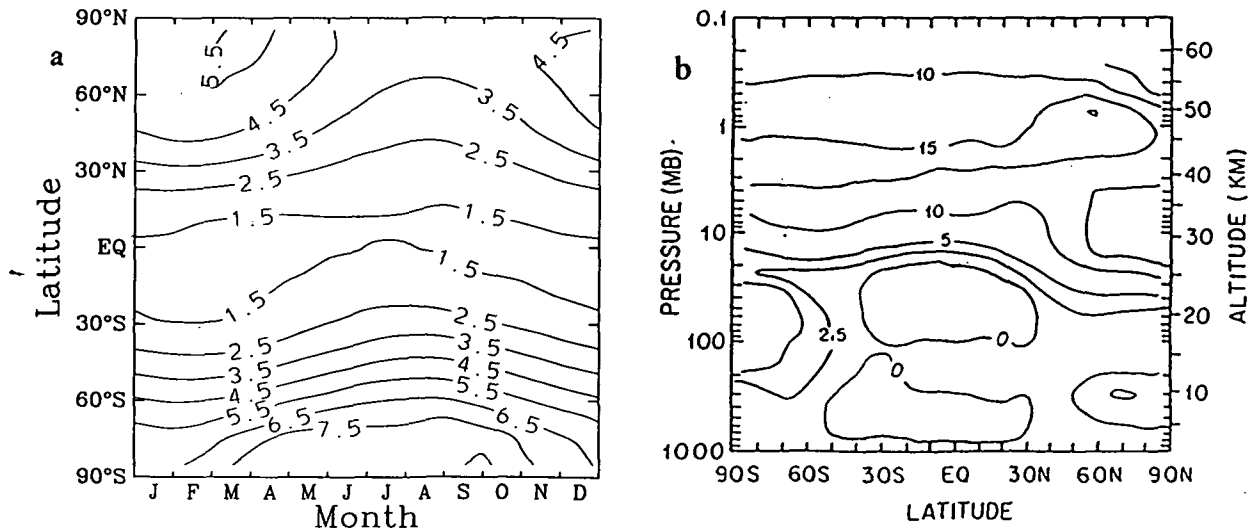


Fig. 7. Ozone change (percent with respect to baseline) obtained in the double  $\text{CO}_2$  scenario. (a) Column differences and (b) mixing ratio differences for December.

The ozone changes obtained in the model run are caused almost entirely by the cooler temperatures. Changes of the transport circulation are very small and are responsible for less than one tenth of the calculated ozone perturbations. Figure 9a shows the differences of the net radiative heating between the baseline and the double  $\text{CO}_2$  case for December. Significant differences occur only above 50-km height. Even with the differential heating being nearly the same in the stratosphere, the strength of the diabatic circulation could be altered if the static stability changed for the perturbed scenario. However, even though the temperature decreases in the stratosphere, as shown in Figure 7, are substantial, their vertical structure is such that the static stability undergoes only small changes. The percentage changes of the Brunt-Vaisala frequency are shown in Figure 9b and are of the order of 5% throughout most of the stratosphere. Contrary to the results obtained in the GISS model, the diabatic circulation calculated in our two-dimensional model decreases slightly for the double  $\text{CO}_2$

scenario. In the GISS model, changes in the structure of planetary wave 1 were responsible for an intensification of the diabatic circulation. Such effects cannot be obtained in a two-dimensional model with parameterized troposphere.

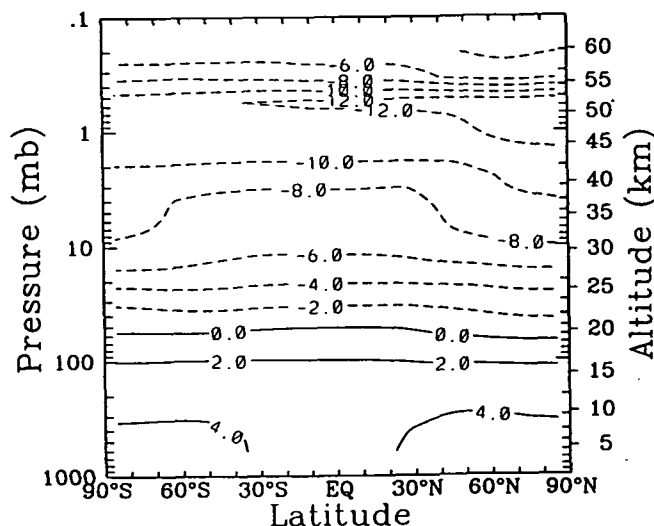
#### 4. COMBINED PERTURBATIONS AND THE GLOBAL IMPACT OF THE TRACE GAS CHANGES

The cases discussed up to now served to illustrate the response of the model to perturbations caused by increased ozone loss frequencies and by changes of the radiative heating, respectively. In the real atmosphere, increases of  $\text{CO}_2$  and CFCs as well as  $\text{CH}_4$  and  $\text{N}_2\text{O}$  are expected to occur over the same time period. Ozone perturbations resulting from the simultaneous increase of several gases are not linear superpositions of the individual cases because of the coupling of the  $\text{Cl}_x$  and  $\text{NO}_x$  cycles. In these calculations the direct radiative effects of increases in  $\text{CH}_4$  and  $\text{N}_2\text{O}$  are not included.

First, we consider the case where  $\text{N}_2\text{O}$  and methane increase in addition to the chlorofluorocarbons. The CFC increases are the same as assumed in section 2 and as summarized in Table 1. The changes for the  $\text{N}_2\text{O}$  and methane lower boundary conditions are also listed in Table 1.

The calculated change in ozone for this scenario is shown in Figures 10a and 10b for the ozone column and ozone mixing ratios for December, respectively. The calculated change in the lower stratosphere is smaller than in the CFC only case and the losses in total ozone are reduced substantially compared to Figure 3. Increases in  $\text{CH}_4$  lead to ozone increases in the troposphere due to smog reactions and also reduce the effect of chlorine increase in the stratosphere.

When  $\text{CO}_2$  is increased in addition to the other trace gases, further compensation of the losses stemming from the CFC increase can be expected as the  $\text{CO}_2$ -induced cooling of the stratosphere slows down ozone removal processes. The ozone perturbation calculated for increasing  $\text{CO}_2$  together with the other gases is shown in Figures 11a and 11b. Ozone losses at high altitudes are reduced substantially, as compared to the CFC only increase, and there are somewhat



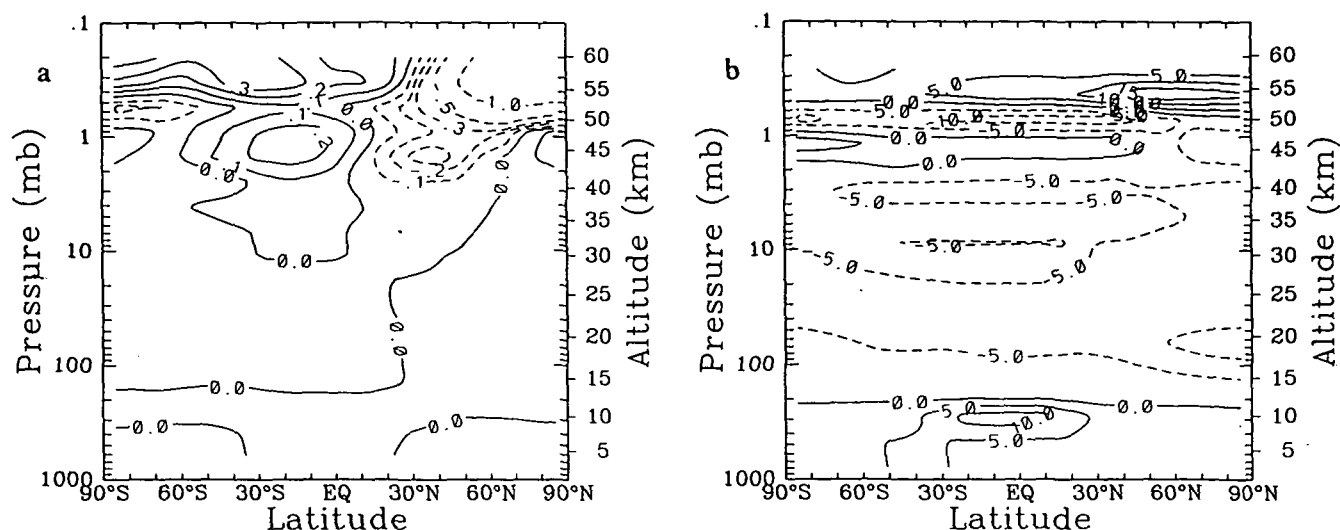


Fig. 9. (a) Net radiative heating difference for the double  $\text{CO}_2$  case. (b) Change (percent) in the Brunt-Vaisala frequency  $\nu_2$ . Values shown are for December.

larger gains in the lower stratosphere as a result of the temperature decreases. Column changes (Figure 11a) range from a net loss of about 1% at the equator to about 3% at the poles in late winter. A globally averaged net ozone loss of 1.3% was calculated.

Figure 12 shows the temperature changes calculated by the model for this case. The stratosphere temperatures decrease substantially as there is no ozone increase to partially compensate the enhanced thermal cooling. As in the individual perturbations, the role of stream function changes turns out to be minor.

### 5. SUMMARY AND CONCLUSIONS

The impacts of increasing  $\text{CO}_2$ , chlorine, and other tracer gases on stratospheric ozone have been investigated, using an interactive two-dimensional model with gas phase chemistry. All ozone perturbations, calculated with the model, exhibit an asymmetry between the northern and the southern

hemispheres. The magnitude of the perturbations is always larger in the southern hemisphere middle and high latitudes. Due to the larger eddy mixing and the larger horizontal advection in the northern hemisphere, quasi-horizontal transport between the equatorial self-healing (or reverse self-healing) region and the high latitudes is more effective, reducing the perturbation in polar regions. In contrast, the response of ozone in the southern high-latitude stratosphere is determined more by downward transport from higher altitudes.

The radiative feedback effect and the role of temperature and circulation changes for the perturbed scenarios were investigated for all cases. In the upper stratosphere, excluding the radiative feedback would lead to 25% larger predicted local ozone losses. In the middle and lower stratosphere the feedback effects are much smaller. The compensation for the calculated reduction in ozone column amounts to a 10% correction of the losses calculated. The reason for this is that

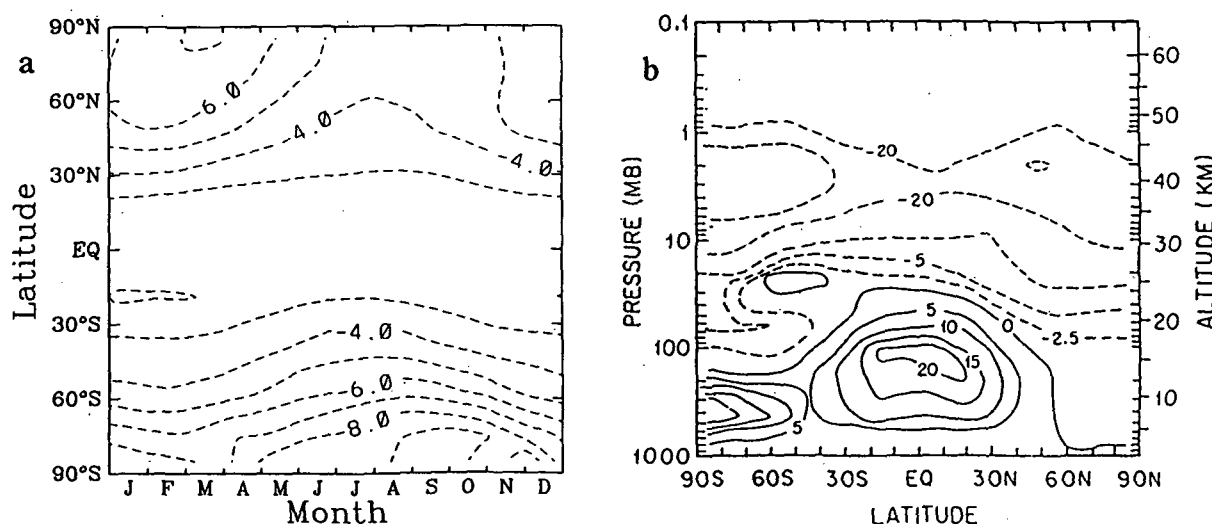


Fig. 10. Calculated ozone losses (percent with respect to baseline) for simultaneous increase of CFCs,  $\text{N}_2\text{O}$ , and methane. (a) Column amount changes and (b) mixing ratio differences for December.





- a two-dimensional model due to dynamical inputs, *J. Geophys. Res.*, **94**, 9873–9887, 1989.
- Ko, M. K. W., D. K. Weisenstein, N. D. Sze, and K. K. Tung, Simulation of  $O_3$  distribution using a two-dimensional zonal-mean model in isentropic coordinate, in *Atmospheric Ozone*, edited by C. S. Zerefos and A. Ghazi, pp. 19–23, D. Reidel, Norwell, Mass., 1985.
- Ko, M. K. W., H. R. Schneider, R.-L. Shia, D. K. Weisenstein, and N.-D. Sze, A two-dimensional model with coupled dynamics, radiation, and photochemistry, I, Simulation of the middle atmosphere, *J. Geophys. Res.*, this issue.
- Newman, P. A., M. R. Schoeberl, R. A. Plumb, and J. E. Rosenfield, Mixing rates calculated from potential vorticity, *J. Geophys. Res.*, **93**, 5221–5240, 1988.
- Pitari, G., S. Palermi, G. Visconti, and R. G. Prinn, Ozone response to a  $CO_2$  doubling: Results from a stratospheric circulation model with heterogeneous chemistry, *J. Geophys. Res.*, **97**, 5953–5962, 1992.
- Prather, M., M. M. Garcia, R. Suozzo, and D. Rind, Global impact of the Antarctic ozone hole: Dynamical dilution with a three-dimensional chemical transport model, *J. Geophys. Res.*, **95**, 3449–3471, 1990.
- Ramaswamy, V., M. D. Schwarzkopf, and K. P. Shine, Radiative forcing of climate from halocarbon-induced global stratospheric ozone loss, *Nature*, **355**, 810–812, 1992.
- Rind, D., R. Suozzo, N. K. Balachandran, and M. J. Prather, Climate change in the middle atmosphere, I, The doubled  $CO_2$  climate, *J. Atmos. Sci.*, **47**, 475–494, 1990.
- Schneider, H. R., and M. K. W. Ko, Response of an interactive two-dimensional model to ozone changes: An estimate of the radiative dynamical feedback effect, *J. Geophys. Res.*, **95**, 5657–5668, 1990.
- Schneider, H. R., M. K. W. Ko, N. D. Sze, G.-Y. Shi, and W.-C. Wang, An evaluation of the role of eddy diffusion in stratospheric interactive two-dimensional models, *J. Atmos. Sci.*, **46**, 2079–2093, 1989.
- Sze, N. D., M. K. W. Ko, D. K. Weisenstein, J. M. Rodriguez, R. S. Stolarski, and M. R. Schoeberl, Antarctic ozone hole: Possible implications for ozone trends in the southern hemisphere, *J. Geophys. Res.*, **94**, 11,521–11,528, 1989.
- United Nations Environment Program, Scientific assessment of ozone depletion: 1991, *WMO Rep. 25*, World Meteorol. Organ., Global Ozone Res. and Monit. Proj., Geneva, 1992.
- Wang, W.-C., and P. B. Ryan, Overlapping effect of atmospheric  $H_2O$ ,  $CO_2$ , and  $O_3$  on the  $CO_2$  radiative effect, *Tellus, Ser. B*, **35**, 81–91, 1983.
- Wang, W.-C., M. P. Dudek, X.-Z. Liang, and J. T. Kiehl, Inadequacy of effective  $CO_2$  as a proxy in simulating the greenhouse effect of other radiatively active gases, *Nature*, **350**, 573–577, 1991.
- World Meteorological Organization (WMO)/NASA, Atmospheric ozone 1985, *WMO Rep. 16*, Global Ozone Res. and Monit. Proj., Geneva, 1986.
- M. K. W. Ko, R.-L. Shia, and N.-D. Sze, Atmospheric and Environmental Research, Inc., 840 Memorial Drive, Cambridge, MA 02139.
- H. R. Schneider, Division of Applied Sciences, Pierce Hall, Harvard University, Cambridge, MA 02138.

(Received January 22, 1993;  
revised July 9, 1993;  
accepted July 9, 1993.)

## **Appendix F**

### **A Three-Wave Atmospheric Model With Coupled Dynamics, Radiation and Photochemistry**

by

Run-Lie Shia, Shuntai Zhou, Malcolm K. W. Ko, Nien-Dak Sze,  
David Salstain and Karen Cady-Pereira

Atmospheric and Environmental Research, Inc.

December 1995

## Abstract

A semi-spectral dynamical model coupled with a zonal mean chemistry transport model is used to simulate the present day atmosphere. With dynamical eddies explicitly calculated, this model is particularly useful for testing eddy parameterization used in zonally mean chemistry transport models. Starting from a linear wave equation, the eddy diffusion coefficients for chemical tracers are calculated from amplitude, frequency and growth rate of dynamical waves and local loss rate of the tracer. Both the contributions to eddy flux from transience of waves (transient eddy) and chemical reactions (chemical eddy) are included in the eddy diffusion coefficients. In spite of the high truncation in the dynamical module (only three longest waves are resolved), the model has simulated many observed characteristics of stratospheric dynamics and distribution of chemical species including ozone. Compared with commonly used parameterized values, the eddy diffusion coefficients for chemical species calculated in the model are smaller. It is found that the chemical eddy diffusion is not essential in determining the tracer distribution in the stratosphere.

## 1. Introduction

Two-dimensional (zonal mean) chemistry transport models (2-D CTM) have played an important role in understanding various physical and chemical processes which control the distributions of chemical constituents in the atmosphere. A comprehensive three-dimensional model probably is too computationally intensive to run for long term simulation of the atmosphere at least in the near future. In addition, two-dimensional models can be very helpful in interpreting the enormous output from three-dimensional model. Therefore, the continuing improvements of two-dimensional models are worthwhile.

A highly truncated semi-spectral dynamical model coupled with a two-dimensional photochemical transport model provides several important improvements with small increase of computing time. First, it calculates eddy terms in the zonal mean momentum and thermodynamical equations, instead of using parameterization for E-P flux divergence and eddy heat transport. Also, it includes wave-mean and wave-wave interactions so the feedback effects through these interactions can be included in the model. Second, with the dynamical waves explicitly calculated, the eddy flux of chemical tracer in two-dimensional chemistry transport module can be calculated directly.

A long standing problem of 2-D CTM is the parameterization of eddy transport. While it is commonly accepted that in the global scale the eddy transport in the middle atmosphere is mainly due to organized planetary waves, rather than chaotic or turbulence mixing, there are still controversies about how to parameterize the eddy fluxes in literature. A series of efforts to understand the mechanism of eddy transport and to derive the mixing coefficients began with Reed and German (1965). However due to an oversimplified assumption about trajectory of air parcel, their results are challenged later on. Matsuno (1980) showed that the trajectory of an air parcel driven by a steady planetary wave is elliptic when projected onto the meridional plane, and, therefore, there is no eddy transport in the presence of steady waves. Plumb (1979) and Pyle and Rogers (1980) reached the same conclusion using the linear eddy equation derived from tracer continuity equation. Their results actually were the manifestation in the Eulerian framework of the earlier study by Andrew and McIntyre (1978), which used the generalized Lagrangian mean formulation.

From the wave correlation point of view (or Eulerian point of view), when the wave is steady, eddy velocity and eddy tracer distribution are orthogonal, i. e. the zonal-mean of the product is zero. Therefore, there is no net eddy flux. When the wave amplitude changes with time or the tracer concentration changes through chemical reactions, the phase relation between the eddy velocity and the eddy tracer distribution changes and the net eddy flux is generated. Thus the eddy flux is connected to the wave transience (transient eddy) and/or chemical reactions (chemical eddy). The formulations following this direction have met with some conceptual and practical difficulties. It is easy to show that growing waves generate down-gradient eddy flux and, therefore, are diffusive. At the same time, the decaying waves produce up-gradient eddy flux and are difficult to interpret. Formally, the total contribution from both growing and decaying waves should compensate each other. But diagnostic calculations using observed wind and ozone suggest that the eddy transport is diffusive most of the time.

A popular parameterization scheme uses the flux-gradient relation of potential vorticity (PV) to derive the eddy diffusion coefficient either from observations or from model calculated PV distribution (Tung, 1987; Hitchman and Brasseur, 1988; Newman et al., 1988; Yang et al., 1991; Garcia et al., 1992, and Garcia and Solomon, 1994). The derived eddy diffusion coefficient for PV is then used for all chemical species. This approach is valid only if the following is true: (1) The local dissipation for PV is small so that the derived diffusion coefficient is a true representation of the transient eddy. (2) The chemical eddy terms for other species are small compared with the transient eddy. But when the eddy transport is important, the air motion in the region usually is turbulent and the dissipation of PV can not be neglected. Therefore it is quite possible that the eddy diffusion coefficient derived from PV eddy fluxes overestimates eddy transport for long lived species. Recent observations of some long lived species in the stratosphere (UARS/CLEAR) display large meridional gradients in the zonal mean distribution. This feature is difficult to simulate in two-dimensional models with the eddy diffusion coefficients as large as  $10^6 \text{ m}^2/\text{sec}$ , which is the typical value used in some two-dimensional models for all species. During past several years, using more powerful computer and new numerical techniques, the problem of transport by planetary waves is revisited by following trajectory of large number of air parcels in the stratosphere or using a 'contour advection technique (Schoeberl and Bacmeister, 1993; Bowman, 1993; Waugh and Plumb, 1994; Chen, 1994). While these studies have provided intuitive

pictures of eddy mixing, it is difficult to define directly from their results a eddy parameterization suitable for global two-dimensional models.

In this paper, we present a scheme of calculating the eddy fluxes appeared in the zonal mean tracer transport equation. The approach is based on the linearized eddy tracer continuity equation similar to that used by Pyle and Rogers (1980), Strobel (1981), and Smith and Brasseur (1990). By adding the contribution from small scale mixing and chemical eddy to the transient eddy, the total eddy transport is mainly diffusive (down-gradient).

The paper is organized as follows. In section 2 we give a brief description of the model, with emphasis on the dynamical module. The scheme to calculate eddy diffusion coefficients are formulated in section 3. The model is used to simulate the present day atmosphere and the results for dynamical fields are discussed in section 4. In section 5, the eddy diffusion coefficients and simulated trace gases distribution, such as  $\text{N}_2\text{O}$ ,  $\text{CH}_4$  and  $\text{O}_3$ , are compared with observations and with previous studies. Some discussions are given in last section.

## **2. Model description**

### **2.1 Equations**

The transformed Eulerian mean (TEM) circulation and the formulation in the isentropic coordinates have been extensively used in the dynamical formulation of 2-D models. Both circulations are reduced to the Lagrangian mean motions for small amplitude steady adiabatic waves (Tung, 1984). In these formulations, only a small, mainly diffusive eddy transport is left in addition to advection in the transport equation. The circulations are driven by diabatic heating, dissipation and eddy forcing. The eddy forcing can be approximated by the eddy flux of potential vorticity, which is usually parameterized using flux-gradient relation with the same eddy diffusion coefficient used for chemical species. The three wave model presented in this paper differs from most interactive two-dimensional models in that the eddy terms in the zonal mean momentum equation is not parameterized using PV flux. Instead a highly truncated three-dimensional dynamical model is used to compute explicitly the zonal mean and wave fields, from which the E-P flux divergence can be calculated. In current version of the

model, only three longest planetary waves are included. The interactive coupling is achieved when the model calculated  $O_3$  is used to compute the radiative heating rates. The model data flow chart is shown in Figure 1. Interactions between different processes and feedbacks can be find easily by following arrows in that figure.

The dynamical module is adopted from Schneider and Geller (1984). It is formulated in the primitive equation system and the vertical coordinate is  $z=z_0 \cdot \ln(p_0/p)$ . The zonal mean equations are

$$\partial_t \bar{u} + \bar{v} \left( \partial_y \bar{u} - f - \frac{\bar{u}}{a} \tan \theta \right) + \bar{w} \partial_z \bar{u} = -E_U + D_U - \beta_R \bar{u}, \quad (1)$$

$$\partial_t \bar{v} + \bar{u} \left( f + \frac{\bar{u}}{a} \tan \theta \right) = -\partial_y \bar{\phi} - E_v + D_v - \beta_R \bar{v} \quad (2)$$

$$\partial_t \bar{\phi}_z + \bar{v} \partial_y \bar{\phi}_z + \bar{w} \partial_z \bar{\phi}_z + \bar{w} N^2 = \frac{\kappa}{H} \bar{J} - E_T + D_T \quad (3)$$

$$\frac{1}{\cos \theta} \partial_y (\bar{v} \cos \theta) + \frac{1}{\rho_0} \partial_z (\rho_0 \bar{w}) = 0. \quad (4)$$

Here  $u$ ,  $v$  and  $w$  are the components of the velocity,  $\phi$  is the geopotential,  $\theta$  is the latitude,  $a$  is the radius of the Earth,  $\rho_0$  is the air density,  $f$  is Coriolis parameter,  $N$  is the Brunt-Vaisalla frequency,  $H$  is the scale height,  $k=2/7$ ,  $\beta_R$  is the Rayleigh friction coefficient which is a function of altitude.  $J$  is the radiative heating.  $E_U$ ,  $E_v$  and  $E_T$  are eddy flux divergence,

$$E_u = \frac{1}{\cos \theta} \partial_y (\overline{u'v'} \cos \theta) + \frac{1}{\rho_0} \partial_z (\rho_0 \overline{u'w'}) - \frac{\overline{u'v'}}{a} \tan \theta, \quad (5)$$

$$E_v = \frac{1}{\cos \theta} \partial_y (\overline{v'v'} \cos \theta) + \frac{1}{\rho_0} \partial_z (\rho_0 \overline{v'w'}) - \frac{\overline{u'u'}}{a} \tan \theta, \quad (6)$$

$$E_T = \frac{1}{\cos \theta} \partial_y (\overline{v'\phi'_z} \cos \theta) + \frac{1}{\rho_0} \partial_z (\rho_0 \overline{w'\phi'_z}). \quad (7)$$

The equations for departure from the zonal mean (eddy), denoted by a prime, are

$$\partial_t u' + \bar{u} \partial_x u' + v' \partial_y \bar{u} - f v' - \frac{\bar{u} v' + \bar{v} u'}{a} \tan \theta = -\partial_x \phi' - W_U + D_u' - \beta_R u', \quad (8)$$

$$\partial_t v' + \bar{u} \partial_x v' + v' \partial_y \bar{v} + w' \partial_z \bar{v} + f u' + 2 \frac{\bar{u} u'}{a} \tan \theta = -\partial_y \phi' - W_v + D_v' - \beta_R v', \quad (9)$$

$$\partial_t \phi'_z + \bar{u} \partial_x \phi'_z + v' \partial_y \bar{\phi}_z + w' \partial_z \bar{\phi}_z + w' N^2 = \frac{\kappa}{H} J' - W_T + D_T', \quad (10)$$



$$\partial_x u' + \frac{1}{\cos \theta} \partial_y (v' \cos \theta) + \frac{1}{\rho_0} \partial_z (\rho_0 w') = 0. \quad (11)$$

where  $W_u$ ,  $W_v$  and  $W_T$  are the terms of second order in the eddy equations, which represent the wave-wave interactions.

$$W_u = \partial_x (u'^2) + \frac{1}{\cos \theta} \partial_y ((u'v' - \overline{u'v'}) \cos \theta) + \frac{1}{\rho_0} \partial_z (\rho_0 (u'w' - \overline{u'w'})) - \frac{u'v' - \overline{u'v'}}{a} \tan \theta, \quad (12)$$

$$W_v = \partial_x (u'v') + \frac{1}{\cos \theta} \partial_y ((v'^2 - \overline{v'^2}) \cos \theta) + \frac{1}{\rho_0} \partial_z (\rho_0 (v'w' - \overline{v'w'})) + \frac{u'^2 - \overline{u'^2}}{a} \tan \theta, \quad (13)$$

$$W_T = \partial_x (u'\phi'_z) + \frac{1}{\cos \theta} \partial_y ((v'\phi'_z - \overline{v'\phi'_z}) \cos \theta) + \frac{1}{\rho_0} \partial_z (\rho_0 (w'\phi'_z - \overline{w'\phi'_z})). \quad (14)$$

$D_u$ ,  $D_v$ ,  $D_T$  in equations (1)-(3) and  $D_u'$ ,  $D_v'$ ,  $D_T'$  in equations (8)-(10) represent sub-grid scale diffusion. A biharmonic diffusion is used along the latitude direction with time scale of 14 days for 2  $\Delta y$ -waves and 200 days for 4  $\Delta y$ -waves (Schneider and Geller, 1984). The  $D_u'$ ,  $D_v'$ ,  $D_T'$  in eddy Eqns. (8)-(10) also include linear damping terms which are the parameterization of wave decaying into smaller unresolved waves with the damping time scale of about 60 days.

The radiative heating in the zonal mean thermodynamical equation (3) is calculated using a narrow-band radiative transfer scheme described by Wang and Ryan (1983). In the eddy thermodynamic equation (7), we use a simple Newtonian cooling form to represent  $J'$ , i.e.  $J' = -\alpha T'$ . The Newtonian cooling coefficient  $\alpha(\theta, z)$  is calculated from the zonal mean radiative heating using

$$\alpha(\theta, z) = -\frac{J(\bar{T} + \Delta T, \theta, z) - J(\bar{T}, \theta, z)}{\Delta T},$$

with  $\Delta T$  taken to be 0.5 °K.

In the stratosphere only a few planetary scale waves prevail according to the wave propagating theory (Charney and Drazin, 1961) and observations. Therefore, we only keep three largest zonal waves, i.e. wavenumber 1, 2 and 3, in the spectral form after the Fourier transforms are applied. Thus, we can represent the eddy behavior of  $u, v, w, \phi$  by

$$\psi' = \sum_{m=1}^3 \psi_m(t, y, z) e^{ik_m x},$$

where  $\psi = (u, v, w, \phi)$ , and  $k_m$  is wavenumber. The wave amplitude  $\psi_m$ 's are determined by solving Eqns (8)-(11). It must be pointed out that severely truncated models may result in kinetic energy build-up on the shortest wave (O'Brien and Branscome, 1989; Zhou and Stone, 1993). This does not occur in our three-wave model because the model has relatively fine resolution in the meridional direction (9.5°).

## 2.2 Wave Forcing

The model's vertical resolution in the troposphere is too crude to generate stationary waves via surface topography. We specify the lower boundary condition for wave amplitudes and phases from a set of climatology data. The data are extracted from an archive of monthly mean grid point analyses of meteorological data (See the appendix for details). We only specify the first 3 wave components of the monthly mean geopotential height ( $Z$ ) at the lower boundary of the model. The monthly mean data are interpolated to each time step and at the bottom layer of the model when the wave equations are integrated. Other dynamic variables, such as velocity and temperature, are calculated by the model accordingly. The amplitudes of wave geopotential height at the lower boundary are shown in Figure 2 for January and July respectively. This lower boundary condition is more appropriate than those used in some two-dimensional model with extended three-dimensional dynamics. For instance, Kinnersley and Harwood (1993) used the Montgomery geopotential from the Stratospheric Sounding Unit (SSU) satellite data at the tropopause (350 K isentropic surface) rather than at the model's bottom. The specified wave fields may not be consistent with the tropospheric dynamics in their model.

## 2.3 Trace Gas transport Equation

The zonal mean transport equation for a chemical species is

$$\partial_t \bar{\chi} + \bar{v}^* \partial_y \bar{\chi} + \bar{w}^* \partial_z \bar{\chi} = \bar{S} - \bar{\gamma} \cdot \bar{\chi} - \nabla \cdot \bar{F}, \quad (15)$$

where  $\bar{\chi}$  is the zonal-mean mixing ratio of chemical species,  $\bar{S}$  denotes the zonal-mean production,  $\bar{\gamma} \cdot \bar{\chi}$  is the zonal-mean removal rate and the last term in the R.H.S. of (15) is the contribution of eddy fluxes. Here we have neglected the second-order term  $\overline{\gamma' \cdot \chi'}$ , which is assumed to be smaller than  $\bar{\gamma} \cdot \bar{\chi}$ . A comprehensive heterogeneous photochemistry model is adopted from the AER two-dimensional chemical transport model (Ko et al. 1984, 1985, 1989).  $\bar{v}^*$  and  $\bar{w}^*$  are velocities of the residual mean meridional circulation, defined as

$$\bar{v}^* = \bar{v} - \frac{1}{\rho_0} \partial_z \left( \frac{\rho_0}{N^2} \overline{v' \phi_z'} \right), \quad (16)$$

$$\bar{w}^* = \bar{w} + \frac{1}{\cos \theta} \partial_y \left( \frac{\cos \theta}{N^2} \overline{v' \phi_z'} \right). \quad (17)$$

$\bar{F}$  is the eddy flux, which can be expressed as

$$\bar{F} = -\bar{K} \cdot \nabla \bar{\chi} \quad (18)$$

where  $\bar{K}$  is the tensor of eddy diffusion coefficients. In the stratosphere the eddy transport is due to planetary waves and its contribution to the zonally averaged tracer distribution is the mixing along the isentropic surfaces (e. g. Tong 1985). In next section the expression used to calculate the dominant component of  $\bar{K}$ ,  $K_{yy}$ , is derived. The remaining components of  $\bar{K}$ ,  $K_{yz}$  and  $K_{zz}$ , in the stratosphere are calculated as the projections of  $K_{yy}$  from the isentropic surface back to the pressure coordinates. In addition, a strong vertical diffusion, which is the same as that used in the AER two-dimensional interactive model (Ko et al., 1993), is added to  $K_{zz}$ , in order to simulate the rapid mixing in the troposphere and gravity wave breaking in the mesosphere ( $K_{zz} = 10 \text{ m}^2/\text{s}$  in the troposphere,  $K_{zz} = 0.1 \sim 1 \text{ m}^2/\text{s}$  in the stratosphere, and  $K_{zz} \sim 1 \text{ m}^2/\text{s}$  in the mesosphere). These diffusion coefficients, along with calculated residual mean circulation, are then used in zonal mean chemical transport model to calculate the distribution of the trace gases.

### 3. Eddy diffusion coefficients

The meridional component of eddy flux,  $\overline{v' \cdot \chi'}$ , can be, in principle, calculated using a linearized eddy tracer transport equation,

$$\partial_t \chi' + \bar{u} \partial_x \chi' + v' \partial_y \bar{\chi} = -\bar{\gamma} \chi'. \quad (19)$$

We have dropped  $\gamma' \cdot \bar{\chi}$  term from Eqn. (19) to simplify the mathematical manipulations.  $\gamma'$  is related to the temperature eddy and eddy mixing ratio of other species which are photochemically related with the tracer being studied. Including  $\gamma' \cdot \bar{\chi}$  in the Eqn. (19) would couple eddy transport equations for all species.

In current version of the model, the eddy mixing ratios  $\chi'$  are not explicitly calculated in the model by solving Eqn. (19). Instead, the contribution of asymmetric distribution of tracer to the zonally mean distribution,  $\overline{v' \cdot \chi'}$ , is expressed as a diffusion flux with eddy diffusion coefficients derived based on the eddy transport equation (19).

All eddy fields, the deviation from the mean, including  $\chi'$  and  $v'$  in Eqn. (19), can be expressed as

$$f = \text{Re} \left( \sum_{m=1}^{\infty} f_m(t) e^{im\lambda} \right), \quad (20)$$

using the Fourier transforms, where  $\lambda$  is the longitude. The Fourier coefficients,  $f_m(t)$ , vary with time and also are the function of the latitude and the altitude. The zonal mean of the product of two eddy fields is

$$\overline{f' \cdot g'} = \frac{1}{2} \text{Re} \left( \sum_{m=1}^{\infty} f_m^*(t) \cdot g_m(t) \right), \quad (21)$$

where  $f_m^*(t)$  is the complex conjugate of  $f_m(t)$ .

In order to find the eddy fluxes generated by waves, we assume that the tracer waves with the wave number  $m$  have the same frequency,  $\omega_m$ , and the same decaying rate,  $\alpha_m$ , as the waves in the meridional velocity, i. e.

$$f_m(t) = f_m e^{-\alpha_m t} e^{-i\omega_m t}, \quad \text{for } \chi_m, v_m, \quad (22)$$

where  $f_m$ ,  $\alpha_m$ , and  $\omega_m$  are functions of latitude and altitude only. In equation (22),  $\alpha_m$  is negative for a growing wave and is positive for a decaying wave. Expression (22) is a reasonable assumption in the stratosphere where only few waves are responsible for the zonally asymmetric motion. For the dynamical variables, they are related through the dynamical equations to form the planetary waves and should have the similar temporal variation. For the tracer density waves, their amplitude should follow the amplitude of the planetary waves if the planetary waves are the main source of the zonal asymmetry. Substituting Eqns. (20) and (22) for  $\chi'$ , the wave equation (19) takes the form as follows

$$(-i\omega_m + ik_m \bar{u} - \alpha_m) \cdot \chi_m + v_m \cdot \bar{\chi}_y = -\bar{\gamma} \cdot \chi_m \quad (23)$$

where  $k_m = \frac{m}{a \cdot \cos \theta}$ , and  $a$  is the radius of the earth. Equation (23) implies

$$\chi_m = \frac{-v_m \cdot \bar{\chi}_y}{(-i\omega_m + ik_m \bar{u} - \alpha_m + \bar{\gamma})} \quad (24)$$

and the eddy flux of tracer is

$$\overline{v' \cdot \chi'} = \sum_{m=1}^{\infty} \left( \frac{(\alpha_m - \bar{\gamma}) \overline{v_m \cdot v_m} \cdot \bar{\chi}_y}{(\omega_m - k_m \bar{u})^2 + (\alpha_m - \bar{\gamma})^2} \right) = -K_{yy}^n \cdot \bar{\chi}_y - K_{yy}^{ch} \bar{\chi}_y = K_{yy}^{tot} \bar{\chi}_y \quad (25)$$

where the following identification can be made.

$$K_{yy}^n = \sum_{m=1}^{\infty} \left( \frac{-\alpha_m \cdot \overline{v_m \cdot v_m}}{(\omega_m - k_m \bar{u})^2 + (\alpha_m - \bar{\gamma})^2} \right), \quad (26)$$

$$K_{yy}^{ch} = \sum_{m=1}^{\infty} \left( \frac{\bar{\gamma} \cdot \overline{v_m \cdot v_m}}{(\omega_m - k_m \bar{u})^2 + (\alpha_m - \bar{\gamma})^2} \right), \quad (27)$$

$$K_{yy}^{tot} \equiv K_{yy}^n + K_{yy}^{ch}. \quad (28)$$

The  $K_{yy}^*$  defined in Eqn. (26) is the transient eddy coefficients. It is approximately proportional to the growing rate of the wave,  $-\alpha_m$ , which is species independent, and represents the mixing of inert gas by transient waves. This is consistent with the conclusion in Plumb (1979) and Pyle and Rogers (1980), that the steady waves, ( $\alpha_m = 0$ , in our case) do not transport chemically inactive tracer, only transient waves do. When a wave is growing ( $\alpha_m < 0$ ), it brings air parcels with higher (lower) mixing ratio into regions with lower (higher) mixing ratio (Leovy et al., 1985). This is so called down-gradient transport and for this period,  $K_{yy}^*$  is greater than zero. After the wave reaches its peak, it decays ( $\alpha_m > 0$ ) and returns these parcels back to their original position. For this period  $K_{yy}^*$  is less than zero and this is so called up-gradient transport. If there is no small scale mixing, there would be no net exchange. It is quite obvious, therefore, that the up-gradient transport just compensate the precedent down-gradient transport in the cycle. However, usually the transient planetary waves are accompanied by small scale eddies and turbulences. In this case the air parcels moved by the planetary waves irreversibly mixed with local air and the compensation in the decaying phase is not as effective as in pure large scale waves case. It results in a net down-gradient eddy flux. It is very difficult to calculate the contribution of small scale eddies and turbulences accurately. Since their effects are limiting the up-gradient transport, in current version of the model a lower limit for total eddy diffusion coefficient is set ( $K_{yy}^{tot} \geq 0$ ) to eliminate the contribution of up-gradient transport.

The  $K_{yy}^{ch}$  defined in Eqn. (27) is the chemical eddy diffusion coefficient, which is approximately proportional to the zonally mean local loss rate of the tracer,  $\bar{\gamma}$ , so is species-dependent and always positive. From Eqns. (27) and (28), it is apparent that even the steady waves ( $\alpha_m = 0$ ) can generate eddy flux for chemically active tracers.

All variables needed for calculating eddy diffusion coefficients from Eqn. (26) and (27) are available in the model except  $\omega_m$  and  $-\alpha_m$ , the frequency and the growing rate of waves. We use the following relation :

$$\left( \frac{d}{dt} v_m(t) \right) / v_m(t) = -\alpha_m - i\omega_m, \quad (29)$$

and model calculated  $v_m(t)$  to find  $-\alpha_m$  and  $\omega_m$ . In the stratosphere, the typical time scale is days for  $\omega_m$  and several weeks for  $-\alpha_m$ , the time scale for wave growing or decaying.

The diffusion coefficient,  $K_{yy}^{ch}$  and  $K_{yy}^*$  are calculated every time step using Eqns. (26), (27), and (29). The mean values of the eddy diffusion coefficients over 10 days period are used in the transport equation for trace gases.

## 4. Model results

### 4.1 Dynamical Variables

The calculated zonally averaged global distributions for zonal wind and temperature for January and July are shown in Figure 3. The magnitudes and locations of the polar jets in the winter hemisphere are in good agreement with observations (e. g., Barnett and Corney, 1985). The seasonal changes of subtropical jets are also well simulated. However the upper easterly in the summer hemisphere are weaker than observations.

The eddy geopotential height from model resolved three longest waves at 50 mb for January and July is shown in Figure 4, along with its counterpart from CDDB observation data. The latitude-height section of wave amplitude of wave 1, 2 and 3 both from model results and from CDDB data for January and July are plotted in Figure 5. In general, the model simulates eddy states well except that the amplitudes in some place are weaker than the observations. Since the stratospheric waves are propagated from the troposphere, the very strong hemispheric asymmetry of eddy activity is attributed to the specified lower boundary conditions. For the CDDB data which we have used to prescribe geopotential height, waves are much weaker in the winter of southern hemisphere than in the winter of northern hemisphere, especially for wavenumbers 2 and 3 (Fig. 2).

### 4.2 Residual mean circulation

We calculate the residual mean circulation from the Eulerian mean circulation and eddy heat fluxes explicitly, according to Eqns. (13) and (14). The stream functions of residual mean meridional circulation are shown in Figure 6 for four seasons. The stream patterns are very similar to those used in the TEM models or from the diabatic circulation (e.g., Hitchman and Brasseur, 1988; Ko et al., 1985). The upwelling motion occurs in the

tropics and summer subtropics, and downward motion in the winter hemisphere. For spring or fall, the downward motion is shown in both hemisphere. These are the features of diabatic circulation. Also it seems that the cancellation of the two terms on the r.h.s. of (16) or (17) is not a serious problem to affect the accuracy. This is because the real atmosphere is far away from radiative equilibrium and the residual mean circulation is of the same order of Eulerian mean circulation and eddy induced circulation.

#### 4.3 Eddy diffusion coefficients

The calculated total eddy diffusion coefficients,  $K_{yy}^{tot}$ , for ozone and for methane are plotted in Figs. 7 and 8 respectively. For the most areas and all seasons  $K_{yy}^{tot}$  is small than  $4 \times 10^9 \text{ cm}^2/\text{sec}$ , except in the northern middle latitudes during winter. The tropical stratosphere has very small eddy diffusion around whole year. Negative values are shown only for methane during spring in northern upper midlatitudes. Owing to the shorter lifetime,  $K_{yy}^{tot}$  for ozone is larger than  $K_{yy}^{tot}$  for methane, which is very close to the transient eddy diffusion coefficient,  $K_{yy}^r$ .

As a comparison, the  $K_{yy}^q$ , which is derived from the flux-gradient relation of the potential vorticity, is also calculated in the model. After obtaining  $\overline{v' \cdot q'}$  and  $\overline{q_y}$  in the dynamical module, the least-square method (Newman et al., 1988) is used to calculate  $K_{yy}^q$ .

$$K_{yy}^q = -\frac{\overline{v' \cdot q' \cdot \overline{q_y}}}{[\overline{q_y}]^2}, \quad (12)$$

where  $q$  is the quasi-geostrophic potential vorticity and  $q'$ , its eddy,

$$q = f + \frac{\partial v}{\partial x} - \frac{\partial u}{\partial y} + \frac{f}{\rho} \frac{\partial}{\partial z} (\rho \theta / \overline{\theta}_z).$$

Here  $f$  is the Coriolis parameter, and  $\theta$  is potential temperature.

Model calculated  $K_{yy}^q$  shown in Fig. 9 shares some features with that in Newman et al. (1988), such as north-south asymmetry, the seasonal variation. Also their magnitudes are similar. But the details in two set of  $K_{yy}^q$  are quite different due to the different wind fields used to calculate the potential vorticity. We are more interested in the differences



between  $K_{yy}^q$  and  $K_{yy}^{tot}$ , both calculated using the quantities generated in the same model. As displayed in Figs. 7, 8 and 9,  $K_{yy}^q$  is larger than the total eddy diffusion coefficient,  $K_{yy}^{tot}$ , for ozone. One feature is shared by all these eddy diffusion coefficients: small diffusion in tropical stratosphere.

#### 4.4 Long-lived species

$N_2O$ ,  $CH_4$  are good tracer because of their long lifetime in the stratosphere and source from surface. Their distributions in the stratosphere are indicative of transport processes. To evaluate how realistic the calculated residual mean circulation and eddy diffusion are, we compare the model results of  $N_2O$  and  $CH_4$  with the SAMS (Stratospheric and Mesospheric Sounder) data (Jones and Pyle, 1984). The SAMS data show that the mixing ratio of  $N_2O$  has two important features. The first is a "double peak" structure in the upper stratosphere during the period from February to May. This feature is attributed to a strong tropical meridional circulation (Choi and Holton, 1991). The second is that the tropical maxima tend to lean toward the summer hemisphere. In the upper stratosphere the maximum location is about  $30^\circ$  away from the equator in solstices. From December to May the ridge leans toward south, while from June to November it leans toward north. The mixing ratios of  $N_2O$  and  $CH_4$ , which are calculated by the model, are shown in Figures 10 and 11 respectively. The "double peak" structure is only vaguely shown up in the model simulations in upper stratosphere during the northern winter. However, the "leaning ridge" feature is apparent in the summer hemisphere for both species and simulated positions of "leaning ridge" are close to where they are observed.

Both simulated distributions for  $CH_4$  and  $N_2O$  have steep "slope" and large meridional gradients in the extratropics. This feature is also shown in recent observations of  $CH_4$  from UARS/CLAES (Fig. 12, from Kumer et al., 1993). It is noted that these features have not been simulated by some two-dimensional models, probably due to large eddy diffusion used in these models. As a demonstration, the simulated  $CH_4$  distributions for 4 seasons using  $K_{yy}^q$  is plotted in Fig. 13. They are more 'flat' compared with Fig. 11.

Because both  $N_2O$  and  $CH_4$  are long-lived constituents, it is not surprising that their mixing ratios show a very similar configuration. According to Plumb and Ko

(1992) all long-lived species tend to maintain a state of slope equilibrium, i.e., horizontal diffusion and vertical convection dominate the whole transport process. In the mid-high latitudes, horizontal diffusion is mostly responsible for the mixing process. The correlation between  $\text{N}_2\text{O}$  and  $\text{CH}_4$  in the northern winter tropics and extratropics is shown in Figure 14. Two compact groups of points are displayed there, one, which is approximately linear, in high latitudes (poleward of  $57^\circ \text{N}$ ) and one in tropics and subtropics. Same feature can be found in the Southern Hemisphere and in other seasons.

The lifetime calculated from the model results is 109 yr, 57 yr and 95 yr for  $\text{N}_2\text{O}$ , F-11 and F-12 respectively. Compared with our previous results of 106 yr, 51 yr and 90 yr using two-dimensional interactive model (Ko et al., 1993), values from 3-wave model are closer to commonly accepted ones. This changes in the lifetimes are due to the different transport and better photochemistry, particularly the new J-rate calculation (Prather, 1993), in the three-wave interactive model.

#### 4.5 Ozone

The calculated  $\text{O}_3$  column abundance is plotted in Figure 15 as a function of month and latitude. There is a strong hemispheric asymmetry, indicating the difference of waves in the two hemispheres, which affects both eddy diffusion and the mean meridional transport circulation. The general feature of  $\text{O}_3$  column distribution is similar to the observations from Total Ozone Mapping Spectrometer (TOMS), which shown in Fig. 16. The modeled spring maximum in both hemispheres appears in the right places with roughly right amplitudes but little later in time. The calculated ozone column abundance in the northern mid- and high-latitudes during late summer and fall is about 40-60 Dobson Units (D. U.) higher than the observations.

It is interesting to discover that the ozone distribution calculated using the transient eddy diffusion coefficient,  $K_{yy}^r$ , (Fig. 17) is quite similar to that using the total eddy diffusion coefficient. This means that the contribution from the chemical eddy diffusion is not essential in our model. But the ozone distribution calculated using  $K_{yy}^q$ , which is derived based on the PV flux-gradient relation, is quite different (Fig. 18). Due to larger eddy diffusion, ozone maximum in the northern polar spring is 40 D. U. less than observations, but the ozone column abundance in the same region during fall is improved, compared with baseline simulation with  $K_{yy}^{\text{tot}}$ .

#### 4.6 Correlation between Ozone and NO<sub>y</sub>

Observations have shown that mixing ratios of O<sub>3</sub> and NO<sub>y</sub> are well correlated in the lower stratosphere (Murphy et al., 1993). The ratio of NO<sub>y</sub> to O<sub>3</sub> is nearly independent of altitude from tropopause to ~~above 20 km~~ 20 km. The ratio shows strong meridional gradients in the subtropics. Previous two-dimensional models (e.g., Ko et al., 1993; Solomon and Garcia, 1984) have simulated general features of the vertical profile of NO<sub>y</sub>/O<sub>3</sub> but not the gradient in the lower stratosphere between tropics and mid-latitudes. The mixing ratio of NO<sub>y</sub>, O<sub>3</sub> and their ratio calculated by this model are shown in Figure 19. The feature of NO<sub>y</sub>/O<sub>3</sub> is very similar to the observation, especially, the strong subtropical meridional gradients are reproduced.

#### 5. Discussions

One feature of the total eddy diffusion coefficient calculated in the model is worth to notice. It is smaller than  $4 \times 10^9$  (cm<sup>2</sup>/sec) from 30° N to 30° S in the lower stratosphere all year around (Fig. 7). Therefore the tropics behaves like a pipe which only transport tracers by upwelling circulation with little exchange between tropics and middle latitudes (Plumb, 1994). This also limits the exchange between two hemispheres. The calculated correlation between N<sub>2</sub>O and CH<sub>4</sub> do distinguish the tropical area from the high latitudes.

The transient eddy diffusion coefficient, which is equal to the total eddy diffusion coefficient for inert tracer and is very close to that for methane (Fig. 8), calculated using the new scheme is smaller than the eddy diffusion coefficients derived based on the flux-gradient relation of potential vorticity (Fig. 9) in our model. We think that a part of the difference is due to the dissipation of the potential vorticity adopted in our model. In current version of the model, the dissipation consists of two parts, radiative cooling and friction. With the dissipation, the potential vorticity is like a chemical active tracer. Therefore the eddy diffusion coefficients derived from the PV flux-gradient relation include both dynamical and 'chemical' eddy contributions for the PV. Our model calculations show that the dissipation do have significant contribution to the eddy diffusion coefficients, otherwise  $K_{yy}^q$  would be close to the dynamical eddy diffusion coefficient,  $K_{yy}^n$ .

During wave breaking events, the amplitude of growing waves reach the saturate condition and stop increasing. Due to the instability, waves with smaller scale increase very fast through non-linear wave-wave interaction. Although the saturated waves don't transport tracers anymore, these fast growing waves with smaller scale can transport tracers very effectively. In this sense, our scheme for calculating eddy diffusion from wave 1, 2 and 3, and the parameterization for smaller scales can include the contribution from wave breaking. But with only 3 waves included in the dynamics module and coarse resolution, our model can not simulate the wave breaking events very well and may underestimate the eddy transport by wave breaking.

The chemical eddy diffusion is irrelevant in our model. This is because where the chemical eddy diffusion coefficient is large, the local lifetime of this species must be short and the distribution is mainly determined by photochemistry not by transport processes, which include eddy diffusion.

## APPENDIX

The data used for the model lower boundary condition and for diagnosis were extracted from an archive of monthly mean grid point analyses of meteorological data, known as the Climate Diagnostics Data Base (CDDDB) (Rasmussen and Arkin, 1985), based on the U.S. National Meteorological Center global analyses, which are generated at 0000 GMT and 1200 GMT daily. The original data were on a 2.5 deg by 2.5 deg grid, at nine standard levels in the atmosphere (1000mb, 850mb, 700mb, 500mb, 300mb, 250mb, 200mb, 100mb and 50mb). The data for use in the model consisted of the first seven complex Fourier components interpolated onto the eighteen edges of the 19 bands of latitude used by the model, over the same nine levels.

The original data set spanned the time period from October 1978 to March 1990, and contained values for the zonal component of the wind velocity ( $u$ ), the meridional component ( $v$ ), temperature ( $T$ ), geopotential height ( $Z$ ), vertical velocity, specific humidity, vorticity and several cross-products. The first step in the extraction process was to create a subset of data from October 1978 to September 1989, which contained  $u$ ,  $v$ ,  $T$  and  $\phi$ , at each of the of the nine pressure levels. The climatological considerations of some of these variables taken from the CDDDB for a similar period, the 1980-89 decade, including estimates of the seasonal and interannual signals, are given by Salstein (1995).

After the spatial series were created, Fourier transforms in space were calculated at each latitude, for each month, variable, and level. The first seven complex harmonics of each transform generated were stored. Four smaller subsets were created: (1) a climatology was calculated for the October 1978 to September 1989 period. (2) a second climatology was created for October 1978 to September 1986. Because a different technique was used to generate temperature fields from October 1986 to March 1989, leading to some very noisy temperature values at low levels near and below topography. (3) one subset was created to represent an active year (October 1978-September 1979) and (4) one subset was created to represent a quiet year (October 1982-September 1983) in the upper atmosphere.

Finally, because the model used nineteen bands of latitude, whose edges were defined by eighteen equally spaced latitude circles, and the model required input values along these edges, area weighted averages of the complex Fourier transforms were calculated around each of these latitude circles.

### References

- Andrew, D. G. and M. E. McIntyre, Generalized Eliassen-Palm and Charney-Drazin theorem for waves on axisymmetric mean flow in compressible atmosphere, *J. Atmos. Sci.*, **35**, 175-185, 1978.
- Barnett, J. J., and M. Corney, Middle atmosphere reference model derived from satellite data. in *Handbook for MAP*, 16, 47-85, ed. K. Labitzke et al. SCOSTEP Secretariat, Univ. of Illinois, Urbana, Ill., 1985.
- Bowman, K. P., Large-scale isentropic mixing properties of Antarctic polar vortex from analyzed winds, *J. Geophys. Res.*, **98**, 23,013-23,023, 1993
- Branscome, L. E., A parameterization of transient eddy heat flux on a beta plane, *J. Atom. Sci.*, **40**, 2508-2521,(1983).
- Brasseur, G., M. H. Hitchman, S. Walters, M. Dymek, E. Falise, and M. Pirre, An interactive chemical dynamical radiative two-dimensional model of the middle atmosphere, *J. Geophys. Res.*, **95**, 5639-5655, 1990.

Charney, J. G., and P. G. Drazin. Propagation of planetary-scale disturbances from the lower into the upper atmosphere. *J. Geophys. Res.*, **66**, 83-109, 1961.

Choi, W. K. and J. R. Holton, Transport of N<sub>2</sub>O in the stratosphere related to the equatorial semiannual oscillation. *J. Geophys. Res.*, **96**, 22,543-22,557, 1991.

Chen, P., The permeability of the Antarctic stratosphere., *J. Geophys. Res.*, **99**, 20,563-20,571, 1994.

Clark, J. H. E., and T. G. Rogers, The transport of conservative trace gases by planetary waves, *J. Atmos. Sci.*, **35**, 2232-2235, 1978.

Garcia, R. R., Parameterization of planetary wave breaking in the middle atmosphere, *J. Atmos. Sci.*, **48**, 1405-1419, 1991.

Garcia, R. G., F Strobel, S Solomon, and J. T. Kiehl, A new numerical model of the middle atmosphere 1. Dynamics and transport of tropospheric source gases. *J. Geophys. Res.*, **97**, 12967-12991, 1992.

Garcia, R.R., and S. Solomon, A numerical model of the middle atmosphere 2. Ozone and related species *J. Geophys. Res.*, **99**, 12,937-12,951, 1994.

Hitchman, M. H., and G. Brasseur, Rossby wave activity in a two-dimensional model: Closure for wave driving and meridional eddy diffusivity, *J. Geophys. Res.*, **93**, 9405-9417, 1988.

Hudson, R. D. and E. I. Reed (Eds.), The stratosphere: Present and future, NASA Ref. Publ. 1049, 65-81, December 1979.

Kinnersley, J. S. and R. S. Harwood, An isentropic two-dimensional model with an interactive parameterization of dynamical and chemical planetary-wave fluxes, *Q. J. R. Meteor. Soc.*, **119**, pp. 1167-1193, 1993.

Ko, M. K. W., H. R. Schneider, R.-L. Shia, D. K. Weisenstein and N.-D. Sze, A two-dimensional model with coupled dynamics, radiation, and photochemistry: 1. Simulation of the middle atmosphere. *J. Geophys. Res.*, **98**, 20429-20440, 1993.

Kumer, J. B., J. L. Mergenthaler, and A. E. Roche, CLAES CH<sub>4</sub>, N<sub>2</sub>O and CCl<sub>2</sub>F<sub>2</sub> (F12) global data. *G. R. L.*, **20**, 1239-1242, 1993.

Leovy, C. B., C.-R. Sun, M. H. Hitchman, E. E. Remsberg, J. M. Russell, III, L. L. Gordley, J. G. Gille and L. V. Lyjak, Transport of ozone in the middle stratosphere: Evidence for planetary wave breaking, *J. Atmos Sci.*, **42**, 230-244, 1985.

Lindzen, R. S., Turbulence and stress owing to gravity wave and tidal breaking down, *J. Geophys. Res.*, **86**, 9707-9714, 1981.

Mahlman, J. D., Some fundamental limitations of simplified transport models as implied by results from a three-dimensional general circulation/tracer model, Proc. Conf. Clim. Impact Assess. Program 4th, 132-146, 1975.

Matsuno, T., Lagrangian Motion of air parcels in the stratosphere in the presence of planetary waves, *Pure and Applied Geophys.*, **118**, 189-216, 1980.

Newman, P.A., M. R. Schoeberl, R. A. Plumb, and J. E. Rosenfield, Mixing rates calculated from potential vorticity, *J. Geophys. Res.*, **93**, 5221-5240 1988.

Murphy, D. M., D. W. Fahey, M. H. Proffitt, S. C. Liu, K. R. Chen, E. S. Eubank, S. R. Kawa, and K. K. Kelly, Reactive nitrogen and its correlation with ozone in the lower stratosphere and upper troposphere, *J. Geophys. Res.* **98**, 8751-8773, 1993.

O'Brien, E., and L. Branscome, Minimal modeling of the extratropical general circulation. *Tellus*, **41A**, 292-307, 1989.

Plumb, R. A., Eddy fluxes of conservative quantities by small-amplitude waves, *J. Atmos. Sci.* **36** 1699-1704, 1979.

Plumb, R.A., and M.K.W. Ko, Interrelationships between mixing ratios of long-lived stratospheric constituents, *J. Geophys. Res.*, **97**, 10,145-10,156, 1992.

Plumb, R. A., Vertical transport in the stratosphere: Global diffuser or tropical pipe?  
Paper presented at the Atmospheric Effects of Aviation Annual Meeting, Virginia Beach,  
VA, June 26-30, 1994.

Prather, M. J., I. GISS photochemical model, pp. 76-85, in The atmospheric effects of  
stratospheric aircraft: report of the 1992 models and measurements workshop, MASA  
Ref. Publ., 1292. eds by M. J. Prather and E. E. Remsberg, 1993.

Pyle, J. A. and C. F. Rogers, Stratospheric transport by stationary planetary waves- the  
importance of chemical processes, *Quart. J. R. Met. Soc.*, **106**, 421-446, 1980.

Reed, R. J., and K. E. German, A contribution to the problem of stratospheric diffusion  
by large-scale mixing. *Mon. Weather Rev.*, **93**, 313-321, 1965.

Rogers, C. F., and J. A. Pyle, Stratospheric tracer transport: a modified diabatic  
circulation model, *Q.J.R. Meteor. Soc.*, **110**, 219-237, 1984.

Schneider, H. R. and M. A. Geller, A comparison of two and  
three-dimensional transport within a stratospheric circulation model. NASA x-964-84-3,  
1984.

Schneider, H. R., M. K. W. Ko, R.-L. Shia, and N.-D. Sze, A two-dimensional model  
with coupled dynamics, radiative transfer, and photochemistry 2. Assessment of response  
of stratospheric ozone to increased levels of CO<sub>2</sub>, N<sub>2</sub>O, CH<sub>4</sub>, and CFC, *J. Geophys. Res.*,  
**98**, 20,441-20,449, 1993.

Schoeberl, M. R. and J. T. Bacmeister, Mixing processes in the extratropical stratosphere.  
The role of the stratosphere in global change, M. L. Chanin Ed., Springer-Verlag, 135-  
152, 1993.

Smith, A., and G. P. Brasseur, The dependence of constituent transport on chemistry in a  
two-dimensional model of the middle atmosphere. *J. Geophys. Res.*, **95**, 13,749-13,764,  
1990.



- Stone, P. H., The meridional variation of the eddy heat fluxes by baroclinic waves and their parameterization. *J. Atmos. Sci.*, **31**, 444-456, (1974).
- Strobel, D. F., Parameterization of linear wave chemical transport in planetary atmospheres by eddy diffusion. *J. Geophys. Res.*, **86**, 9806-9810, 1981.
- Tuck, A. F., A comparison of one-, two-, and three-dimensional model representations of stratospheric gases, *Philos. Trans. R. Soc. London Ser. A*, **290**, 477-494, 1979.
- Tung, K. K., Modeling of tracer transport in the middle atmosphere. Dynamics of the middle atmosphere. J. R. Holton and T. Matsuno, Eds., Terra Scientific, 412-444, 1984.
- Tung, K. K., A coupled model of zonally averaged dynamics, radiation and chemistry. in Transport processes in the middle atmosphere. G. Visconti and R. R. Garcia, Eds., 183-198, 1987.
- Wang, W.-C. and P. B. Ryan: Overlapping effect of atmospheric H<sub>2</sub>O, CO<sub>2</sub> and O<sub>3</sub> on the CO<sub>2</sub> radiative effect. *Tellus*, **35B**, 81-91, 1983.
- Waugh, D. W., R. A. Plumb, Contour advection with surgery: A technique for investigating finescale structure in tracer transport. *J. Atmos. Sci.* **51**, 530-540, 1994.
- Yang, H., E. Olaguer, and K. K. Tung, Simulation of the present-day atmospheric ozone, odd nitrogen, chlorine and other species using a coupled 2-D model in isentropic coordinates, accepted by *J. Atmos. Sci.*, **48**, 442-471, 1991.
- Zhou, S., and P. H. Stone, The role of large-scale eddies in the climate equilibrium. Part I: Fixed static stability. *J. Climate*, **6**, 985-1001, 1993.

### Figure captions

Fig. 1 The flow chart of the three-wave interactive model. The arrows indicate the direction of data flow. The loops formed by arrows represent feedbacks.

Fig. 2 The prescribed wave amplitude in the model's lower boundary, for a) January and b) July respectively. The solid lines is for wave 1, dash line for wave 2, and dot line for wave 3.

Fig. 3 The model calculated mean zonal wind,  $\bar{u}$ , and temperature,  $\bar{T}$ , a)  $\bar{u}$  in January, b)  $\bar{T}$  in January, c)  $\bar{u}$  in July, and d)  $\bar{T}$  in July.

Fig. 4 Comparison of the model results and the observations for the eddy (the sum of three resolved waves) geopotential height at 50 mb. (a) January, (b) July.

Fig. 5 Comparison of the model results and the observations for the wave amplitude of geopotential height. (a) January; (b) July.

Fig. 6 The model calculated meridional circulation for a) January, b) April, c) July, and d) October

Fig. 7. The total eddy diffusion coefficient,  $K_{yy}^{tot}$ , ( $10^{10}$  cm<sup>2</sup>/sec) for ozone, in (a) January, (b) April, (c) July, and (d) October. The contour levels are -0.4, -0.2, -0.1, 0, 0.1, 0.2, 0.4, 0.8, 1.0 and 1.5.

Fig. 8 Same as Fig. 7, but for Methane.

Fig. 9. The eddy diffusion coefficient derived based on PV flux-gradient relation,  $K_{yy}^q$ , ( $10^{10}$  cm<sup>2</sup>/sec), in (a) January, (b) April, (c) July, and (d) October. The contour levels are -0.4, -0.2, -0.1, 0, 0.1, 0.2, 0.4, 0.8, 1.0 and 1.5.

Fig. 10 Latitude-altitude cross section of calculated N<sub>2</sub>O mixing ratio (ppbv) for (a) January, (b) April, (c) July, and (d) October. The contour levels are 5, 10, 25, 50, 100, 150, 200, 250, and 300 ppbv.

Fig. 11 Latitude-altitude cross section of calculated CH<sub>4</sub> mixing ratio (ppmv) for (a) January, (b) April, (c) July, and (d) October. The contour increment is 0.2 ppmv.

Fig. 12. Zonal mean of UARS/CLAES CH<sub>4</sub> for (a) Jan. 10, 92 and (b) Jul. 10, 92 (Kumer et al., 1993).

Fig. 13 Same as Fig. 11, but using eddy diffusion coefficient derived based on PV flux-gradient relation,  $K_{yy}^q$ , instead of  $K_{yy}^{tot}$ .

Fig. 14 The correlation of  $N_2O$  and  $CH_4$  mixing ratio (a) in the northern mid-high latitudes, and (b) in the tropics.

Fig. 15 Latitude-time cross section of calculated ozone column abundance (D.U.). The contour increment is 20 D.U.

Fig. 16 Same as Fig. 15. but for ozone data from TOMS measurements.

Fig. 17 Same as Fig. 15, but using transient eddy diffusion coefficient,  $K_{yy}^r$ , for all trace gases instead of  $K_{yy}^{tot}$ .

Fig. 18 Same as Fig. 15, but using eddy diffusion coefficient derived based on PV flux-gradient relation,  $K_{yy}^q$ , for all trace gases instead of  $K_{yy}^{tot}$ .

Fig. 19 The mixing ratio of (a)  $NO_y$  and (b)  $O_3$ , as well as (c) their ratio,  $NO_y/O_3$  along with the AAOE, STEP, and AASE data (Murphy et al., 1993) in the lower stratosphere (64 mb), in January.

# 3-Wave Interactive Model

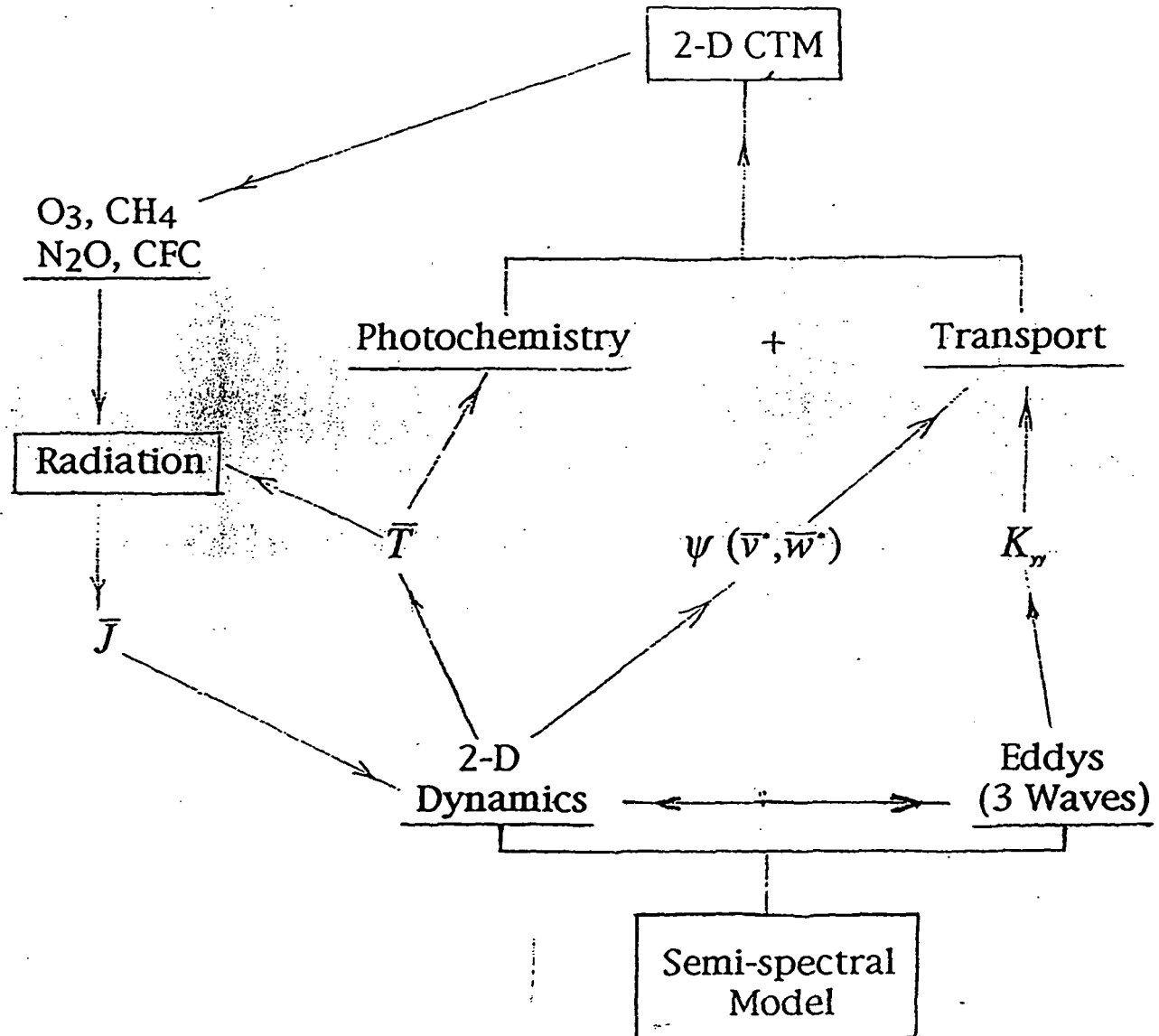


Figure 1

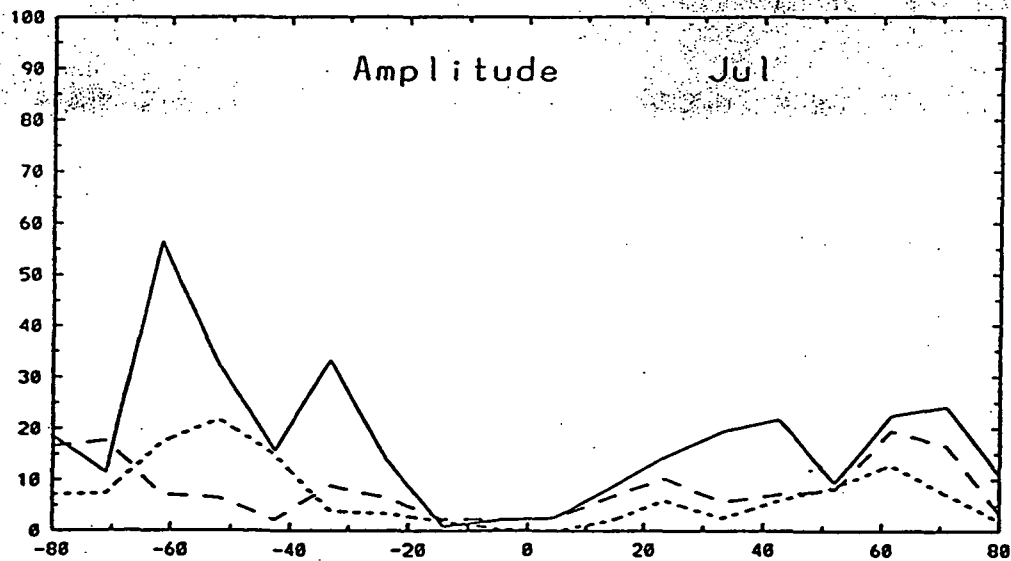
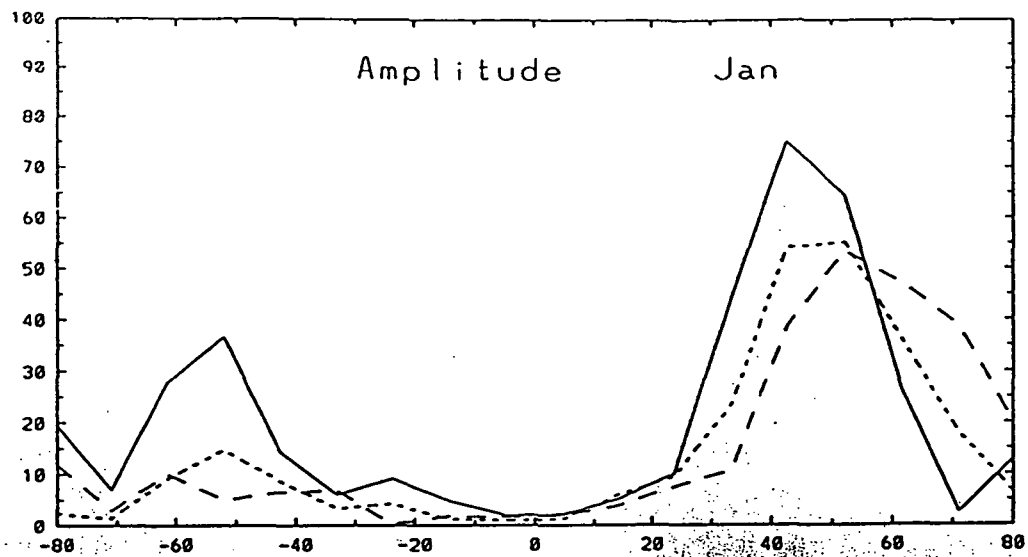


Figure 2

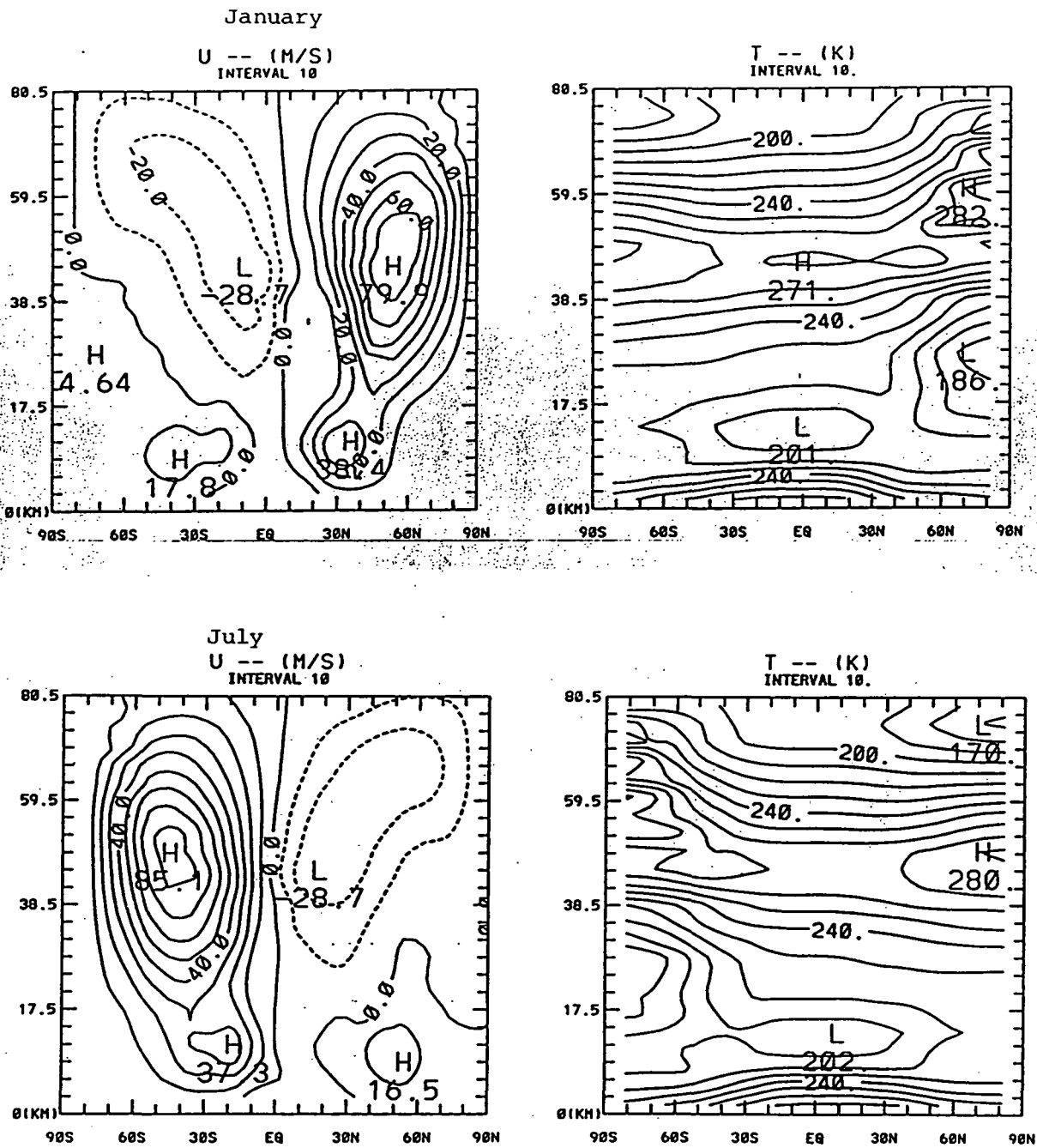
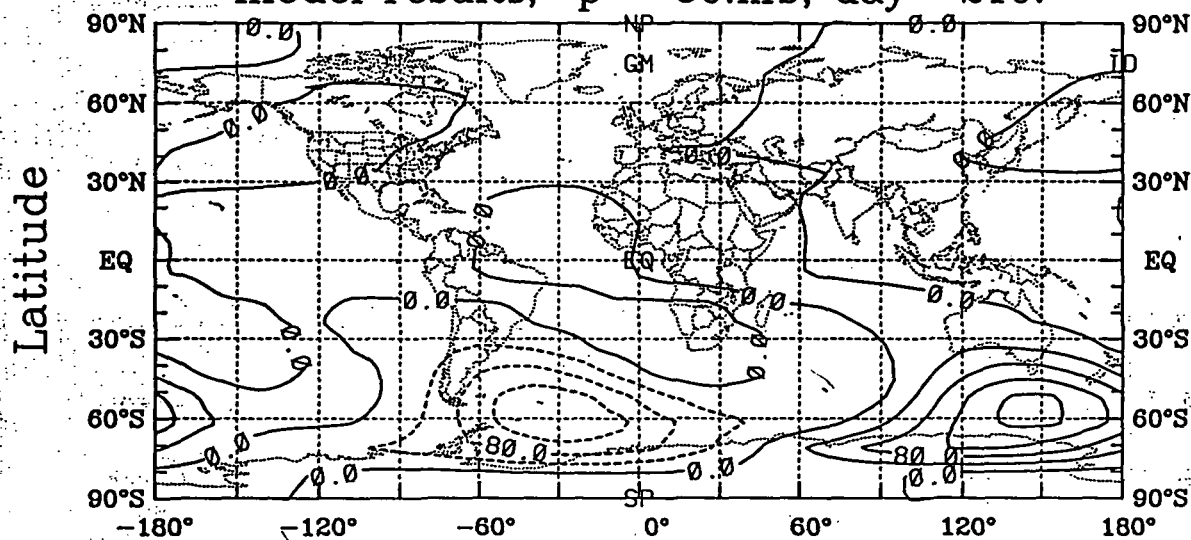


Figure 3



z (wave components only) (m)

model results, p= 50.mb, day= 210.



observations, p= 50.mb, month= 7

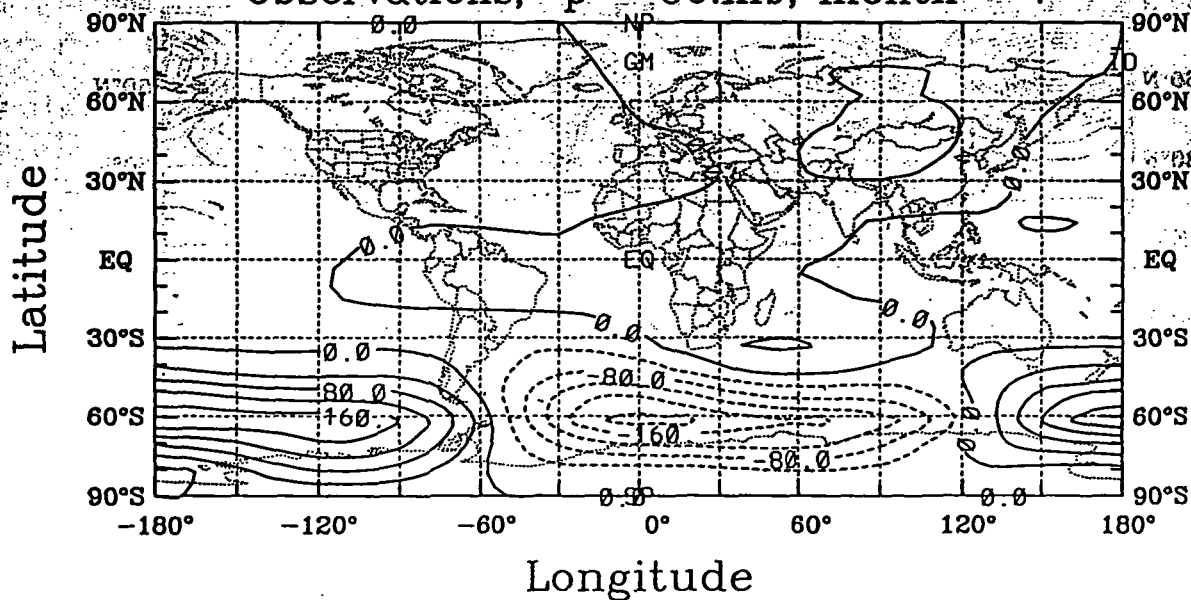


Figure 4b



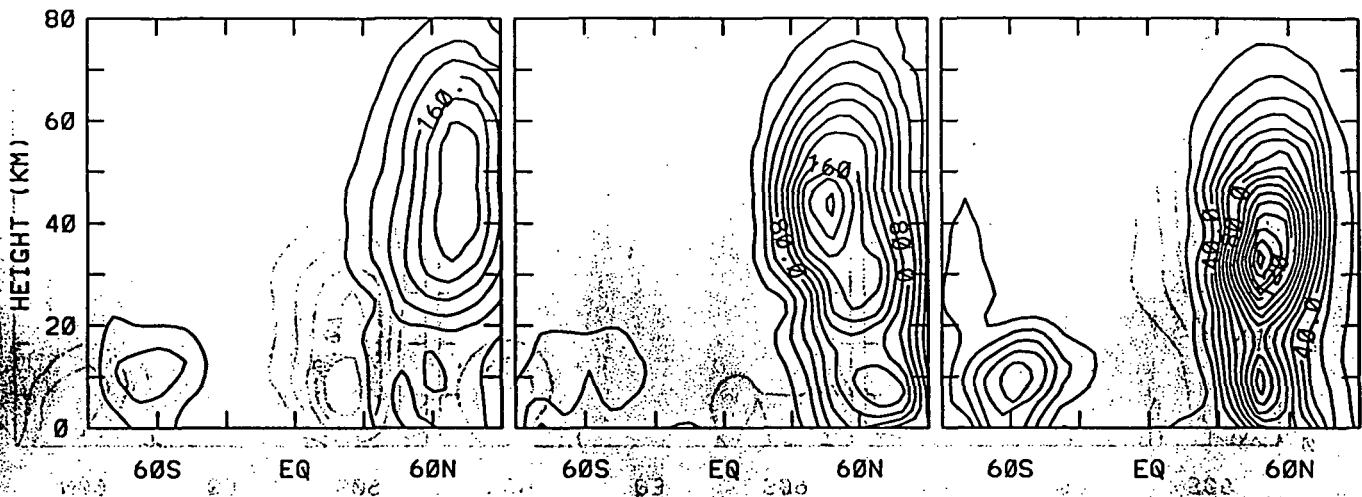
# MODEL RESULTS

month= 1

WAVE1 by 40

WAVE2 by 20

WAVE3 by 10



# OBSERVATION

month= 1

WAVE1 by 40

WAVE2 by 20

WAVE3 by 10

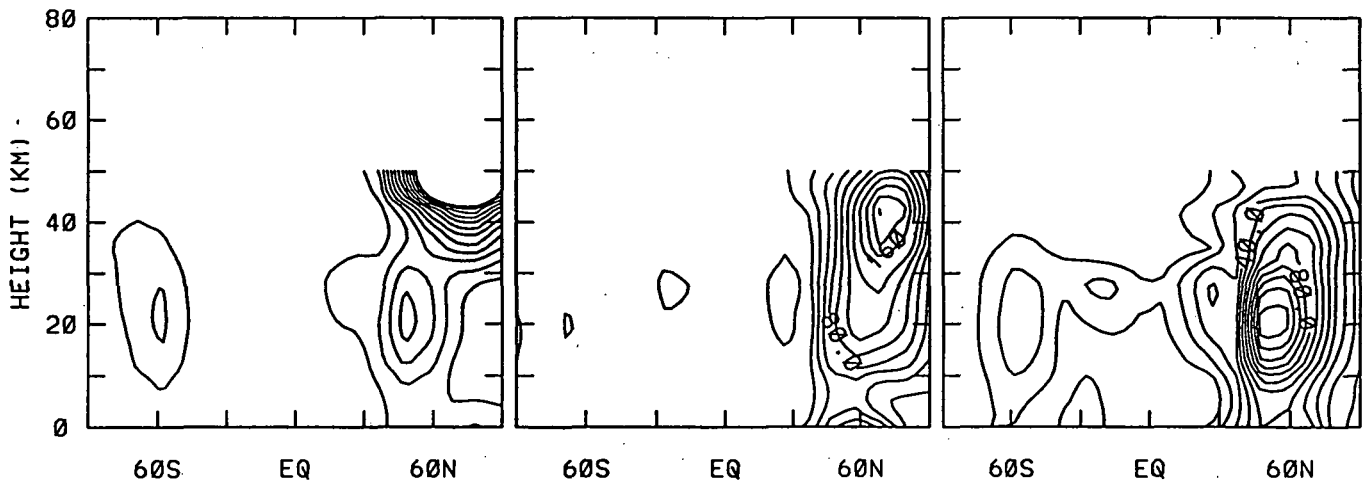


Figure 5a

F.30

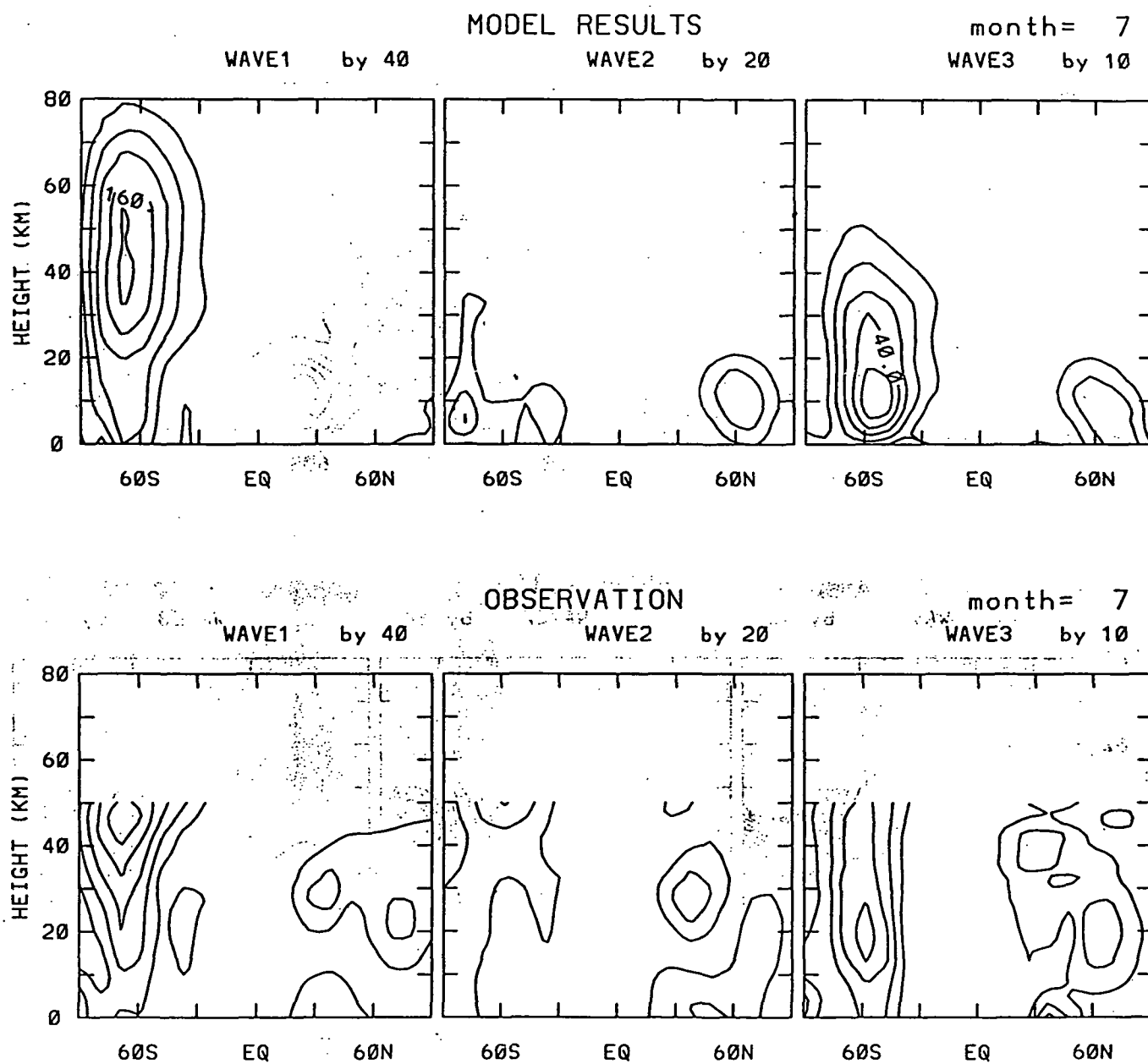


Figure 5b

PSI yr51

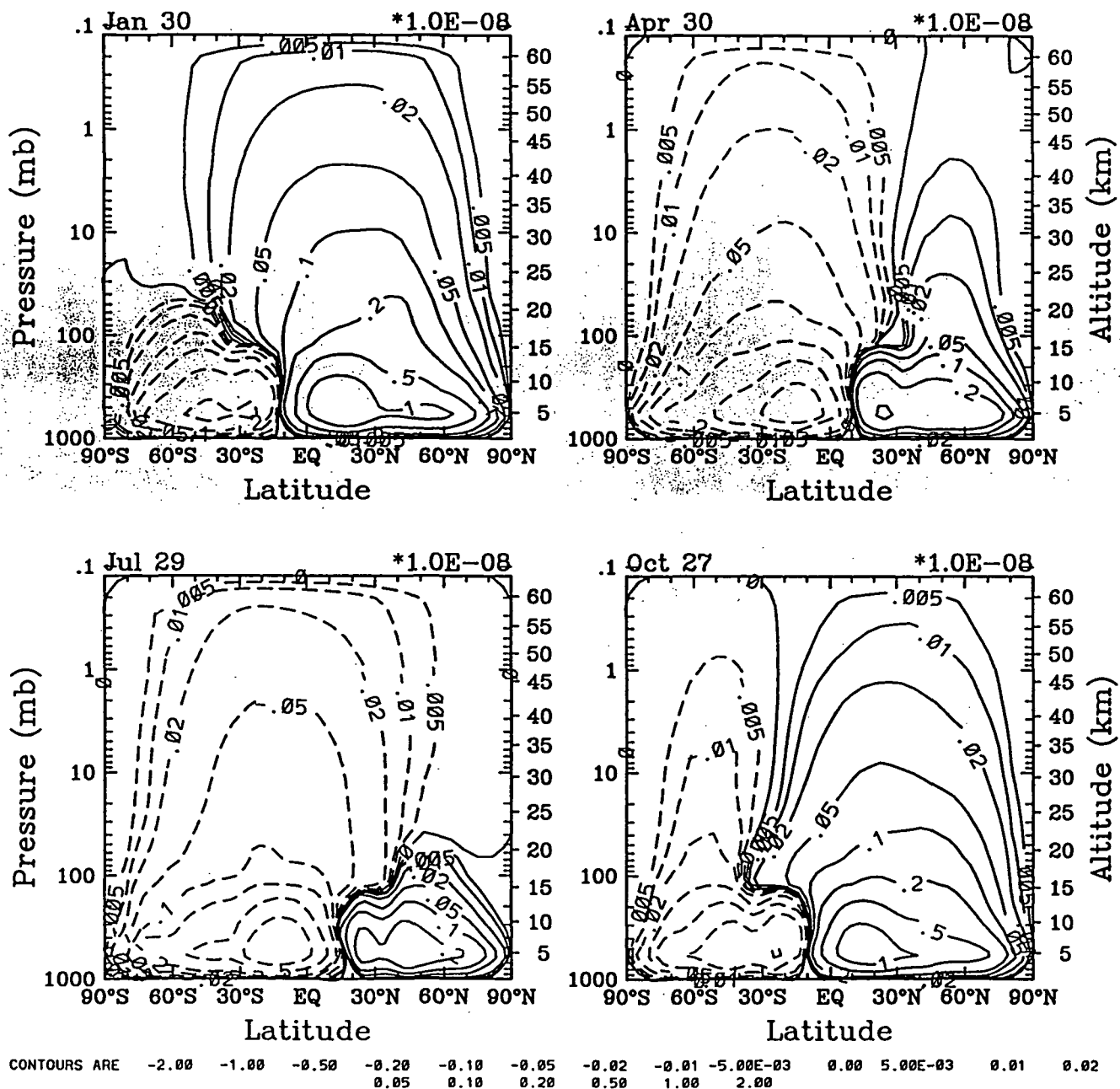


Figure 6

F.32

Tue Nov 14 14:46:40 EST 1995

# Kyy for 03

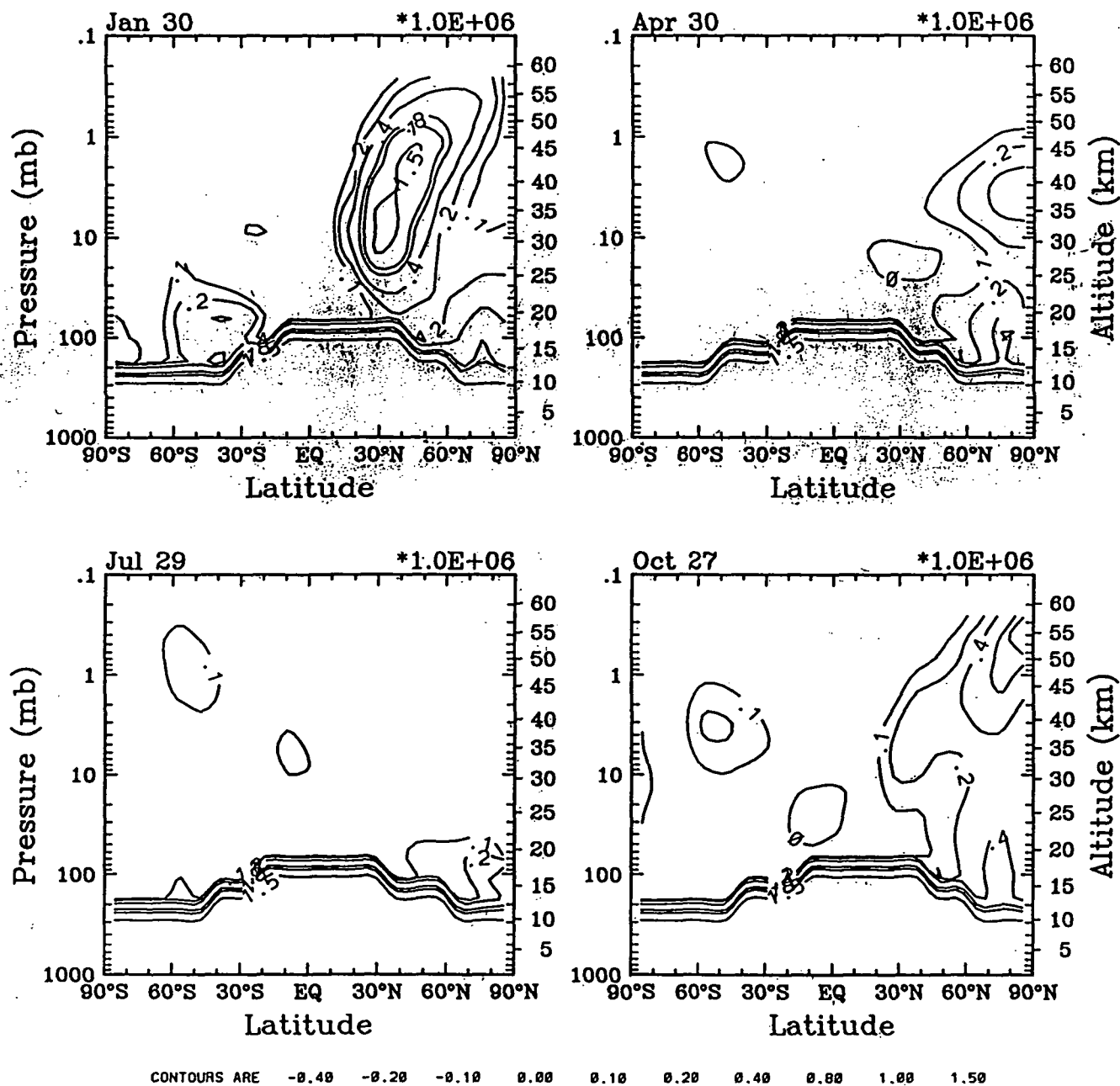


Figure 7

F.33

Fri Oct 13 10:22:04 EDT 1995

# Kyy for CH4

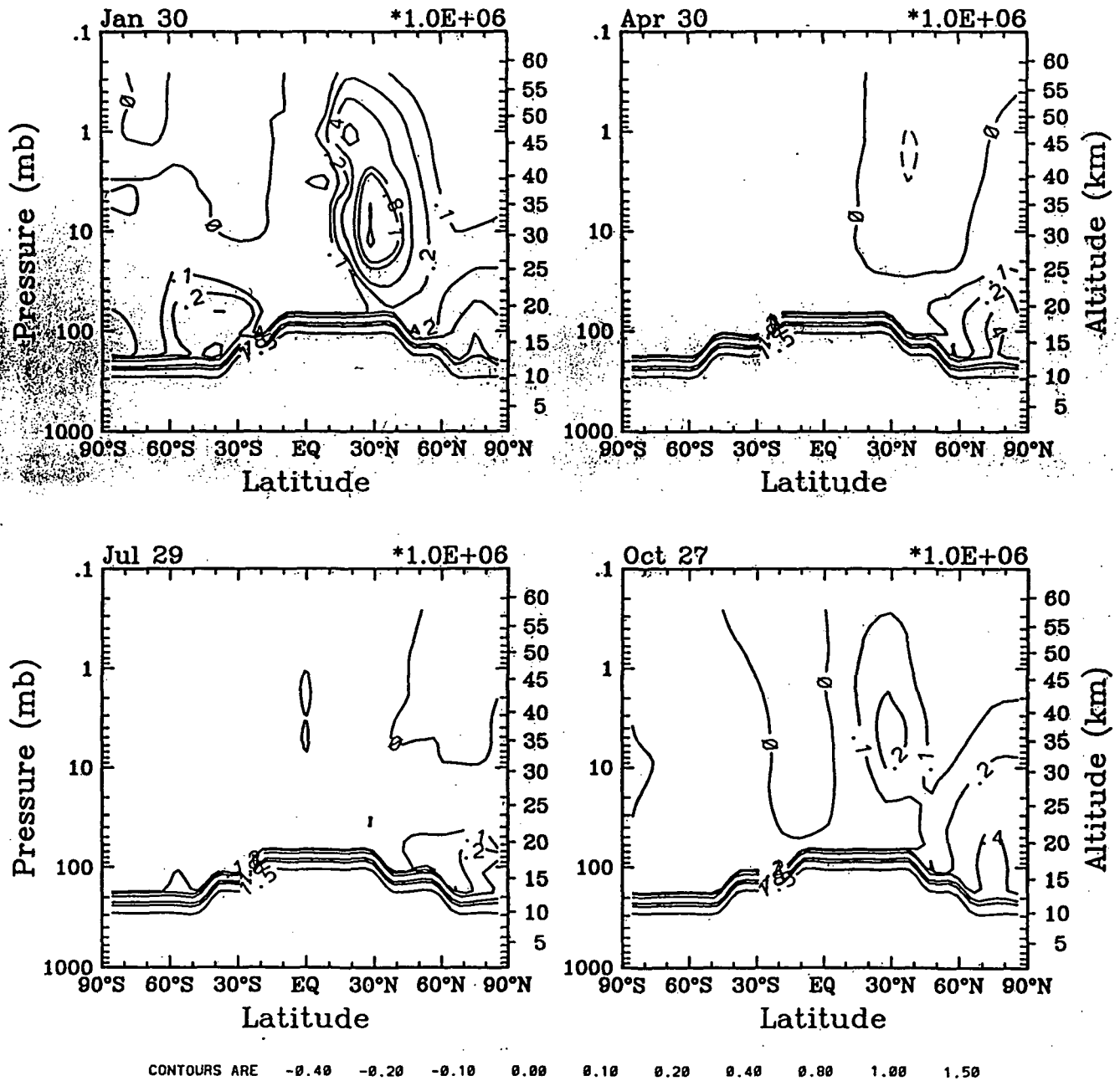


Figure 8

Kyy(n)

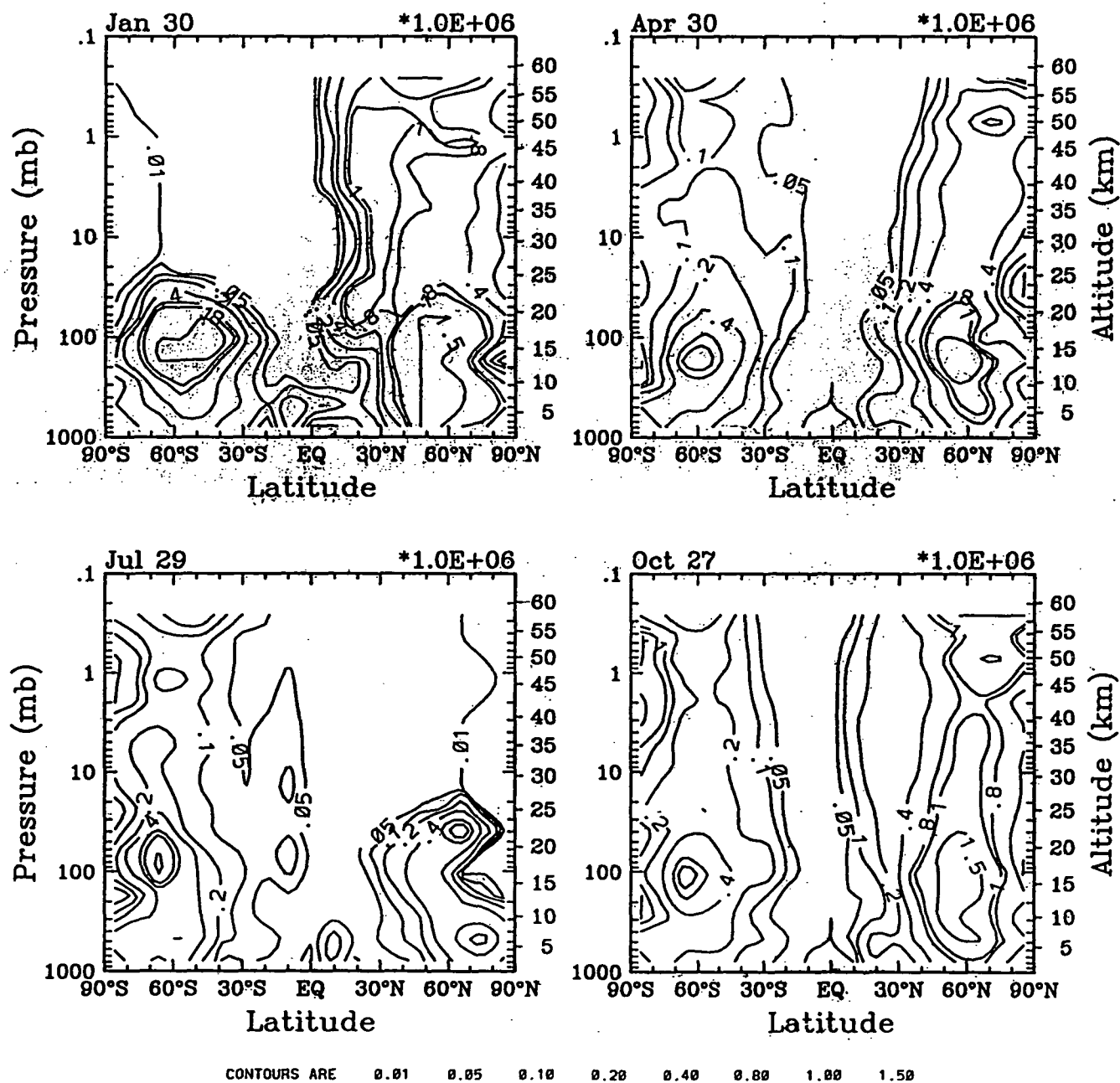


Figure 9

N20 yr51

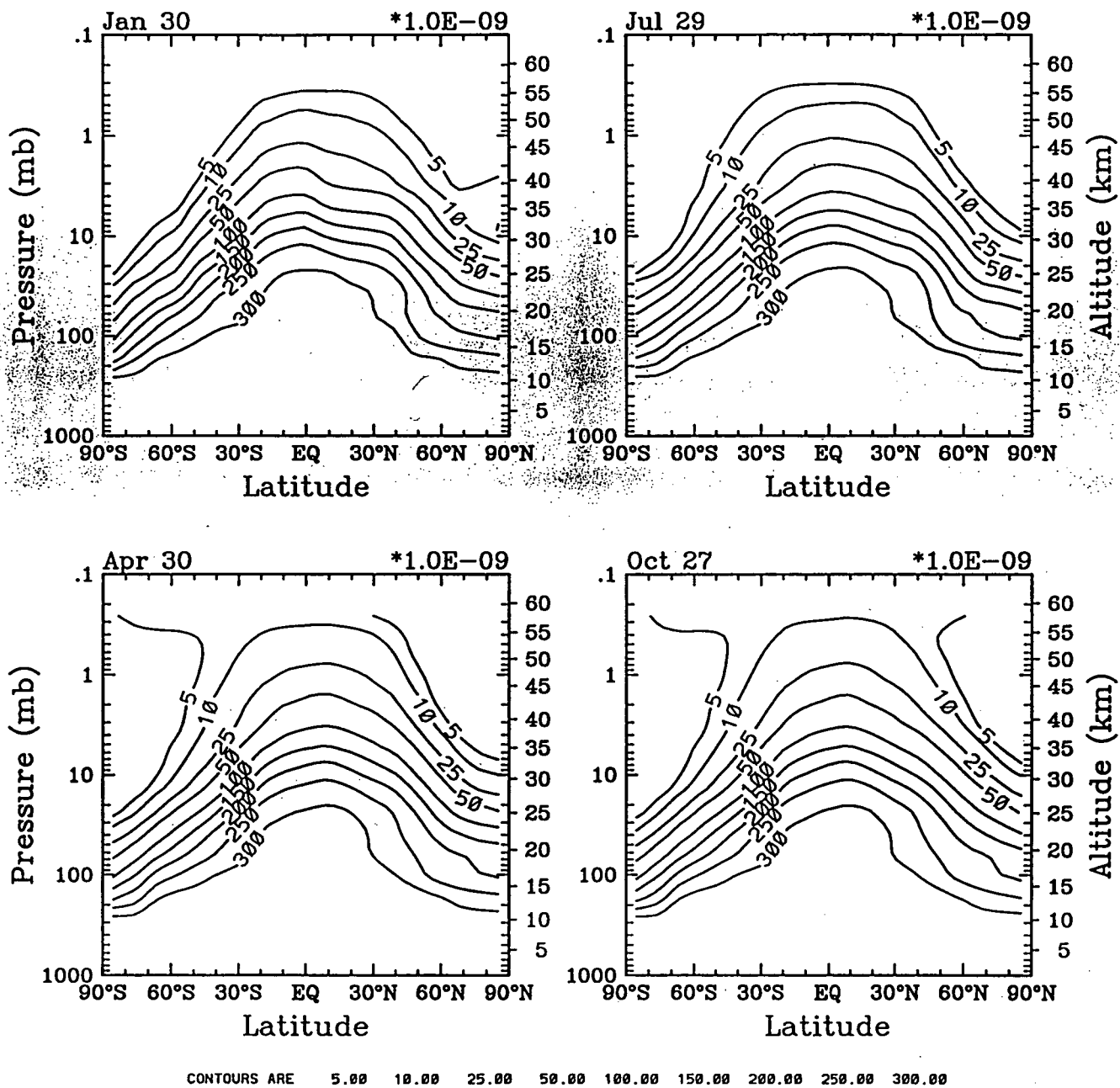


Figure 10

F.36

Tue Nov 21 10:59:53 EST 1995

## CH4

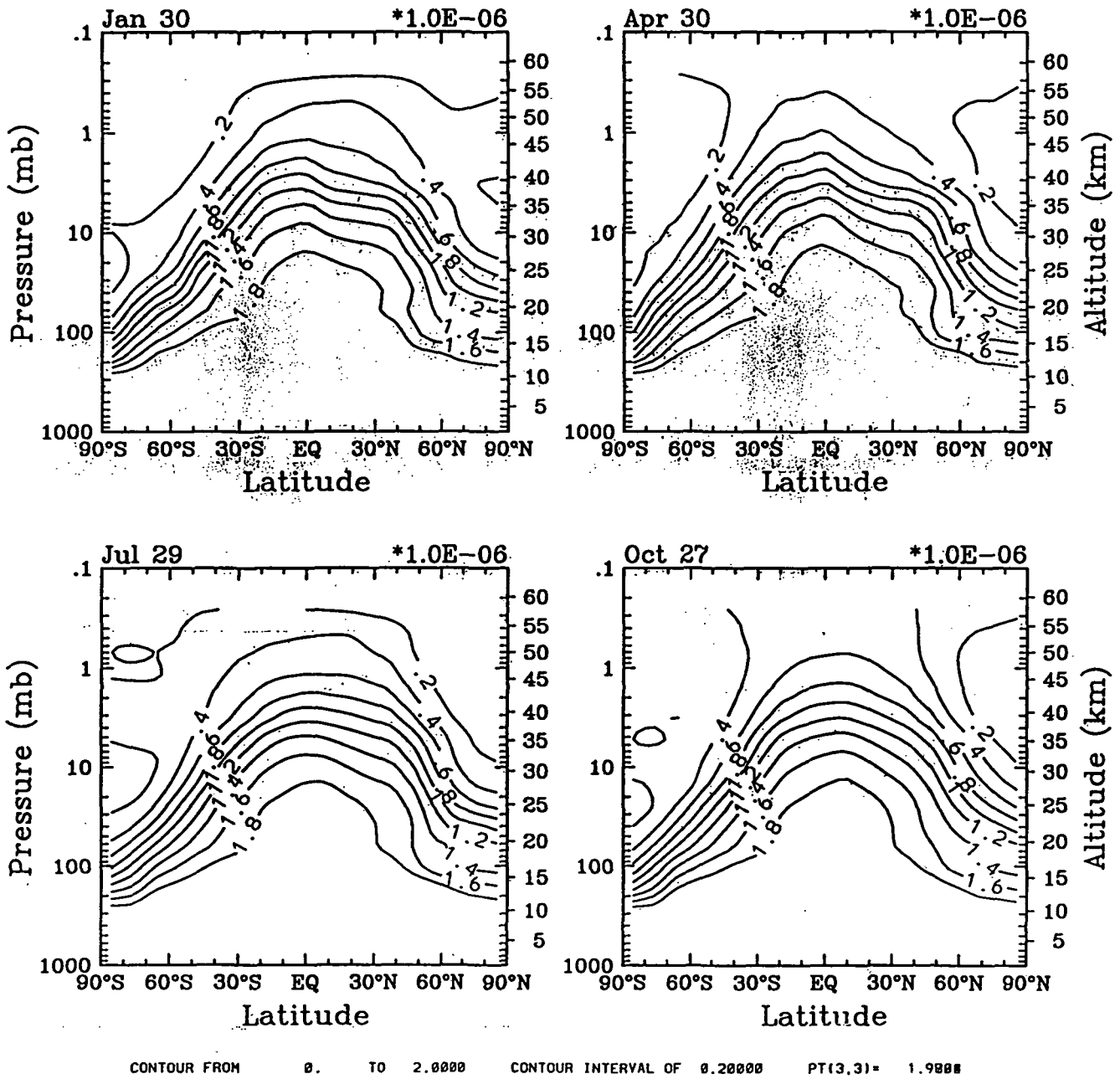


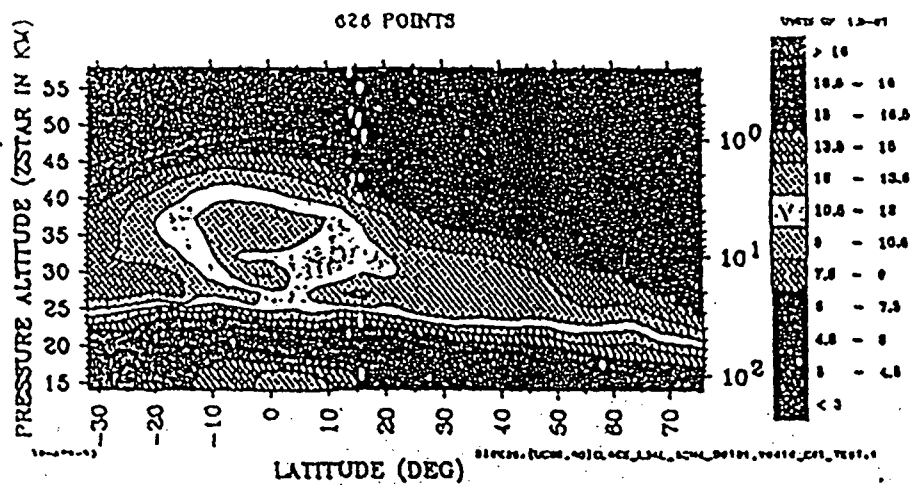
Figure 11

F.37

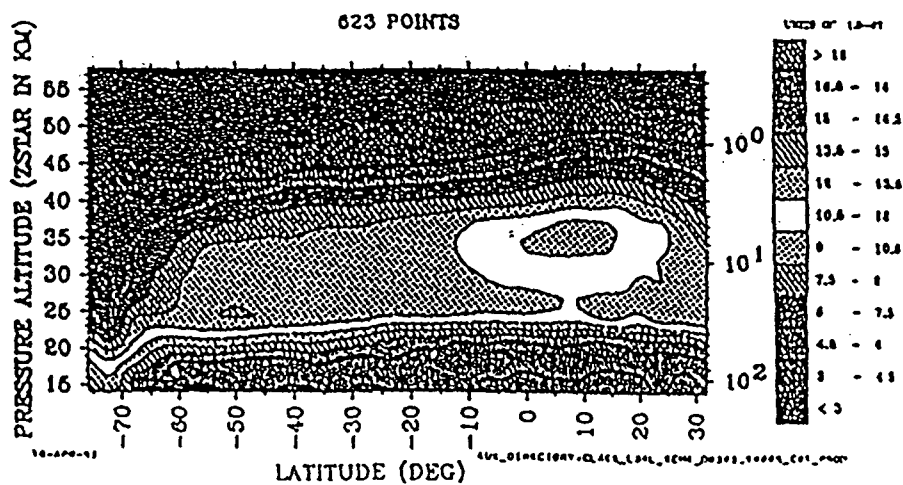
Thu Oct 12 11:00:18 EDT 1995



CLAES ZONAL MEAN CH<sub>4</sub> DISTRIBUTION ON DAY 01-10-92



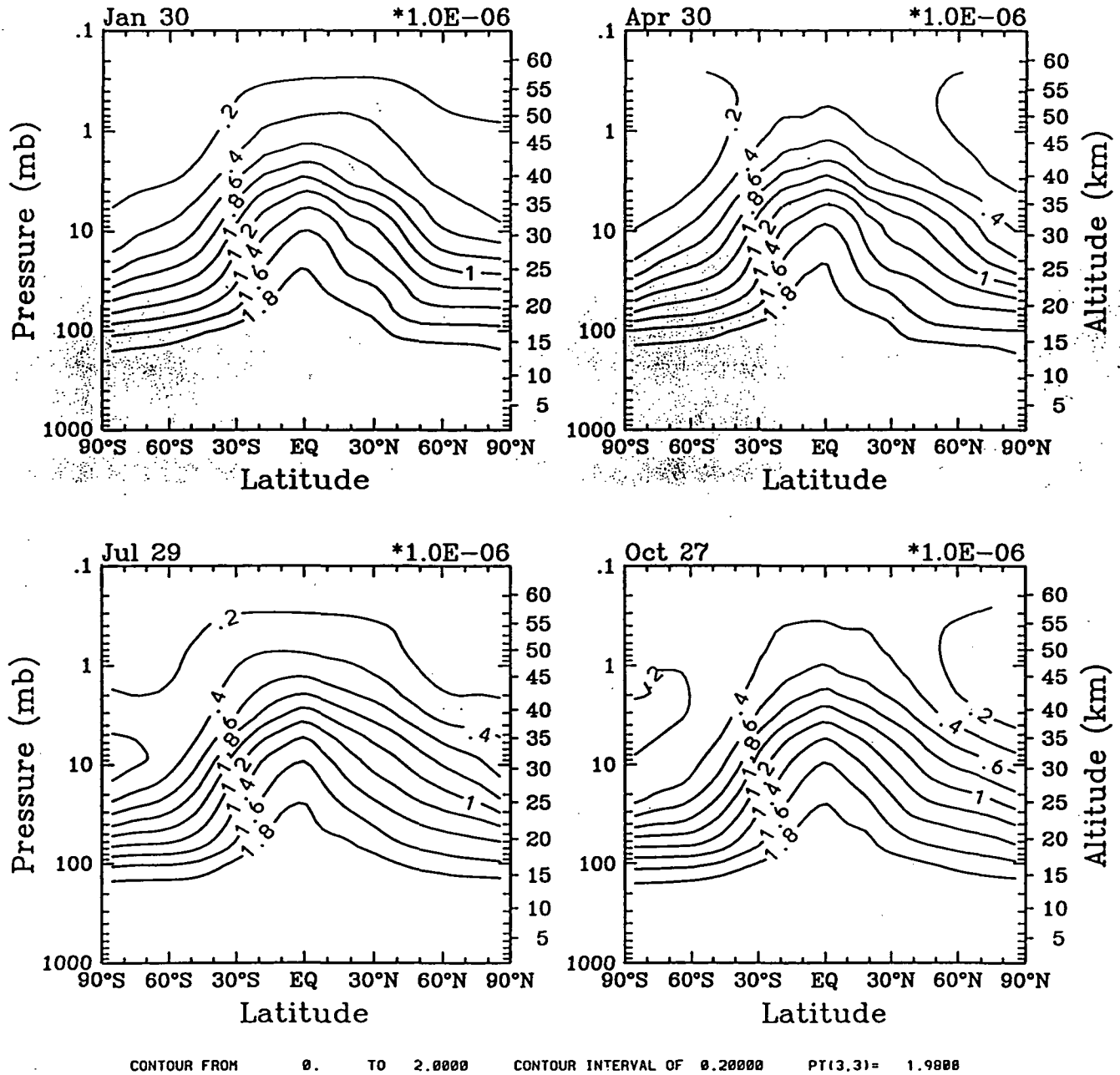
CLAES ZONAL MEAN CH<sub>4</sub> DISTRIBUTION ON DAY 07-10-92



UARS/CLAES CH<sub>4</sub> zonal means for Jan. 10, 92 and Jul. 10, 92 (Kumer et al., 1993).

Figure 12

CH4



Tue Nov 14 15:00:01 EST 1995

Figure 13

# $N_2O-CH_4$ Correlation for Jan

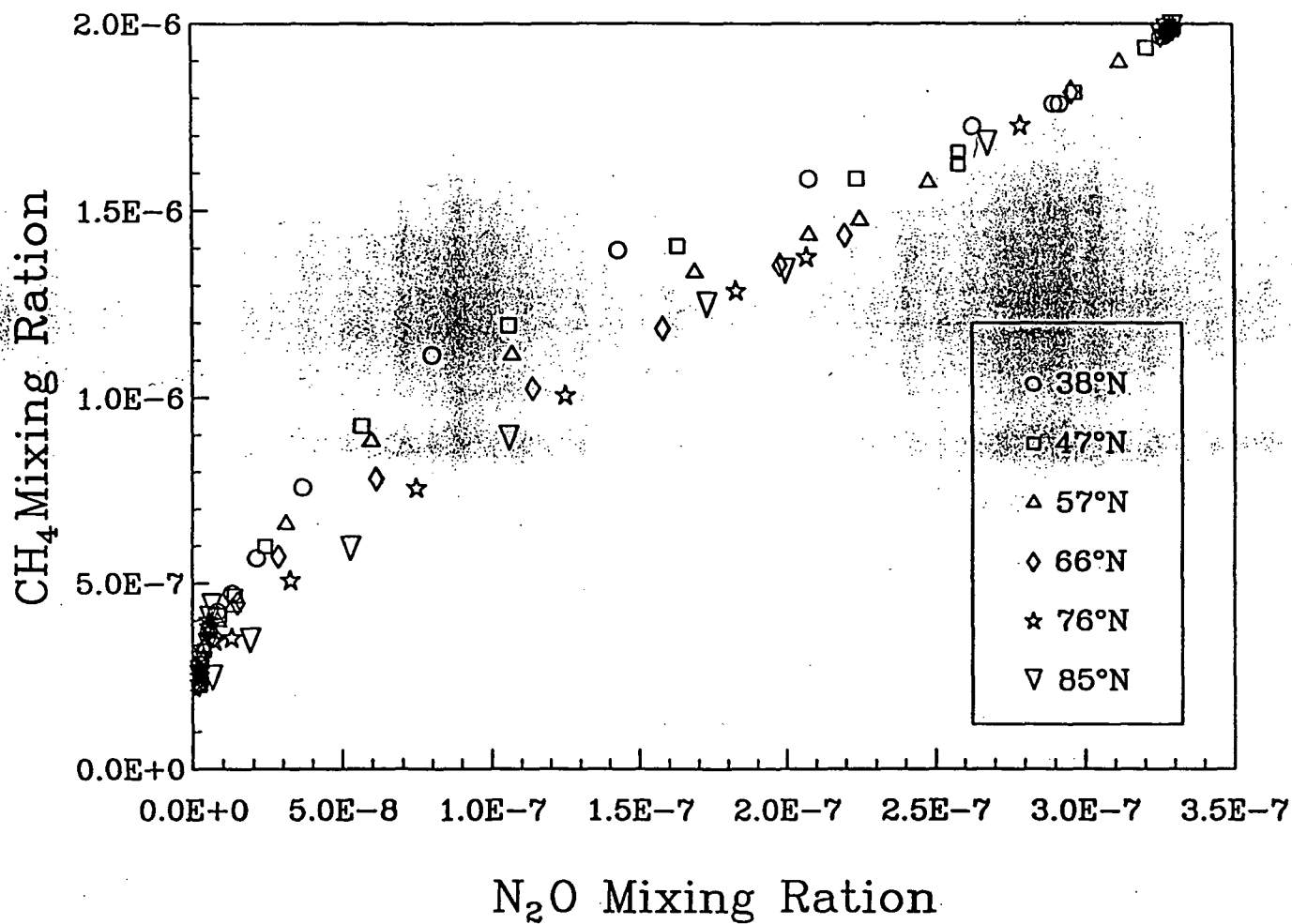


Figure 14a

# $\text{N}_2\text{O}-\text{CH}_4$ Correlation for Jan

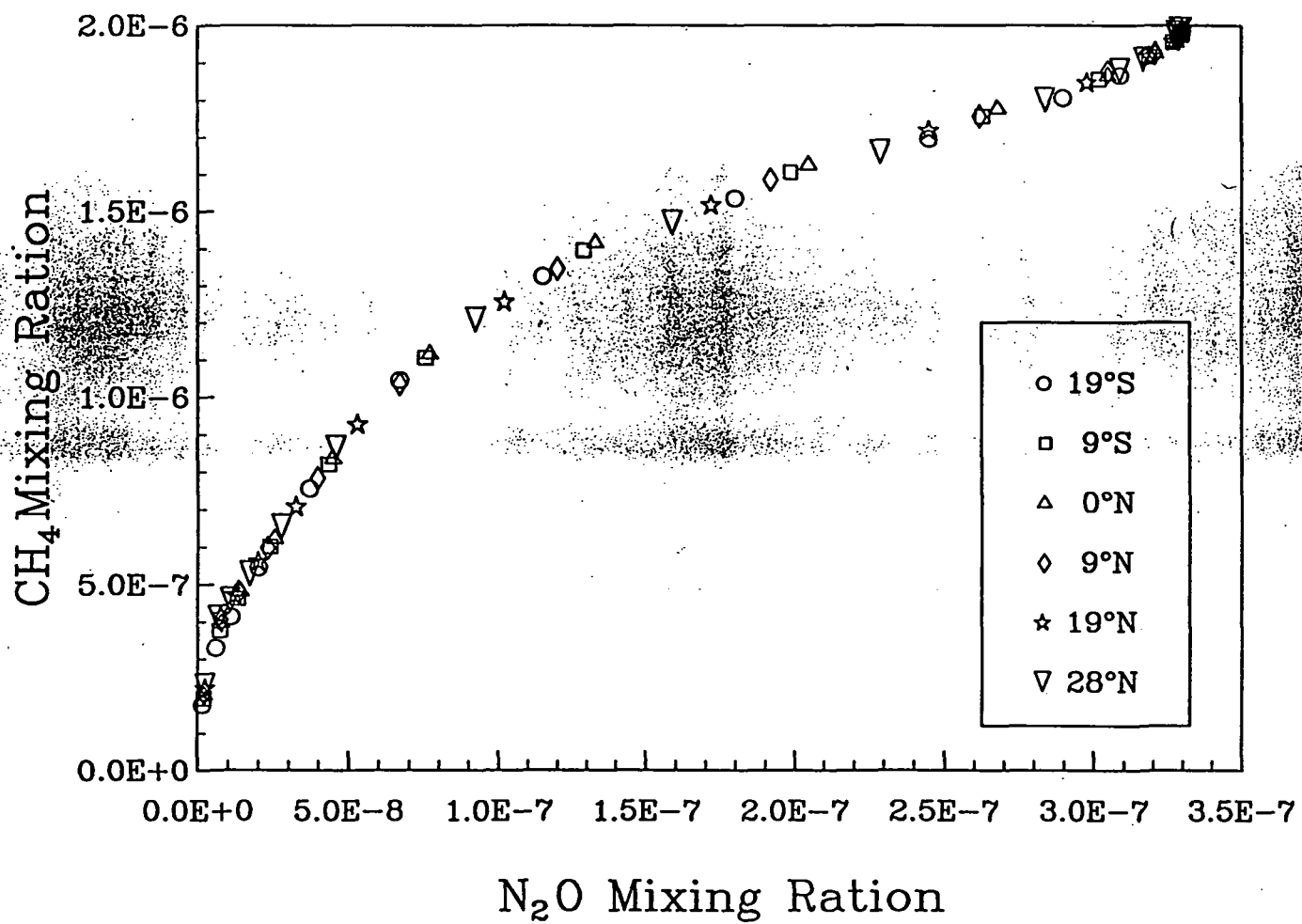
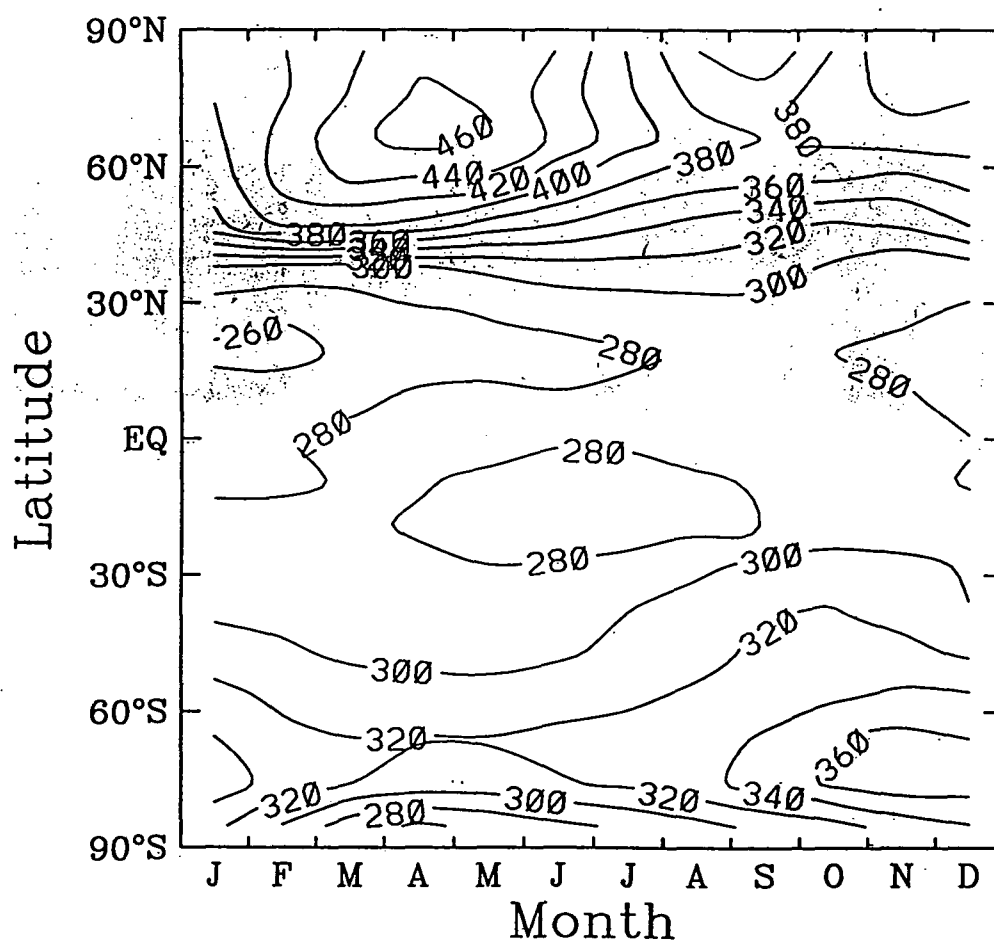


Figure 14b

03 new Chem yr51

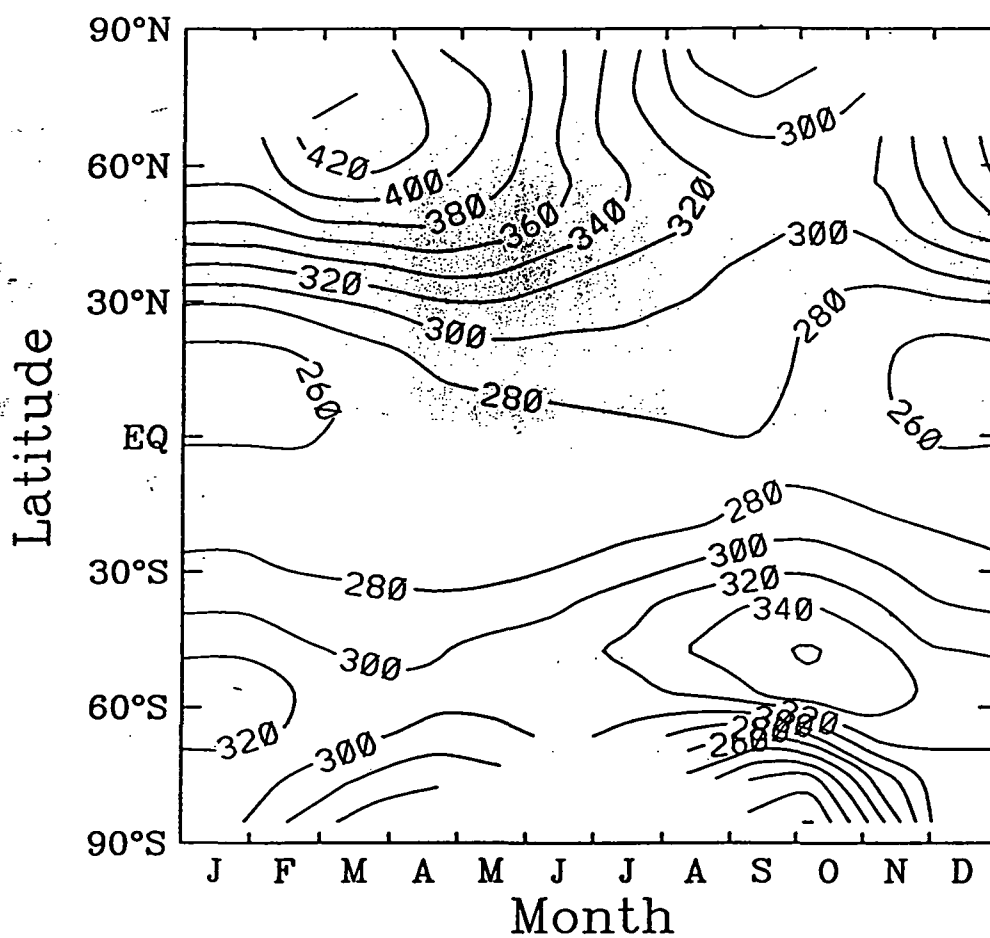


CONTOUR FROM 180.00 TO 700.00 CONTOUR INTERVAL OF 20.000 PT(3,31)= 320.45

Figure 15

Thu Oct 12 10:31:40 EDT 1995

# TOMS Climatology



CONTOUR FROM 160.00 TO 780.00 CONTOUR INTERVAL OF 20.000 PT(3,31)= 316.00

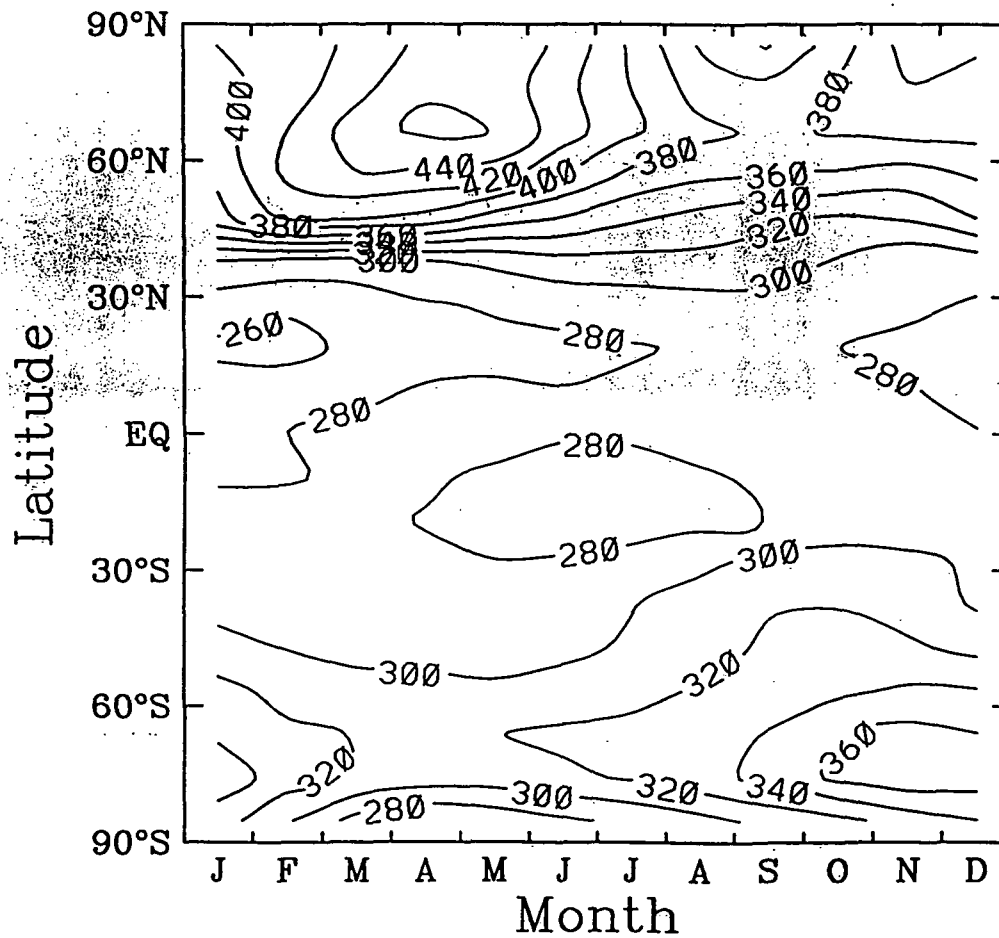
Figure 16

Fri Jul 28 10:22:44 EDT 1995

F.43

ORIGINAL PAGE IS  
OF POOR QUALITY

03 new Chem yr94



CONTOUR FROM 180.00 TO 700.00 CONTOUR INTERVAL OF 20.000 PT(3,3)= 319.18

Figure 17

ORIGINAL PAGE IS  
OF POOR QUALITY

F.44

Mon Oct 16 08:19:18 EDT 1995

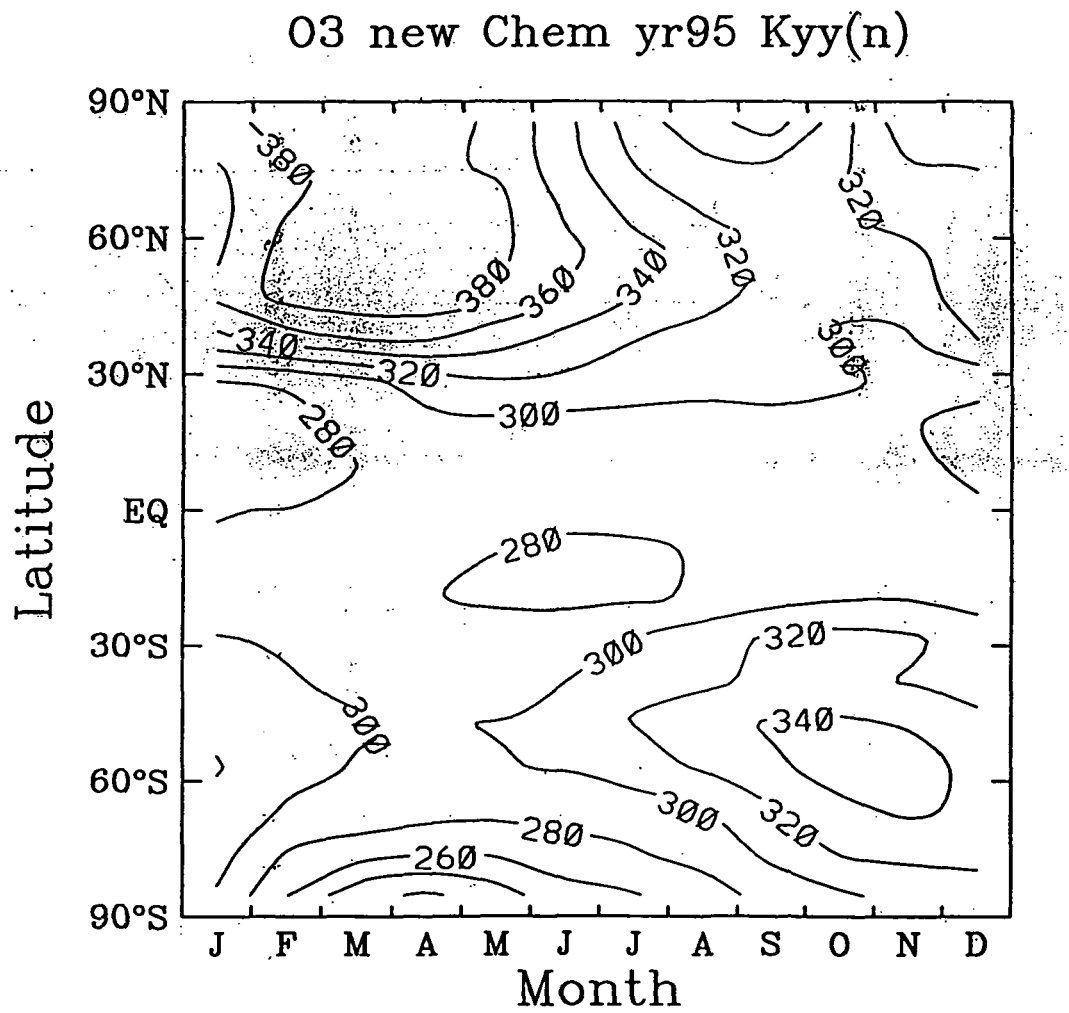


Figure 18

Tue Oct 17 10:33:28 EDT 1995



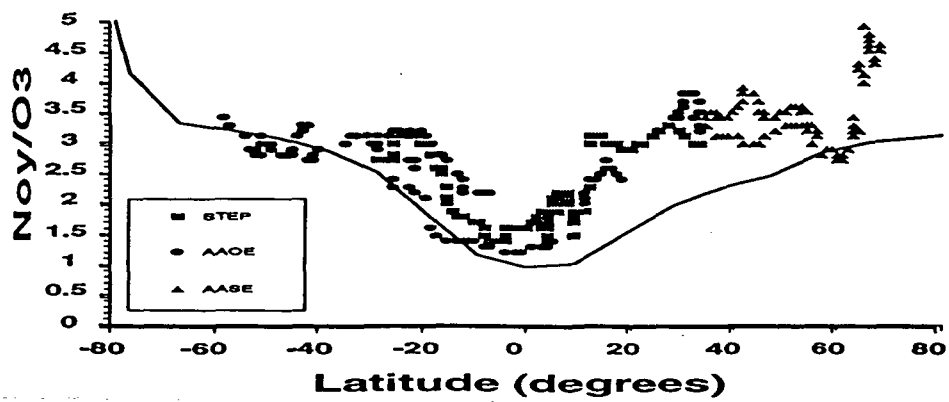
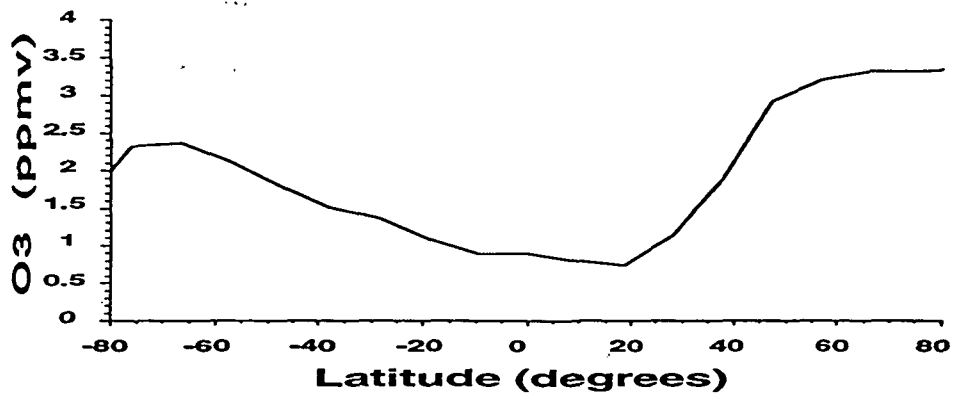
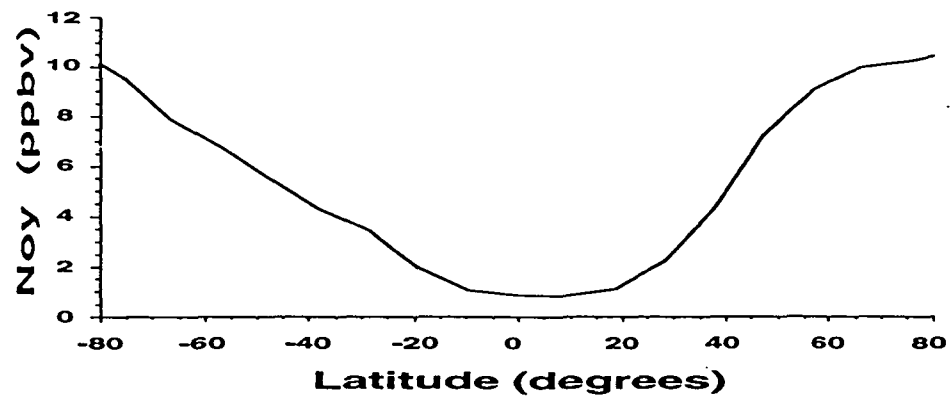


Figure 19

## Appendix G

Shia, R.-L. and M.K.W. Ko (1995) Three-dimensional transport model and cross isentroopic surface transport.

## Appendix G

### Three-Dimensional Transport Model and Cross Isentropic Surface Transport

Run-Lie Shia and Malcolm K. W. Ko

AER Inc., 840 Memorial Dr. Cambridge, MA 02139

#### 1. Introduction

Vertical transport is crucial for long term simulation of tracer distribution in the stratosphere. The ozone simulations using winds from a data assimilation system have shown large biases compared with TOMS and LIMS measurements (Rood et al. 1991; Allen et al. 1991). Weaver et al. (1993) argued that the periodic insertion of observational data during the assimilation process shocks the general circulation model, violates the thermodynamic balance and generates vertical velocities which are different with the vertical velocities of the residual circulation calculated using diabatic heating rates. Our previous assessment studies using two-dimensional model have shown that the calculated atmospheric effects of projected supersonic fleet are quite sensitive to the small change ( $\sim 1$  km) in the flight altitude (Ko et al., 1991). Therefore, it is important to determine the vertical transport velocity accurately in the stratosphere.

We have developed a three-dimensional transport model in isentropic coordinates with the emphasis on the vertical transport. The daily NMC temperature and geopotential data are used to define the location of isentropic surfaces and the Montgomery streamfunction. The horizontal velocities in the isentropic surface are calculated from the Montgomery streamfunction as the geostrophic winds or the "linear balance" winds. The velocities of cross isentropic surfaces can be derived from the net heating rates. A fast radiation code (X. Zhu et al. 1992) is used to calculate the zonal mean net heating rate and the Newtonian cooling rates (Fig. 1) from NMC temperature and SBUV ozone distribution to derive a 3-D heating rates.

Two more schemes to derive the cross isentropic surface transport are tested in the model to be compared with the radiative heating scheme. In addition to the radiative

heating, other diabatic processes, such as friction and dissipation also contribute to the cross isentropic surface transport. We derive two sets of winds for cross isentropic surface transport directly from the NMC data using the mass conservation equation and the Ertel's potential vorticity equation respectively. The derived vertical velocities should include all contribution from diabatic processes. The vertical velocities from these two approaches are much larger than the vertical velocity derived from the net radiative heating. It could mean that other diabatic processes are more important than the radiative heating.

Since the vertical velocities derived from the mass conservation equation or from the potential vorticity equation are quite sensitive to the horizontal velocity fields using different methods (e. g. geostrophic winds or balanced winds), we think it is premature to draw any conclusion from these experiments and further investigation are required.

A global version of the 3-D isentropic transport model has been used to simulate the initial dispersion of HSCT engine emissions immediately after being deposited. The purpose is to generate the source functions for 2-D CTM assessment calculations. It is found that the vertical transport of engine emissions in the initial stage does not affect their potential of ozone depletion seriously if the net radiative heating is used to calculate the velocity of vertical transport.

## 2. 3-D Transport Equation and Vertical Transport Velocity in Isentropic Coordinates

The 3-D transport equation for tracer is

$$\frac{D\chi}{Dt} \equiv \left( \frac{\partial}{\partial t} + \vec{V} \cdot \nabla_{\theta} + \dot{\theta} \frac{\partial}{\partial \theta} \right) \chi = S \quad , \quad (1)$$

where  $\frac{D}{Dt}$  is the total derivative,  $\nabla_{\theta}$  is the gradient on an isentropic surface,  $\vec{V}$  is the velocity on the isentropic surface,  $S$  is the source/sink of the tracer, and  $\dot{\theta}$  is the time derivative of the potential temperature. For adiabatic motions,  $\dot{\theta} = 0$ , and air parcel will stay in the same isentropic surface. In other situation,  $\dot{\theta}$  arises from all diabatic processes.

The mixing ratio of tracer in the isentropic coordinates is

$$\chi \equiv \frac{N}{\sigma} \quad ,$$

where  $N$  is the "mass density" of the tracer in isentropic coordinates, (units:  $\text{kg/m}^2/\text{K}$ ), and

$$\sigma \equiv -\frac{1}{g} \frac{\partial p}{\partial \theta}$$

is the "mass density" of the air in isentropic coordinates (units:  $\text{kg/m}^2/\text{K}$ ). The mass conservation equation in isentropic coordinates is

$$\frac{\partial \sigma}{\partial t} + \nabla_{\theta} \cdot (\sigma \vec{V}) + \frac{\partial}{\partial \theta} (\sigma \dot{\theta}) = 0 \quad . \quad (2)$$

The definition of the Ertel's potential vorticity is

$$P \equiv (\zeta_{\theta} + f) / \sigma \quad ,$$

where  $f$  is the Coriolis parameter,  $\zeta_{\theta}$  is the vertical component of relative vorticity,

$$\zeta_{\theta} \equiv \frac{1}{a \cos \phi} \frac{\partial v}{\partial \lambda} - \frac{1}{a \cos \phi} \frac{\partial (u \cos \phi)}{\partial \phi} \quad ,$$

where  $(u, v)$  are velocity components on the isentropic surface and  $(\lambda, \phi)$  are longitude and latitude coordinates.

The potential vorticity equation (Holton, 1992, p112) in isentropic coordinates is

$$\frac{\partial P}{\partial t} + \vec{V} \cdot \nabla_{\theta} P = \frac{P}{\sigma} \frac{\partial}{\partial \theta} (\sigma \dot{\theta}) + \frac{1}{\sigma} \vec{k} \cdot \nabla_{\theta} \times (\vec{F}_r - \dot{\theta} \frac{\partial \vec{V}}{\partial \theta}) \quad , \quad (3)$$

where  $\vec{F}_r$  is the friction term,  $\vec{k}$  is the unit vector in the vertical direction. By neglecting  $\vec{F}_r$  and rearranging other terms, Eqn. (3) can be written in the form of a transport equation

$$\frac{\partial P}{\partial t} + \vec{V} \cdot \nabla_{\theta} P + \dot{\theta} \frac{\partial P}{\partial \theta} = S_P \quad , \quad (4)$$

and the source term for the Ertel's potential vorticity is

$$S_P \equiv P \frac{\partial \dot{\theta}}{\partial \theta} + \frac{1}{\sigma} \vec{k} \cdot \left[ \left( \frac{\partial \vec{V}}{\partial \theta} \times \nabla_{\theta} \right) \dot{\theta} \right] \quad . \quad (5)$$

Eqns. (4) and (5) show that if  $\dot{\theta}$  is non zero, not only is there transport off isentropic surface (last term in the right hand side of Eqn.(4)), there are also sources and sinks for Ertel's potential vorticity as well.

### 3. Model description

In the 3-D isentropic transport model, Eqn. (2) is put into finite difference form for a model grid that covers the northern hemisphere from  $\theta = 325$  to  $1400$  °K. The model resolution used for this study is  $2^{\circ}$  (Latitude)  $\times$   $5^{\circ}$  (Longitude) with 7 layers. The time step is 15 min. The second moment advection scheme (Prather, 1986) is used for horizontal transport in the model to reduce the numerical diffusion.

The daily NMC temperature and geopotential height data are used to locate isentropic surfaces and to calculate the Montgomery stream function  $M$  on isentropic surface,

$$M \equiv C_p T + \Phi \quad .$$

The horizontal winds,  $\vec{V}$ , are derived from  $M$  using as geostrophic winds or balanced winds. They are interpolated at every time step.

The nonlinear terms in the balance wind equation make the iteration procedure very difficult to converge. A much simpler estimation of higher-order balance can be

made, following Randel (1987), by linearizing these terms about the zonal mean wind. A 6-wave filter is used to smooth the Montgomery streamfunction longitudinally. In most cases, the so called "linear" wind converges after 4-5 iterations.

The rate of cross isentropic surface transport,  $\dot{\theta}$ , is derived using three different approaches. The first approach uses a fast radiation code (X. Zhu et al. 1992) to calculate the zonally averaged heating rates,  $\bar{J}$  in log pressure coordinates. In the calculations, the NMC temperature  $[\bar{T}(z, \phi)]$  and the ozone distribution from SBUV  $[\bar{O}_3(z, \phi)]$  are used. The upper bar denotes zonal-mean quantities. The zonal mean Newtonian cooling coefficient is defined by

$$\alpha(z, \phi) = (\bar{J}(\bar{T} + \Delta T) - \bar{J}(\bar{T})) / \Delta T. \quad (6)$$

In Eqn. (6)  $\Delta T$  is taken to be 0.2 °K. The local 3-D net heating rates can be defined as

$$J(z, \lambda, \phi) = \bar{J}(z, \phi) + \alpha(z, \phi) \cdot (T(z, \lambda, \phi) - \bar{T}(z, \phi)). \quad (7)$$

The vertical transport velocity off the isentropic surface is given as,

$$\dot{\theta} \equiv \frac{D\theta}{Dt} = \left(\frac{J}{C_p}\right) \cdot e^{\kappa z/H}, \quad (8)$$

where  $C_p$  the specific heat at constant pressure,  $H$  is the scale height,  $z$  is the geometric height,  $\kappa = 0.286$ , and  $J$  is the local heating rates defined in Eqn. (7).

The second approach uses the mass conservation equation, Eqn. (2), and assumes that at the top of the atmosphere the mass flux,  $\dot{\theta}\sigma$ , is zero so the mass flux at any level can be expressed as

$$\dot{\theta}\sigma = - \int_{\theta_{top}}^{\theta} \left[ \frac{\partial \sigma}{\partial t} + \nabla_{\theta} \cdot (\sigma \vec{V}) \right] d\theta,$$

or

$$\dot{\theta} = -\frac{1}{\sigma} \int_{\theta_{top}}^{\theta} \left[ \frac{\partial \sigma}{\partial t} + \nabla_{\theta} \cdot (\sigma \bar{V}) \right] d\theta. \quad (9)$$

The third approach is similar to the second one, but uses the potential vorticity equation, Eqn. (4), instead of Eqn. (2). An iteration procedure is used to calculate  $\dot{\theta}$ . The initial guess  $\dot{\theta}_0$  is obtained by inverting Eqn. (4) with  $S_p = 0$ . Eqn. (4) is then iterated to solve for  $\dot{\theta}_i$  where  $S_p$  in the RHS is calculated using  $\dot{\theta}_{i-1}$  from the previous iteration.

#### 4. Vertical Dispersion of Engine Emissions Using 3 Different Schemes for Deriving $\dot{\theta}$

The engine emissions are treated as an inert tracer (the source term in Eqn. (1),  $S = 0$ ). Initially, the engine emissions are evenly distributed along the flight route from L. A. to Tokyo at model layer 4 (50 mb, 20 km or  $\theta = 500$  °K). The seven model layers are at  $\theta = 350, 400, 450, 500, 600, 800, 1200$  °K.

The model was used to perform 20 days simulations for the following 4 cases:

- 1) use meteorological data from June 1-20, 1983 and the vertical velocity derived from the net radiative heating rates,
- 2) use meteorological data from December 1-20, 1984 and the vertical velocity derived from the net radiative heating rates,
- 3) same as 2), but use the vertical velocity derived from the mass conservation equation,
- 4) same as 2), but use the vertical velocity derived from the potential vorticity equation.

Because the vertical transport velocities produced by the net radiative heating rates are small and negative, only slight downwards dispersion are observed in the case 1) and 2). The vertical velocities derived from the mass conservation equation and the potential vorticity equation are much larger and in both direction. Therefore, much strong vertical dispersion are calculated in the case 3) and 4), (See Table 1).



**Table 1: The distribution of engine emissions (%) after 20 days**

layer	$\theta$ °K	case 1	case 2	case 3	case 4
1	350 (~12km)	0.3	0.4	13.2	21.3
2	400 (~15km)	2.1	2.9	12.2	8.9
3	450 (~18km)	17.3	21.7	17.1	11.1
4	500 (~20km)	80.2	75.0	23.5	17.2
5	600 (~24km)	0.	0.	19.9	25.6
6	800 (~30km)	0.	0.	13.6	13.5
7	1200 (~38km)	0.	0.	0.5	2.4

#### 5. Global version of 3-D isentropic transport model

In order to generate the source function for 2-D models, the original 3-D isentropic transport model for northern hemisphere is expanding into a global 3-D model. The  $\theta$  derived from net radiative heating rates (see section 3) is used to get the vertical transport velocity. Two test runs using the global model have been completed, with an initial distribution representing the HSCT engine emissions along the LA to Tokyo route and LA to Sydney route respectively. In both cases the initial sources are transported by the balanced wind derived from the daily NMC data for January of 1983. Taking into account that the balanced wind is not a good approximation in the tropics, the wind in the tropics are obtained instead by interpolating balanced winds at 20° S. and 20° N.

In the LA to Tokyo case, the distribution of engine emissions is almost exact as the counterpart calculated in the model for the northern hemisphere because of weak cross tropics transport. Fig. 2 illustrates how the engine emissions moving around and spreading along the longitudinal direction in 30 days. The simulated emission distributions in the second case of LA to Sydney route show some interesting features. Due to the differences in the zonal winds and the weak exchange between the two hemispheres, originally continuous distribution is broken into two segments after several days. At the end of the month, the emissions are stretched along the latitude direction more evenly in the northern hemisphere than in the southern hemisphere (Fig. 3).

The HSCT emission distribution with  $1^\circ \times 1^\circ \times 1$  km resolution for the double fleet scenario of  $M=2.4$ ,  $EI=15$  has been retrieved from NASA database and the  $\text{NO}_x$  emission in its top 8 layers, (from 13 km to 21 km) is used as a continuous source added everyday into the global 3-D isentropic transport model to generate source function for 2-D chemistry transport models. The original model vertical structure of 7 layers from potential temperature =  $325^\circ$  to  $1400^\circ$  has been changed to 12 layers from  $325^\circ$  to  $1000^\circ$ . Most of these layers are in the lower stratosphere, where the engine emissions from supersonic aircraft are deposited. The horizontal resolution is  $10^\circ$  (longitude)  $\times$   $5^\circ$  (latitude) instead of  $5^\circ \times 2^\circ$  used in the northern hemisphere version to speed the calculation. The model runs start at the beginning of every month. After being transported for 30 days, the  $\text{NO}_x$  distribution is more zonally spread, but still not really zonally symmetric. The zonal mean of the 3-D distribution obtained after the 30 day simulation was used as the source in 2-D CTM for that month. We are especially interested in the effects of vertical transport, which could change the residence time of engine emissions in the stratosphere and thus change the calculated ozone depletion. For every month two runs using 3-D isentropic transport model are completed, one with cross isentropical surface transport calculated from radiative heating rates and one without. The 2-D source functions with and without 3-D transport and their differences are plotted in Figs. 4, 5 and 6, with resolutions of  $5^\circ$  (latitude)  $\times$  1 km (altitude, from 13 km to 21 km), i.e.  $36 \times 8$  grid boxes. Fig. 4 shows the 2-D source function from zonal mean of NASA source distribution, i. e. source function without 3-D transport. Note that the total source is  $2.8 \times 10^{34}$  mol/yr and the averaged source in one box is  $9.6 \times 10^{31}$  mol/yr. Fig. 5 displays the differences between 2-D source function without 3-D transport, i.e. shown in Fig. 4 and 2-D source functions generated by 3-D transport with cross isentropic surface. Fig. 6 shows the differences between 2-D source functions generated by 3-D isentropic transport model runs with and without cross isentropical surface transport. Due to the 3-D transport  $\text{NO}_x$  increase in northern high latitudes and most southern hemisphere in all seasons by about  $5 \times 10^{31}$  mol/yr (Fig. 5). This is because there are few exhausts deposited there directly by aircraft. The differences between the 2-D source functions generated by two 3-D model runs demonstrate that the effects of transport across isentropic surface are smaller (Fig. 6).

The source functions for January with and without cross isentropical surface transport are put into AER 2-D CTM with  $19$  (latitude)  $\times$   $51$  (altitude, from surface to about 60 km) resolution to calculate ozone depletion. The results are compared with the model results using original source function (directly zonally averaged NASA  $1^\circ \times 1^\circ \times 1$

km emission distribution). Fig. 7 shows the ozone depletion caused by engine emissions. In most of the northern hemisphere the ozone depletion is about 1.5% to 3% (Fig. 7a). The 3-D transport changes these values only by less than 0.04% (Fig. 7b). The contribution of the cross isentropical surface transport to this change is significant in the middle northern hemisphere. Therefore, if the cross isentropical surface transport is much larger than that calculated by radiative heating, 3-D dispersion could have more effects on ozone depletion potential of HSCT exhausts. We think more works are required to clarify this puzzle.

## REFERENCE

- Allen, D. J., A. R. Douglass, and R. B. Rood: Application of a monotonic upstream transport scheme to three-dimensional constituent transport calculations. *Mon. Wea. Rev.*, **119**, 2456-2464, 1991.
- Holton, J. R., An introduction to dynamic meteorology, Third edition, Academic Press Inc., 1992.
- Ko, M. K. W., D. K. Weisenstein, N. D. Sze, R.-L. Shia, J. M. Rodriguez, and C. Heisey, Effects of engine emissions from high-speed civil transport aircraft: A two-dimensional modeling study, NASA Contractor Report 4346, Part II, 1991.
- Prather, M. J., Numerical advection by conservation of second order moments. *J. Geophys. Res.*, **91**, 6671-6681, 1986.
- Randel, W. J.: The Evaluation of Winds from Geopotential Height Data in the Stratosphere. *J. Atmos. Sci.*, **44**, 3097-3120, 1987.
- Rood, R. B., A. R. Douglass, J. A. Kaye, M. A. Geller, C. Yuechen, D. J. Allen, E. M. Larson, E. R. Nash, and J. E. Nielsen: Three-dimensional simulations of wintertime ozone variability in the lower stratosphere. *J. Geophys. Res.*, **96**, 5055-5071, 1991.
- Weaver, C. J., A. R. Douglass and R. B. Rood, Thermodynamic Balance of three-dimensional stratospheric winds derived from a data assimilation procedure. *J. Atmos. Sci.*, **50**, 2987-2993, 1993.

Zhu, X., M. E. Summers, and D. F. Strobel: Calculation of CO<sub>2</sub> 15- $\mu$ m Band Atmospheric Cooling Rates by Curtis Matrix Interpolation of Correlated-k Coefficients. *J. Geophys. Res.*, **97** 12,787-12,797, 1992.

### Figure Captions

Fig. 1 The zonally averaged net radiative heating rates, ( $^{\circ}$ K/day) calculated using Zhu et al. (1992), for a) June, b) December; and the Newtonian cooling coefficient, (1/day), for c) June, d) December.

Fig. 2 The distribution of engine emissions deposited on L. A. to Tokyo route after being transported by winds of January for a) 0 day, b) 10 days, c) 20 days, and 30 days. The solid lines are contours of mixing ration of NO<sub>x</sub>, double dotted lines are the streamfunction, and the arrows are the horizontal velocity vectors.

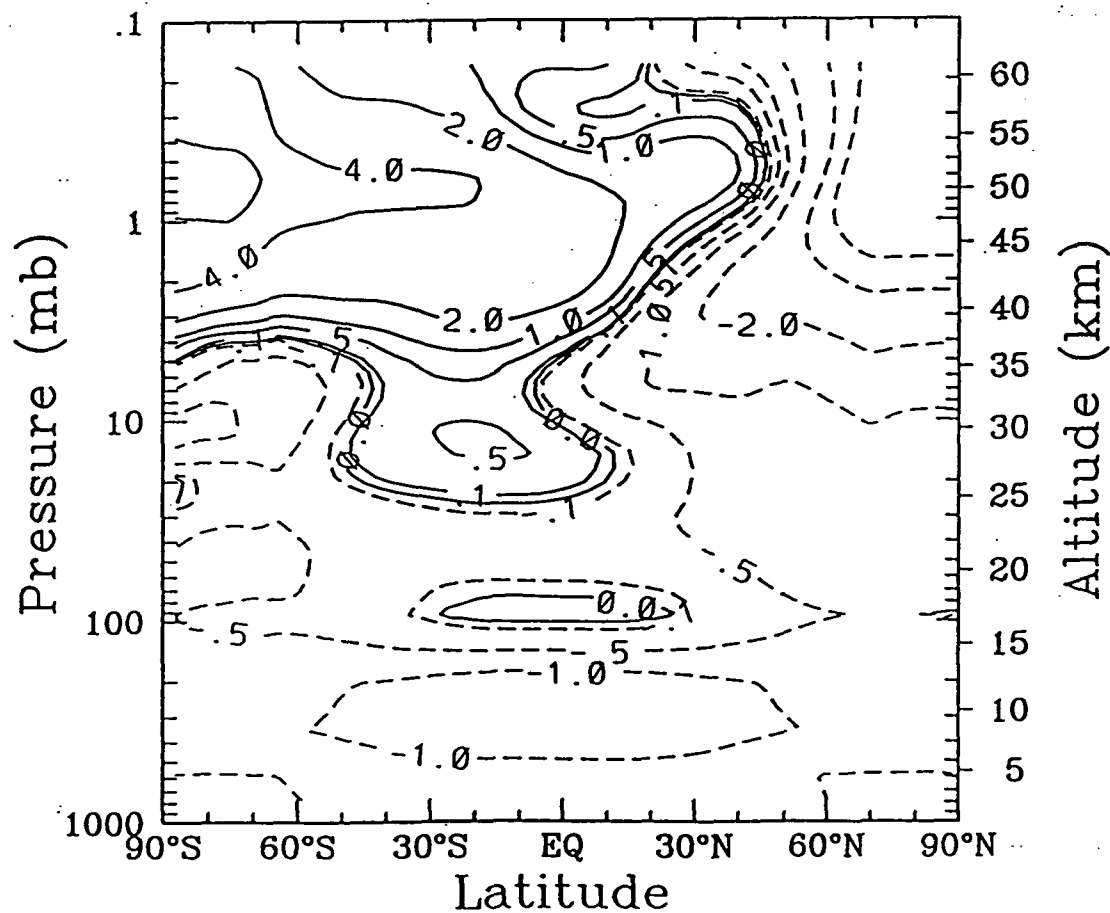
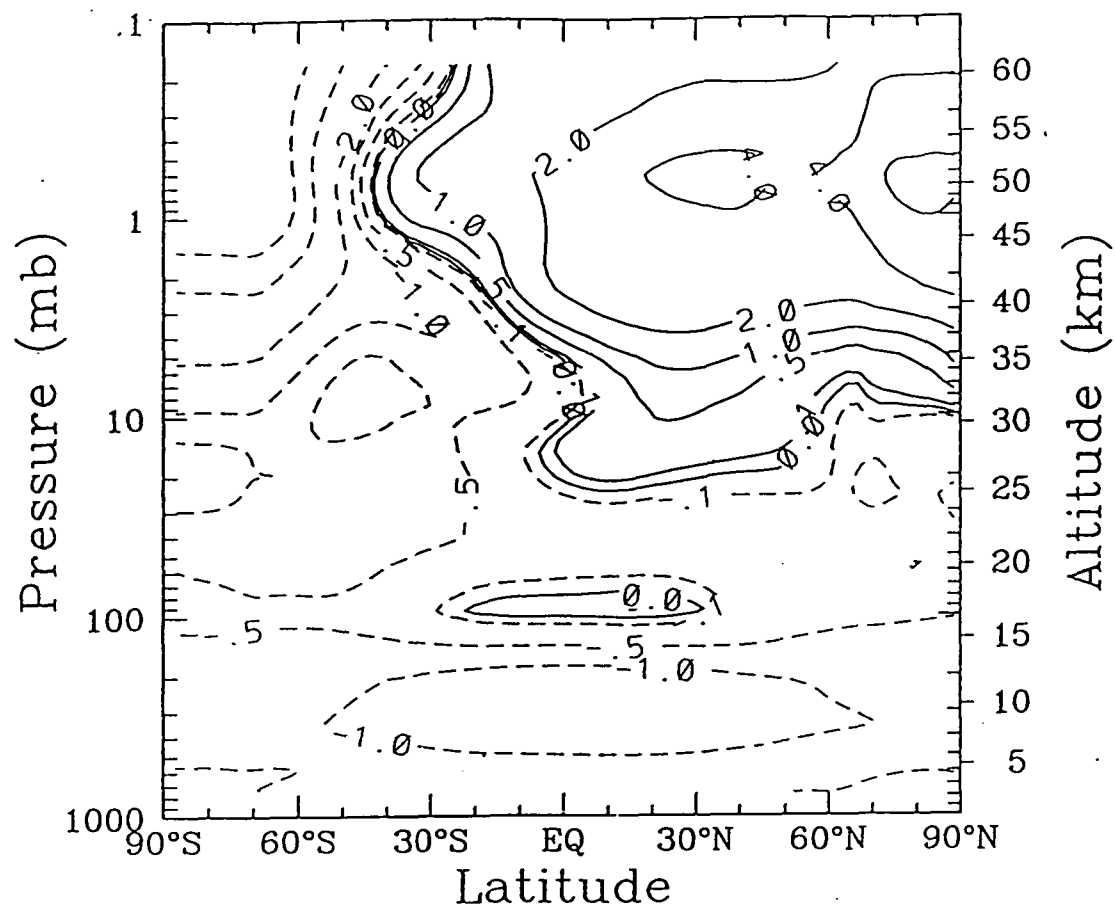
Fig. 3 Same as Fig. 2, but for L. A. to Sydney route.

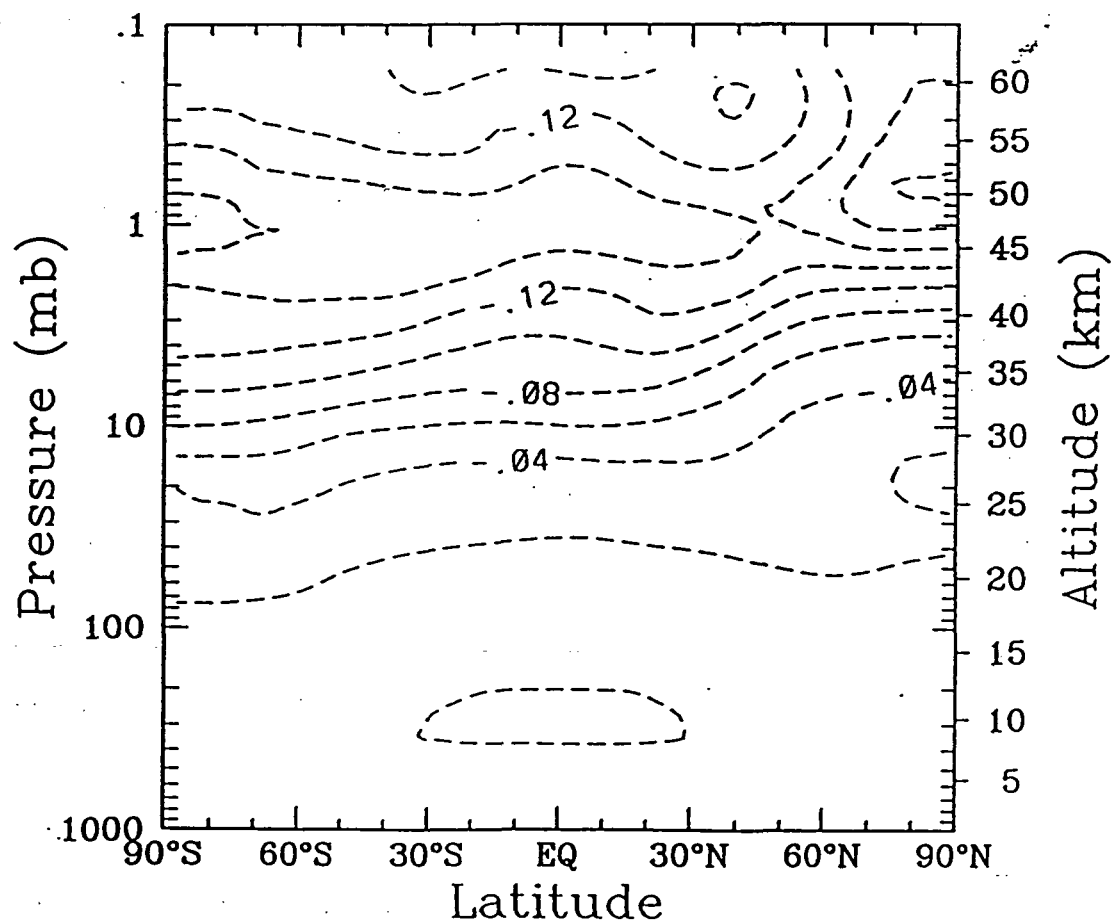
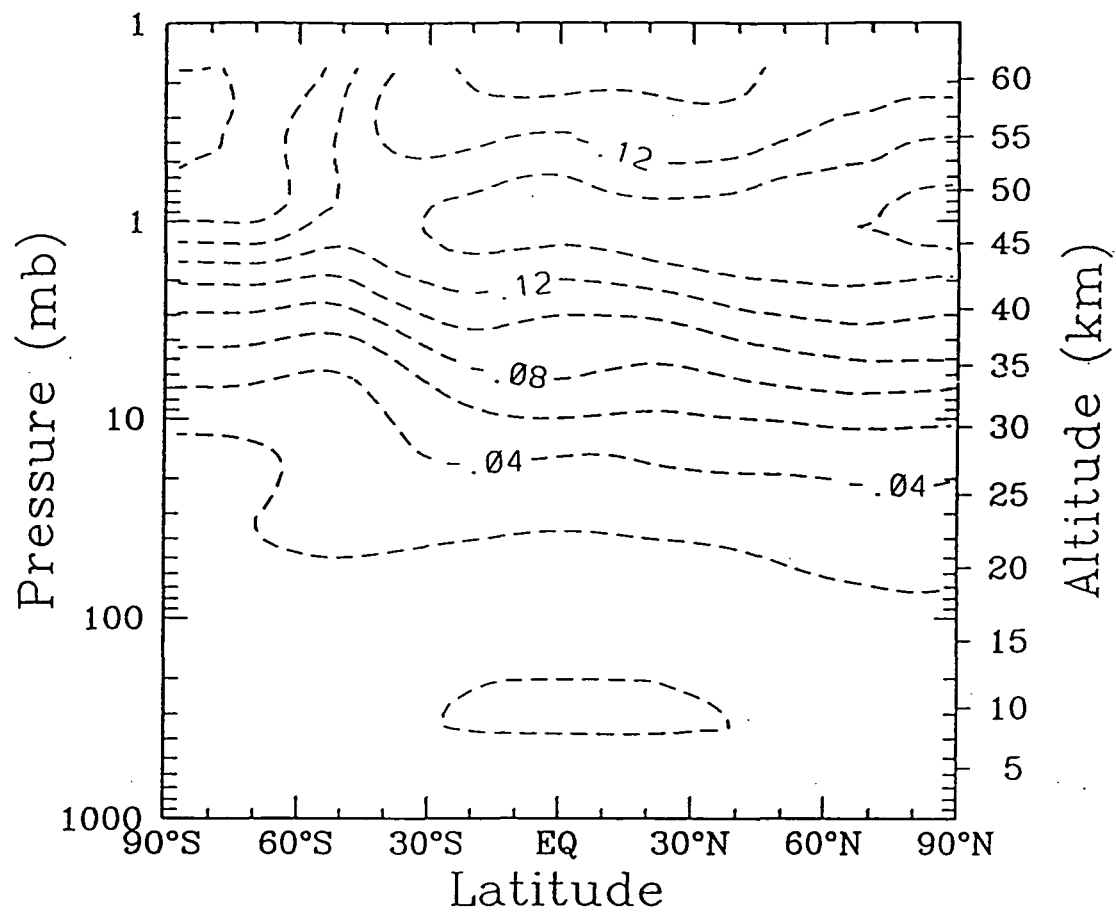
Fig. 4 The two-dimensional NO<sub>x</sub> source distribution directly from NASA 1 $^{\circ}$  x 1 $^{\circ}$  x 1 km source, (unit: 10<sup>32</sup> Mol/yr).

Fig. 5 The NO<sub>x</sub> difference (10<sup>32</sup> Mol/yr) in the two-dimensional source functions due to 3-D transport. Results are shown for four seasons.

Fig. 6 The NO<sub>x</sub> difference (10<sup>32</sup> Mol/yr) in the two-dimensional source functions for the cases with and without cross isentropic surface transport. Results are shown for four seasons.

Fig. 7 The ozone depletion (%) caused by a) the zonally averaged NASA engine emission distribution, b) the source function after 3-D transport.





TRACER

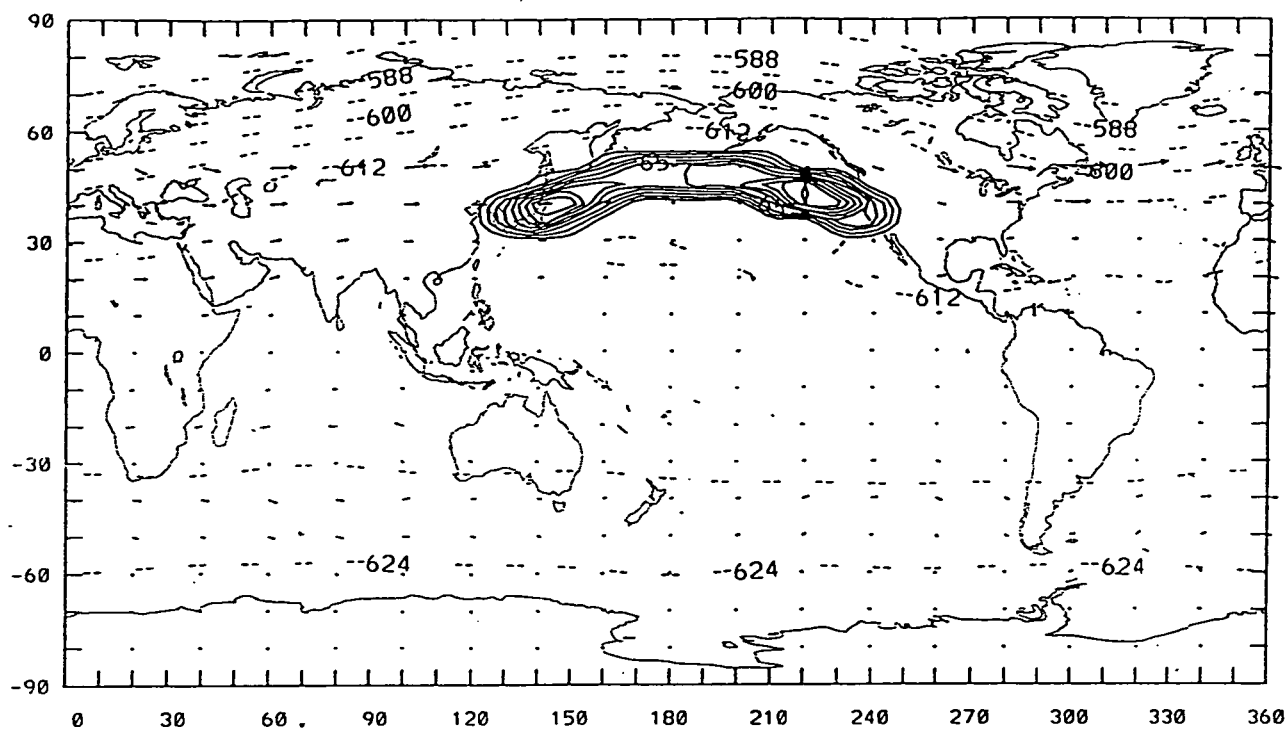
GL

DAYT

0.000

NST

4



TRACER

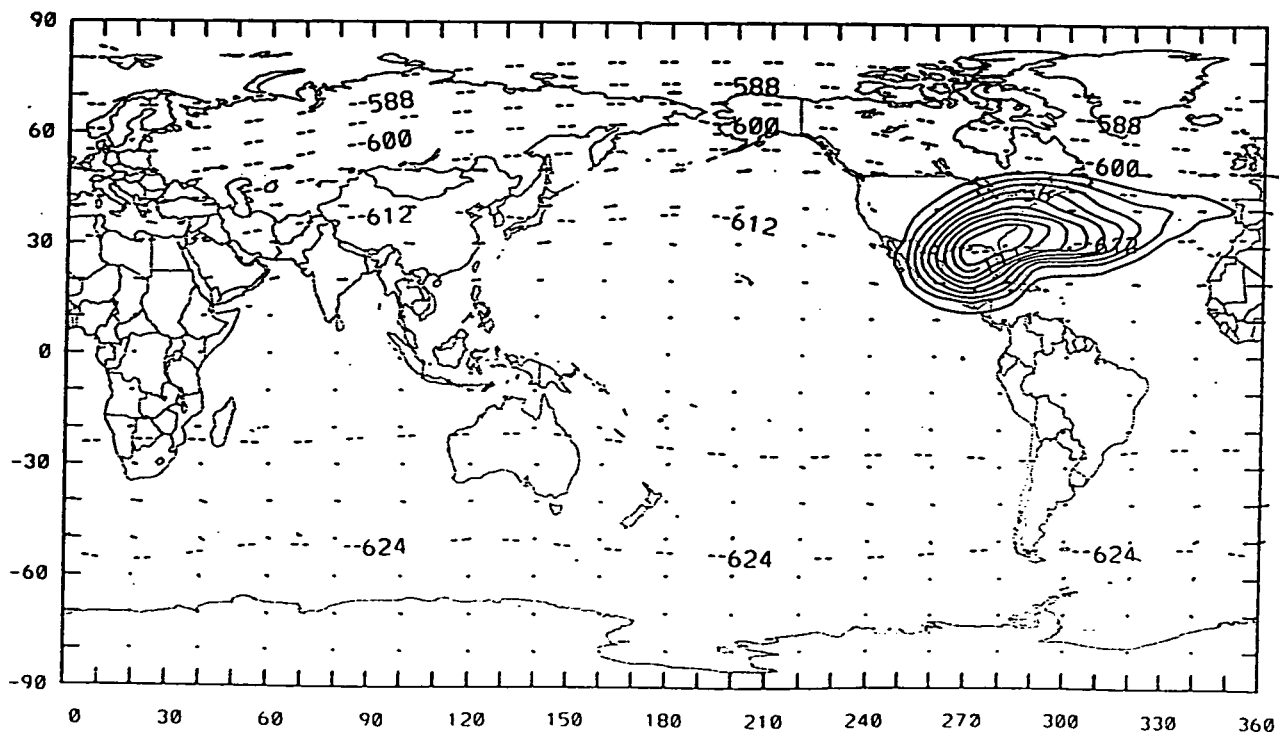
GL

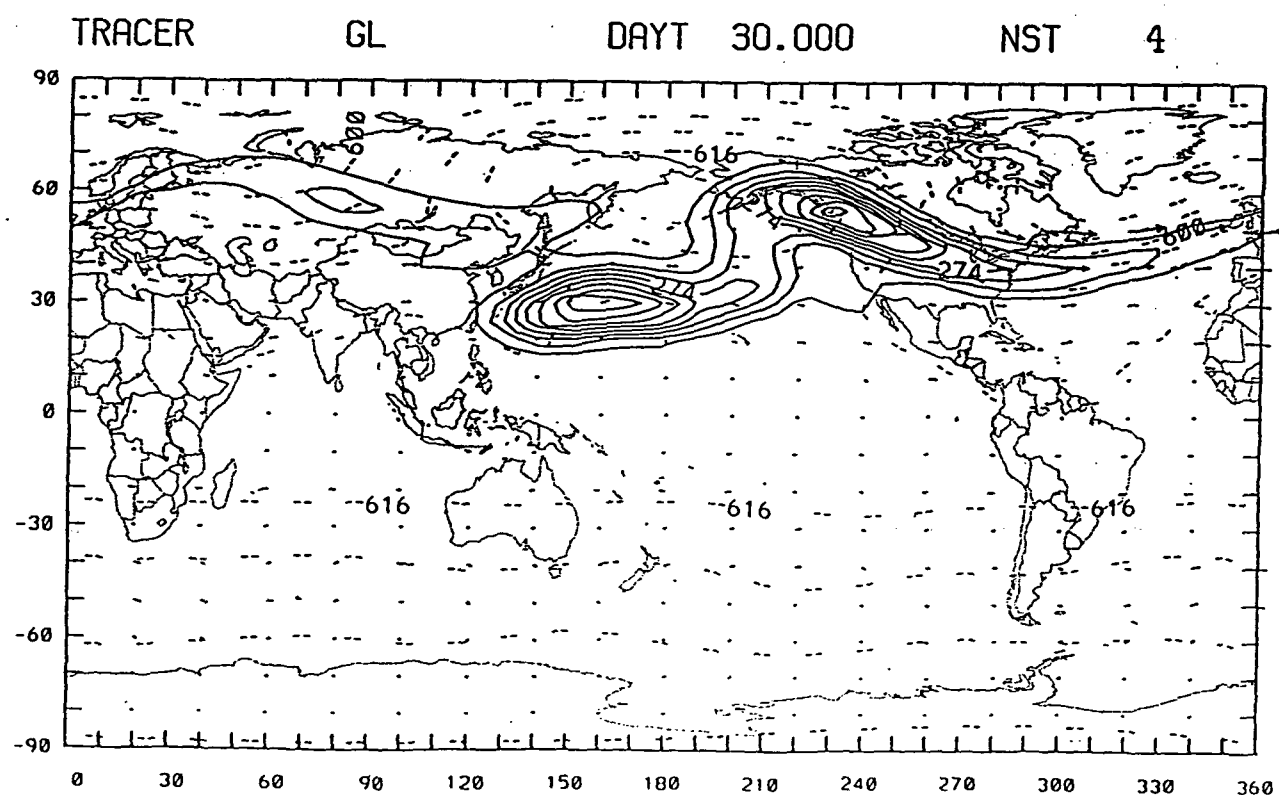
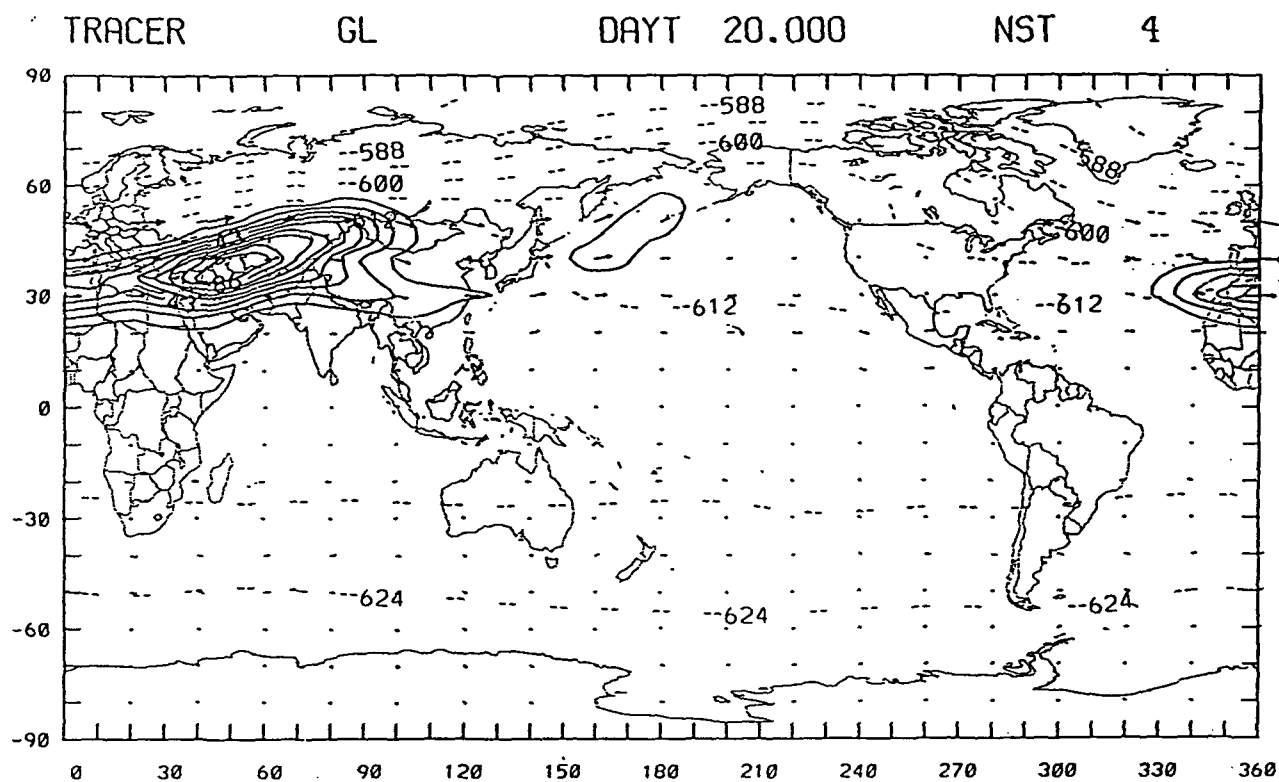
DAYT

10.000

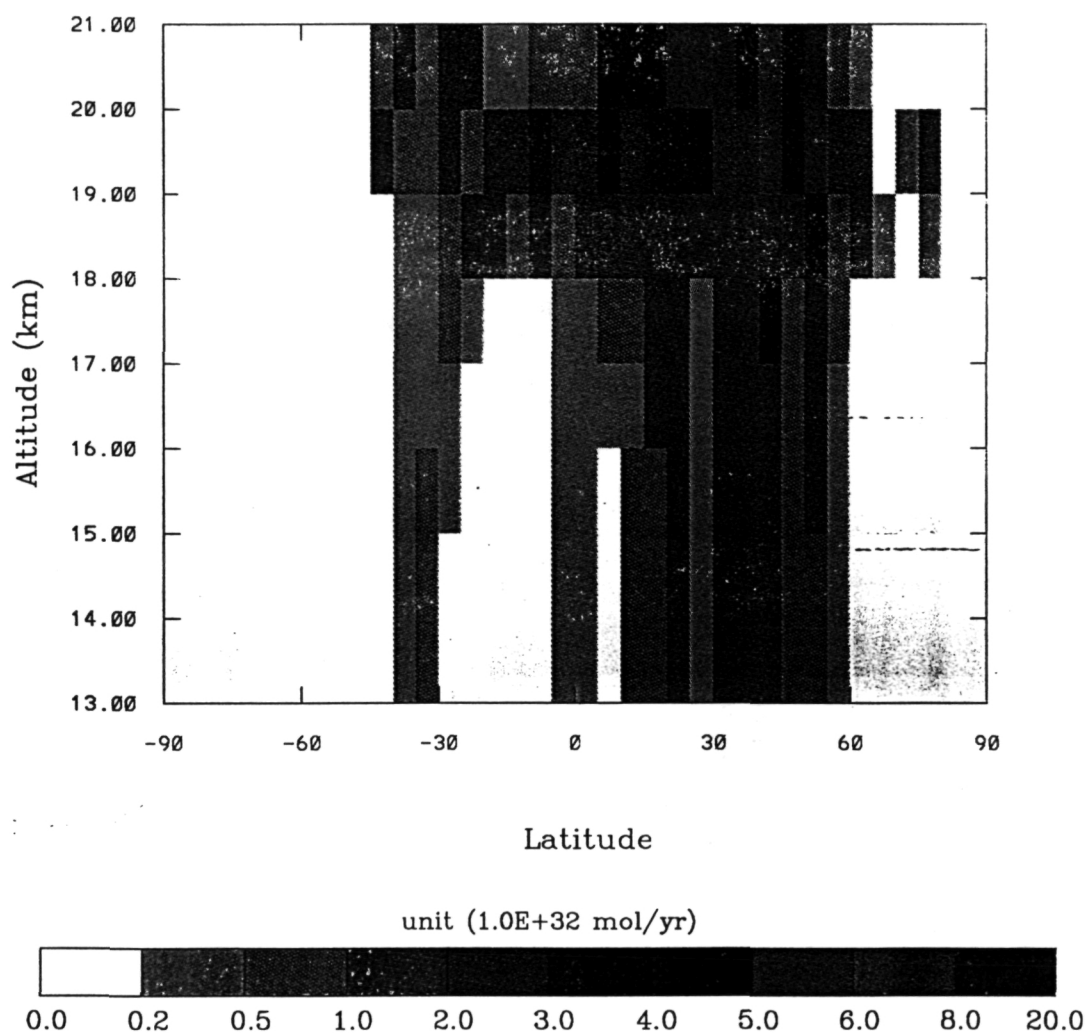
NST

4





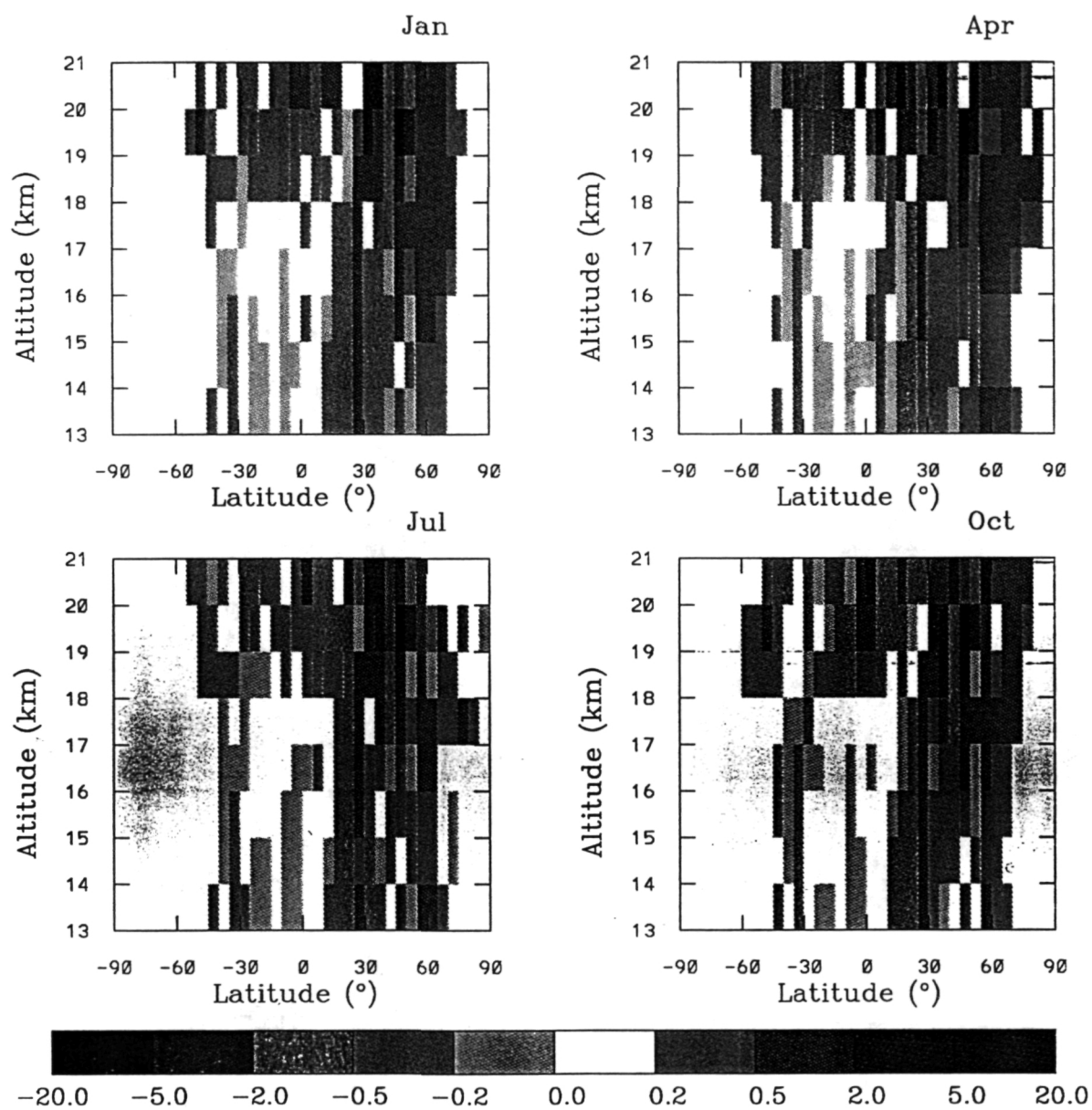


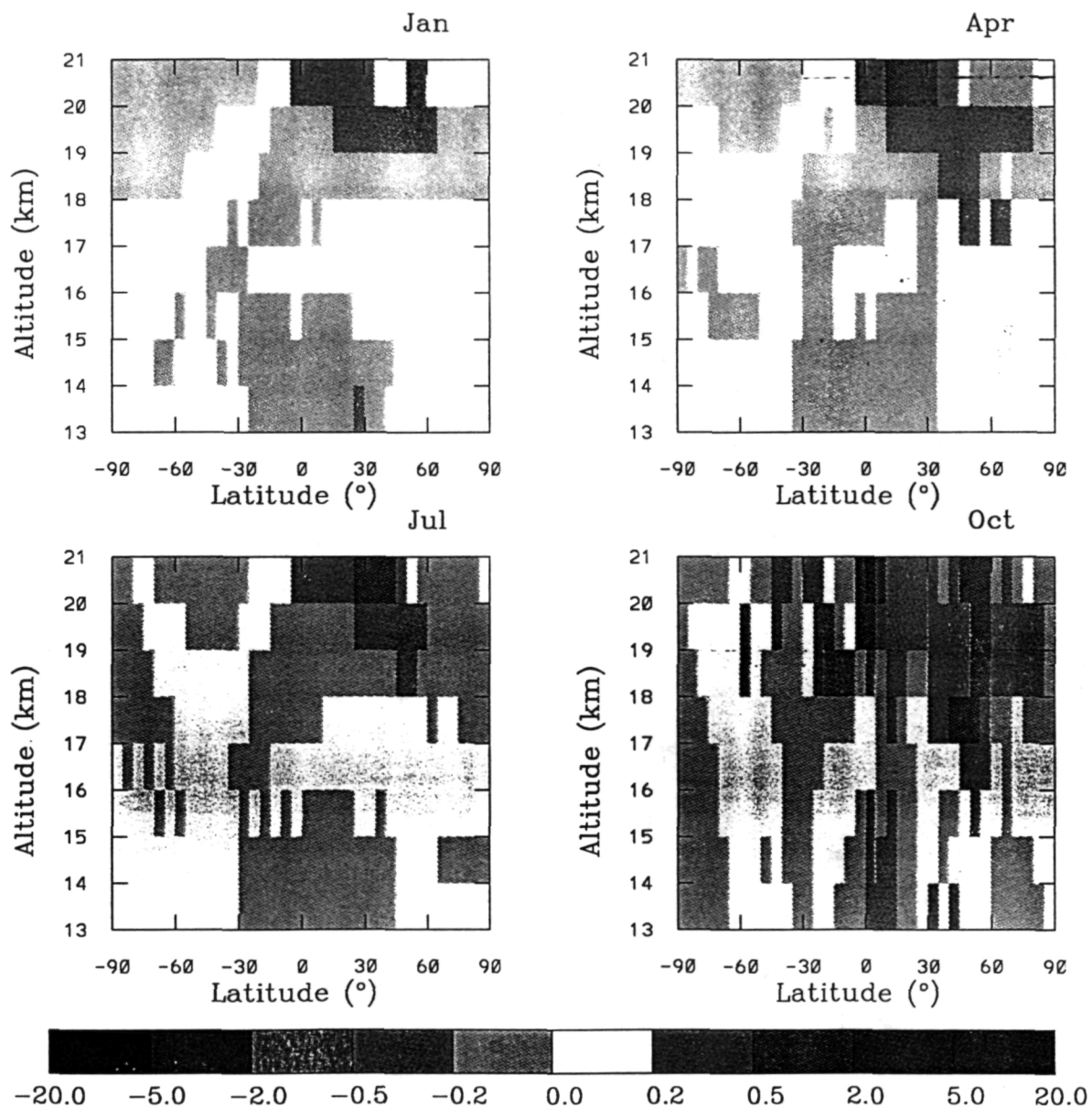


G.17

Fri Dec 8 08:37:18 EST 1995

PRECEDING PAGE BLANK NOT FILMED

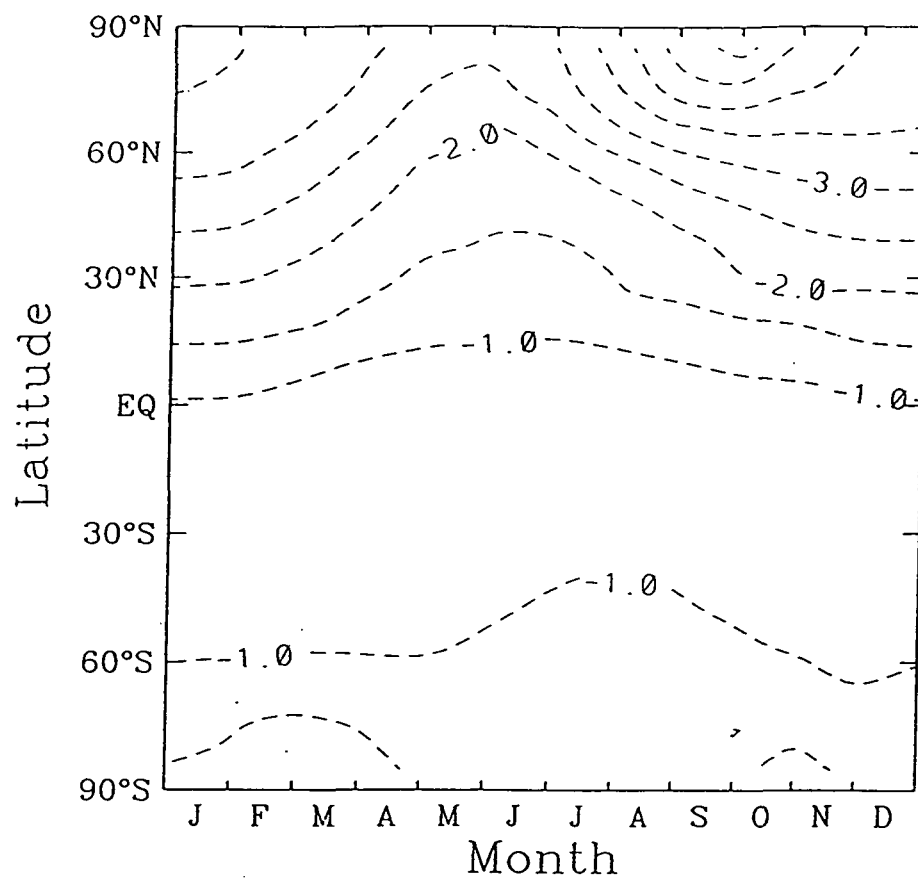




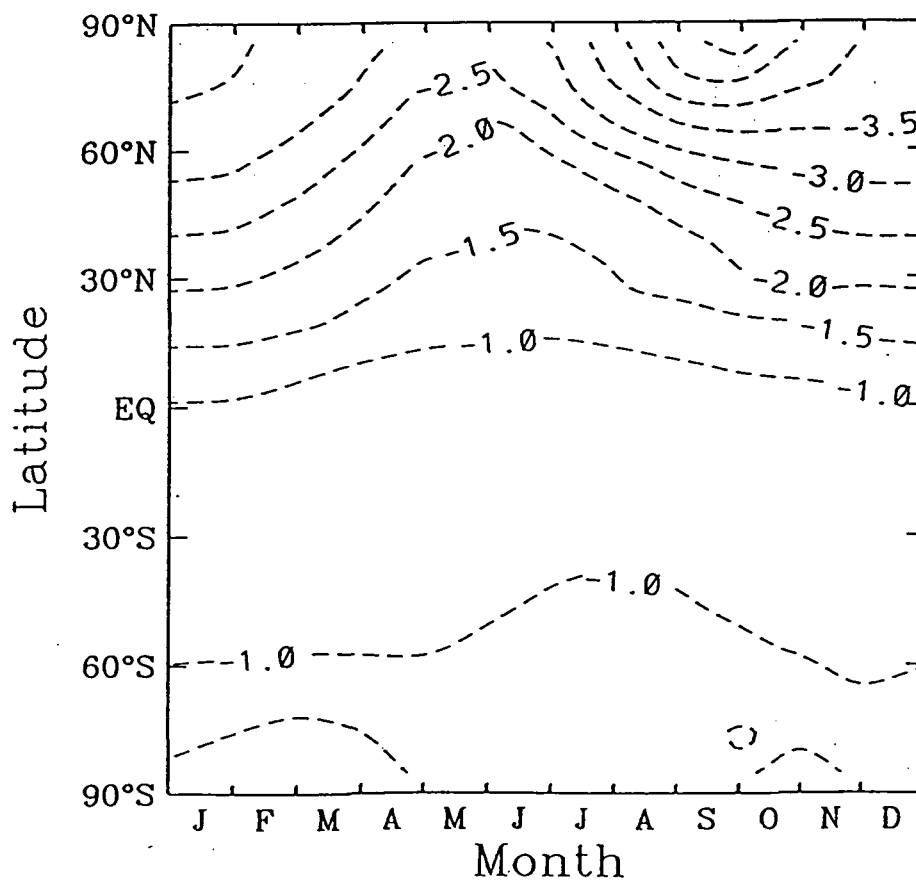
G.18<sub>a</sub>

Fri Dec 8 08:35:44 EST 1995

# EI15 0km Double Fleet - Subsonic (3ppb) Column 03



## EI 15 1000 run 36 yyang compare



## **Appendix H**

Molnar, G.I., M.K.W. Ko, S. Zhou, and N.D. Sze (1994) Climatic consequences of observed ozone loss in the 1980s: Relevance to the greenhouse problem. *J. Geophys. Res.*, **99**, 25,755-25,760

## Climatic consequences of observed ozone loss in the 1980s: Relevance to the greenhouse problem

G. I. Molnar,<sup>1</sup> M. K. W. Ko, S. Zhou, and N. D. Sze

Atmospheric and Environmental Research, Incorporated, Cambridge, Massachusetts

**Abstract.** Recently published findings using satellite and ground-based observations indicate a large winter and summertime decrease in the column abundance of ozone at high and middle latitudes during the last decade. Using a simple ozone depletion profile reflecting the observed decrease in ozone column abundance, Ramaswamy et al. (1992) showed that the negative radiative forcing that results from the ozone decrease between 1979 and 1990 approximately balanced the greenhouse climate forcing due to the chlorofluorocarbons emitted during the same period. Here, we extend the forcing analyses by calculating the equilibrium surface temperature response explicitly, using an updated version of the Atmospheric and Environmental Research two-dimensional radiative-dynamical seasonal model. The calculated steady state responses suggest that the surface cooling due to the ozone depletion in the lower stratosphere offsets about 30% of the surface warming due to greenhouse gases emitted during the same decade. The temperature offset is roughly a factor of 2 larger than the corresponding offset obtained from forcing intercomparisons. This result appears to be related to the climate feedback mechanisms operating in the model troposphere, most notably that associated with atmospheric meridional heat transport. Thus a comprehensive assessment of ozone change effects on the predicted greenhouse warming cannot be accomplished based on forcing evaluations alone. Our results also show that calculations adopting a seasonally and latitudinally dependent ozone depletion profile produce a negative forcing about 50% smaller than that calculated for the depletion profile used by Ramaswamy et al. (1992).

### 1. Introduction

The TOMS satellite data [Stolarski et al., 1991, 1992] clearly show a reduction in the total column abundance of ozone in the past decade. The SAGE satellite analyses [McCormick et al., 1992] and northern midlatitude ozone-sonde data [Staehelin and Schmid, 1991] indicate that these losses have occurred mainly below 25 km in the stratosphere. Model calculations [Wang et al., 1980; Wang and Sze, 1980; Lacis et al., 1990; Ramaswamy et al. [1992], hereinafter referred to as (R92); Schwarzkopf and Ramaswamy, 1993] indicate that while ozone depletion above about 25 km produces positive surface-troposphere forcing, decreases below that level have the opposite effect. The mechanisms responsible for this behavior can be summarized qualitatively as follows: Ozone depletion in the lower stratosphere causes an immediate "initial" forcing (IF) change at the tropopause arising from two competing effects. Because less UV radiation is absorbed by the thinner ozone layer above it, there is an increase in the shortwave radiation at the tropopause leading to an increase in forcing. With the current temperature and ozone profile, ozone depletion just above the tropopause leads to a reduction of the downward longwave flux at the tropopause and a decrease in forcing. If

fixed dynamical heating is assumed above the tropopause [e.g., Ramanathan and Dickinson, 1979; Fels et al., 1980; Kiehl and Boville, 1988], the stratospheric temperatures will adjust until a new equilibrium is reached. In the layers affected by the ozone loss, the local heating is reduced because then there is less ozone molecules to act as absorber. Local temperature cools to reduce the local thermal cooling rate to maintain the balance with the reduced local solar heating rate. This, in turn, further reduces the downward thermal radiation reaching the tropopause. We refer to the tropopause forcing computed following the radiative equilibrium stratospheric temperature adjustment (during which tropospheric parameters are kept fixed) as the adjusted forcing (AF) term.

The R92 study finds that the greenhouse forcing due to halocarbons emitted to the atmosphere during the 1979–1990 period is almost canceled by the AF due to the observed ozone depletion, when a simple, seasonally and latitudinally constant ozone depletion profile is used. The high sensitivity of the ozone greenhouse effect to the vertical distribution of changes in ozone concentration [Wang et al., 1980; Wang and Sze, 1980; Lacis et al., 1990] makes it imperative to use a more realistic ozone depletion profile to assess its effect on the AF. Schwarzkopf and Ramaswamy [1993] reexamined the AF changes for a combination of SAGE-inferred and assumed stratospheric depletion profile changes but did not account for possible seasonal dependencies in the depletion profile. Furthermore, the assessments performed so far [World Meteorological Organization (WMO) 1992; R92; Wigley and Raper, 1992; Schwarzkopf and Ramaswamy,

<sup>1</sup>Now at Universities Space Research Association, NASA Goddard Space Flight Center, Greenbelt, Maryland.

1993] did not address the actual response of the climate system explicitly. We stress that the usual view that there is a simple, linear relationship between the forcing at the tropopause and the steady state surface temperature change ( $\Delta T_s$ ) may not hold for certain types of climate perturbations. Thus we extend previous forcing calculations to determine the equilibrium surface temperature response of the climate system and compare them to the AF changes.

Ideally, general circulation models (GCMs) should be used for climate forcing and response assessments. However, it is difficult to isolate the response due to relatively small perturbations because of the intrinsic model interannual variability in GCMs. Simpler zonal energy balance type climate models (see *North et al.* [1981] for a review) or radiative-convective energy balance models (see *North and Coakley* [1979] for a review) are less plagued by this problem. However, they lack the vertical and horizontal resolution necessary to address the ozone depletion problem. The AER seasonal-radiative-dynamical (ASRD) model has both the horizontal and the vertical structures to address these issues.

We describe the ASRD model and introduce the ozone depletion distributions used for this study in sections 2 and 3, respectively. The results of our experiments are discussed in section 4. Summary and conclusions are presented in section 5.

## 2. Model Descriptions

The ASRD model is an extension of the two-dimensional annual model of *Wang et al.* [1984] and *Molnar and Wang* [1984], as well as the two-dimensional seasonal model of *Gutowski and Molnar* [1988] and *Wang et al.* [1990]. Besides these studies, basic modules of the model have been used in the *Molnar and Wang* [1992] study. The model-calculated seasonal variation of the atmospheric temperature structure, heat fluxes, planetary, and surface albedos are also in good agreement with available observations.

The ASRD version used here includes three zones representing the tropics (30°S–30°N), southern extratropics (30°S–90°S), and northern extratropics (30°N–90°N). Because of the large difference in thermal inertia between ocean and land surfaces, separate land and ocean sectors are included within each latitude zone. Although the model's meridional resolution is coarse, this may be adequate since it has been demonstrated [cf. *North and Coakley*, 1979] that the observed zonal mean surface temperature distribution can be represented rather well using a three-mode Legendre-polynomial expansion (i.e., requiring the computation of only three zonal mean surface temperature values), both on an annual and on a seasonal basis. This can be taken as an indication that the present-day climate can be described by responses to the average seasonal forcing in each zone. Higher meridional resolution would be more appropriate for this study. However, it will be necessary to develop more complicated parameterization schemes of dynamical heat transport for both the Hadley circulation transport in the atmosphere and the heat transport in the ocean. Because no rigorous scheme has yet been developed, we choose to use the three-zone ASRD model for this study. A model with 19 zones is under development.

The model is a "time-marching" type (through the whole seasonal cycle) with 1-day time steps for updating most

model variables. It computes the evolution and spatial distribution of atmospheric (18 vertical layers) and ground temperatures from the heat balance for the atmosphere and the subsurface. The heat transport scheme between the zones is parameterized by the eddy heat flux proportional to the square of the meridional temperature gradient [*Branscome*, 1983; *Stone and Yao*, 1990]. Observations show that heat fluxes associated with the Hadley cells are mostly within the model tropical zone, even in the solstices [*Oort and Peixoto*, 1983]. Consequently, they could have little effect on the transport of heat between the model zones. Surface sensible and latent heat fluxes are parameterized using drag laws, while their vertical distribution is calculated through moist adiabatic or baroclinic adjustments. The shortwave and longwave radiative transfer parameterizations used in this study are described by *Wang and Ryan* [1983], *Wang and Molnar* [1985], and *Wang et al.* [1990]. Water vapor mixing ratios are calculated from prescribed observed seasonal cycle of relative humidity. Cloud amounts and altitudes are fixed at their observed annual cycle in the version of the model used for this study.

The snow cover is parameterized according to *Robock* [1980]. The ice-albedo feedback is parameterized using a thermodynamic sea ice model (for details, see *Molnar and Gutowski* [1994]) based on *Semptner's* [1976] thermodynamic ice model that has been used in many GCMs. For a proper implementation we subdivide the ocean portion of the model zones into 10° wide zones in latitude and compute ice separately for each subzone. The surface radiative fluxes for the ice model are computed at 10° latitude resolution. The seasonally varying hemispheric ice and snow extents are in good agreement with observations.

Heat transport in the ocean is parameterized using the "q-flux" method of the Goddard Institute for Space Studies GCM [*Hansen et al.*, 1984]. The ocean heat flux is obtained from energy balance requirements in a control run that uses specified ocean temperature and ice volume in each zone, based on observations. There are two more steps of model tuning: (1) The "coupling constant" for land-ocean zonal heat transports is adjusted to properly represent the amplitude and phase of the seasonal surface temperature cycle over land. (2) Optical thicknesses of low and middle-level clouds are tuned to provide planetary albedo values close to those observed.

The model's sensitivity to forcing perturbations is rather close to the lower end of climate sensitivities exhibited by GCMs [cf. *Intergovernmental Panel on Climate Change (IPCC)*, 1990, 1992]. For example, doubling atmospheric CO<sub>2</sub> produces a 1.7 K increase in global mean annual surface temperature.

## 3. Inputs for Numerical Experiments

We performed numerical experiments to obtain the change in radiative forcing and surface temperature for three scenarios. In the first case, referred to as the fixed ozone case, ozone is assumed to stay fixed and the change in the concentrations of the greenhouse gases (CO<sub>2</sub> from 334 to 350 parts per million by volume (ppmv), N<sub>2</sub>O from 300 to 308 parts per billion by volume (ppbv), CH<sub>4</sub> from 1538 to 1685 ppbv, CFC-11 from 149 to 253 parts per trillion by volume (pptv), CFC-12 from 250 to 434 (pptv) are from chapter 8, *WMO* [1992], the same as those used in R92. The scale

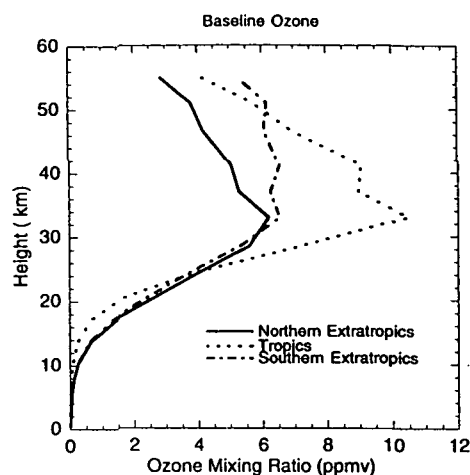


**Figure 1.** Annual mean ozone distributions for the AER seasonal-radiative-dynamical model zones based on the National Center for Atmospheric Research ozone profiles, plotted as ozone mixing ratio as a function of altitude.

heights for the gases are from the AER two-dimensional model [Weissenstein *et al.*, 1992]. The ozone concentration is taken from the NCAR [Forderhase *et al.*, 1980] ozone profiles (see Figure 1, illustrating the mean annual ozone profiles for the three zones). This same ozone is used for both 1979 and 1990 in the fixed ozone case.

We performed two other calculations which we will refer to as cases A and B that use two different 1979–1990 ozone depletion profiles. For both cases the percent change in total ozone column is based on the zonal-mean TOMS data [WMO, 1992]. Absent data for some high-latitude locations were extrapolated from the available data. The total ozone column trend is given as a function of month and model zone in Table 1, where zones 1, 2, and 3 denote 30°N–90°N, 30°S–30°N, and 30°S–90°S, respectively. Previous studies (R92) have prescribed uniform percentage ozone losses in model layers between the tropopause and about 7 km above it. However, observations [WMO, 1992; Staehelin and Schmid, 1991; Wang *et al.*, 1993] show that the vertical profiles of the ozone trend tend to exhibit a seasonal dependence. For instance, during December to March, considerable ozone loss was observed between 20 mbar and 200 mbar (a layer about 14 km thick), while in other seasons, ozone loss can be found in a much shallower layer. For case A the ozone concentration in a given model layer for the year 1990 is obtained by multiplying the 1979 concentration by the coefficients given in Table 2.

To compare our results with R92, we repeated our calculations in case B where the percent ozone change is assumed to be uniform 7 km above 100 mbar in zone 2 and 7 km above

200 mbar for zones 1 and 3. The scaling coefficients for case B (not shown) are smaller than those listed in Table 2, because a smaller number of model layers will be affected by the depletion. Note that the tropopause height is computed in the model and varies between 300 mbar and 100 mbar in the extratropics (associated with the strength of convective activity) during the seasonal cycle. The 200-mbar value for extratropical tropopause was used for evaluating the forcing terms only, in order to be consistent with the R92 work.

#### 4. Results and Discussion

Table 3 summarizes the ASRD model calculated annual mean forcing for the different cases. To avoid uncertainties related to the absolute value of climate sensitivity, we will compare the calculated effects of the observed decadal ozone trend relative to the “fixed ozone” case. The corresponding R92 results are shown for comparison. To make sure that differences in latitudinal resolution are not the cause for large discrepancies in AF for case B between R92 and our results, we have calculated both initial and adjusted forcing terms using a 10° resolution and compared them to those computed by the ASRD model. The AER one-dimensional RC model [Wang and Molnar, 1985; Molnar and Wang, 1992] was applied for each 10° zone and each season to compute the forcing terms using ozone input at 10° resolution both in the 1979 ozone profile and in the depletion coefficient. The results show very good agreement for the net (sum of solar and thermal) IFs (within about 5%), whilst somewhat larger differences can be seen in the net AF values (within about 10–15%). It should be noted that the differences tend to be somewhat larger when comparing solar and longwave forcing separately. Our conclusion is that differences in vertical ozone distribution and/or tropopause heights are more likely causes for the difference. This conclusion is in agreement with previous work of Lacis *et al.* [1990], Schwarzkopf and Ramaswamy [1993], and Hauglustaine *et al.* [1994].

The IF values for all the cases are within 10% of each other. However, the AF values differ significantly among the fixed ozone case and cases A and B. The AF values for the cases including ozone depletion are considerably smaller than that for the fixed ozone case, indicating the overwhelming role of the stratospheric temperature adjustment on the ozone depletion forcing. We may quantify the effect of stratospheric temperature adjustment on tropopause forcing by defining the percent change in IF as  $\%IF = (AF - IF)/IF$ . First of all, the  $\%IF$  differences between case A and case B clearly illustrate the sensitivity of AF to the vertical distribution of the ozone depletion itself. Moreover, while the  $\%IF$  values in the tropics are about the same for all cases, the values for cases A and B in the extratropics are about a

**Table 1.** Percentage Changes in Total Ozone Between 1979 and 1990 for each month for Model Zones 1, 30°N–90°N; 2, 30°S–30°N; and 3, 30°S–90°S

Zone	Month											
	1	2	3	4	5	6	7	8	9	10	11	12
1	-6.10	-6.50	-6.50	-4.90	-3.60	-2.80	-2.50	-2.70	-3.10	-4.10	-4.60	-5.80
2	-0.60	-0.20	-0.10	-0.40	-0.80	-0.90	-0.70	-0.40	-0.40	-0.70	-1.10	-1.30
3	-4.00	-4.30	-5.40	-6.80	-7.30	-7.10	-6.40	-6.40	-8.70	-9.60	-7.80	-5.10



**Table 2.** Case A Ozone Depletion Coefficients in the ASRD Model

Model Level, mbar	Month											
	1	2	3	4	5	6	7	8	9	10	11	12
<i>Zone 1</i>												
200	0.949	0.944	0.942	0.955	1.000	1.000	1.000	1.000	1.000	1.000	1.000	0.951
100	0.886	0.877	0.873	0.901	0.942	0.956	0.961	0.958	0.953	1.000	1.000	0.892
70	0.897	0.888	0.884	0.909	0.914	0.934	0.941	0.937	0.930	0.931	0.922	0.901
40	0.933	0.927	0.925	0.941	0.928	0.945	0.951	0.948	0.942	0.911	0.900	0.936
20	0.974	0.972	0.971	0.977	1.000	1.000	1.000	1.000	1.000	0.961	0.956	0.975
<i>Zone 2</i>												
200	0.994	0.998	0.999	0.996	1.000	1.000	1.000	1.000	1.000	1.000	1.000	0.986
100	0.986	0.995	0.998	0.990	0.987	0.985	0.988	0.993	0.993	1.000	1.000	0.969
70	0.987	0.996	0.998	0.991	0.980	0.977	0.983	0.990	0.990	0.989	0.983	0.972
40	0.991	0.997	0.999	0.994	0.983	0.981	0.985	0.992	0.992	0.986	0.978	0.982
20	0.997	0.999	0.999	0.998	1.000	1.000	1.000	1.000	1.000	0.994	0.990	0.993
<i>Zone 3</i>												
200	1.000	1.000	1.000	1.000	1.000	0.938	0.943	0.942	0.920	0.909	1.000	1.000
100	0.938	0.935	0.920	1.000	1.000	0.863	0.875	0.873	0.823	0.800	0.875	0.920
70	0.908	0.902	0.881	0.884	0.873	0.875	0.886	0.884	0.838	0.818	0.812	0.881
40	0.923	0.919	0.901	0.851	0.836	0.919	0.926	0.924	0.895	0.881	0.844	0.901
20	1.000	1.000	1.000	0.934	0.927	0.969	0.971	0.971	0.959	0.954	1.000	1.000

Coefficient is 1 for levels not listed. ASRD, AES seasonal-radiative-dynamical model.

factor of 3 and 4 larger than those for the fixed ozone case. There is also a hemispherical asymmetry, with the southern extratropics exhibiting about a 50% larger %IF than the northern extratropics. This is due to the larger ozone depletion in the southern extratropics adopted in the calculations.

We now examine the change in surface temperature ( $\Delta T_s$ ) if we assume that the forcing is sustained until an equilibrium state is reached. Several recent studies indicate that relationship between  $\Delta T_s$  and the forcing may depend on the nature of the climate perturbation itself and/or what kind of feedbacks are considered and how they are parameterized in a given model [Molnar and Wang, 1992]. Table 4 shows our model-calculated sensitivity factor (SF), defined as the ratio of  $\Delta T_s$  to AF, as well as AF and  $\Delta T_s$  values. We find that on a global average basis, case A leads to about a 10% smaller SF value than that for the fixed ozone case. A much smaller SF value is calculated for case B. Our results clearly show that the surface temperature response is not a simple linear function of the AF distribution.

The latter point can be further clarified by calculating the fraction of the 1979–1990 nonozone gases greenhouse forcing (or surface temperature response) compensated by the observed ozone depletion. The term “percent compensation” in Table 5 refers to the ozone-depletion-induced differences in AF ( $\Delta T_s$ ) expressed as percentage of the AF ( $\Delta T_s$ ) in the fixed-ozone case. An important finding is that in each case, the compensation in the global mean ( $\Delta T_s$ ) is approximately a factor of 2 larger than the AF compensation. In particular, there is a significant compensation in the tropical temperature increase even though there is virtually no change in the corresponding AF. This behavior is caused by model feedback mechanisms operating in the troposphere-surface system. Our analysis indicates that changes in the meridional heat transport are largely responsible. In the fixed ozone case, the warming is considerably larger in the extratropics than in the tropics, due mainly to ice/snow-albedo and convection-related feedback, leading to a decrease in the meridional temperature gradient. This in turn leads to a

**Table 3.** Changes in Tropopause Forcing for the Period 1979–1990 for Different Cases

Experiment	Spatial Average	IF, $\text{W m}^{-2}$	AF, $\text{W m}^{-2}$	Change in Forcing Due to Stratospheric Temperature Adjustment, %IF = (AF-IF)/IF
Fixed ozone	global mean	0.499 (0.450)	0.443	-11%
	northern extratropics	0.447 (0.381)	0.402	-10%
	tropics	0.553 (0.522)	0.486	-12%
	southern extratropics	0.442 (0.390)	0.399	-10%
Case A	global mean	0.536	0.367	-32%
	northern extratropics	0.489	0.305	-38%
	tropics	0.560	0.488	-13%
	southern extratropics	0.537	0.189	-65%
Case B	global mean	0.524 (0.510)	0.289 (0.370)	-45% (-27%)
	northern extratropics	0.460 (0.458)	0.177 (0.246)	-62% (-46%)
	tropics	0.567 (0.538)	0.489 (0.509)	-14% (-5%)
	southern extratropics	0.500 (0.479)	0.003 (0.229)	-99% (-52%)

Whenever applicable, R92 values are shown in parentheses. IF, initial forcing; AF, adjusted forcing.

decrease of the poleward heat fluxes [Stone and Yao, 1990; Stone and Risbey, 1990], resulting in a warming of the tropics. The opposite is happening when the ozone depletion is introduced. The AF compensation is negative in the extratropics while the effect in the tropics is negligible. Consequently, the meridional temperature gradient increases, and heat is transported more efficiently out of the tropics.

The results show that the global annual mean surface cooling due to lower stratospheric ozone depletion offsets 28% of the decadal surface greenhouse warming. This is roughly a factor of 2 larger than the corresponding offset of 17% obtained from forcing comparisons. There is also an approximate factor of 2 difference between the case A and the case B compensation values, both for the forcings and the responses.

The model-calculated surface temperature changes are steady state responses. The "ocean-delay" effect would lessen the magnitude of the actual response. On the other hand, stratospheric temperature response is practically unaffected by ocean heat capacity, so the model results for the stratosphere can be more meaningfully compared with observations. Unfortunately, there are other agents which could have affected lower stratospheric temperatures (e.g., volcanic eruptions), so the measured trend does not necessarily reflect the effects of ozone depletion alone. Spencer and Christy [1993] reported a cooling of 0.44°C/decade based on the microwave sounding unit data from the TIROS N series of NOAA satellite between 1979 and 1991. This can be compared to the linear trend of 0.4°C cooling/decade based on the time series between 1959 and 1988 reported by Oort and Liu [1993]. However, the derived trend could be larger when corrected for the warming following the el Chichon eruption. The model-calculated cooling is about 0.6° to 0.8°C cooling/decade.

## 5. Summary and Conclusions

In addition to radiative forcing calculated using seasonally and latitudinally dependent ozone depletion profiles, we also computed the equilibrium temperature response for both the

**Table 5.** Percent "Compensation" of the 1979–1990 Greenhouse Adjusted Forcing and Surface Temperature Change Due to Ozone Depletion

Experiment	Spatial Average	AF Compensation, %	$\Delta T_s$ Compensation, %
Case A	global mean	-17	-28
	northern extratropics	-24	-27
	tropics	0.4	-22
	southern extratropics	-52	-36
Case B	global mean	-35	-69
	northern extratropics	-56	-63
	tropics	0.6	-52
	southern extratropics	-99	-100

nonozone greenhouse forcing and the ozone depletion forcing.

The calculated change in radiative forcing is sensitive to the vertical profile of the ozone depletion. We found that the change in forcing for a seasonally and latitudinally dependent ozone depletion profiles is a factor of 2 smaller than the case calculated using a depletion profile described in the R92 studies (Table 5).

The observed ozone depletion leads to a decrease in the calculated radiative forcing and surface warming that compensate for part of the change in radiative forcing and surface warming due to accumulation of greenhouse gases. The compensation in surface temperature that results from the decadal ozone depletion is about twice as large as the compensation in forcing. Our analysis indicates that dynamical tropospheric feedbacks associated with atmospheric meridional heat transport are most likely responsible.

In this study we used a three-zone model to illustrate that the forcing and the equilibrium warming depend on the ozone depletion profiles assumed in the calculation. We showed that the adjusted forcing calculated using the average ozone depletion profiles in each zone agrees with the average forcing calculated using 10° resolution. It will be necessary to use a model with finer latitudinal resolution to determine whether the calculated temperature depends on the model resolution. We will use such a model in our future study. At that point, it would be necessary to use more realistic ozone depletion profiles and examine the impact of the effect of decrease in ozone in the upper stratosphere and increase in the troposphere.

**Table 4.** Annual Mean AF and  $T_s$  Changes Together With the SF (=  $\Delta T_s/\text{AF}$ ) Parameter for the Different Cases

Experiment	Spatial Average	AF, W m <sup>-2</sup>	$\Delta T_s$ , °C	SF, °C/W m <sup>-2</sup>
Fixed ozone	global mean	0.443	0.20	0.45
	northern extratropics	0.402	0.26	0.64
	tropics	0.486	0.16	0.34
	southern extratropics	0.399	0.23	0.58
Case A	global mean	0.367	0.15	0.41
	northern extratropics	0.305	0.19	0.62
	tropics	0.488	0.13	0.26
	southern extratropics	0.189	0.15	0.79
Case B	global mean	0.289	0.06	0.21
	northern extratropics	0.177	0.09	0.53
	tropics	0.489	0.08	0.16
	southern extratropics	0.003	0.00	...*

SF, sensitivity factor.

\*This number is not reported because of the very small value of AF.

**Acknowledgments.** This research was supported by the Office of Health and Environmental Research, Carbon Dioxide Research Division of the U.S. Department of Energy (DE-FGO2-86ER60485), by the National Aeronautics and Space Administration (NASW-4775), and by the Alternative Fluorocarbon Environmental Acceptability Studies (AFEAS) program. We thank R. D. Rosen, S. A. Clough, and the reviewers for helpful comments on the manuscript.

## References

- Branscome, L. E., A parameterization of transient eddy heat flux on a beta-plane, *J. Atmos. Sci.*, **40**, 2508–2521, 1983.
- Fels, S. B., J. D. Mahlman, M. D. Schwarzkopf, and R. W. Sinclair, Stratospheric sensitivity to perturbations in ozone and carbon dioxide: Radiative and dynamical response, *J. Atmos. Sci.*, **37**, 2265–2297, 1980.
- Forderhase, K., W. M. Washington, R. M. Chervin, V. Ramanathan, D. L. Williamson, and D. J. Knight, Lower boundary

- conditions for the NCAR global circulation model, *NCAR Tech Note NCAR/TN-157+ STR*, Natl. Cent. for Atmos. Res., Boulder, Colo., 1980.
- Gutowski, W. J., and G. Molnar, Accelerating the convergence of seasonal climate models with mixed-layer oceans, *J. Geophys. Res.*, **93**, 1737–1744, 1988.
- Hansen, J., A. Lacis, D. Rind, G. Russell, P. Stone, I. Fung, R. Ruedy, and J. Lerner, Climate sensitivity: Analysis of feedback mechanisms, in *Climate Processes and Climate Sensitivity*, *Geophys. Monogr. Ser.*, vol. 29, edited by J. E. Hansen and T. Takahashi, pp. 130–163, AGU, Washington, D. C., 1984.
- Hauglustaine, D. A., C. Granier, G. P. Brasseur, and G. Megie, The importance of atmospheric chemistry in the calculation of radiative forcing on the climate system, *J. Geophys. Res.*, **99**, 1173–1186, 1994.
- Intergovernmental Panel on Climate Change (IPCC), Climate change, in *The IPCC Scientific Assessment*, edited by J. T. Houghton, G. J. Jenkins, and J. J. Ephraums, Cambridge University Press, New York, 1990.
- IPCC, Climate change, in *The Supplementary Report to the IPCC Scientific Assessment*, edited by J. T. Houghton, B. A. Callander, and S. K. Varney, Cambridge University Press, New York, 1992.
- Kiehl, J. T., and B. A. Boville, The radiative-dynamical response of a stratospheric general circulation model to changes in ozone, *J. Atmos. Sci.*, **45**, 1798–1817, 1988.
- Lacis, A. A., D. J. Wuebbles, and J. A. Logan, Radiative forcing of climate by changes in the vertical distribution of ozone, *J. Geophys. Res.*, **95**, 9971–9981, 1990.
- McCormick, M. P., R. E. Veiga, and W. P. Chu, Stratospheric ozone profile and total ozone trends derived from the SAGE I and SAGE II data, *Geophys. Res. Lett.*, **19**, 269–272, 1992.
- Molnar, G., and W. J. Gutowski Jr., The faint young Sun paradox: Further exploration of the role of dynamical heat flux feedbacks in maintaining global climate stability, *Int. J. Glaciol.*, in press, 1994.
- Molnar, G., and W.-C. Wang, Dynamical heat-flux feedbacks and global climate stability, *Ann. Glaciol.*, **5**, 106–110, 1984.
- Molnar, G., and W.-C. Wang, Effects of cloud optical property feedbacks on the greenhouse warming, *J. Clim.*, **5**, 814–821, 1992.
- North, G. R., and J. A. Coakley Jr., Difference between seasonal and mean annual energy balance model calculations of climate and climate sensitivity, *J. Atmos. Sci.*, **36**, 1189–1204, 1979.
- North, G. R., R. F. Cahalan, and J. A. Coakley Jr., Energy balance climate models, *Rev. Geophys.*, **19**, 91–121, 1981.
- Oort, A. H., and H. Liu, Upper-air temperature trends over the globe, 1958–1989, *J. Clim.*, **6**, 292–307, 1993.
- Oort, A. H., and J. P. Peixoto, Global angular momentum and energy balance requirements from observations, *Adv. Geophys.*, **25**, 355–490, 1983.
- Ramanathan, V., and R. E. Dickinson, The role of stratospheric ozone in the zonal and seasonal radiative energy balance of the earth-troposphere system, *J. Atmos. Sci.*, **36**, 1084–1104, 1979.
- Ramaswamy, V., M. D. Schwarzkopf, and K. P. Shine, Radiative forcing of climate from halocarbon-induced global stratospheric ozone loss, *Nature*, **355**, 810–812, 1992.
- Robock, A., The seasonal cycle of snow cover, sea ice, and surface albedo, *Mon. Weather Rev.*, **108**, 267–285, 1980.
- Schwarzkopf, M. D., and V. Ramaswamy, Radiative Forcing due to Ozone in the 1980s: Dependence on Altitude of Ozone Change, *Geophys. Res. Lett.*, **20**, 205–208, 1993.
- Semptner, A. J., Jr., A model for the thermodynamic growth of sea ice in numerical investigations of climate, *J. Phys. Oceanogr.*, **6**, 379–389, 1976.
- Spencer, R. W., and J. R. Christy, Precision and lower stratospheric temperature monitoring with the MSU: Technique, validation and results 1979–1991, *J. Clim.*, **6**, 1194–1204, 1993.
- Stahelin, J., and W. Schmid, Trend analysis of tropospheric ozone concentrations utilizing the 20-year data set of ozone balloon soundings over Payerne (Switzerland), *Atmos. Environ.*, **25**(A), 1739–1749, 1991.
- Stolarski, R. S., P. Bloomfield, R. D. McPeters, and J. R. Herman, Total ozone trends deduced from NIMBUS 7 TOMS data, *Geophys. Res. Lett.*, **18**, 1015–1018, 1991.
- Stolarski, R. S., R. Bojkov, L. Bishop, C. Zerefos, J. Stahelin, and J. Zawodny, Measured trends in stratospheric ozone, *Science*, **256**, 342–349, 1992.
- Stone, P. H., and Risbey, On the limitations of general circulation climate models, *Geophys. Res. Lett.*, **17**, 2173–2176, 1990.
- Stone, P. H., and M.-S. Yao, Development of a two-dimensional zonally averaged statistical-dynamical model, III, The parameterization of eddy fluxes of heat and moisture, *J. Clim.*, **3**, 726–740, 1990.
- Wang, W.-C., and G. Molnar, A model study of the greenhouse effects due to increasing atmospheric CH<sub>4</sub>, N<sub>2</sub>O, CF<sub>2</sub>Cl<sub>2</sub>, and CFCl<sub>3</sub>, *J. Geophys. Res.*, **90**, 12,971–12,980, 1985.
- Wang, W.-C., and P. B. Ryan, Overlapping effect of atmospheric H<sub>2</sub>O, CO<sub>2</sub>, and O<sub>3</sub> on the CO<sub>2</sub> radiative effect, *Tellus*, **35**(B), 81–91, 1983.
- Wang, W.-C., and N. D. Sze, Coupled effects of atmospheric N<sub>2</sub>O and O<sub>3</sub> on the Earth's climate, *Nature*, **286**, 589–590, 1980.
- Wang, W.-C., J. P. Pinto, and Y. L. Young, Climatic effects due to halogenated compounds in the Earth's atmosphere, *J. Atmos. Sci.*, **37**, 333–338, 1980.
- Wang, W.-C., G. Molnar, T. Mitchell, and P. Stone, Effects of dynamical heat fluxes on model climate sensitivity, *J. Geophys. Res.*, **89**, 4699–4711, 1984.
- Wang, W.-C., G. Molnar, M. K. W. Ko, S. Goldenberg, and N. D. Sze, Atmospheric trace gases and global climate: A two-dimensional model study, *Tellus*, **42**(B), 149–161, 1990.
- Wang, W.-C., Y.-C. Zhuang, and R. D. Bojkov, Climate implications of observed changes in ozone vertical distributions at middle and high latitudes of the northern hemisphere, *Geophys. Res. Lett.*, **20**, 1567–1570, 1993.
- Weissenstein, D. K., M. K. W. Ko, and N.-D. Sze, The chlorine budget of the present-day atmosphere: A modeling study, *J. Geophys. Res.*, **97**, 2547–2559, 1992.
- Wigley, T. M. L., and S. C. B. Raper, Implications for climate and sea level of revised IPCC emissions scenarios, *Nature*, **357**, 293–300, 1992.
- World Meteorological Organization (WMO), Scientific Assessment of Ozone Depletion: 1991, *WMO Rep. 25*, Geneva, 1992.
- M. K. W. Ko, N. D. Sze, and S. Zhou, Atmospheric and Environmental Research, Incorporated, 840, Memorial Drive, Cambridge, MA 02139.
- G. I. Molnar, Universities Space Research Association, NASA Goddard Space Flight Center, Code 913, Greenbelt, MD 20771.

(Received July 20, 1993; revised July 23, 1994;  
accepted August 12, 1994.)

## Appendix I

MacKay, R.M., M.K.W. Ko, S. Zhou, G. Molnar, R.-L. Shia, and Y. Yang  
(1995) An estimation of the climatic effects of ozone during the 1980s:  
The role of the ozone hole. Submitted to the *J. of Climate*.

# **An estimation of the climatic effects of ozone during the 1980s: The role of the ozone hole**

R.M. MacKay, M.K.W. Ko, S. Zhou<sup>†</sup>, G. Molnar<sup>††</sup>, R.-L. Shia, Y. Yang

## **ABSTRACT**

In order to study the potential climatic effects of the ozone hole more directly and to assess the validity of previous lower resolution model results, the latest high spatial resolution version of the AER seasonal radiative dynamical climate model is used to simulate the climatic effects of ozone changes relative to the other greenhouse gases. The steady state climatic effect of a sustained decrease in lower stratospheric ozone, similar in magnitude to the observed 1979 to 1990 decrease, is estimated by comparing three steady state climate simulations; I) 1979 greenhouse gas concentrations and 1979 ozone, II) 1990 greenhouse gas concentrations with 1979 ozone, and III) 1990 greenhouse gas concentrations with 1990 ozone. The simulated increase in surface air temperature resulting from non-ozone greenhouse gases is 0.26 K. When changes in lower stratospheric ozone are included, the greenhouse warming is 0.15 K which is approximately 42% lower than when ozone is fixed at the 1979 concentrations. Ozone perturbations at high latitudes result in a cooling of the surface-troposphere system that is greater (by a factor of 3) than that estimated from the change in radiative forcing resulting from ozone depletion and the model's  $2\times\text{CO}_2$  climate sensitivity. We find that changes in meridional heat transport from low to high latitudes combined with the decrease in the infrared opacity of the lower stratosphere are very important in determining the steady state response to high latitude ozone losses. The 42% compensation in greenhouse warming resulting from lower stratospheric ozone losses is also larger than the 28% compensation simulated previously by the lower resolution model. The higher resolution model is able to resolve the high latitude features of the assumed ozone perturbation which are important in determining the overall climate sensitivity to these perturbations.

## **1. Introduction.**

Assessing the climatic effects of changes in atmospheric trace gas concentrations is an important scientific issue as well as an essential component of social, economic, and political policy development. The major atmospheric greenhouse gases ( $\text{H}_2\text{O}$ ,  $\text{CO}_2$ ,  $\text{CH}_4$ ,  $\text{O}_3$ ,  $\text{N}_2\text{O}$ , CFC-11, and CFC-12) absorb infrared radiation emanating from the Earth's

---

<sup>†</sup> Now at NMC, Washington DC

<sup>††</sup> Now at NASA Goddard Space Flight Center

radiative forcing to that calculated with ozone held fixed and found that the assumed ozone decreases in the lower stratosphere reduced the net radiative forcing at the tropopause. Schwarzkopf and Ramaswamy (1993) explored the sensitivity of the above radiative forcing to the assumed vertical profile of ozone changes and also found that their results were particularly sensitive to the assumed changes in stratospheric ozone near the tropopause. Since the total ozone mapping spectrometer (TOMS) measures total column ozone and Stratospheric Aerosol and Gas Experiment (SAGE) measures ozone down to about 17 km, the actual ozone profile in the layer between the tropopause and 17 km is highly uncertain. This results in correspondingly large uncertainties in the actual radiative forcing of the surface-troposphere system, particularly at high latitudes where the tropopause is lowest.

In addition to stressing the importance of the vertical and latitudinal variations in ozone changes, Molnar et al. (1994) heretofore M94, have emphasized the importance of seasonal variations in percent ozone changes to the resulting net radiative forcing. They have also noted that although it is often assumed that the surface temperature response is linearly related to the net radiative forcing in 1-D RCMs, this is a poor assumption for higher dimensional climate models, or for the real climate system, which include nonlinear feedback processes. Ramanathan and Dickinson (1979) note that perturbations in solar radiation (due to ozone changes) most strongly influence the surface heating and perturbations of longwave radiation strongly influence the heating of the upper troposphere. This redistribution of heating rates adds to the complexity of estimating changes in surface air temperature from net radiative forcing of the troposphere. To avoid the problems associated with using radiative forcing as a proxy for climate change, Molnar et al. (1994) used the three-zone AER seasonal-radiative-dynamical (ASRD) model to investigate the steady state response of the surface-troposphere system to sustained 1979 to 1990 greenhouse gas changes with and without variations in lower stratospheric ozone. In M94 the seasonal and latitudinal variations of total column ozone changes from 1979 to 1990 were estimated from TOMS.

The three-zone ASRD used in M94 divided the earth into three latitude zones 90N-30N (northern extratropics), 30N-30S (tropics), and 30S-90S (southern extratropics) and hence had limited horizontal resolution. Here we follow the study of M94 using the newest version of the ASRD which has a much higher horizontal resolution (nineteen latitude zones each of approximately 9.5 degrees). Since the percent changes in column ozone are greatest at high latitudes, our hypothesis is that this increased latitudinal resolution will provide additional insights into ozone's influence on the climate system than was possible with the three-zone model of M94.

Seasonally varying cloud amounts, relative humidity, and ozone are all prescribed in the model based on observations. The primary differences between the ASRD-19 and the three-zone version described by Molnar et al. (1994) are outlined below.

#### *a. Oceanic meridional heat transport*

The meridional heat transfer in the mixed layer ocean is calculated assuming that the turbulent diffusion of ocean heat energy is directly proportional the meridional gradient of mixed layer temperature. Using the notation of Watts and Morantine(1990) the temperature change of the mixed layer ocean is calculated from,

$$\frac{\partial T_o}{\partial t} = \frac{K_H}{f_o R^2} \frac{1}{\cos \phi} \frac{\partial}{\partial \phi} \left( \cos \phi \frac{\partial T_o}{\partial \phi} \right) + \frac{(S + IR - LH - SH)}{\rho C_w D} \quad (1)$$

where  $T_o$  is the mixed layer temperature,  $K_H$  the horizontal thermal diffusivity,  $R$  the radius of the earth, and  $\phi$  is the latitude in radians,  $S+IR$  is the net flux of solar plus terrestrial radiation into the ocean,  $LH$  and  $SH$  are the latent and sensible heat fluxes from the ocean surface,  $\rho$  is the density of water (taken as  $1000 \text{ kg/m}^3$ ),  $C_w$  the specific heat capacity of water ( $4186 \text{ J/kg/K}$ ), and  $D$  is the mixed layer depth (50 m). The term  $f_o$ , which is implicitly assumed to be unity in the study of Watts and Morantine, is the zonal fraction of ocean in a latitude belt. We use  $K_H=1.6 \times 10^{12} \text{ m}^2/\text{yr}$  for both the northern southern hemispheres during all seasons. This is comparable to the value of  $1.2 \times 10^{12} \text{ m}^2/\text{yr}$  used by Watts and Morantine (1990) and was adjusted to give a good simulation of observed ice cover and ocean temperature in each hemisphere. The thermodynamic sea ice model used is that described by M94 except that here ocean heat fluxes are calculated as described above instead of using the "q-flux" flux adjustment method described in M94. Thus, the present model has a fully prognostic determination of sea-ice.

#### *b. Atmospheric meridional heat transport*

Meridional heat transport by the atmosphere in the middle to high latitudes is dominated by large scale eddies. In this work we assume that the stratosphere is heated by radiant energy only and that all atmospheric meridional heat transport is confined to the troposphere. There have been a variety of parameterization schemes for tropospheric eddy heat transport in the literature, which are based on baroclinic theory. Here we adopt the scheme developed by Stone (1974) and modified by Peng et al. (1982). It is based in part on the Eady (1949) model and in part on the two-layer model (Holton, 1979).

Meridional heat transport in the tropics is dominated by the Hadley cell transport. Unfortunately, the theoretical basis for the parameterization of Hadley cell heat transport is weak, and empirical correlation between heat transport and temperature gradient is

adiabatic lapse rate (MAL)  $\gamma_m$  at the surface is used to calculate  $\partial\theta/\partial p|_{z=0}$  (the rate of change of potential temperature,  $\theta$ , with respect to pressure,  $p$ , at the surface) using,

$$\frac{\partial\theta}{\partial p} = \frac{0.288\theta}{p} \left( \frac{\gamma_m}{9.8} - 1 \right) \quad (2)$$

[see Houghton (1986) for a derivation of (2)]. The critical lapse rate,  $\gamma_c$ , at other vertical levels is then calculated by assuming that  $\partial\theta/\partial p$  is constant (and equal to  $\partial\theta/\partial p|_{z=0}$ ) throughout the troposphere and inverting (2) with  $\gamma_c$  replacing  $\gamma_m$ . This moist critical lapse (MCL) rate is then compared with the critical lapse rate predicted by baroclinic instability theory. The critical lapse rate used for convective adjustment is the smaller of the two. Once the critical lapse rate is determined, the convective adjustment scheme described by Wang et al. (1984) is used to ensure that all levels are statically stable with respect to the critical lapse rate.

The rationale for assuming  $\partial\theta/\partial p$  is constant throughout the troposphere is based on two primary factors. First, the scheme described above gives a better simulation of the tropical temperature profile than the moist adiabatic lapse rate used by Stone and Carlson (1979). Second, as noted by Rennick (1977) an empirical fit of the observed lapse rates match a constant  $\partial\theta/\partial p$  profile much better than the assumed constant  $\partial T/\partial z$  profile which is often used.

### 3. Climate sensitivity to a doubling of CO<sub>2</sub>.

#### a. The control run (1979)

For the control run climate simulation we use the same realistic 1979 greenhouse gas concentrations as in M94 (see simulation I in Table 1). To ensure a steady state climate, we perform a twenty year simulation run and use the mean of the last five years of this simulation as the control climate year. For example, day 1 (January 1) of the control climate year is the arithmetic mean of day 1 from the last five years of the simulation.

The optical depths of low and middle clouds, and the thermal diffusion of the mixed layer ocean are used to tune the model's surface temperature and seasonal sea-ice area coverage to the observed climate. The global mean annual average surface air temperature and planetary albedo simulated by the model are 288.70 K and 0.29 respectively; both in good agreement with observations. Fig. 2 shows the simulated zonal mean surface air temperatures for Annual, Winter (DJF), and Summer (JJA) averages compared to the observations reported by Willmott and Legates (1993). Inspection of Fig. 2 shows very good agreement between the simulated and observed surface air temperature for all seasons. The simulated two-dimensional temperature fields are shown



large as that due to doubling CO<sub>2</sub>. The global mean albedo change is greatest during the late spring and early summer of each hemisphere May, June, and July, and November, December, January, reflecting an earlier break-up each year of surface ice and snow cover in the 2xCO<sub>2</sub> run compared to the 1xCO<sub>2</sub> run. The simulated 2xCO<sub>2</sub>-1xCO<sub>2</sub> temperature change of 2.70 K simulated by the ASRD-19 is about 60 % higher than that simulated by the three-zone model of M94. Inclusion of the sensitive high latitudes and an interactive sea ice model both contribute to the greater climate sensitivity of the ASRD-19 relative to the three-zone model of M94.

Fig. 6 also shows that the annually averaged simulated 2xCO<sub>2</sub>-1xCO<sub>2</sub> surface air temperature increase at the poles is two to three times greater than in the tropics and that this amplified warming in the polar region is greatest during winter in the northern hemisphere. In an analysis of the response of their eighteen-zone 2-D statistical dynamical climate model, MacKay and Khalil (1995) analyzed the diagnostic output of their model and identified several mechanisms responsible for the larger  $\Delta T_{\text{co}_2}$  at the poles relative to the tropics. Among these were: regions with low surface temperatures are naturally more sensitive to a given forcing than warm regions ( $\Delta T_g \propto T_g^{-3}$ )\*\*, reduction in solar energy reaching the surface in the tropics for 2xCO<sub>2</sub>, differences in static stability between the tropics and polar region, lapse rate feedback, and dynamical heat transport which helps maintain the temperature structure of the atmosphere. These processes also contribute to the response of our 2-D energy balance model. However, for our model  $\Delta T_s$  is larger than the model of MacKay and Khalil by at least 70 % at all latitudes. The greater climate sensitivity of our model is primarily due to the much larger polar warming (primarily associated with sea ice changes) which is in turn propagated to other latitudes through meridional heat transport.

The simulated latitudinal and seasonal structure of the 2xCO<sub>2</sub>-1xCO<sub>2</sub> temperature change (Fig. 7) has several characteristics in common with general circulation model (GCM) simulations (see for example Held, 1993) and other two-dimensional climate models (see for example MacKay and Khalil, 1995). In particular, the ASRD has amplified warming at the poles, a small local warming maximum in the upper troposphere of the tropics, and substantial stratospheric cooling.

One feature present in both our 2-D model and the 2-D model of MacKay and Khalil (1995) is that the difference between high latitude winter surface warming and summer surface warming is much more pronounced for the northern hemisphere than for the southern hemisphere. Many GCM simulations also exhibit this interhemispheric asymmetry, see Washington and Meehl (1993) or Colman et al. (1994). There is little

---

\*\* Where the subscript g stands for the ground which is assumed to be a black body for infrared radiation.

the three-zone model experiments of M94, the seasonal and vertical distributions of percent ozone change used in M94 were first estimated for a grid that is identical to the present nineteen-zone model grid; averages were then taken to obtain the ozone distributions used for the three-zone experiments. Thus the percent ozone changes used here for the VOE are identical to those used in M94 for their Experiment A. This makes the comparison between the two models more meaningful.

We begin by comparing the response of the nineteen-zone model to that of the M94 three-zone model for each experiment described above. Fig. 8 shows the annual mean adjusted forcing simulated by the three-zone and nineteen-zone ASRD models for 1990-1979 greenhouse concentration changes of the FOE (top) and VOE (bottom) at the specified latitude zones. In addition to the global (G), northern extratropical (NX), tropical (T), and southern extratropical (SX) averages for both the three and nineteen-zone models, we have also included the averages of the north and south polar regions (NP and SP) of the nineteen-zone model. Since the assumed ozone changes are largest near the south pole, including this additional information is useful in understanding the behavior of the nineteen-zone model.

For the FOE, the adjusted forcing simulated by the two models are in close agreement with each other. This is to be expected since the non-ozone greenhouse gas concentrations do not depend on latitude in either model. The global average forcing is  $0.42 \text{ W/m}^2$  and  $0.44 \text{ W/m}^2$  for the nineteen-zone and three-zone models respectively. For both models the fixed ozone adjusted forcing is greatest in the tropics, reflecting the higher atmospheric temperatures there. For the VOE, the difference between the two models is larger. This is primarily because of the strong latitudinal dependency of the assumed ozone changes combined with the large difference in latitudinal resolution of the two models. For example, the near zero net adjusted forcing simulated by the nineteen-zone model for the southern polar region (SP=62-90S) can not be simulated (or inferred) by the three-zone model because the magnitude of the decrease in ozone concentration averaged over the southern extratropics (SX=24S-90S) is too small. That is, since the distribution of ozone change has significant structure on scales that are smaller than the three-zone model resolution, some aspects of the climatic effects of ozone change are missed by the three-zone model.

The zonally averaged mean steady state surface air temperatures,  $\Delta T_s$ , for the two experiments are shown in Fig. 9, FOE (top) and VOE (bottom). The global mean annual averaged change in surface temperature is 0.26 K and 0.15 K for FOE and VOE respectively. Thus the assumed reductions in lower stratospheric ozone results in an absolute decrease in global mean annual average surface warming of 0.11 K.

southern extratropics where the assumed ozone losses are greatest. Although some spatial variability does exist in the surface air temperature response to a given forcing, changes in meridional heating significantly reduces the spatial variability of surface air temperature relative to that of the adjusted forcing. Our results indicate that the percent compensation to the global averaged annual mean surface air temperature warming due to ozone depletion is 42 %. This is about 1.5 times larger than the 28 % compensation reported in M94. Table 3 clearly shows the point stressed by M94; the adjusted forcing is a poor proxy for the response of the climate system.

It is important to understand how a small change in global mean adjusted forcing can result in such a large compensation in global mean steady state surface temperature increase (VOE adjusted forcing is only 12 % less than FOE, while the VOE increase above 1979 temperature is 42 % less than FOE). The ozone hole in the southern hemisphere essentially provides a pathway of lower resistance to longwave radiation leaving the surface-troposphere system. This "leak", combined with changes in meridional heat transport, allows a relatively small percent compensation to the global mean adjusted forcing to result in a substantially larger percent compensation in global mean temperature.

Changes in both the meridional heat transport and the infrared opacity of the lower stratosphere accompanying the assumed high latitude ozone loss tend to enhance the global climate sensitivity factor as follows. The initial response to the adjusted forcing is a large cooling at high latitudes. This results in an increase in the equator to pole temperature gradient, causing an increase in the meridional heat transport from the tropics to high latitudes. This normally serves as a negative feedback mechanism to limit the high latitude cooling. For the troposphere, the temperature gradient increase is greatest near the tropopause (i.e. in the vicinity of the largest ozone losses). Thus, the increase in meridional heat transport is largest for the upper troposphere. The decreased infrared opacity of the lower stratosphere (associated with ozone loss at the same location) increases the ability of the upper troposphere to radiatively cool into space. This increased cooling of the high latitude lower stratosphere weakens the negative feedback loop associated with an increase in meridional temperature gradient and the corresponding increased meridional heat transport. As a result, the cooling is larger with the lower efficiency negative feedback. Fig. 11 shows the steady state temperature change associated with ozone loss VOE-FOE. Also drawn on Figure 11 are bold arrows that qualitatively follow the flow of energy from the tropics, to higher latitudes, and then out of the system as infrared radiation. In summary, for the assumed ozone losses in the high latitude lower stratosphere, energy flows out of the tropics, resulting in cooler

amount of low and middle level clouds prescribed for the southernmost zone, and its high static stability results in an increase in the 80-90°S surface air temperature for the VOE relative to the FOE (see Fig. 10) during SON.

Our results illustrate the potentially large influence of the temporal and spatial distribution of perturbations in atmospheric composition to the climate sensitivity. For example, Daniel et al. (1995) estimated the global warming potentials of halocarbons by considering the warming from them and the indirect cooling from the assumed ozone loss resulting from halocarbon increase. Our results suggest that using global mean radiative cooling as an estimate of the climatic effects due to halocarbon induced ozone perturbations may underestimate the greenhouse compensation of ozone and overestimate the net (direct and indirect) warming associated with increased halocarbons.

## 5. Conclusions

The physics and performance of the most recent version of the AER two-dimensional seasonal radiative dynamical climate model has been described. We show that the model simulates many features of the present climate system rather well. The model's sensitivity to a doubling of atmospheric carbon dioxide in regards to the global mean annual average change in surface air temperature is 2.70 K. We also find that the  $2\times\text{CO}_2$ - $1\times\text{CO}_2$  temperature change simulated by our model has many of the spatial and temporal features found in other climate models.

We have estimated the climatic effects of sustained ozone changes relative to the other greenhouse gases and have found that including decreases in stratospheric ozone (similar to those observed from 1979 to 1990) in the steady state climate simulation reduces the modeled greenhouse warming by 42% relative to the fixed ozone case. We attribute this large compensation in global mean annual averaged greenhouse warming, resulting from the relatively small global mean annual averaged adjusted forcing, to increases in high latitude meridional heat transport in the upper troposphere coupled with the low infrared opacity of the lower stratosphere, both a result of ozone loss in the lower stratosphere at high latitudes. There are significant differences between the simulations reported here and those reported by M94 who used a similar model but of much lower latitudinal resolution. Because both ozone changes and the model's climate sensitivity are greatest at high latitudes, using a model of appropriately high latitudinal resolution is essential when simulating the latitudinal and seasonal effects of recent ozone changes. The primary difference between the global mean annual averaged surface temperature compensation between our simulation and that of M94 (42% compared to 28%) is also

## REFERENCES

- Breigleb, B.P., P. Minnis, V. Ramanathan, and E. Harrison, 1986: Comparison of regional clear-sky albedos inferred from satellite observations and model computations, *J. Climate Appl. Meteor.*, **25**, 214-226.
- Colman, R.A., B.J. McAvaney, J.R. Fraser, and S.B. Power, 1994: Annual mean meridional energy transport modelled by a general circulation model for present and 2xCO<sub>2</sub> equilibrium climates, *Clim. Dyn.*, **10**, 221-229.
- Daniel, J.S., S. Solomon, and D.L. Albritton, 1995: On the evaluation of halocarbon radiative forcing and global warming potentials, *J. Geophys. Res.*, **100**, 1271-1285.
- Eady, E. T., 1949: Long waves and cyclone waves. *Tellus*, **1**, No. 3, 33-52.
- Gleckler, P.J., and Other Authors, 1995: Cloud-radiative effects on implied oceanic energy transports as simulated by atmospheric general circulation models. *Geophys. Res. Lett.*, **22**, 791-794.
- Hansen, J., G. Russell, D. Rind, P. Stone, A. Lacis, S. Lebedeff, R. Ruedy and L. Travis, 1983: Efficient Three-Dimensional Global Models for Climate Studies: Models I and II. *Mon. Wea. Rev.*, **111**, 609-662.
- Held, I. M., and A. Y. Hou, 1980: Nonlinear axially symmetric circulations in a nearly inviscid atmosphere. *J. Atmos. Sci.*, **37**, 515-533.
- Held, I.M., 1993: Large-Scale Dynamics and Global Warming. *Bull. Amer. Meteor. Soc.*, **74**, 228-241.
- Holton, J. R., 1979: An introduction to dynamic meteorology. Academic Press, 319 pp.
- Houghton, J.T., 1986: *The Physics of Atmospheres*, second edition, Cambridge University press, New York.
- IPCC. *Climate Change, The IPCC scientific assessment, WMO/UN Environment programme*, 1990: Cambridge University Press, New York.
- IPCC. *Climate Change 1994. Radiative forcing of climate change and an evaluation of the IPCC IS92 emission scenarios*. Cambridge University Press, New York.
- Lacis, A., and J. Hansen, 1974: A parameterization for the absorption of solar radiation in the earth's atmosphere. *J. Atmos. Sci.*, **31**, 118-133.
- Lacis, A., D. Wuebbles, and J. Logan, 1990: Radiative forcing of climate by changes in the vertical distribution of ozone. *J. Geophys. Res.*, **95**, 9971-9981.

- Stone, P. H., and J. H. Carlson, 1979: Atmospheric lapse rate regimes and their parameterization. *J. Atmos. Sci.*, **36**, 415-423.
- Schwarzkopf, M.D., and V. Ramaswamy, 1993. Radiative Forcing due to ozone in the 1980s: Dependence on Altitude of Ozone Change. *Geophys. Res. Lett.*, **20**, 205-208.
- Trenberth, K.E. and A. Solomon, 1994: The global heat balance: heat transports in the atmosphere and ocean, *Clim. Dyn.*, **10**, 107-134.
- Wang, W.-C., and N. D. Sze, 1980: Coupled effects of atmospheric N<sub>2</sub>O and O<sub>3</sub> on the earth's climate. *Nature*, **286**, 589-590.
- Wang, W.-C., and P. B. Ryan, 1983: Overlapping effect of atmospheric H<sub>2</sub>O, CO<sub>2</sub>, and O<sub>3</sub> on the CO<sub>2</sub> radiative effect. *Tellus*, **35B**, 81-91.
- Wang, W.-C., G. Molnar, T. P. Mitchell and P. H. Stone, 1984: Effects of dynamical heat fluxes on model climate sensitivity. *J. Geophys. Res.*, **89**, 4699-4711.
- Wang, W.-C., G. Molnar, M. K. W. Ko, S. Goldenberg and N. D. Sze, 1990: Atmospheric trace gases and global climate: a seasonal model study. *Tellus*, **42B**, 149-161.
- Washington, W.M., and G.A.Meehl, 1993: Greenhouse sensitivity experiments with penetrative cumulus convection and tropical cirrus albedo effects, *Climate Dynamics*, **8**, 211-223.
- Watts, R.G. and M. Morantine, 1990: Rapid climatic changes and the deep ocean. *Clim. Change*, **16**, 83-97.
- Willmont, C.J. and D.R. Legates, 1993: A comparison of GCM-simulated and observed mean January and July surface air temperature, *J. Climate*, **6**, 274-291.

**Table 3.** Percent compensation  $(1-\Delta X_A/\Delta X_{\text{fixed O}_3}) \times 100\%$  for the nineteen-zone and three-zone models. X is either adjusted forcing AF or temperature. G (90N-90S), NX (90-24N), T (24N-24S), SX (24S-90S), NP(90-62N), SP (62-90S). (For the 3-zone model NX (90-30N), T (30N-30S), SX (30S-90S))

Experiment	G	NX	T	SX	NP	SP
<b>AF</b>						
19-zone	-12	-16	-5	-21	-25	-94
3-zone	-17	-24	0.4	-52		
<b>Temp</b>						
19-zone	-42	-38	-37	-52	-39	-54
3-zone	-28	-27	-22	-36		

**Fig. 9.** Same as Figure 8 but for the change in surface air temperature,  $\Delta T$ . (units are K)

**Fig. 10.** (Left) Steady state surface air temperature change (K) for 1990 -1979 greenhouse gas changes. FOE, solid, and VOE, dashes. (Right) Adjusted Forcing; 1990-1979 fixed ozone (FOE) , solid; 1990 -1979 (VOE), dashes; VOE-FOE (ozone forcing) for infrared radiation only solid diamonds; VOE-FOE (ozone forcing) for solar radiation only is difference between dash and solid-diamonds (dash minus solid diamonds).

**Fig. 11.** The 2-D change in annual mean temperature due to ozone perturbation VOE(1990 greenhouse gases with 1990 ozone) - FOE (1990 greenhouse gases 1979 ozone). Bold lines are qualitative indications of the change in energy flow from the tropics out of the system.



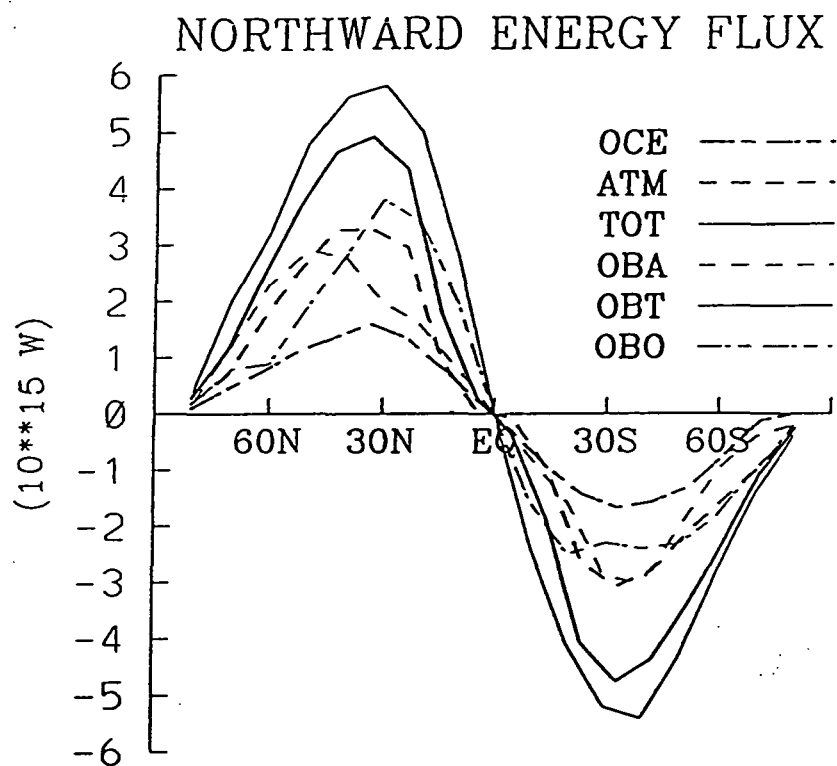
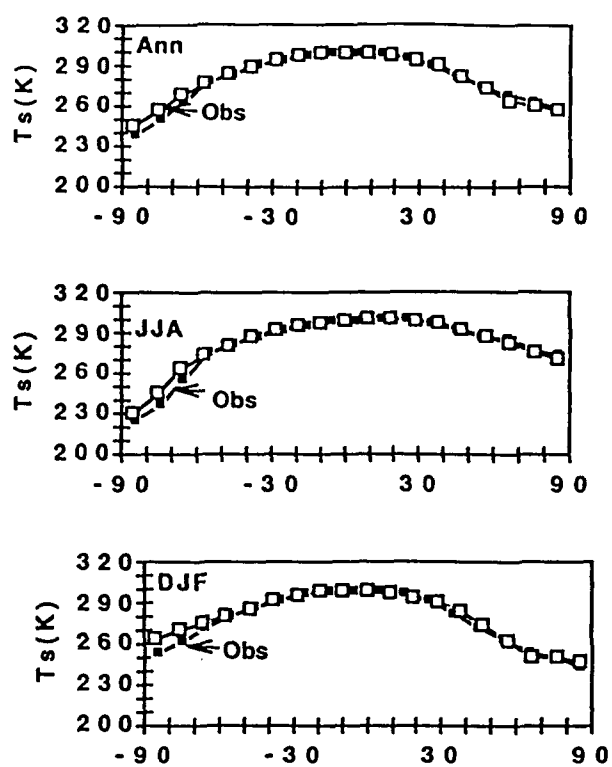


**Fig. 1.** Model simulated meridional heat transport in Oceans (OCE, heavy dash-dot) Atmosphere (ATM, heavy dash) and Total Atmosphere plus Oceans (TOT, heavy solid) compared with observed (OB) values given by Piexoto and Oort (1992); light lines (Units are  $10^{15}$  Watts (PW)).



Latitude

Figure 2. Zonal-mean annual, summer (JJA), and winter (DJF) surface air temperature. Observations are from Willmott and Legates (1993).

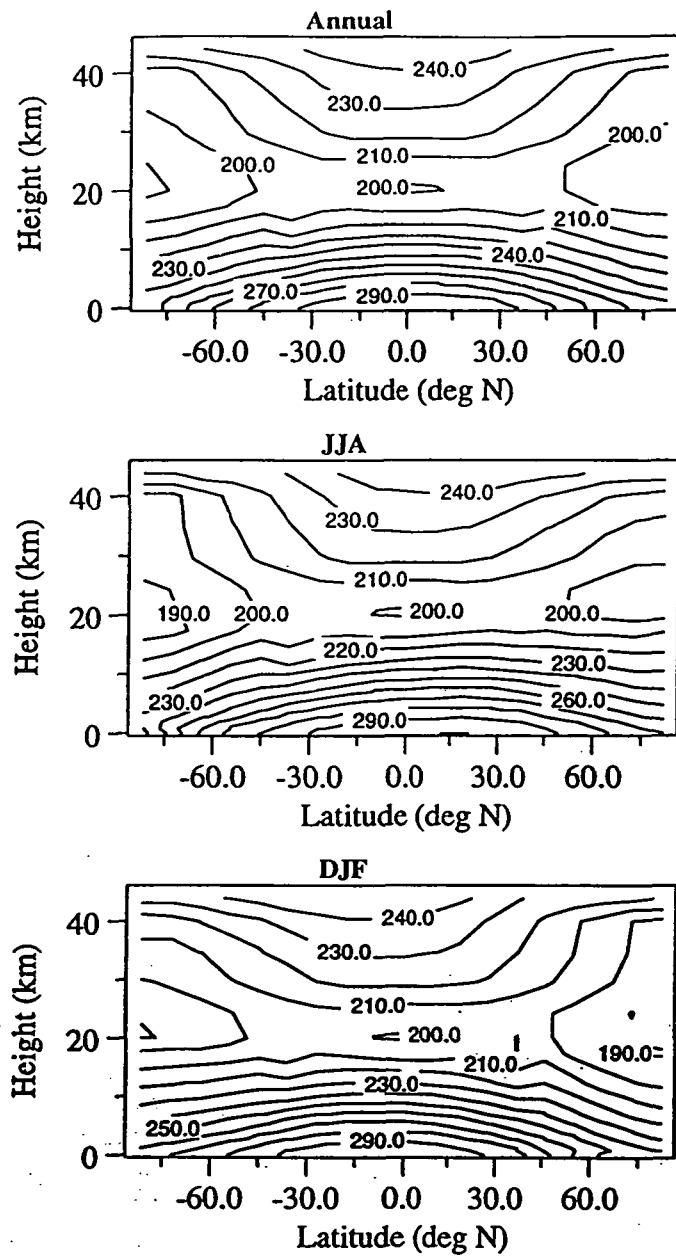


**Fig. 3a.** Zonal mean temperature profile simulated by the 19-zone ASRD for annual, JJA, and DJF means. Contour intervals are 10 K and height is approximate.

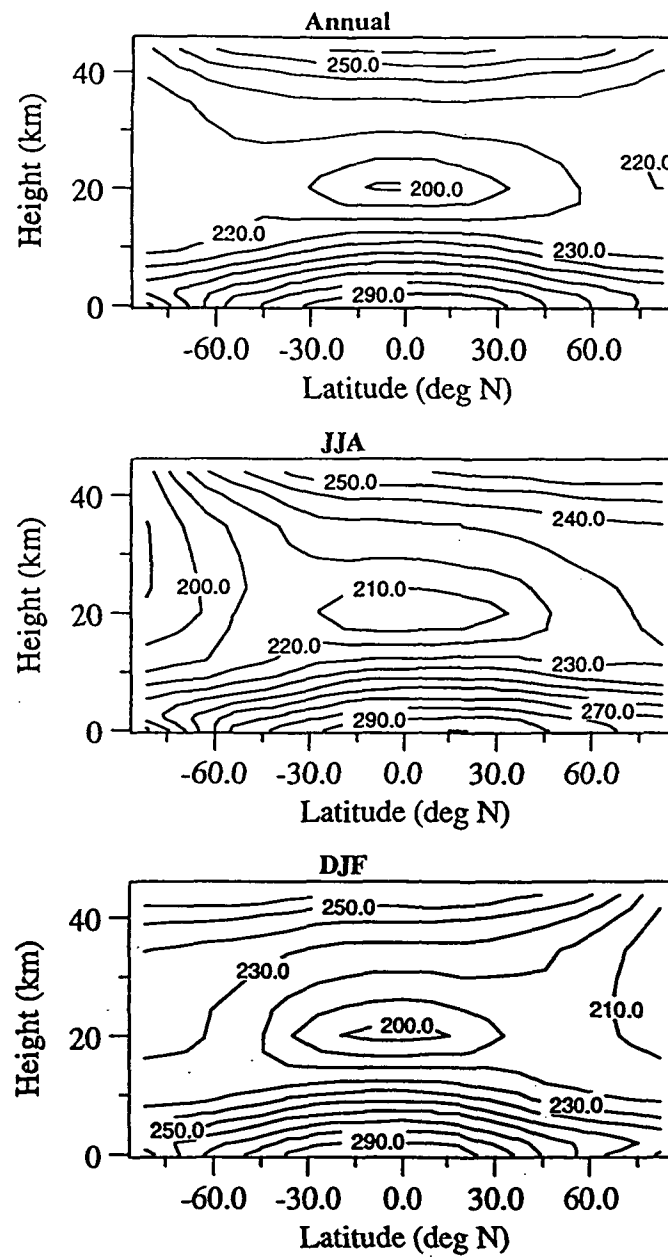


Fig. 3b. Zonal mean observed temperature profile for annual, JJA, and DJF means. Contour intervals are 10 K.

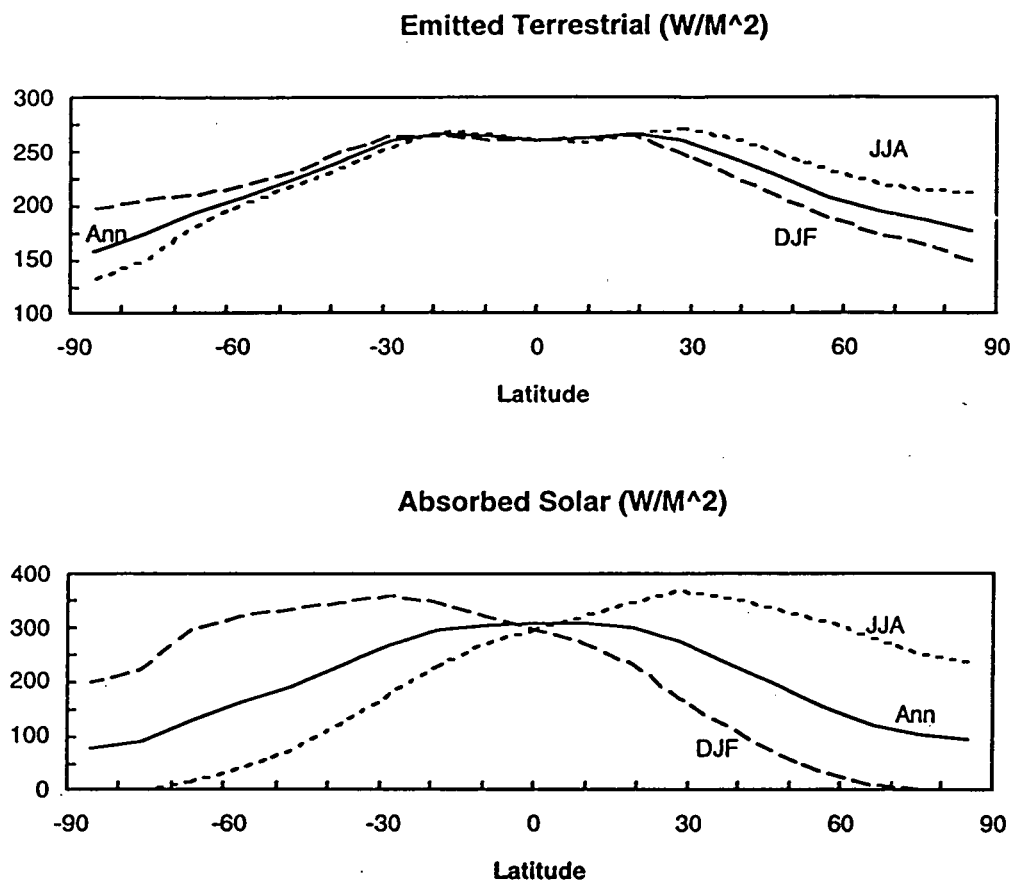


Figure 4. Model simulated net flux of outgoing longwave radiation at the top of the atmosphere (top) and total absorbed solar radiation by the earth atmosphere system (bottom) for Annual, Winter (DJF), and Summer (JJA) means.

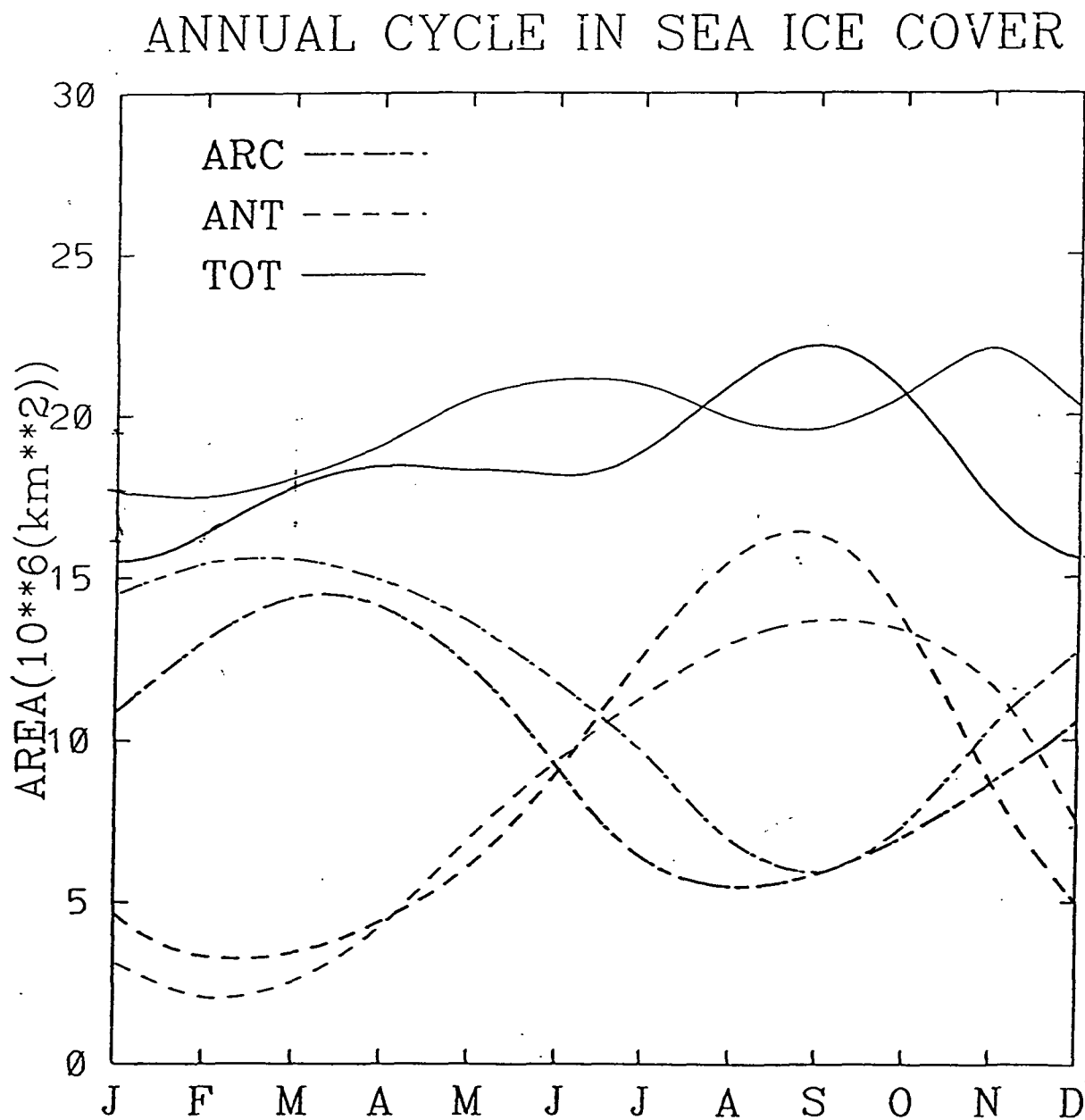


Figure 5. The annual cycle of model simulated sea-ice area coverage For the Arctic, Antarctic, and Globe (units are  $10^6 \text{ km}^2$ ).

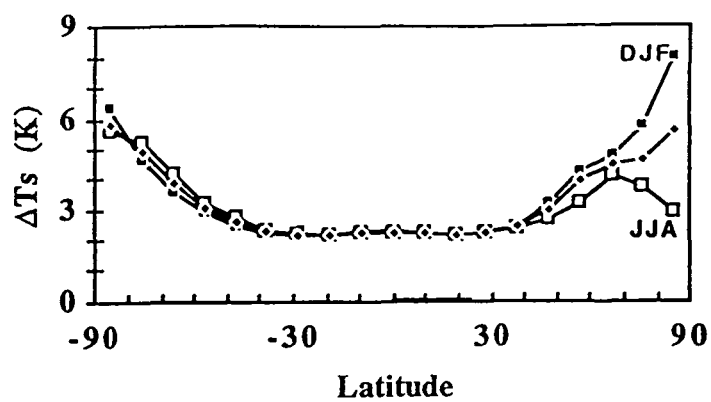
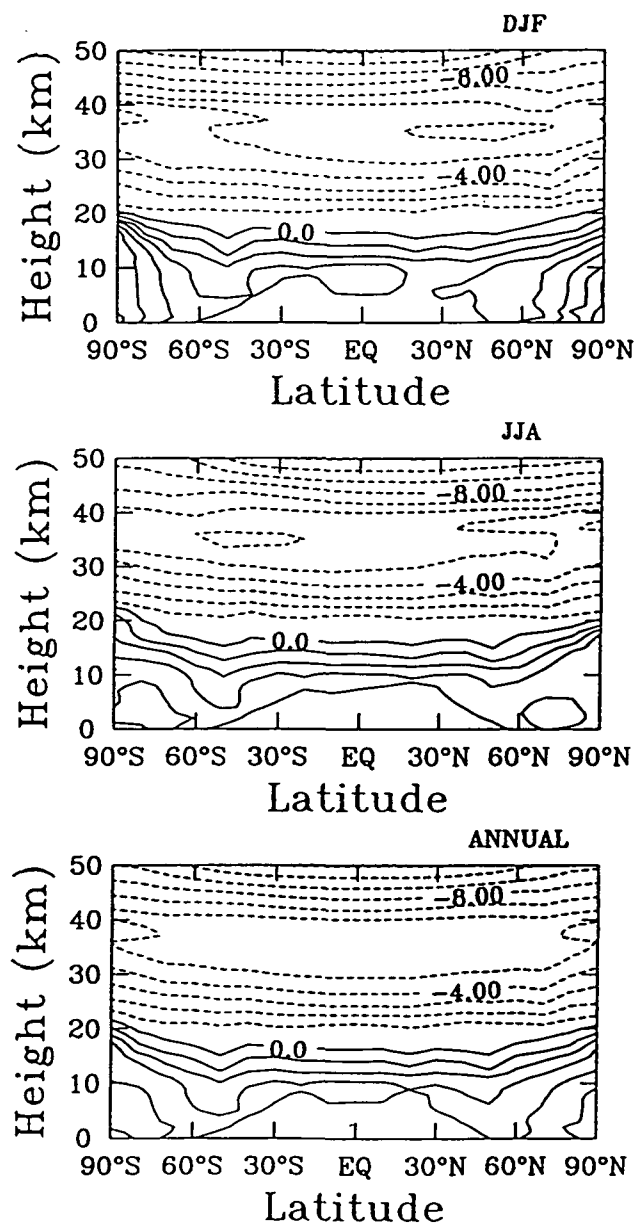


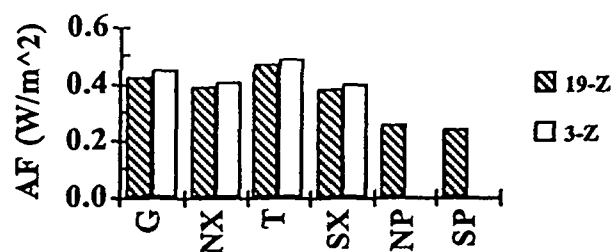
Fig. 6. The  $2\times\text{CO}_2$ - $1\times\text{CO}_2$  surface air temperature change  $\Delta T_s$  simulated by the ASRD model, for winter (DJF), summer (JJA), and annual means.



**Fig. 7.** The calculated two-dimensional temperature ( $2xCO_2-1xCO_2$ ) changes for Annual, DJF, and JJA means. Units are K and temperature changes less than or equal to zero are shown by dashed lines.



# 1990-1979 Fixed Ozone



# 1990-1979 with Ozone Changes

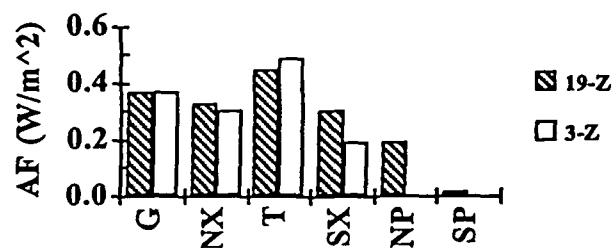
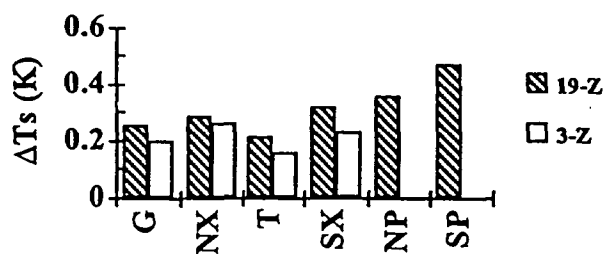


Fig. 8. The annual mean adjusted forcing for the nineteen-zone and three-zone models averaged over different zones. G-Global average, NX-Northern extratropics, T-Tropics, SX- Southern extratropics for the three and nineteen zone models. Also the northern and southern polar regions, NP and SP, corresponding to 60° to 90.° are given for the nineteen-zone model. Units are W/m<sup>2</sup>

1990-1979 Fixed Ozone



1990-1979 with Ozone Changes

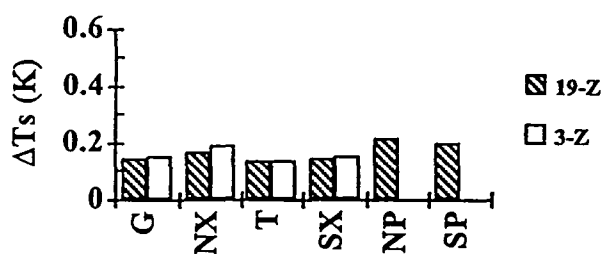


Fig. 9. Same as Figure 10 but for the change in surface air temperature,  $\Delta T$ . (units are K)

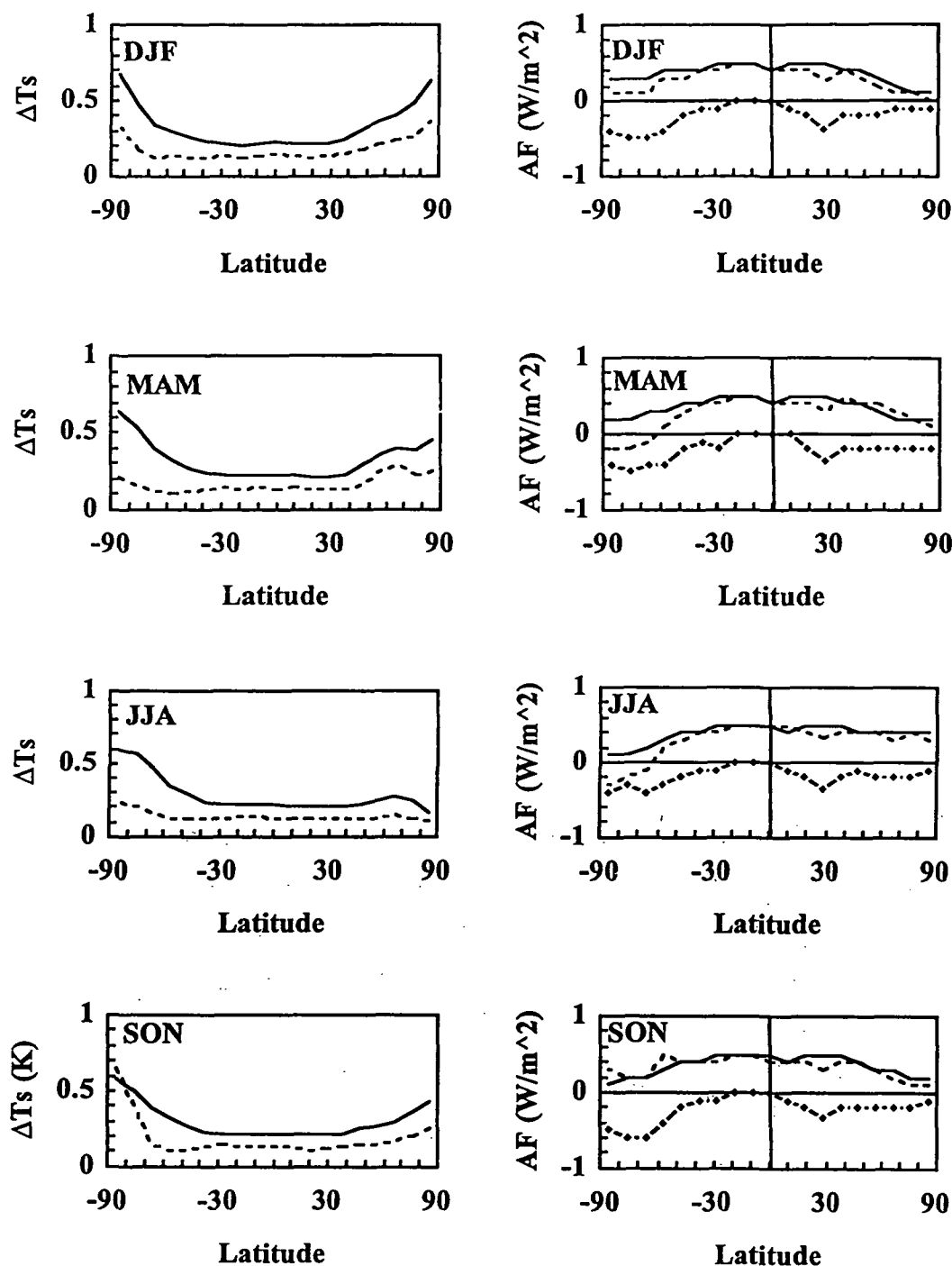
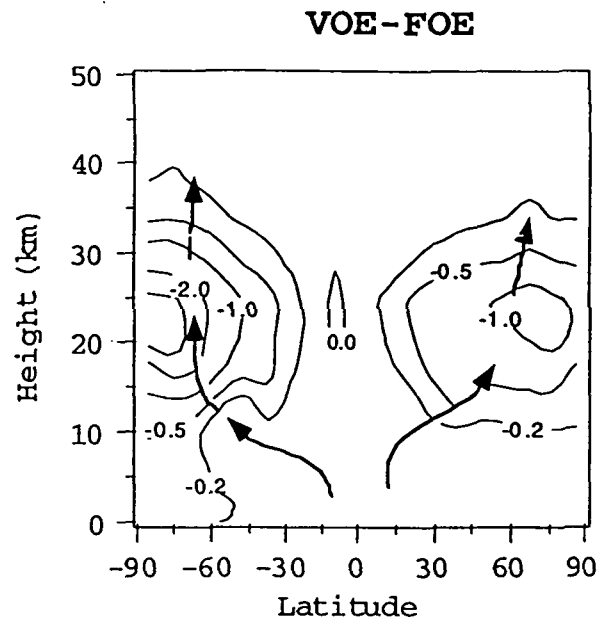


Fig. 10. (Left) Steady state surface air temperature change (K) for 1990 -1979 greenhouse gas changes. FOE, solid, and VOE, dashes. (Right) Adjusted Forcing; 1990-1979 fixed ozone (FOE), solid; 1990 -1979 (VOE), dashes; VOE-FOE (ozone forcing) for infrared radiation only solid diamonds; VOE-FOE (ozone forcing) for solar radiation only is difference between dash and solid-diamonds (dash minus solid diamonds).



**Fig. 11.** The 2-D change in annual mean temperature due to ozone perturbation VOE(1990 greenhouse gases with 1990 ozone) - FOE (1990 greenhouse gases 1979 ozone). Bold lines are qualitative indications of the change in energy flow from the tropics out of the system.

## **Appendix J**

**Ko, M.K.W., R.M. MacKay, G. Molnar, Y. Yang, and S. Zhou (1995) The Global Change of Temperature and Ozone Simulated by a Coupled Climate-Chemistry Model. In preparation.**

## **Appendix J**

### **The Global Change of Temperature and Ozone Simulated by a Coupled Climate-Chemistry Model**

by

Malcolm K. W. Ko, Robert M. MacKay, Gyula Molnar, Yajiang Yang,

and Shuntai Zhou,

Atmospheric and Environmental Research, Inc.

#### **1. Introduction**

Current projections indicate that by the middle of next century the earth's climate may be considerably different from that of today, due to increasing concentrations of greenhouse gases and accompanying changes in aerosols and clouds (e.g., IPCC, 1990). Although increases in atmospheric concentration of CO<sub>2</sub> is the most important single contributor to the greenhouse warming, changes in concentrations of other greenhouse gases (H<sub>2</sub>O, CH<sub>4</sub>, N<sub>2</sub>O, O<sub>3</sub>, CFC's as well as their substitutes) are expected to modify the CO<sub>2</sub>-warming significantly.

Previous studies of greenhouse effect have concentrated on the surface temperature response to CO<sub>2</sub> in the belief that the responses for other greenhouse gases are proportional to the corresponding changes in radiative forcing at the tropopause. However, recent results reported by Wang et al. (1991) show that because of differences in the vertical distribution of the radiative forcing, the calculated temperature responses do not scale as the net forcing at the tropopause. The temperature response to each greenhouse gas must be calculated on a case by case basis along with any indirect effect so that their climatic impact can be assessed.

Emission of some greenhouse gases also leads to changes in O<sub>3</sub>, which is itself a greenhouse gas. A recent WMO (1992) report documented strong evidence to support the conjecture that emissions of CFC's are responsible for the decrease in the column abundance of O<sub>3</sub> during the past decade. The O<sub>3</sub> loss is observed to have occurred below the (approximately) 25 km level. According to radiative forcing calculations (Wang and Sze, 1980; Lacis et al., 1990; Ramaswamy et al., 1992; Molnar et al., 1994), decreases in ozone in the lower stratosphere at mid-latitudes lead to a decrease in radiative forcing at the tropopause, while decreases in ozone above 25 km lead to an increase in forcing.

The complex relationship between surface temperature change and a given radiative forcing manifests itself in a myriad of feedbacks. As the surface temperature responds to the imposed forcing, many physical quantities will also change. These include moisture content, cloud cover, cloud optical properties, and behavior of sea ice. Changes in these quantities will modify the initial forcing and the final temperature response. The large range in model-predicted temperature responses is largely due to the different methods adopted in treating the feedbacks.

One-dimensional (vertical column) radiative-convective models (see Ramanathan et al., 1987, for a review) have been used to study the climate-chemistry interactions. The utility of these models is limited by their inability to address latitudinal and seasonal variations of the radiative forcing, and the role of horizontal heat transport in determining the actual temperature response. Higher dimensional models have been used to address climate-chemistry interactions only in an "open-loop" fashion. For example, Wang et al. (1990) used the AER 2-D seasonal-radiative-dynamical climate model to address the effects of stratospheric changes on the climate of the troposphere by using O<sub>3</sub> redistribution calculated from the AER 2-D photochemical model. The numerical experiment is "open-loop" in that the calculated changes in temperature did not feedback to the chemical model.

It is important to use higher dimensional, at least 2-D, models to conduct "closed-loop" (continuously coupled) experiments to address this issue, i.e., how the O<sub>3</sub> redistribution and changes in dynamical heating in the stratosphere affect the tropospheric climate, and vice versa. The model we used in this study is a 2-D coupled climate-chemistry model, which is based on coupling of two operational models developed in AER, i.e., the refined seasonal-radiative-dynamical climate model (Wang et al., 1990; Molnar et al., 1994) and the interactive chemistry-dynamics model (Schneider et al., 1989; Ko et al., 1993). A brief description of the individual modules and the coupling method is given in the next section. To evaluate the model's performance, we have carried out a number of common climate sensitivity experiments such as doubling CO<sub>2</sub> and changing solar constant.

These results are given in Section 3. In Section 4, we present model results of radiative forcing and temperature responses due to observed increases in greenhouse gases and ozone depletion in past decade. Because fixed dynamical heating method is used, these results are still not "closed-loop". The "closed-loop" experiments are reported in Section 5, in which ozone depletion and temperature change due to increases in greenhouse gases are calculated simultaneously.

## 2. The Climate-Chemistry Model

### The climate module

The climate module is a refined version of the AER seasonal radiative-dynamical (ASRD) climate model (Wang et al., 1990; Molnar et al., 1994) with higher meridional resolution (nineteen latitude zones versus three). It is a global energy balance model which computes the seasonal 2-D temperature field from the radiative and dynamical heat balance of the atmosphere and subsurface layer. The atmosphere is divided into 8 vertical layers in the stratosphere and 10 layers in the troposphere. It includes 19 latitudinal zones from pole to pole, each approximately 9.47 degrees in width. Separate land and ocean sections are included within each latitudinal zone, and the heat exchange between the land and ocean sections is computed according to a turbulent diffusion law with empirical diffusion coefficients. Radiative transfer for both solar and terrestrial radiation are calculated as described by Wang and Ryan (1983), Wang and Molnar (1985), and Wang et al. (1990). Seasonally varying cloud amounts and relative humidity are prescribed in the model based on observations. The primary differences between the present nineteen zone version of the ASRD and the three zone version described by Molnar et al. (1994) are outlined below.

The meridional heating of the mixed layer ocean is calculated assuming that the turbulent diffusion of ocean heat energy is directly proportional the meridional gradient of mixed layer temperature. Using the notation of Watts and Morantine (1990) the temperature change of the mixed layer ocean is calculated from,

$$\frac{\partial T_o}{\partial t} = \frac{K_H}{f_o R^2} \frac{1}{\cos \phi} \frac{\partial}{\partial \phi} \left( \cos \phi \frac{\partial T_o}{\partial \phi} \right) + \frac{(S + IR - LH - SH)}{\rho C_w D} \quad (1)$$

where  $T_o$  is the mixed layer temperature,  $K_H$  the horizontal thermal diffusivity,  $R$  the radius of the earth, and  $\phi$  is the latitude in radians,  $S+IR$  is the net flux of solar plus terrestrial radiation into the ocean,  $LH$  and  $SH$  are the latent and sensible heat fluxes from the ocean surface,  $\rho$  is the density of water (taken as  $1000 \text{ kg/m}^3$ ),  $C_w$  the specific heat capacity of water ( $4186 \text{ J/kg/K}$ ), and  $D$  is the mixed layer depth (50 m). The term  $f_o$ , which is implicitly assumed to be unity in the study of Watts and Morantine, is the zonal fraction of ocean in a latitude belt. We use  $K_H = 1.6 \times 10^{12} \text{ m}^2/\text{yr}$  for both the northern southern hemispheres during all seasons. This is comparable to the value of  $1.2 \times 10^{12} \text{ m}^2/\text{yr}$  used by Watts and Morantine (1990) and was adjusted to give a good simulation of observed ice cover and ocean temperature in each hemisphere. The thermodynamic sea



ice model used is that described by M94 except that here ocean heat fluxes are calculated as described above instead of using the "q-flux" flux adjustment method described in M94. Thus, the present model has a fully prognostic determination of sea-ice.

The meridional heat transport by the atmosphere is also parameterized differently in the mid-high latitudes and in the tropics. In the mid to high latitudes atmospheric heat transport is dominated by large scale eddies. There have been a variety of parameterization schemes in the literature, which are based on baroclinic theory. Here we adopt the scheme developed by Stone (1974) and modified by Peng et al. (1982). It is based in part on the Eady (1949) model and in part on the two-layer model (Holton, 1979). This scheme is somewhat different from that used previously in the 3-zone climate model (Molnar et al., 1994), which is developed by Branscome (1983) and based on the Charney (1947) model and quasi-geostrophic scaling analysis. We have evaluated and compared these physical schemes and another empirical scheme, based on empirical relations between total heat transport and temperature structure (North, 1975; Stone and Miller, 1980). The first scheme we adopted yields the best simulation of the total atmospheric heat transports as well as vertical structures of heat transport. Figure 1 (top) shows the meridional heat transport simulated by the model control run for the ocean, atmosphere, and total ocean plus atmosphere. Figure 1 (bottom) compares the total meridional heat flux simulated by the model with the observations reported by Peixoto and Oort (1992). Compared to observations, the simulated meridional heat transport is somewhat low (high) for the oceans (atmosphere), while the total is in close agreement.

Meridional heat transport in the tropics is dominated by the Hadley cell transport. Unfortunately, theoretical basis for parameterization of Hadley cell heat transport is weak, and empirical correlation between heat transport and temperature gradient is poor. It seems to us that the only practical scheme for the energy balance model is that developed by Peng et al. (1987). This parameterization scheme is based on the theoretical results of Held and Hou (1980) and the empirical study of Rennick (1977). We use Peng et al.'s scheme in our model as a framework, and make some modifications on the vertical distribution of heat transport. Peng et al. calculated the total heat transport first, then distributed to each layer according to an empirical relation which is a third order polynomial of surface temperature, multiplied by the surface adiabatic lapse rate. In order to be consistent with parameterization schemes for vertical heat transport in our

model, we do not use that empirical relation. Instead, we use the moist adjustment described above, which is a good approximation for the tropical atmosphere.

The temperatures in the lower polar stratosphere during winter simulated by the model are about 20 K too low when there is no meridional heat transport. This is consistent with the results of Shine (1987). Thus, we have included meridional heat transport in the stratosphere based on a temperature gradient driven turbulent diffusion. This has improved the simulated winter polar temperatures of the lower stratosphere for climate model runs that are not coupled to the interactive chemistry module.

Vertical heat transport is implicitly included by using the baroclinic adjustment scheme in the mid-high latitudes and a moist lapse rate adjustment in the tropics (Stone and Carlson, 1979). The lapse rate adjustment scheme of Stone and Carlson has been modified slightly to improve the model's simulation of temperatures in the upper tropical troposphere. The moist adiabatic lapse rate (MAL)  $\gamma_m$  at the surface is used to calculate the rate of change of potential temperature,  $\theta$ , with respect to pressure,  $p$ , at the surface using,

$$\frac{\partial \theta}{\partial p} = \frac{0.288\theta}{p} \left( 1 - \frac{\gamma_m}{9.8} \right) \quad (2)$$

; see Houghton (1986) for a derivation of (2). The critical lapse rate,  $\gamma_c$ , at other levels is then calculated by assuming that  $\partial\theta/\partial p$  is constant throughout the troposphere and inverting (2) with  $\gamma_c$  replacing  $\gamma_m$ . This moist critical lapse (MCL) rate is then compared with the critical lapse rate predicted by baroclinic instability theory and the actual critical lapse rate used is the smaller of the two.

The rationale for assuming  $\partial\theta/\partial p$  is constant is two fold. First, as was noted by Rennick (1977) an empirical fit of the observed lapse rates match a constant  $\partial\theta/\partial p$  profile much better than the assumed constant  $\partial T/\partial z$  profile which is often used. Second, from theoretical considerations, the conservation of potential vorticity during an adiabatic process requires that,

$$(\zeta + f) \frac{\partial \theta}{\partial p} = \text{Constant.}$$

This implies that  $\partial\theta/\partial p$  is approximately constant when there is little change of  $\zeta+f$  with height; where  $\zeta = \frac{\partial v}{\partial x} - \frac{\partial u}{\partial y} = -\frac{\partial u}{\partial y}$  (for  $v$  and  $u$  representing zonal mean meridional and zonal velocities) and  $f$  is the Coriolis parameter. Thus, in regions where  $\zeta$  is independent of height this scheme is physically well motivated. It is worth emphasizing that the lapse rate calculated from (2) is physically related to surface static stability and hence this scheme also includes a mechanism for lapse rate feedback processes to be included in climate simulations.

Figure 2 compares the model control run simulation using the MCL-baroclinic adjustment scheme described here and the MAL-baroclinic scheme of Stone and Carlson (1979) with the observed temperature structure of the atmosphere for the equator, 47°N. The MCL-baroclinic scheme does a much better job at simulating the observed structure in the tropics. Since at mid-latitudes the MCL and MAL are both larger than the lapse rate predicted from baroclinic theory, the model uses the baroclinic lapse rate for both methods there. Thus, the differences between the two methods are much less in mid latitudes, but, because of horizontal energy transport, the mid-latitudes are influenced by the tropics resulting in some differences.

The solar radiation scheme used in the model is based on Lacis and Hansen (1974), except that the improved frequency integration scheme described by Wang and Ryan (1983) is used to calculate the total solar flux. The thermal radiation parameterization is based on the correlated  $k$ -distribution method described by Wang and Ryan (1983). This method allows a rigorous treatment of coupled radiative processes of absorption and multiple scattering due to gases and particles in an inhomogeneous atmosphere. Twenty-seven narrow spectral intervals are used to account for the non-gray gaseous absorption of H<sub>2</sub>O, CO<sub>2</sub>, O<sub>3</sub>, N<sub>2</sub>O, CH<sub>4</sub>, and CFCs and spectral properties of clouds, especially for high cirrus.

### The chemistry module

The chemistry module is adopted from the AER's interactive 2-D dynamics-chemistry model (Schneider et al., 1989; Ko et al, 1993). In the studies reported here, a comprehensive gas phase chemistry is used for chemical reaction. The zonal mean chemical transport is described by mean transport circulation and eddy diffusion. The

mean transport circulation is calculated from a set of dynamical equations interactively. The eddy diffusion coefficients, such as  $K_{yy}$ , are externally specified from Newman et al. (1988). The same  $K_{yy}$  is also used in the parameterization of eddy forcing in the mean momentum equation. This module can be updated to a new version of the interactive model in which  $K_{yy}$  is internally calculated (Zhou et al., 1994).

The primitive equation system is used for the dynamical and thermodynamic equations. Stratospheric temperature field is driven by local heating and dynamical transport. The effects of  $\text{CO}_2$ ,  $\text{N}_2\text{O}$ ,  $\text{CH}_4$ ,  $\text{O}_3$ ,  $\text{CFCL}_3$ ,  $\text{CF}_2\text{Cl}_2$  and  $\text{H}_2\text{O}$  are included in the thermal radiative transfer calculation, which is consistent with the climate module. Local heating is not explicitly calculated in the troposphere. It is assumed to take a Newtonian cooling form, in which the equilibrium temperature is that from climatology (Cunnold et al., 1975). Above 55 km a relaxation to standard atmospheric temperature is also used.

### 3) Module coupling

The two modules have the same meridional resolution, but different vertical coordinates. The climate module has better tropospheric representation with finer vertical resolution, more complete physical mechanisms and land-ocean separation. The chemistry module has better stratospheric representation, more realistic scale height for the trace gases and explicit calculation of heat transport. Because the physics and numerics of the two modules are very different, we use a "modular" method to couple them. This method allows the two modules to run in parallel, and to exchange information continuously during time integrations. Specifically, we input the chemistry module results of stratospheric temperature and gas concentrations to the climate module during the time integration by replacing the stratosphere temperature field in the climate module using the temperature calculated from the chemistry module. We also input the climate module results of tropospheric temperature to the chemistry module. In the troposphere of chemistry module, however, we cannot directly replace the temperature field because the model's stratosphere is very sensitive to the change of lower boundary condition. Instead, we use an alternative method. Since Newtonian cooling is used in the troposphere of the chemistry module, with climatological temperature (Cunnold et al., 1975) used as the "target" temperature, we use the temperature calculated from the climate module to replace the climatological "target" temperature. This is equivalent to forcing the tropospheric temperature gradually toward that calculated by the climate module. This data exchanging procedure provides the coupling behavior of the two modules.

### 3. Climate Sensitivity

#### 1) The control run

We carried out an experiment in which realistic gas concentrations are used in the model based on the observational data of Year 1979. The simulated global mean annual average surface air temperature and planetary albedo are 288.7 and 0.29 respectively; both in good agreement with observations. The latitudinal and seasonal variations of thermal and solar radiation are shown in Figure 3. The simulated seasonal radiative fluxes are in good agreement with observations (e.g. Peixoto and Oort, 1992, Figure 6.14). We must point out that the equatorial minimum of emitted thermal radiation could not be simulated by the 3-zone climate model at all, because its resolution is too coarse and its stratospheric temperature is not accurate. This minimum thermal radiation is clearly related to the cool tropopause in the tropics. The coupled model can simulate this feature owing to the better representation of the ozone distribution in the stratosphere.

The two-dimensional temperature field simulated by the coupled climate/chemistry model for Annual, December-January-February (DJF), and June-July-August (JJA) means are shown in Figure 4. The Primary Differences between the simulated temperature structure and observations are confined to the Antarctic region where at present the model does not simulate the Antarctic continent very well. Also during Arctic and Antarctic winter the temperatures of the polar lower stratosphere are 5 to 10 % (10 to 15 K) below observations in the coupled Climate/Chemistry model. Aside from these difference the simulated temperature profiles are in good agreement with observations.

The total column ozone profile by the model is shown in Figure 5 and the simulated two-dimensional ozone profiles for Jan, April, July, and October are shown in Figure 6. Except for the lack of a strong ozone hole in the high latitudes of the southern hemisphere, the model simulations are consistent with measured ozone concentrations.

#### 2) CO<sub>2</sub>-doubling experiment

We have run the coupled model with CO<sub>2</sub>-doubling (334 to 668 ppmv) to a steady state climate. Since this experiment has been performed many times by others we use it as a bench mark of the sensitivity of the Interactive Climate/Chemistry model. There are several potential feedbacks included in this experiment. These include possible changes in atmospheric chemistry, water vapor, meridional heat transport in both the atmosphere

and ocean, atmospheric lapse rate, sea-ice cover (ocean sector albedo), and land surface albedo. The calculated two-dimensional temperature changes due to CO<sub>2</sub>-doubling are shown in Figure 7 for Annual, DJF, and JJA means. To reduce uncertainties associated with interannual variability of the model, we have run the model for 20 years and have used an average of the last five years of the model simulation for the temperature shown. The change in global mean annual averaged surface air temperature,  $\Delta T_s$ , simulated by the ASRD is 2.4 K. This compares well with the range of 1.5 K to 4.5 K given by the IPCC 1990 with a "best guess" of 2.5 K. It is interesting to note that when the climate model is not coupled to the chemistry model the simulated value of  $\Delta T_s$  is 3.0 K. More time is needed for a detailed analysis of model diagnostics and the development and implementation of carefully designed experiments to properly assess the influence of the climate-chemistry feedback.

The simulated changes in two-dimensional temperature structure have several characteristics in common with general circulation model (GCM) simulations (see for example Held, 1993). In particular, the ASRD has amplified warming at the poles (greatest during winter), local warming maximum in the upper troposphere of the tropics, and a substantial stratospheric cooling. This good agreement between our model and other more sophisticated GCMs give us confidence that our zonally averaged climate simulations are indicative of what GCMs would simulate if they performed the same experiment and took zonal averages. The 2-D ASRD model has several advantages over GCMs. First, it is computationally faster allowing for multiple experiments involving long time integrations. This is particularly attractive when investigating the coupling of the atmosphere to slower components of the climate system such as sea-ice and deep ocean dynamics. Second, since it is faster a more detailed treatment of atmospheric chemistry can be included for the investigation of climate-chemistry interactions.

The simulated (2xCO<sub>2</sub>-1xCO<sub>2</sub>) changes in ozone, methane, and nitrous oxide are shown in Figures 8, 9 and 10. Since few, if any have performed this experiment, it is hard to compare our results with others. At this point it is important to realize the coupled climate-chemistry model has the ability to use the fundamentals of atmospheric chemistry and physics to estimate climate chemistry interactions. More time will be needed to explore this important aspect of global change science.

## References

- Branscome, 1983: A parameterization of transient eddy heat flux on a beta-plane. *J. Atmos. Sci.*, **40**, 2508-2521.
- Charney, J. G., 1947: The dynamics of long waves in a baroclinic westerly current. *J. Meteor.*, **4**, 135-162.
- Cunnold, D., F. Alyea, N. Phillips, and R. Prinn, 1975: A three-dimensional dynamical-chemical model of atmospheric ozone. *J. Atmos. Sci.*, **32**, 170-194.
- Eady, E. T., 1949: Long waves and cyclone waves. *Tellus*, **1**, No. 3, 33-52.
- Held, I. M., and A. Y. Hou, 1980: Nonlinear axially symmetric circulations in a nearly inviscid atmosphere. *J. Atmos. Sci.*, **37**, 515-533.
- Holton, J. R., 1979: An introduction to dynamic meteorology. Academic Press, 319 pp.
- Ko, M. K. W., H. R. Schneider, R.-L. Shia, D. K. Weisenstein, and N. D. Sze, 1993: A two-dimensional model with coupled dynamics, radiation, and photochemistry: 1. Simulation of the middle atmosphere. *J. Geophys. Res.*, **98**, 20429-20440.
- Lacis, A., and J. Hansen, 1974: A parameterization for the absorption of solar radiation in the earth's atmosphere. *J. Atmos. Sci.*, **31**, 118-133.
- Lacis, A., D. Wuebbles, and J. Logan, 1990: Radiative forcing of climate by changes in the vertical distribution of ozone. *J. Geophys. Res.*, **95**, 9971-9981.
- Molnar, G. I., M. K. W. Ko, S. Zhou, and N.-D. Sze, 1994: Climate consequences of the observed ozone loss in the 1980's: Relevance to the greenhouse problem. Submitted to *J. Geophys. Res.*
- Newman, P. A., M. R. Schoeberl, R. A. Plumb, and J. E. Rosenfield, 1988: Mixing rates calculated from potential vorticity. *J. Geophys. Res.*, **93**, 5221-5240.
- North, G. R., 1975: Theory of energy-balance climate models. *J. Atmos. Sci.*, **32**, 2033-2043.
- Peng, L., M.-D. Chou, and A. Arking, 1982: Climate studies with a multi-layer energy balance model, I, Model description and sensitivity to the solar constant. *J. Atmos. Sci.*, **39**, 2639-2656.
- Peng, L., M.-D. Chou, and A. Arking, 1987: Climate warming due to increasing atmospheric CO<sub>2</sub>: Simulations with a multilayer coupled atmosphere-ocean seasonal energy balance model. *J. Geophys. Res.*, **92**, 5505-5520.
- Peixoto, J. P. and A. H. Oort, 1992: Physics of Climate. American Institute of Physics. New York. 520pp.
- Ramanathan, V., L. Callis, R. Cess, J. Hansen, I. Isaksen, W. Kuhn, A. Lacis, F. Luther, J. Mahlman, R. Reck, and M. Schlesinger, 1987: Climate-chemical interactions and effects of changing atmospheric trace gases. *Rev. Geophys.*, **25**, 1441-1482.

- Ramaswamy, V., M. D. Schwarzkopf, and K. P. Shine, 1992: Radiative forcing of climate from halocarbon-induced global stratospheric ozone loss. *Nature*, 355, 810-812.
- Rennick, M. A., 1977: The parameterization of tropospheric lapse rates in terms of surface temperature. *J. Atmos. Sci.*, 34, 854-862.
- Schneider, H. R., M. K. W. Ko, N. D. Sze, G.-Y. Shi, and W.-C. Wang, 1989: An evaluation of the role of eddy diffusion in stratospheric interactive two-dimensional models. *J. Atmos. Sci.*, 46, 2079-2093.
- Schneider, H. R., M. K. W. Ko, R.-L. Shia and N.-D. Sze, 1993: A two-dimensional model with coupled dynamics, radiative transfer, and photochemistry: 2. Assessment of the response of stratospheric ozone to increased levels of CO<sub>2</sub>, N<sub>2</sub>O, CH<sub>4</sub> and CFC. *J. Geophys. Res.*, 98, 20441-20449.
- Stone, P. H., 1974: The meridional variation of the eddy heat fluxes by baroclinic waves and their parameterization. *J. Atmos. Sci.*, 31, 444-456.
- Stone, P. H., and J. H. Carlson, 1979: Atmospheric lapse rate regimes and their parameterization. *J. Atmos. Sci.*, 36, 415-423.
- Stone, P. H., and D. A. Miller, 1980: Empirical relations between seasonal changes in meridional temperature gradients and meridional fluxes of heat. *J. Atmos. Sci.*, 37, 1708-1721.
- Wang, W.-C., G. Molnar, T. P. Mitchell and P. H. Stone, 1984: Effects of dynamical heat fluxes on model climate sensitivity. *J. Geophys. Res.*, 89, 4699-4711.
- Wang, W.-C., G. Molnar, M. K. W. Ko, S. Goldenberg and N. D. Sze, 1990: Atmospheric trace gases and global climate: a seasonal model study. *Tellus*, 42B, 149-161.
- Wang, W.-C., and N. D. Sze, 1980: Coupled effects of atmospheric N<sub>2</sub>O and O<sub>3</sub> on the earth's climate. *Nature*, 286, 589-590.
- Wang, W.-C., G. Molnar, W. J. Gutowski, P. H. Stone, S. Goldenberg and S. J. Ghan, 1991: Effects of dynamical heat fluxes on model climate sensitivity: A seasonal model study. Submitted to *J. Geophys. Res.*
- Wang, W.-C., and P. B. Ryan, 1983: Overlapping effect of atmospheric H<sub>2</sub>O, CO<sub>2</sub>, and O<sub>3</sub> on the CO<sub>2</sub> radiative effect. *Tellus*, 35B, 81-91.
- Watts, R.G. and M. Morantine, 1990. Rapid Climatic Changes and The Deep Ocean. *Climatic Change* 16, 83-97.
- Zhou, S., M. K. W. Ko, R.-L. Shia, D. Salstein, K. Cady-Pereira, and N.-D. Sze, 1994: A three-wave model with interactive dynamics and chemistry. To be submitted to *J. Geophys. Res.*



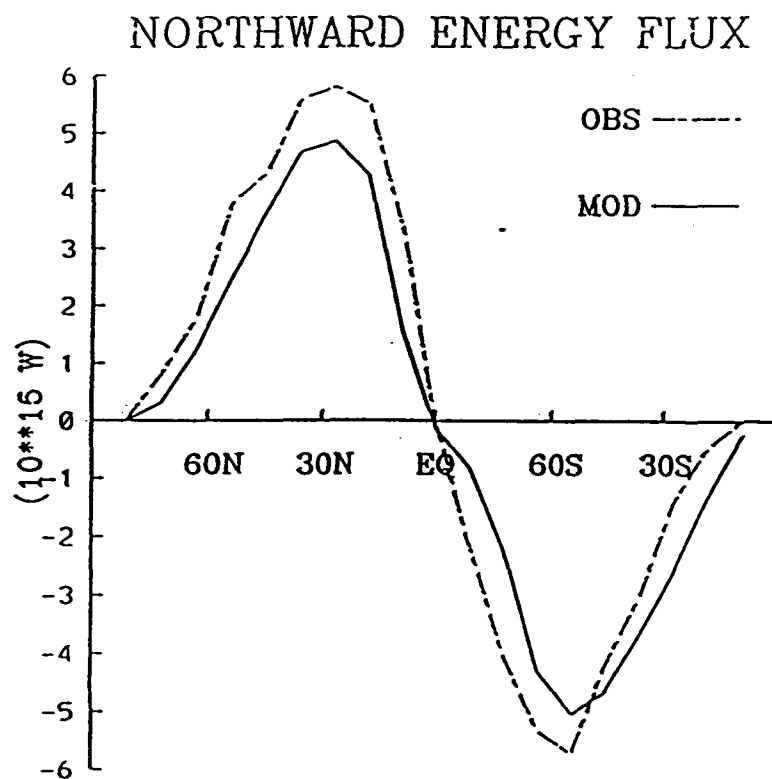
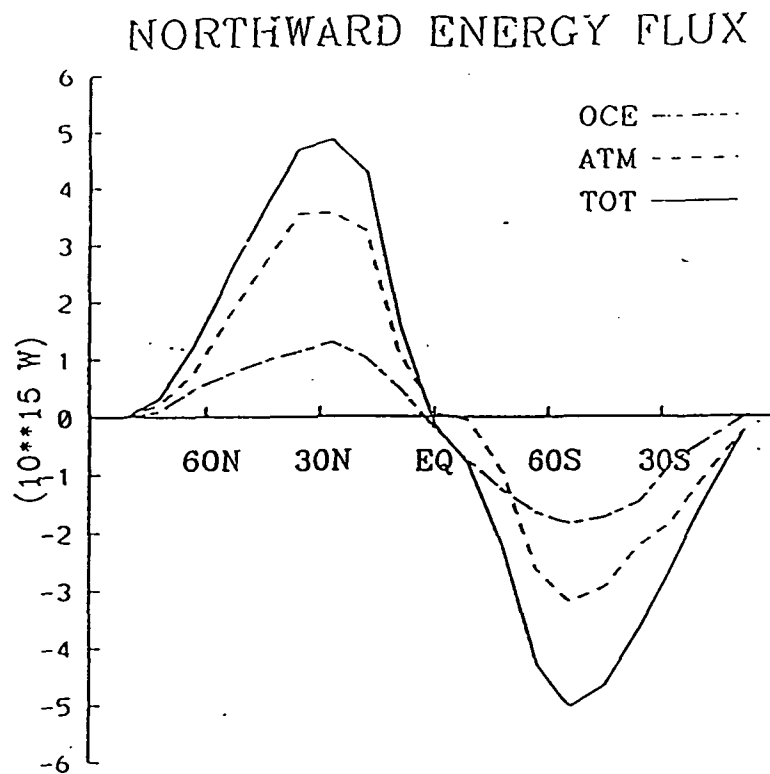


Figure 1. (Top) Model simulated meridional heat transport in Oceans (dash-dot) Atmosphere (dash) and Total Atmosphere plus Oceans (solid). (Bottom) Total simulated meridional heat transport compared with observed values given by Piexoto and Oort (1992). Units are  $10^{15}$  Watts.

# JANUARY

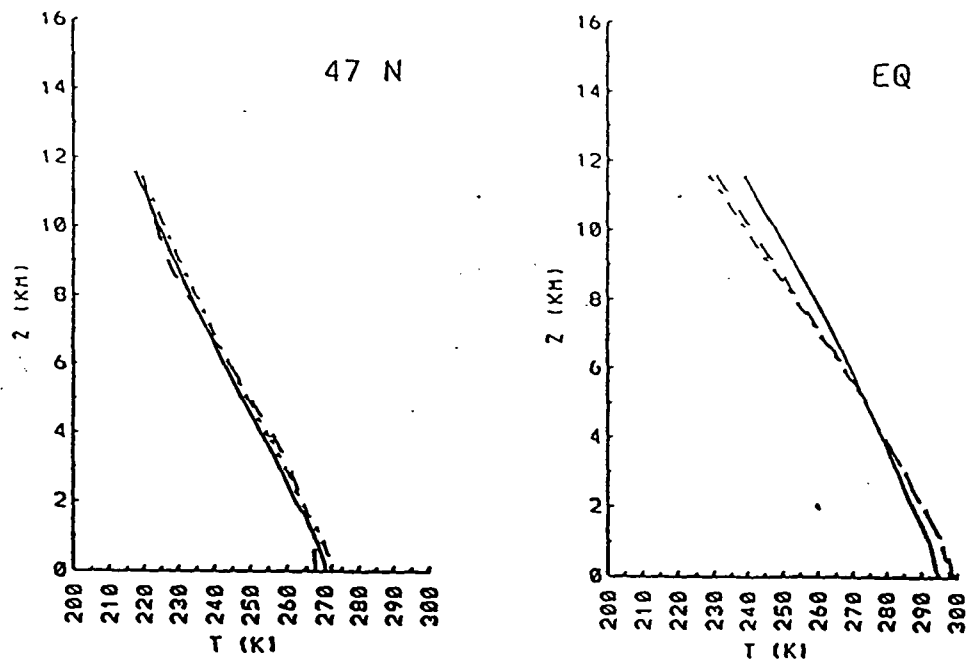


Figure 2. Difference between observed temperature profile (dashed) and Moist Adiabatic Lapse rate (solid line) and Moist Critical Lapse rates (dash dot) schemes described in text.

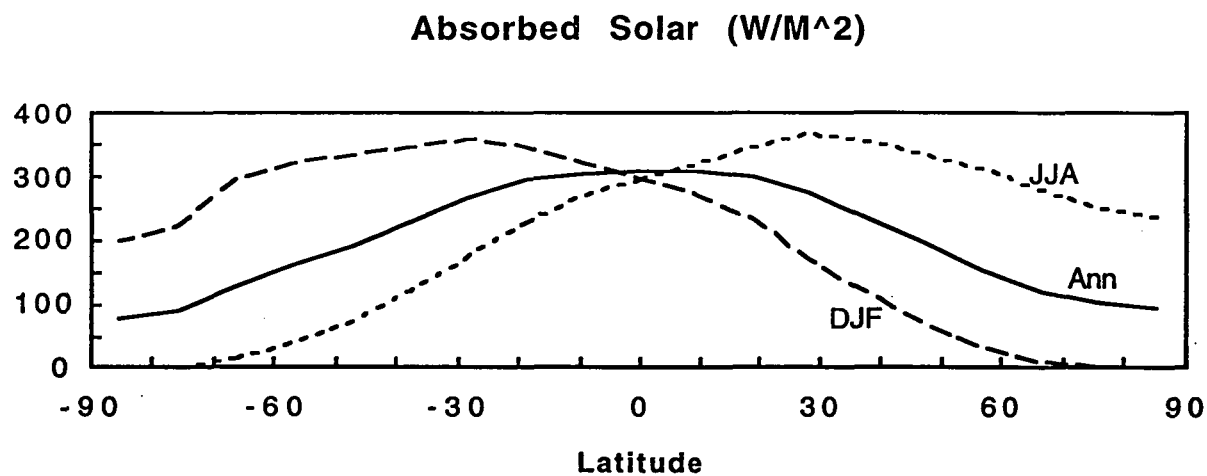
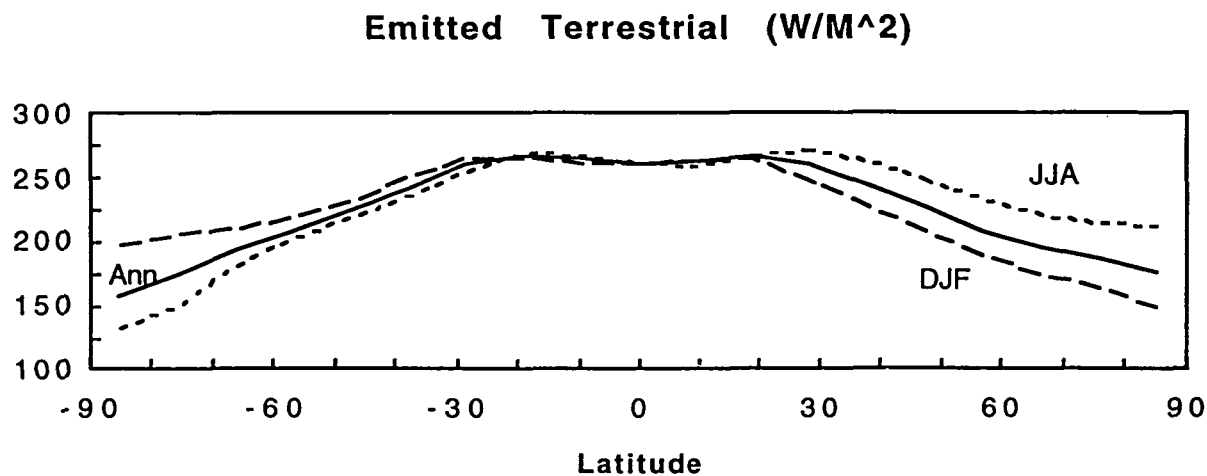


Figure 3. Model simulated net flux of outgoing longwave radiation at the top of the atmosphere (top) and total absorbed solar radiation by the earth atmosphere system (bottom) for Annual, Winter (DJF), and Summer (JJA) means.

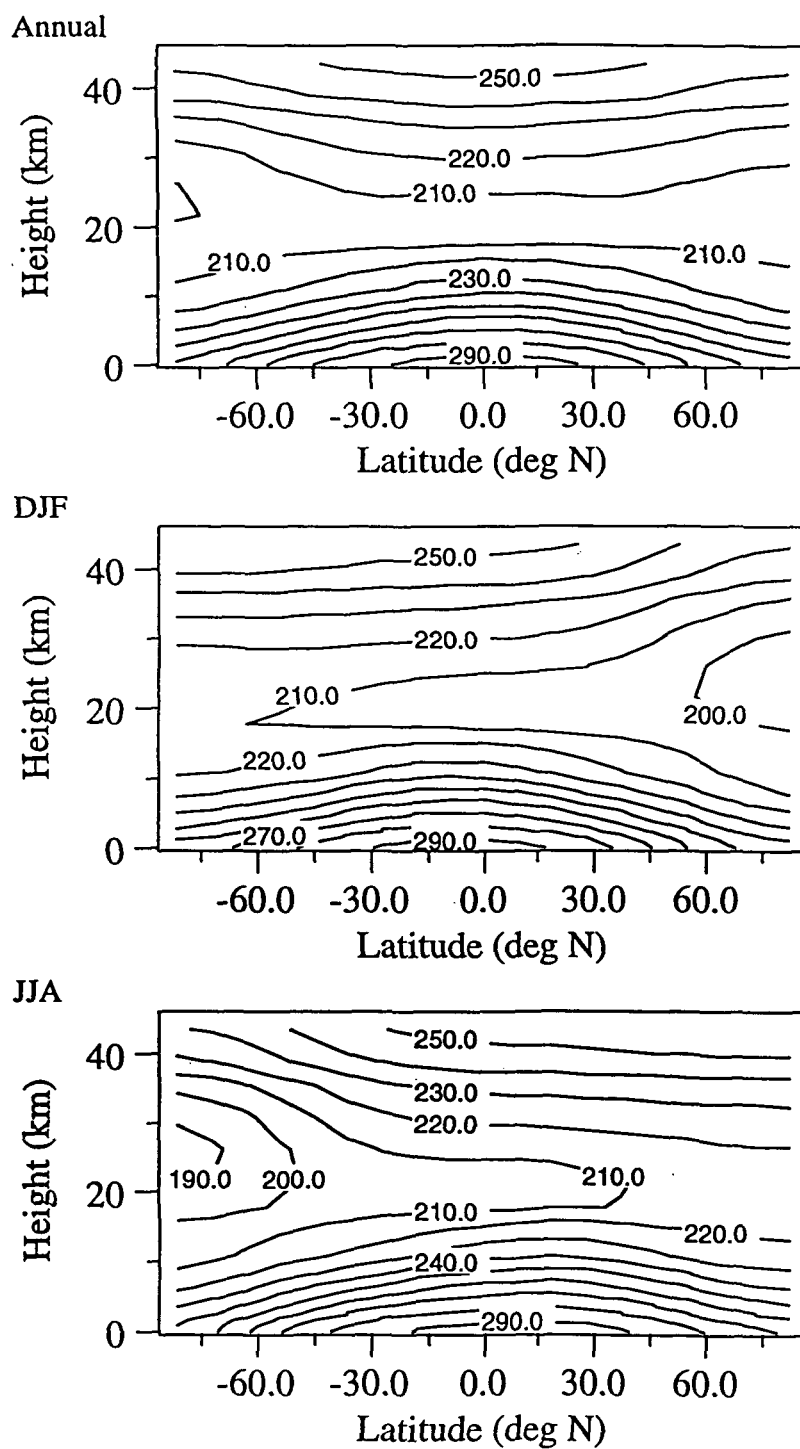


Figure 4. Two-dimensional temperature profile simulated by the coupled Climate/Chemistry Model for Annual, DJF, and JJA means.

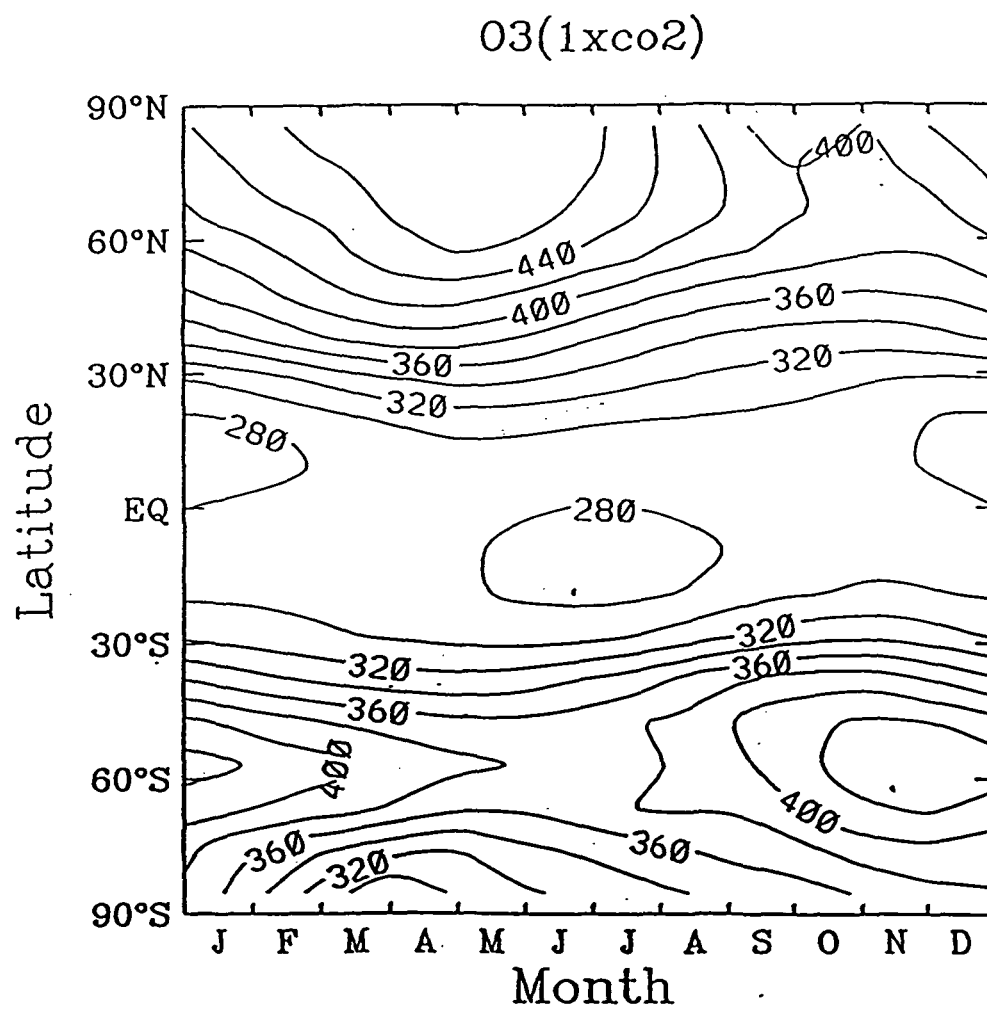


Figure 5. Baseline column ozone amount simulated by the Climate/Chemistry Model.

03(1xco2)

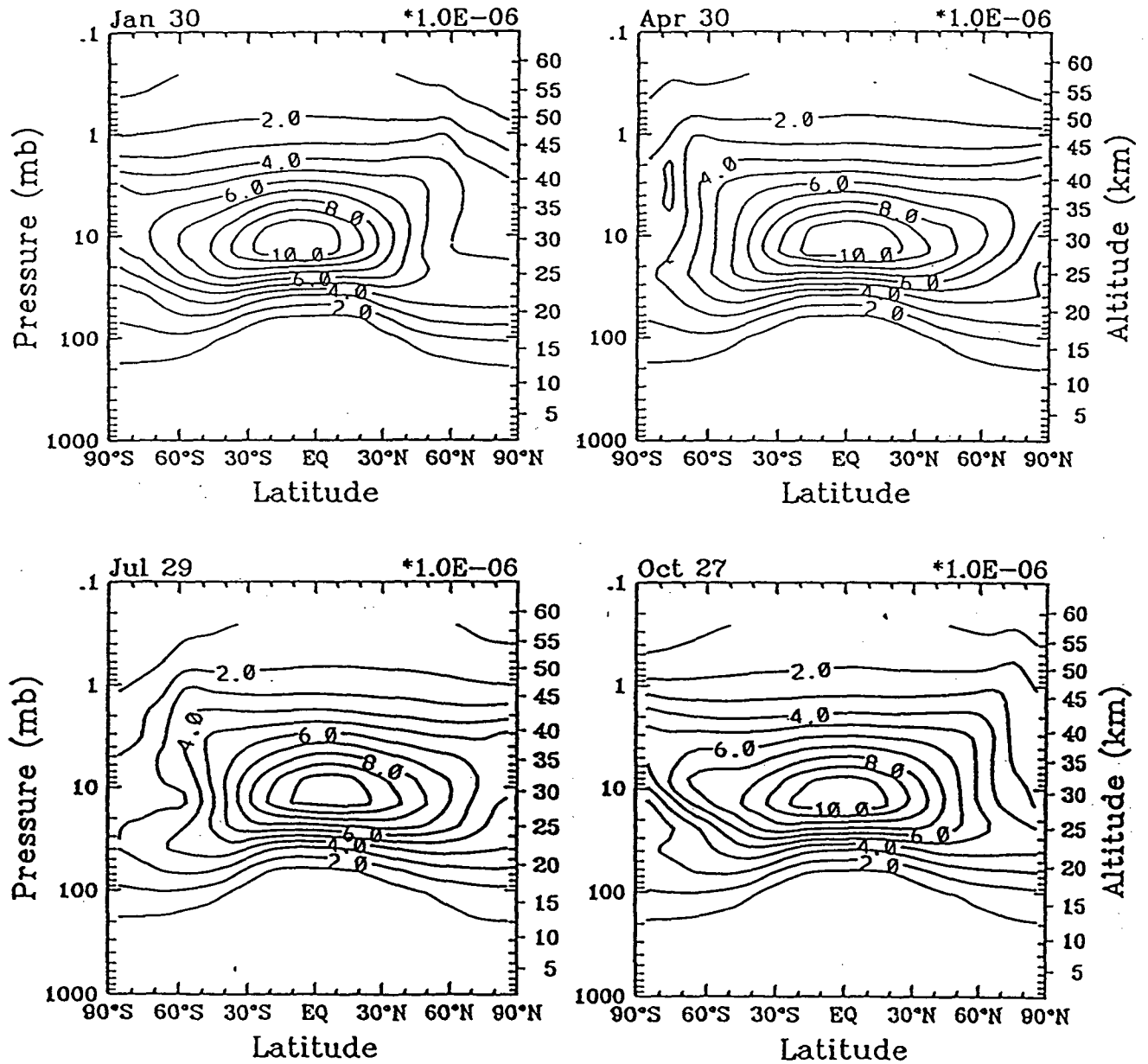


Figure 6. Two-dimensional ozone profile simulated by the coupled Climate/Chemistry Model for Jan., Apr., Jul., and Oct.

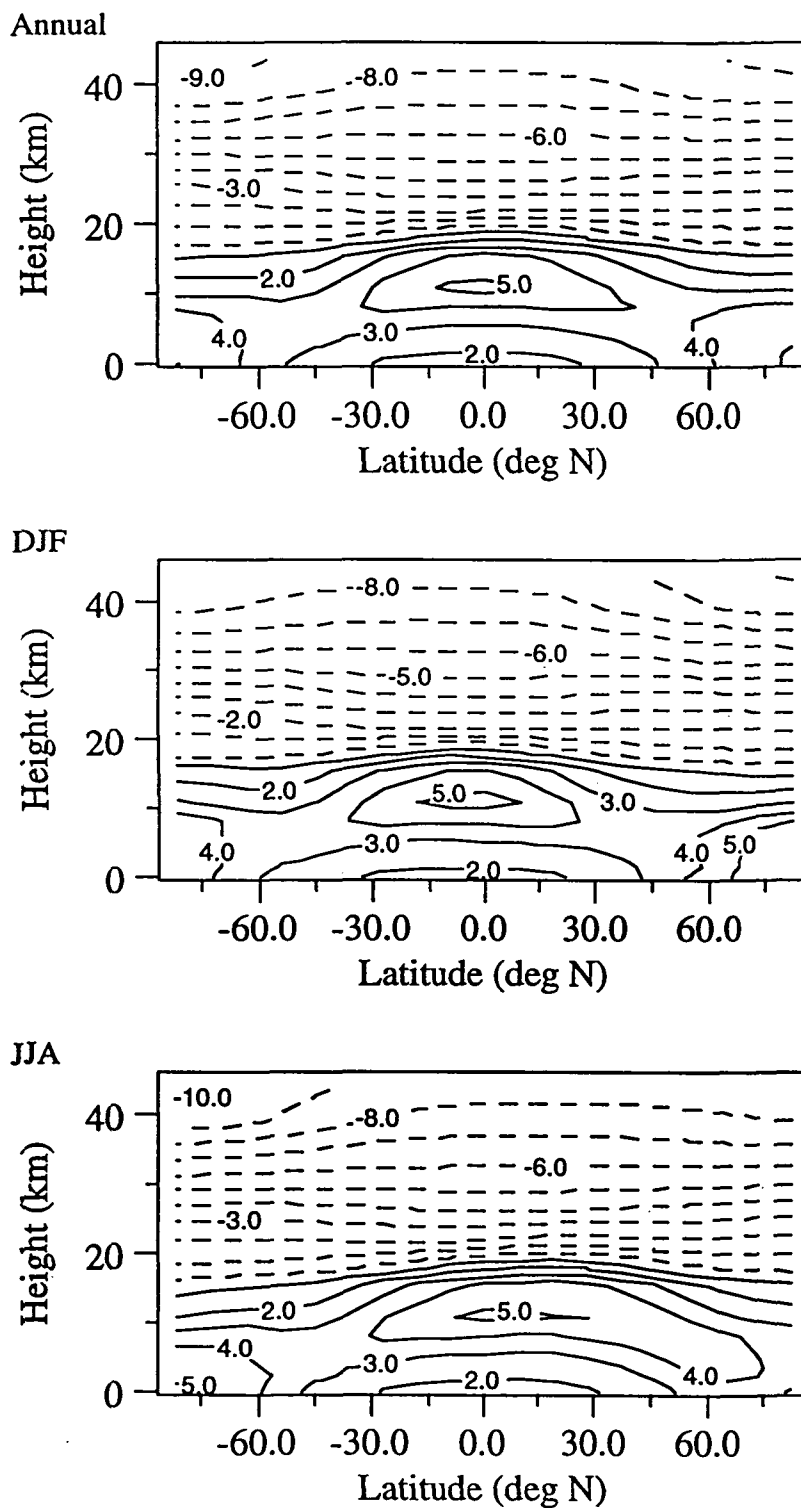


Figure 7. The calculated two-dimensional temperature ( $2\times\text{CO}_2$ - $1\times\text{CO}_2$ ) changes for Annual, DJF, and JJA means. Units are K and temperature changes less than or equal to zero are shown by dashed lines.

# O<sub>3</sub> concentration difference (%)

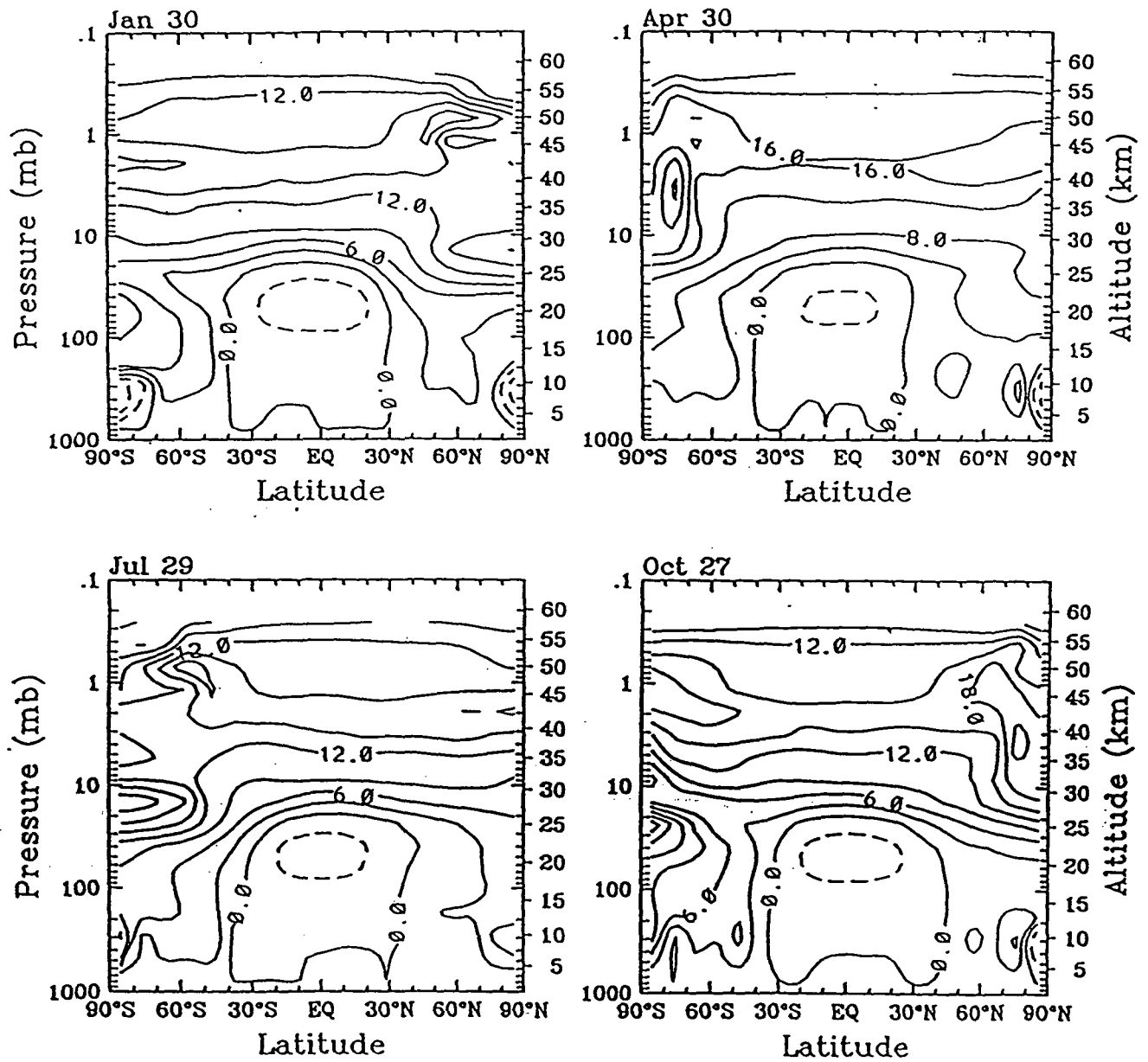


Figure 8. Two-dimensional (2xCO<sub>2</sub>-1xCO<sub>2</sub>) percent changes of ozone simulated by the coupled Climate/Chemistry Model for Jan., Apr., Jul, and Oct.



# CH<sub>4</sub> concentration difference (%)

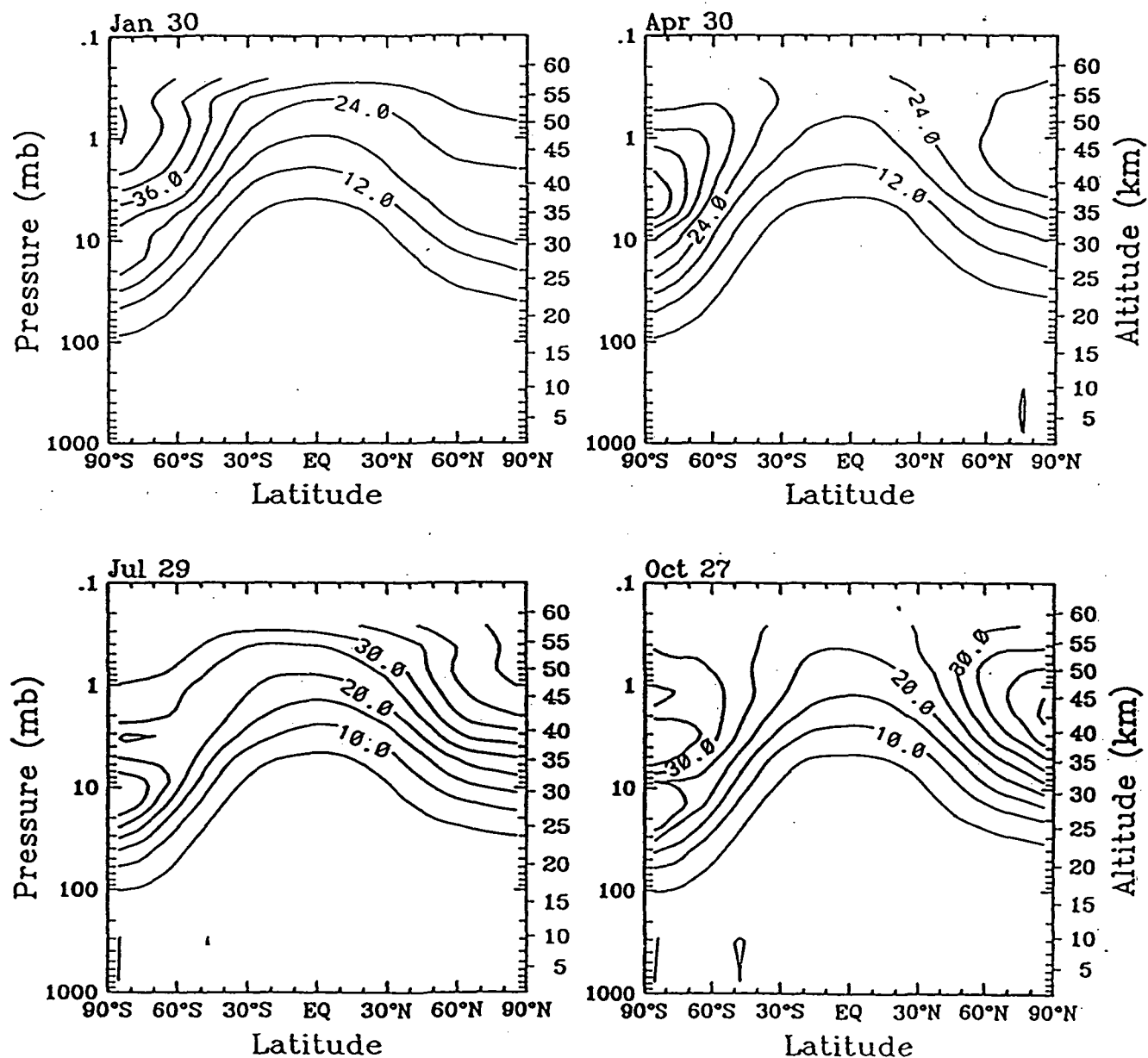


Figure 9. Two-dimensional (2xCO<sub>2</sub>-1xCO<sub>2</sub>) percent changes of methane simulated by the coupled Climate/Chemistry Model for Jan., Apr., Jul, and Oct.

# N<sub>2</sub>O concentration difference (%)

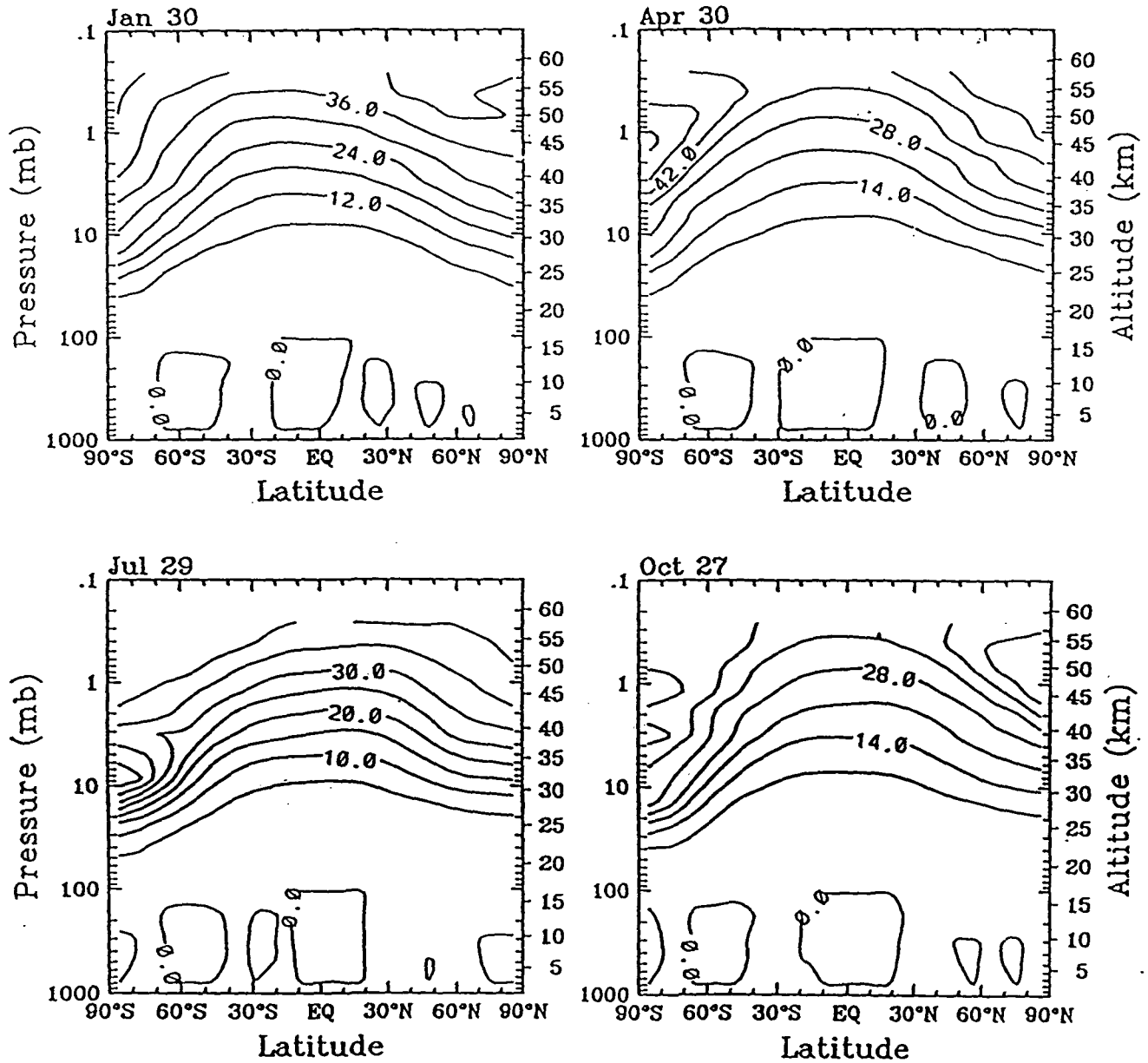


Figure 10. Two-dimensional (2xCO<sub>2</sub>-1xCO<sub>2</sub>) percent changes of nitrous oxide simulated by the coupled Climate/Chemistry Model for Jan., Apr., Jul, and Oct.

## **Appendix K**

**Proceedings of the PRC/USA Third Workshop on Atmospheric Chemistry  
Studies, Beijing, PRC, August 1-4, 1994.**

## **SUMMARY REPORT**

### ***Third PRC/US Workshop on Atmospheric Chemistry Studies***

Beijing, PRC, August 1—4, 1994

#### **1. Introduction**

The Third PRC/US Workshop on Atmospheric Chemistry Studies, sponsored by the U. S. National Aeronautics and Space Administration (NASA) and the China State Meteorological Administration (SMA), and hosted by Chinese Academy of Meteorological Sciences (CAMS) was held in Beijing on August 1—4, 1994. Over 20 Scientists representing both countries (7 American scientists and more than 15 Chinese scientists) attended the workshop.

The first two and the half days were devoted to individual presentations of ongoing research and progress made since the last workshop by delegates from both countries. More than 20 papers were presented during the meeting, covering a variety of topics of current interest presentations included atmospheric trace gases observations from both space-, aircraft-, and ground—based platforms, laboratory studies and regional and global scale models of atmospheric chemical radiative and transport processes. The agenda and abstracts of presentations are given in appendix A and B.

#### **2. Summary of discussions and future plans (Afternoon, August 3, 1994)**

Both PRC and US participants believe that after the three workshops, we have now reached a good understanding on areas of mutual interest as well as strength and limitations on both sides. Subsequent workshops should focus only on co—operative projects that are doable and capable of making substantial progress to our understanding of global atmospheric processes. The general principles of cooperations between PRC and US were discussed:

- Data, if any, from future cooperative projects should be freely exchanged between US and PRC and publishable with appropriate credits to the global change community
- Each side should be responsible for funding due to summary report of US—PRC Joint Working Group on cooperation in the field of atmospheric sciences and technology
- Any cooperative project should utilize the unique strength of both coun-

tries and have the potential of making substantial contribution to our understanding of global atmospheric chemistry

### 3. Proposed projects for future cooperation

a) Satellite data: Both PRC and U. S. believe that there is great merit in using U. S. satellite data (eg TOMS, UARS) to better define the stratospheric and tropospheric ozone and other trace gases distribution over China. The project will, at the very least, involve the U. S. providing the available space-borne data to PRC and PRC making vertical ozone measurements at appropriate locations, frequencies and duration (to be determined by a joint working committee) to provide the necessary ground truth to the space data. A workshop should be held within the next 12 months but only after feasibility studies from both sides have been satisfactorily completed. It is agreed to propose to the JWG that a joint plan for such a project be developed by a joint planning workshop that would define the research to be undertaken and the responsibilities of both sides.

b) Base-line station: A proposal on establishing another regional background station in Xiamen proposed from Research Center of Environmental Sciences of Peking University was tabled. This station could augment the data now being taken over the Hongkong and Taiwan station. It is however not clear that funding can be secured from PRC government or an international agent such as GEF.

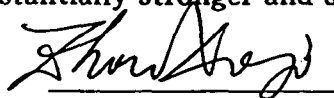
c) Flux measurement: PRC will be able to collect and validate certain emission data to contribute to the existing Global Emission Inventory Activity (GEIA). Such data might include CO<sub>2</sub>, SO<sub>2</sub>, CO, CH<sub>4</sub>, CFC<sub>3</sub>, NMHC, COS, DMS and NO<sub>x</sub>. Estimation of emission of certain gases (eg CH<sub>4</sub>) might have to involve introducing advanced flux measurement technique and capability for CH<sub>4</sub> and N<sub>2</sub>O. Such capability, however is both expensive and time-consuming to build and maintain. Thus it is best to have the equipment transferred to an appropriate site in China with assistance from U. S. scientists, if this can be arranged. While the equipment is being successfully deployed in U. S., it is not clear that it can be easily applied under specific condition in China. The US side will determine the feasibility of providing technical support including software and specifications to assist the PRC scientists in developing a fast flux measurement capability in China.

d) Development and improvement of models: Both sides should join efforts to explore the feasibility and resource requirements for developing, improving and adapting East Asia and West Pacific three-dimensional regional and global models of atmospheric chemistry and climate. Specifically, exchange of reliable data on emission inventories would fundamentally improve model performance. Although such information is available its quality has not been thoroughly assessed and properly documented. Where possible, the exchange of quality assured emission inventories would be carried out, if needed by short-term visits of scientists.

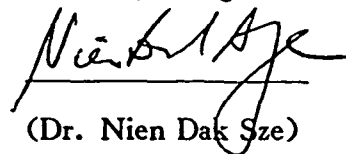
e) Joint experiment for study atmospheric chemistry over Qinhai-Tibet Plateau: Considering the baseline station of Qinhai completed soon, and obtained the important and interest of atmospheric ozone variation from analyses of data over Qinhai-Tibet, both scientists proposed that it is very worthwhile to joint study of the processes of atmospheric ozone and chemistry over Qinhai-Tibetan plateau. So it is suggest that a joint experts group for designing plan should be established, and joint study project at atmospheric chemistry and ozone over Qinhai-Tibet should be work out a plan by joint experts.

#### **Supplementary Funding from GEF**

Both PRC and U.S. participants recognize that realization of the above projects critically depends on our ability to obtain additional funding support. Aside from securing funds from its own governments, one possible funding source being identified is GEF. Both U.S. and PRC participants believe that they should jointly explore the feasibility of applying for GEF's fund. From a pure technical and scientific point of view, it is also felt that a joint PRC/US proposal should be substantially stronger and superior than one from either country doing it alone.



(Prof. Zhou Xuiji)  
PRC Chief Scientist



(Dr. Nien Dak Sze)  
U.S. Chief Scientist

# LIST OF THE PRC/USA 3th WORKSHOP ON ATMOSPHERIC CHEMISTRY

*(in order of alphabet)*

## American Delegation

### *Participants*

Bhartia, P. K	NASA/Goddard Space Flight Center
Carmichael, Gregory	University of Iowa
Ko, Malcolm K. W.	Atmospheric Environmental Research, Inc.
Liu, Shaw. C	NOAA/Aeronomy Laboratory
Marland, Gregg	Environmental Sciences Division, Oak Ridge National Laboratory
McNeal, Joe	NASA/Goddard Space Flight Center
Sze, Nien-Dak	Atmospheric Environmental Research, Inc.

## Chinese Delegation

### *Participants*

Ding Guoan	Chinese Academy of Meteorological Sciences
Guo Song	Chinese Academy of Meteorological Sciences
Hu Min	Center of Environmental Sciences, Peking University
Li Jinglong	Department of Technique Physics, Peking University
Li Weiliang	Chinese Academy of Meteorological Sciences
Li Xingsheng	Chinese Academy of Meteorological Sciences
Liu Yu	Chinese Academy of Meteorological Sciences
Luo Chao	Chinese Academy of Meteorological Sciences
Qin Yu	Department of Geophysics, Peking University
Qiu Lianxiong	Department of Chemistry, Graduate School, Academia Sinica, Beijing
Shi Guangyu	Inst. of Atmospheric Physics, Academia Sinica
Tang Xiaoyan	Peking University

## PROGRAMME

*For PRC/USA Third Workshop on Atmospheric Chemistry Studies  
(August 1-4, 1994)*

### August 1     Monday

#### **Joint Session**

*Chairman: Prof. Zhou Xiuji*

- 09:00—10:00    Opening ceremony (Spoken by the CMA administrator and leaders of NSFC and US delegation)
- 10:00—10:30    Break
- 10:30—11:00    Title to be determined, Nien Dak Sze
- 11:00—11:30    "A review of temperature variations in China during the past 100 years", — Ding Yihui
- 11:30—12:00    "Modeling Regional Climate," — Wei-chyung Wang
- Lunch

#### **Session 1: Tropospheric Ozone Modeling and Observation (1)**

*Chairman: Prof. Shaw C. Liu*

*Prof. Li Xingsheng*

- 14:00—14:25    "Ozone observation and global aspect", — Shaw C. Liu
- 14:25—14:50    "Chinese Ozone Research Program(CORP)", — Zhou Xiuji
- 14:50—15:15    "Study of ozone and its precursors at Linan China during PEM — WEST Experiment", — Luo Chao
- 15:15—15:45    Break
- 15:45—16:10    "Long range transport of trace species in Asia", — G. R. Carmichael
- 16:10—16:35    "The vertical transport, transformation and deposition of air pollutants by convective clouds", — Zhao Chunsheng
- 16:35—17:00    "Air quality model for photochemical smog in Beijing", — Li Jinlong

### August 2     Tuesday

#### **Session 2: Tropospheric Ozone Modeling and Observation (2)**

*Chairman: Prof. G. R. Carmichael*

*Prof. Tang Xiaoyan*

- 09:00—09:25    "The global emissions inventory activity(GEIA)", — Gregg Mar-



land

09:25—09:50 "Measurement of emission flux from forest soil and the mixing ratio of nitrous oxide in China", —Yang Wenxiang

**Session 3 Stratospheric Ozone Modeling and Observation (1)**

09:50—10:15 "Behavior of atmospheric ozone observed from space—challenges in stratospheric ozone modeling", —P. K. Bhartia

10:15—10:45 Break

10:45—11:10 "Measurement and analyses of atmospheric ozone profile in Qinhai plateau", —Guo Song

11:10—11:35 "Trifluoroacetic acid and the global environment", —Nien Dak Sze

11:35—12:00 "Measurements of O<sub>3</sub>, UV-B, NO<sub>2</sub> at Zhongshan Station Antarctica in the 93 'ozone hole', —Zheng Xiangdong

Lunch

**Session 4: Stratospheric Ozone Modeling and Observation (2)**

*Chairman: Dr. Joe McNeal, Prof. Qin Yu*

14:00—14:25 "Balloon observation of ozone and aerosol", —Xu Li

14:25—14:50 "The photolysis character of HCFC-22 in the presence of hydrogen peroxide", —Zhong Jinxian

14:50—15:15 "Model simulation of stratospheric ozone", —Malcolm K. W. Ko

15:15—15:45 Break

15:45—16:00 "Ozone climate: an interaction between radiation and chemistry", —Shi Guangyu

16:10—16:35 "Numerical analysis of internal gravity waves in an irrotational zonal vertical plane", —Zhang Daizhou

16:35—17:00 "Effect on ozone from tropospheric aerosol", —Liu Yu

**August 3      Wednesday**

**Session 5 Data/Model Intercomparison and Assessment**

*Chairman: Dr. P. K. Bhartia      Prof. Yang Wenxiang*

09:00—09:30 "The effect of the stratospheric ozone depletion on the tropospheric ozone change", —Tang Xiaoyan

09:30—10:00 "Rate Constants for the Reactions of OH with 8 Ketones from 270 to 430K", —Qiu Lianxiong

10:00—10:30 ODP: Nien Dak Sze

10:30—11:00 Break

11:00—11:30 OPP:Shaw C. Liu  
11:30—12:00 GWP:Malcolm K. W. Ko  
Lunch

14:00—15:30 Discussion of future collaborative research to be recommended to  
the 11th US—PRC Joint Working Group on Atmospheric Science  
and Technology  
15:30—16:00 Break  
16:00—17:00 Preparation of workshop summary

August 4      Thursday  
Scientific visit and signing ceremony

# REPORT DOCUMENTATION PAGE

Form Approved  
OMB No. 0704-0188

Public reporting burden for this collection of information is estimated to average 1 hour per response, including the time for reviewing instructions, searching existing data sources, gathering and maintaining the data needed, and completing and reviewing the collection of information. Send comments regarding this burden estimate or any other aspect of this collection of information, including suggestions for reducing this burden, to Washington Headquarters Services, Directorate for Information Operations and Reports, 1215 Jefferson Davis Highway, Suite 1204, Arlington, VA 22202-4302, and to the Office of Management and Budget, Paperwork Reduction Project (0704-0188), Washington, DC 20503.

1. AGENCY USE ONLY (Leave blank)		2. REPORT DATE January 1996	3. REPORT TYPE AND DATES COVERED Final January 1993 - December 1995	
4. TITLE AND SUBTITLE  Continued Development and Validation of the AER Two-Dimensional Interactive Model			5. FUNDING NUMBERS	
6. AUTHOR(S)  Malcolm K. W. Ko et al.				
7. PERFORMING ORGANIZATION NAME(S) AND ADDRESS(ES) Atmospheric and Environmental Research, Inc. 840 Memorial Drive Cambridge, MA 02139			8. PERFORMING ORGANIZATION REPORT NUMBER	
9. SPONSORING/MONITORING AGENCY NAME(S) AND ADDRESS(ES) NASA - Office of Mission to Planet Earth Science Division 300 E Street, S.W. Washington, DC 20546			10. SPONSORING/MONITORING AGENCY REPORT NUMBER	
11. SUPPLEMENTARY NOTES Stratosphere Ozone Climate - Chemistry interaction				
12a. DISTRIBUTION/AVAILABILITY STATEMENT  Unrestricted			12b. DISTRIBUTION CODE	
13. ABSTRACT (Maximum 200 words) Results from two-dimensional chemistry-transport models have been used to predict the future behavior of ozone in the stratosphere. Since the transport circulation, temperature, and aerosol surface area are fixed in these models, they cannot account for the effects of changes in these quantities, which could be modified because of ozone redistribution and/or other changes in the troposphere associated with climate changes. Interactive two-dimensional models, which calculate the transport circulation and temperature along with concentrations of the chemical species, could provide answers to complement the results from three-dimension model calculations. In this project, we performed the following tasks in pursuit of the respective goals: (1) We continued to refine the 2-D chemistry-transport model; (2) We developed a microphysics model to calculate the aerosol loading and its size distribution; (3) The treatment of physics in the AER 2-D interactive model were refined in the following areas--the heating rate in the troposphere, and wave-forcing from propagation of planetary waves.				
14. SUBJECT TERMS Stratosphere, ozone, chemistry-climate interaction, Stratospheric transport			15. NUMBER OF PAGES 147	
			16. PRICE CODE	
17. SECURITY CLASSIFICATION OF REPORT	18. SECURITY CLASSIFICATION OF THIS PAGE	19. SECURITY CLASSIFICATION OF ABSTRACT	20. LIMITATION OF ABSTRACT	